IAEA TECDOC SERIES

IAEA-TECDOC-1923

Material Properties of Unirradiated Uranium–Molybdenum (U–Mo) Fuel for Research Reactors

IAEA
International Atomic Energy Agency

MATERIAL PROPERTIES OF UNIRRADIATED URANIUM–MOLYBDENUM (U–MO) FUEL FOR RESEARCH REACTORS

The following States are Members of the International Atomic Energy Agency:

AFGHANISTAN
ALBANIA
ALGERIA
ANGOLA
ANTIGUA AND BARBUDA
ARGENTINA
ARMENIA
AUSTRALIA
AUSTRIA
AZERBAIJAN
BAHAMAS
BAHRAIN
BANGLADESH
BARBADOS
BELARUS
BELGIUM
BELIZE
BENIN
BOLIVIA, PLURINATIONAL STATE OF
BOSNIA AND HERZEGOVINA
BOTSWANA
BRAZIL
BRUNEI DARUSSALAM
BULGARIA
BURKINA FASO
BURUNDI
CAMBODIA
CAMEROON
CANADA
CENTRAL AFRICAN REPUBLIC
CHAD
CHILE
CHINA
COLOMBIA
CONGO
COSTA RICA
CÔTE D'IVOIRE
CROATIA
CUBA
CYPRUS
CZECH REPUBLIC
DEMOCRATIC REPUBLIC OF THE CONGO
DENMARK
DJIBOUTI
DOMINICA
DOMINICAN REPUBLIC
ECUADOR
EGYPT
EL SALVADOR
ERITREA
ESTONIA
ESWATINI
ETHIOPIA
FIJI
FINLAND
FRANCE
GABON
GEORGIA
GERMANY
GHANA
GREECE
GRENADA
GUATEMALA
GUYANA
HAITI
HOLY SEE
HONDURAS
HUNGARY
ICELAND
INDIA
INDONESIA
IRAN, ISLAMIC REPUBLIC OF
IRAQ
IRELAND
ISRAEL
ITALY
JAMAICA
JAPAN
JORDAN
KAZAKHSTAN
KENYA
KOREA, REPUBLIC OF
KUWAIT
KYRGYZSTAN
LAO PEOPLE'S DEMOCRATIC REPUBLIC
LATVIA
LEBANON
LESOTHO
LIBERIA
LIBYA
LIECHTENSTEIN
LITHUANIA
LUXEMBOURG
MADAGASCAR
MALAWI
MALAYSIA
MALI
MALTA
MARSHALL ISLANDS
MAURITANIA
MAURITIUS
MEXICO
MONACO
MONGOLIA
MONTENEGRO
MOROCCO
MOZAMBIQUE
MYANMAR
NAMIBIA
NEPAL
NETHERLANDS
NEW ZEALAND
NICARAGUA
NIGER
NIGERIA
NORTH MACEDONIA
NORWAY
OMAN
PAKISTAN
PALAU
PANAMA
PAPUA NEW GUINEA
PARAGUAY
PERU
PHILIPPINES
POLAND
PORTUGAL
QATAR
REPUBLIC OF MOLDOVA
ROMANIA
RUSSIAN FEDERATION
RWANDA
SAINT LUCIA
SAINT VINCENT AND THE GRENADINES
SAN MARINO
SAUDI ARABIA
SENEGAL
SERBIA
SEYCHELLES
SIERRA LEONE
SINGAPORE
SLOVAKIA
SLOVENIA
SOUTH AFRICA
SPAIN
SRI LANKA
SUDAN
SWEDEN
SWITZERLAND
SYRIAN ARAB REPUBLIC
TAJIKISTAN
THAILAND
TOGO
TRINIDAD AND TOBAGO
TUNISIA
TURKEY
TURKMENISTAN
UGANDA
UKRAINE
UNITED ARAB EMIRATES
UNITED KINGDOM OF GREAT BRITAIN AND NORTHERN IRELAND
UNITED REPUBLIC OF TANZANIA
UNITED STATES OF AMERICA
URUGUAY
UZBEKISTAN
VANUATU
VENEZUELA, BOLIVARIAN REPUBLIC OF
VIET NAM
YEMEN
ZAMBIA
ZIMBABWE

The Agency's Statute was approved on 23 October 1956 by the Conference on the Statute of the IAEA held at United Nations Headquarters, New York; it entered into force on 29 July 1957. The Headquarters of the Agency are situated in Vienna. Its principal objective is "to accelerate and enlarge the contribution of atomic energy to peace, health and prosperity throughout the world''.

IAEA-TECDOC-1923

MATERIAL PROPERTIES OF UNIRRADIATED URANIUM–MOLYBDENUM (U–MO) FUEL FOR RESEARCH REACTORS

INTERNATIONAL ATOMIC ENERGY AGENCY
VIENNA, 2020

COPYRIGHT NOTICE

For further information on this publication, please contact:

Research Reactor Section
International Atomic Energy Agency
Vienna International Centre
PO Box 100
1400 Vienna, Austria
Email: Official.Mail@iaea.org

Printed by the IAEA in Austria
July 2020

IAEA Library Cataloguing in Publication Data

Names: International Atomic Energy Agency.
Title: Material properties of unirradiated uranium–molybdenum (U–Mo) fuel for research reactors / International Atomic Energy Agency.
Description: Vienna : International Atomic Energy Agency, 2020. | Series: IAEA TECDOC series, ISSN 1011–4289 ; no. 1923 | Includes bibliographical references.
Identifiers: IAEAL 20-01344 | ISBN 978–92–0–115720–1 (paperback : alk. paper) |
ISBN 978–92–0–115820–8 (pdf)
Subjects: LCSH: Nuclear fuels. | Nuclear reactors — Materials — Testing. | Alloys — Thermal properties.

FOREWORD

Research reactors have been operating globally since the 1940s, and fuel research and development continues to the present. Since the mid-1990s, the focus has been on developing fuels to enable a reduction of uranium enrichment in civilian research reactor fuels. One of the most promising fuel forms for conversion to low enriched uranium (LEU) fuel is a uranium–molybdenum (U–Mo) alloy. There have been many significant advances in the understanding and development of U–Mo fuels, stimulated in the early years by the need to understand irradiation behaviour and early fuel failures during testing.

This publication presents the current knowledge on the unirradiated material properties of the different constituents of low enriched U–Mo fuel for research reactors. The information on material properties of all LEU U–Mo fuel constituents provided here is essential for fuel designers and reactor operators for evaluating the performance and safety of these new fuels.

The IAEA wishes to thank all the contributors to this publication. Special thanks are due to J. Snelgrove (United States of America) and H. Ryu (Republic of Korea), who led the effort to collect and compile the research results. The IAEA officer responsible for this publication was F. Marshall of the Division of Nuclear Fuel Cycle and Waste Technology.

EDITORIAL NOTE

This publication has been prepared from the original material as submitted by the contributors and has not been edited by the editorial staff of the IAEA. The views expressed remain the responsibility of the contributors and do not necessarily represent the views of the IAEA or its Member States.

Neither the IAEA nor its Member States assume any responsibility for consequences which may arise from the use of this publication. This publication does not address questions of responsibility, legal or otherwise, for acts or omissions on the part of any person.

The use of particular designations of countries or territories does not imply any judgement by the publisher, the IAEA, as to the legal status of such countries or territories, of their authorities and institutions or of the delimitation of their boundaries.

The mention of names of specific companies or products (whether or not indicated as registered) does not imply any intention to infringe proprietary rights, nor should it be construed as an endorsement or recommendation on the part of the IAEA.

The authors are responsible for having obtained the necessary permission for the IAEA to reproduce, translate or use material from sources already protected by copyrights.

The IAEA has no responsibility for the persistence or accuracy of URLs for external or third party Internet web sites referred to in this publication and does not guarantee that any content on such web sites is, or will remain, accurate or appropriate.

CONTENTS

1. INTRODUCTION

This publication provides information on the properties of uranium–molybdenum (U–Mo) fuel constituents for use in research reactor fuel. There has been substantial research and development of U–Mo fuel since the mid 1990s in the efforts to develop low enriched uranium (LEU) research reactor fuel. While much of this research and development included material properties studies of the U–Mo fuel constituent materials, there has not been a comprehensive overview of the results of these studies. This publication provides the compilation of results from multiple research programs into a single volume of U–Mo fuel material properties.

1.1. BACKGROUND

Since 1996, U–Mo alloys in the metastable γ phase have been the focus of the worldwide effort to develop and qualify a very-high-density fuel that would allow all research reactors to use LEU fuel [1], owing to their stability previously demonstrated during irradiation under the low-burnup, high-temperature conditions typical of fast reactors [2]. Gamma phase U–Mo alloys were extensively studied beginning around 1944 [3] through the early 1960s for use both as pressurized water reactor fuel [4] and as fast reactor fuel [2]. Materials property data for these alloys in the lower temperature, higher fission rate, and higher burnup regime of research reactors were needed to support fuel design, core performance, and safety analysis for research and test reactor fuels.

In this publication, the term ‘U–Mo’ is used as a shorthand notation for ‘U–Mo alloy’, normally with 6–12 wt% Mo, remainder U. In some cases, the term ‘U–Mo alloy′ is used explicitly for emphasis. The same nomenclature is used to represent binary, ternary, and quaternary metallic alloys or systems; specific alloy compositions are represented by ‘XaWbYcZ,’ where X is the dominant constituent element and ‘a,’ ‘b,’ and ‘c’ are the amounts of the alloying elements ‘W,’ ‘Y,’ and ‘Z’ in weight percent respectively. For example, U–10Mo represents a U–Mo alloy containing, nominally, 10 wt% Mo and 90 wt% U, while U–9Mo–1Nb denotes an alloy containing 9 wt% Mo, 1 wt% Nb, and 90 wt% U.

Because the uranium content of the alloy is maximized, and parasitic neutron absorption is minimized by minimizing the molybdenum content, 12 wt% of molybdenum is considered the maximum practical content for research reactor fuels. Most of the experimental work on U–Mo research reactor fuels has been with alloys containing nominally 7, 9, or 10 wt% Mo. Although some properties data presented in this publication were obtained from measurements on U–Mo alloys with varying Mo content, many properties data were measured only for U–10Mo samples. Users should take care when using the data presented in this publication for U–10Mo to estimate materials properties of U–Mo alloys with different Mo content. In addition, as will be seen in the discussions that follow, many U–Mo alloy properties are affected by the alloy’s processing history.

1.2. OBJECTIVE

The objective of this publication is to present the material properties of all U–Mo fuel constituents that are essential for fuel designers and reactor operators to evaluate the fuel’s performance and safety for research reactors. Many significant advances in the understanding and development of LEU U–Mo fuels have been made since 2004, stimulated in the early years

by the need to understand irradiation behavior and early fuel failures during testing. As the research into U–Mo fuel continues, it is considered a suitable time to complete a publication presenting the current knowledge on the unirradiated material properties of the different constituents of LEU U–Mo fuel for research reactors.

1.3. SCOPE

This publication provides an overview of the most important physical and mechanical property data available by the end of 2016 for unirradiated U–Mo alloys in the composition range now being developed for use in research reactors. Although U–Mo alloys were extensively studied in the 1960s as potential light water and fast power reactor fuels, their material property data still need to be collected and modelled into correlations for possible application as research reactor fuels. This publication is designed to provide an overview of property data available for U–Mo alloys for use in research reactors.

LEU U–Mo fuels consist not only of U–Mo alloys but also of fuel structural materials and new materials that are formed as a result of thermally and/or irradiation-induced reactions between the constituent materials of the fuel system. Discussed in this publication are structural materials, such as Al or Al–Si for the U–Mo/Al or U–Mo/Al–Si dispersion fuel matrix, Al alloys for the cladding, fuel–matrix/cladding interaction products, coating layer materials for a diffusion barrier on U–Mo fuel particles or foils, and burnable absorbers materials. Understanding the properties of these materials is as important as understanding the properties of the U–Mo alloys themselves in terms of the fuel design, fuel performance evaluation, and safety analysis of U–Mo fuel. The properties of composite and alloy material, such as the dispersion fuel meat, will be also described in the publication.

Users of this publication are expected to be mainly research reactor fuel designers and fabricators intending to analyze use of U–Mo fuels in current and future reactors, as well as regulators intending to analyze applications for licenses for use of U–Mo fuels.

1.4. STRUCTURE

For research reactors, U–Mo alloys can be used as a thin foil in a monolithic fuel[1] or as a particulate in a dispersion fuel. Section 2 of this publication describes U–Mo alloy material properties, that are directly applicable to monolithic fuel meat and to the U–Mo fuel particles in dispersion fuel meat. Melting temperature, specific heat capacity, thermal conductivity, thermal expansion, density, elastic moduli, strength, and elongation of U–Mo alloys are discussed. Many of these properties have been modelled as a function of Mo content or temperature. Most correlations are expressed as polynomial functions fit to the data, while a few are semiempirical correlations employing analytical functions suggested by theory, where the parameters in the correlations were determined by fits to the data.

The properties of U–Mo/Al or U–Mo/Ai–Si dispersion fuel meat are described in Section 3, along with properties of aluminium alloy cladding and aluminium matrix materials. A number of material properties of dispersion fuel meat can be derived from those of both U–Mo alloys and the matrix material using models for composite materials. However, some properties cannot easily be estimated due to the lack of available data. One of the largest deficiencies is that the area of the properties of U–Mo/Al_x (x = 3 or 4) compounds that form as a result of fuel–matrix interaction for aluminium–matrix dispersion fuel or fuel–cladding

[1] The term ‘monolithic’ is used to describe a fuel plate/foil, tube, or pin in which the fuel meat is comprised of a solid piece (or monolith) of U–Mo rather than of a dispersion of U–Mo particles in a matrix material.

interaction for U–Mo monolithic fuel clad in aluminium or aluminium alloy have not yet been characterized. For example, the thermal conductivity of these interaction compounds, which has a large impact on dispersion fuel behaviour, has not been measured. Instead, out-of-pile properties data of uranium aluminides with similar compositions have typically been used to estimate the in-pile properties of the interaction layers. Also, some of the mechanical properties of these compounds likely are needed to model fuel plate integrity.

The Appendix (Section A.1) provides information on how some of the properties data have been obtained and examined. The Appendix also contains an expanded discussion of the original sources of properties data; apparent errors in the source data; discrepancies and errors that have been introduced or propagated by subsequent authors citing an original source; and expanded discussion of recommended values of the materials properties included herein, when appropriate.

2. MATERIAL PROPERTIES OF U–Mo ALLOYS

This section of the publication presents the material properties of the U–Mo alloys, based on early research focused on light water and fast power reactors and more recent research based on research reactor fuel development programs.

2.1. INTRODUCTION

Prior to the current effort to develop LEU U–Mo fuels, most of the data on the physical properties of U–Mo alloys were produced between the early 1940s and the mid-1960s. These data were originally reported with limited access and, sometimes, with limited information on test specimen properties and experiment conditions. The data in the original reports were later compiled and published by various authors. The information provided in this section is intended to guide the reader on the sources and use of the properties presented.

2.1.1. Data sources

Perhaps the earliest open publication of U–Mo alloy property data related directly to U–Mo use as reactor fuel occurred at the first United Nations International Conference on the Peaceful Uses of Atomic Energy in 1955 [5, 6]. Soon thereafter, previously secret reports began to be declassified; McGeary's[2] 1955 report on corrosion resistance of uranium-based alloys [4], declassified in 1957, seems to be the earliest major report to become publicly available. This was followed by compilations of U–Mo data by Klein [7], Farkas et al. [8], Beghi [2], and Fackelmann et al. [9], along with a number of more narrowly focused reports.

Beghi's compilation is the most extensive, and it was used during the early days of U–Mo fuel development by the United States Reduced Enrichment for Research and Test Reactors (RERTR) program in the mid-1990s. The Soviet Union was also developing U–Mo fuel in the 1940s and 1950s; the first nuclear power plant in the Soviet Union began operation in Obninsk in 1954 using U–9Mo fuel in a magnesium matrix [10]. However, most of the information gained during the early development of Soviet U–Mo fuel remains classified. During the

[2] To conform with past citations of Ref. [4], the editor, R.K. McGeary, is cited singly rather than as one of the alphabetically listed authors: W.A. Bostrum, M.W. Burkart, E.K. Halteman, R.D. Leggett, R.K. McGeary, and T.R. Padden.

RERTR program, Rest et al. produced another compilation that included some of the U–Mo properties data developed during the first ten years of the program [11], and Burkes et al. published evaluations of thermophysical and mechanical properties data that covered both the data from the literature and newly measured data [12, 13, 14].

Fortunately, many of the references cited contained much more detailed descriptions of experiment conditions and analyses than could be included in this publication. The reader is encouraged to consult the original references as necessary to help discern the applicability of the data or correlations to particular situations; one example where such a review of information in the original reference(s) might be needed is when applying a U–10Mo based correlation to a different U–Mo alloy, as pointed out above.

When preparing a compilation of data, as was the objective of this publication, one often relies expeditiously on sources that were rather recent compilations of such data themselves, e.g. Ref. [11]; or that provided newly acquired data along with previously published data, many times from even earlier compilations, for comparison with the new data, e.g. Refs [12, 13, 14]. Sometimes an author will copy a citation from an earlier publication without verifying that both the citation and the data copied from the cited publication are correct. Though time saving and sometimes unavoidable, this practice may result in the propagation of errors contained in the earlier publications. Additionally, of course, the chance of transcription errors also exists. When possible, therefore, the U–Mo alloy data, except for mechanical properties[3], cited in the references used in this publication have been traced back to their origins in an effort to ensure the accuracy of the data presented herein. Specific corrections, interpretations, and references are discussed in the relevant sections below and, especially, in the Appendix. When relevant data were presented only in graphical format, numerical data were obtained by manual digitization; these data are tabulated in the Appendix to allow users of the present compilation full access to them.

2.1.2. Units, conversions, and temperature scales

The International System of Units (SI) is used with one minor exception: the density unit g/cm^3 is used instead of the numerically equivalent SI unit Mg/m^3 or the conventional SI unit kg/m^3 to conform to common usage by research reactor designers and operators. Also, correlations involving temperature are given in terms of degrees Celsius (°C) when that is the commonly used unit; however, some figures copied directly from the references will be in the Kelvin (K) temperature scale.

As described in Section 1.1, this publication adopts the terminology U–*x*Mo to describe a specific U–Mo alloy containing x wt% molybdenum and $(100 - x)$wt% uranium, again because weight percent is commonly used by reactor operators and fabricators. Technically, the terminology mass percent or mass fraction should be used because the amount of uranium or molybdenum in the alloy is measured in grams (g), a unit of mass. However, the tradition of referring to the quantity as weight is continued to avoid confusion.

The alloying contents can also be expressed in terms of atomic percent, and the following equations can be used to convert from one of these units to the other:

[3]Many of the mechanical properties of U–Mo alloy are very dependent on the metallurgical state of the alloy, resulting in considerable scatter in the properties; hence, the mechanical properties data in Section 2.7 are considered adequately representative and reliable, pending further measurements to be made during the U–Mo research reactor fuel development programs currently being pursued.

$$x \equiv x_{\mathrm{w}}^{\mathrm{Mo}} = 100\left[1 + \left(\frac{M^{\mathrm{U}}}{M^{\mathrm{Mo}}}\right)\left(\frac{100}{x_{\mathrm{a}}^{\mathrm{Mo}}} - 1\right)\right]^{-1} \quad (1)$$

$$x_{\mathrm{a}}^{\mathrm{Mo}} = 100\left[1 + \left(\frac{M^{\mathrm{Mo}}}{M^{\mathrm{U}}}\right)\left(\frac{100}{x_{\mathrm{w}}^{\mathrm{Mo}}} - 1\right)\right]^{-1} \quad (2)$$

$$x_{\mathrm{a}}^{\mathrm{U}} + x_{\mathrm{a}}^{\mathrm{Mo}} = 100 \quad (3)$$

$$x_{\mathrm{w}}^{\mathrm{U}} + x_{\mathrm{w}}^{\mathrm{Mo}} = 100 \quad (4)$$

$$M^{UxMo} = 0.01\, x_a^U M^U + 0.01\, x_a^{Mo} M^{Mo} = M^U - 0.01\, x_a^{Mo}(M^U - M^{Mo}) \quad (5)$$

where:
$x_{\mathrm{w}}^{\mathrm{U}}$, $x_{\mathrm{w}}^{\mathrm{Mo}}$ are the weight fractions (wt%) of U and Mo in the alloy;
$x_{\mathrm{a}}^{\mathrm{U}}$, $x_{\mathrm{a}}^{\mathrm{Mo}}$ are the atomic (molar) fractions (at.%) of the uranium and molybdenum in the alloy ;
M^{UxMo}, M^{U}, $M^{\mathrm{Mo}}$are the atomic (molar) masses of: the U–*x*Mo alloy, the uranium in the alloy, and the molybdenum in the alloy, (g/mol). [4]

When calculating M^{U} it is sufficiently accurate to ignore the ^{234}U and ^{236}U isotopic contents of the uranium and assume that the uranium consists only of ^{235}U and ^{238}U. The error is negligible for natural or depleted uranium (DU), less than 0.01% for LEU and less than 0.02% for highly enriched uranium.

However, it is important to account for the ^{235}U isotopic content of the uranium when calculating M^{U}, especially when interpreting the results of experiments. For example, most of the material properties reported herein were measured for U–Mo alloys prepared with either natural or depleted uranium, both of which have an atomic mass that rounds to 238.0 g/mol. However, most irradiation experiments are conducted using alloys produced with enriched uranium, where the uranium atomic mass ranges from 237.5 g/mol for 19.75% enrichment[5], to 235.3 g/mol for 93% enrichment. Thus, the molar mass of U–*x*Mo made with depleted uranium is ~1% larger than that made with 93%-enriched uranium.

Research and publication of results related to the U–Mo phase diagram began around 1943. From that time through 1990, the temperature scale has been redefined a number of times owing to experience gained in using the scales and from advances in measurement techniques. Any revision to a temperature scale that affected only temperatures below 0°C was not considered. The temperature scales used in this publication are:

(a) International Temperature Scale (ITS) of 1927 (ITS-27) [15]. This was the first internationally accepted practical temperature standard.
(b) International Temperature Scale of 1948 (ITS-48) [16]. The ITS-48 scale was amended in 1960, without changing the numerical values of the temperatures, and it was redesignated as the International Practical Temperature Scale (IPTS) of 1948 (IPTS-48). In the present work, the IPTS-48 scale designation has been used also for the time period

[4] The molar mass of molybdenum and its uncertainty have changed several times since 1938. The values published by the International Union of Pure and Applied Chemistry (IUPAC) [110, 111] are 95.95 ± 0.03 g/mol (1938), 95.94 ± 0.03 g/mol (1961), 95.94 ± 0.03 g/mol (1975), 95.96 ± 0.02 g/mol (2007), and 95.95 ± 0.01 g/mol (2013), where the date is that of the IUPAC recommendation, not its publication. These changes are negligible compared with uncertainties of other data used with it in calculations. Most calculations discussed in this book dependent on the value of the molar mass of molybdenum have been made using 95.94 g/mol, except as noted in the Appendix.

[5] The term 'enrichment' applies when $MU^5/MU > 0.72\%$ (the U^5 content of natural U); if $e < 0.72\%$, e is called the U^5 content or U^5 assay of the depleted U.

between 1948 and 1960. In changing from the ITS-27 to the IPTS-48, the melting points of uranium and molybdenum were reduced by 0.5°C and 13.8°C, respectively.

(c) International Practical Temperature Scale of 1968 (IPTS-68) [17]. There were changes from the IPTS-48 of 1°C from 740 to1109°C, 2°C from 1109 to 1656°C, 3°C from 1656 to 2105°C, 4°C from 2105 to 2500°C, and 5°C from 2500 to 2860°C, where the temperature intervals are based on the IPTS-48 scale.

(d) International Temperature Scale of 1990 (ITS-90) [18]. There was a change from IPTS-68 of -1ºC from 1621 to 3100ºC.

As each new temperature scale was approved, tables of corresponding temperatures on the various scales were tabulated by various authors [18, 19, 20]. Piecewise quadratic fits of the tabulated data were developed during the present work and used to transform temperatures from one scale to another in order to compare phase diagrams using a common temperature scale. It was assumed that unless the temperature scale being used was explicitly stated in the reference, the scale appropriate to the time the measurements were made was used. The temperature changes were small enough to have been ignored over the temperature range of interest for U–Mo fuel since the uncertainties in the temperatures were comparable or larger; however, the melting point of pure Mo is numerically ~10°C higher when using ITS-27 than when using ITS-90.

2.1.3. General comments on data accuracy and use

The Appendix in this publication describes the effort that has been made to identify possible mistakes in the transcriptions of the data into the original reports and subsequent compilations. Corrections have been suggested when appropriate to improve the accuracy of the data. These early reports, however, included little to no discussion of the uncertainties in the data. In many cases, the data were published only as curves, so digitization was used to extract numerical data, adding additional uncertainty to the data points. Extensive use of quadratic fits, either as single curves or as piecewise fits, has been made to make these data more user friendly. The fits have been shown with the data, in order to allow the user to assess the accuracy of the fits, assuming the data to be accurate.

Even though care has been taken to present accurate data, the possibility of errors still exists. More importantly, it will be seen that some material properties depend strongly on the metallurgical state of the U–Mo or on some other (perhaps, unidentified) parameters. For some properties, several distinctly different datasets are presented. Therefore, the user needs to make a judgment about which dataset or combination of datasets is most appropriate and about how much conservatism should be applied.

2.2. U–Mo EQUILIBRIUM PHASE DIAGRAM

An equilibrium phase diagram of an alloy allows one to predict its phase composition based upon its constituent contents and its temperature after all transformations have been completed. Even though the U–Mo alloy in the fuel is never in its equilibrium condition, the equilibrium phase diagram provides a starting point when studying the effects of composition on the fabrication and operation of the fuel.

2.2.1. Equilibrium phase diagram

The U–Mo equilibrium phase diagram published in 1990 by Massalski [21], and discussed in Section A.2.2 point (8) of the Appendix, has been the reference diagram for the current LEU U–Mo fuel development effort. Massalski's diagram shows the eutectoid transformation of γ' phase material (body centred cubic [bcc] γ–U containing Mo in solid solution) to form α phase material (orthorhombic α–U containing Mo in solid solution) and tetragonal γ' phase material (U_2Mo) to occur at 550°C, instead of at 565°C as measured by Dwight during the most recent measurement [22]. This apparent discrepancy ultimately led to review of the data in Massalski's phase diagram and tracing the data to their origins. The results of this effort are described in Section A.2 of the Appendix. The development of the U–Mo phase diagram was first reported by Ahmann et al. in 1945 [3]; however, that work and most other work on U–Mo were classified until the mid-1950s. Most of the work on the phase diagram until around 1960 was focussed on determining the phase boundaries and phase fields from ~60 to 100 wt% U and from room temperatures to temperatures above the uranium β phase to γ phase transition temperature (776°C). Saller et al. [23] proposed that the decomposition of the γ phase was a eutectoid reaction, and Bostrum and Halteman [24] confirmed that proposed reaction. Haltemann [25] described the structure of the γ' phase, and Dwight [22] published the last study of the U–Mo phase diagram below 19 wt% Mo and 900°C in 1960, reporting the eutectoid composition and temperature. Interestingly, the high-temperature (solidus and liquidus) data were provided either by Ahmann et al. [3] in 1945 or by Garg and Ackermann [26] in 1977, the earliest and the most recent studies, respectively.

Considerable information regarding the development of the U–Mo equilibrium phase diagram from around 1944 through 1990 is contained in Section A.2.1 and A.2.2 of the Appendix. Based on this information, a new phase diagram that more closely fits the measured data, shown in Fig. 1, has been developed; its use is recommended. Section A.2.4 of the Appendix provides a detailed description of how the proposed new phase diagram was constructed. The coordinates of the phase boundary junctions are shown on the diagram, and coefficients of the quadratic equations used to represent the phase transition boundaries are given in Table 8 found in section A.4.4 of the Appendix.

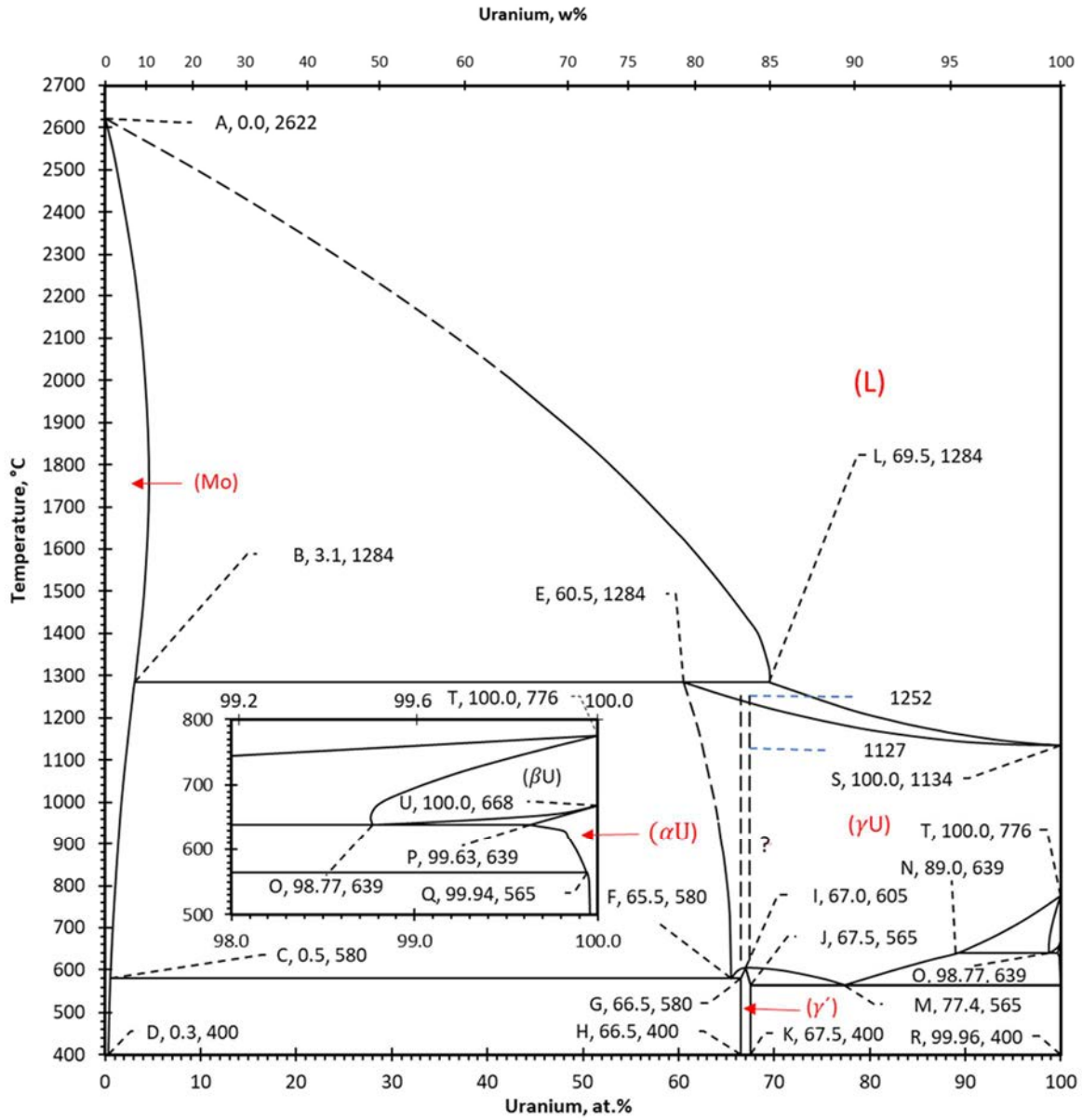

FIG. 1. Phase diagram of the uranium–molybdenum system developed during this work. The coordinates (atomic percent uranium, temperature) are shown for each transition-line junction (courtesy of James L. Snelgrove).

2.2.2. Melting temperature

An alloy generally does not melt at a single temperature upon heating; melting occurs progressively as the temperature increases from the solidus temperature (at which the first bit of solid melts, i.e. at which liquid first appears) to the liquidus temperature (at which the last of bit of solid melts and all is liquid). Those concerned with reactor design and safety usually think of the solidus temperature as the 'melting' temperature because that is the temperature at which the alloy begins to lose its integrity and begins to provide pathways through the liquid for the release of fission products. A fuel fabricator, on the other hand, might consider the liquidus temperature to be the 'melting' temperature since that is the temperature at which the alloy is fully molten, allowing rapid mixing of all constituents. The melting temperature of unalloyed uranium is 1134°C, and the melting temperature of U–Mo increases with Mo content for alloys of interest ($7 \leq x_w^{Mo} \leq 12$ wt% or $16 \leq x_a^{Mo} \leq 25$ at.%) as indicated by the solidus and liquidus

lines in the U–Mo binary phase diagram shown in Fig. 1. The equations of the solidus line and liquidus line are given by Eqs (38) and (39) of the Appendix, respectively, and are reproduced here as Eqs (6) and (7):

$$T_{\text{U–Mo solidus}} = 0.09982(x_a^U)^2 - 19.81(x_a^U) + 2117, (60.5 \le x_a^U \le 100) \quad (6)$$

$$T_{\text{U–Mo liquidus}} = 0.1236(x_a^U)^2 - 25.87(x_a^U) + 2485, (69.5 \le x_a^U \le 100) \quad (7)$$

2.2.3. Transformation kinetics

Cubic-structured γ phase U–Mo alloys are preferred for use in nuclear fuel because of the greater irradiation stability of the cubic structure compared to that of the orthorhombic structure of α phase uranium alloys. After high-temperature annealing at 800-1000ºC followed by quenching, U–Mo alloys above a certain Mo content will remain in the γ phase, but the γ phase will immediately begin to decompose into two phases at a temperature lower than the eutectoid reaction temperature. The rate of transformation of γ phase U–Mo solid solution to the $\alpha + \gamma'$ phases below the eutectoid temperature (~565°C) decreases with increasing molybdenum content.

It is useful to know the minimum Mo content required for U–Mo to retain its γ phase structure following quenching to room temperature. In 1951 Saller et al. [23] reported that U–Mo alloys with Mo content ≤12 at.% (5.2 wt%) decomposed during furnace cooling. In 1957 Bostrum and Halteman [24] reported that U–Mo with Mo content >7 wt% (15.7 at.%) retained the γ phase,[6] while U–Mo with Mo content from 2–7 wt% (4.8 – 15.7 at.%) underwent a diffusionless phase transformation following quenching. McGeary [4] had reported in 1955 that the diffusionless transformation does not occur consistently for Mo content between 5 and 7 wt%, a phenomenon he attributed to a dependence on quenching rate. In 1960 Dwight reported that his 12.7 at.% (5.54 wt%) specimen, as well as those with higher Mo content, had retained the γ phase. Beghi [2] reported the minimum Mo content for retaining the γ phase after quenching to be 5.4 wt% (12.4 at. %, citing a 1963 report by Repas et al., But, it was not clear where Repas et al. obtained this lower limit. Because it was stated so exactly, however, this value likely came from Van Thyne and McPherson [27], who had published a TTT curve for a 5.4 wt% alloy in 1959.

At temperatures below ~565°C, this γ phase alloy will gradually decompose into the $\alpha+\gamma'$ phases, hence the γ phase is metastable. During research reactor operation this is not an issue, because although U–Mo fuel is used at temperatures well below 565°C in research reactors, fission-induced processes stabilize the γ phase during irradiation [28]. In contrast, for fuel fabrication it is particularly important to understand metastable behaviour, since temperatures approaching the eutectoid temperature are used.

Of particular interest is the time required for an isothermally heated alloy to show the first sign of decomposition; such data are typically reported as time-temperature-transformation (TTT) diagrams, or TTT curves. Beghi [2] has provided a good summary of the results of a number of investigations of U–Mo decomposition rates performed in the 1950s and 1960s. Manually digitized data obtained from these TTT diagrams at temperatures between 450 and 550°C are plotted in Fig. 2. These data were originally produced by: Van Thyne and McPherson [27] Bellot et al. [29] (obtained from Beghi's [2] fig. 7), Donze and Cabane [30] (obtained from Beghi's fig.8), McGeary [4], Peterson et al. [31], and Repas el al. [32]; using primarily the

[6] Parida et al. [47] quoted Bostrum and Halteman's value of 7 wt% [24], but mistakenly reported it as 7 at.% (2.94 wt%). Burkes et al. [35] also reported Parida's erroneous value, as did Leenaers [36].

following measurement techniques, respectively: dilatometry, metallography; metallography, combination of resistivity, hardness, and metallography; and combination of metallography, hardness, and dilatometry.

The reconstructed TTT diagrams shown in Fig. 2 are not as smooth as the original diagrams because of the limited number of temperatures at which digitization was performed; nevertheless, the basic characteristics of the diagrams can be seen. There is considerable spread in the positions and shapes of the diagrams for a given alloy from different investigators, especially for the 7 and 8 wt% alloys, much of which results from the measurement techniques used. As discussed briefly in Section A.3 of the Appendix, certain measurement techniques are better suited to detect the onset of transformation than others, depending on the speed of the transformation mechanism at the temperature of interest. Therefore, one could consider making a composite TTT diagram for each of the different alloys shown in Fig. 2 by tracing along the smallest-time portions of intersecting curves of a given color. The change of the color of the groups of curves from left to right clearly shows that increasing the Mo content significantly increases the time required for the transformation to begin. An expanded discussion of U–Mo TTT diagrams can be found in Section A.3 of the Appendix.

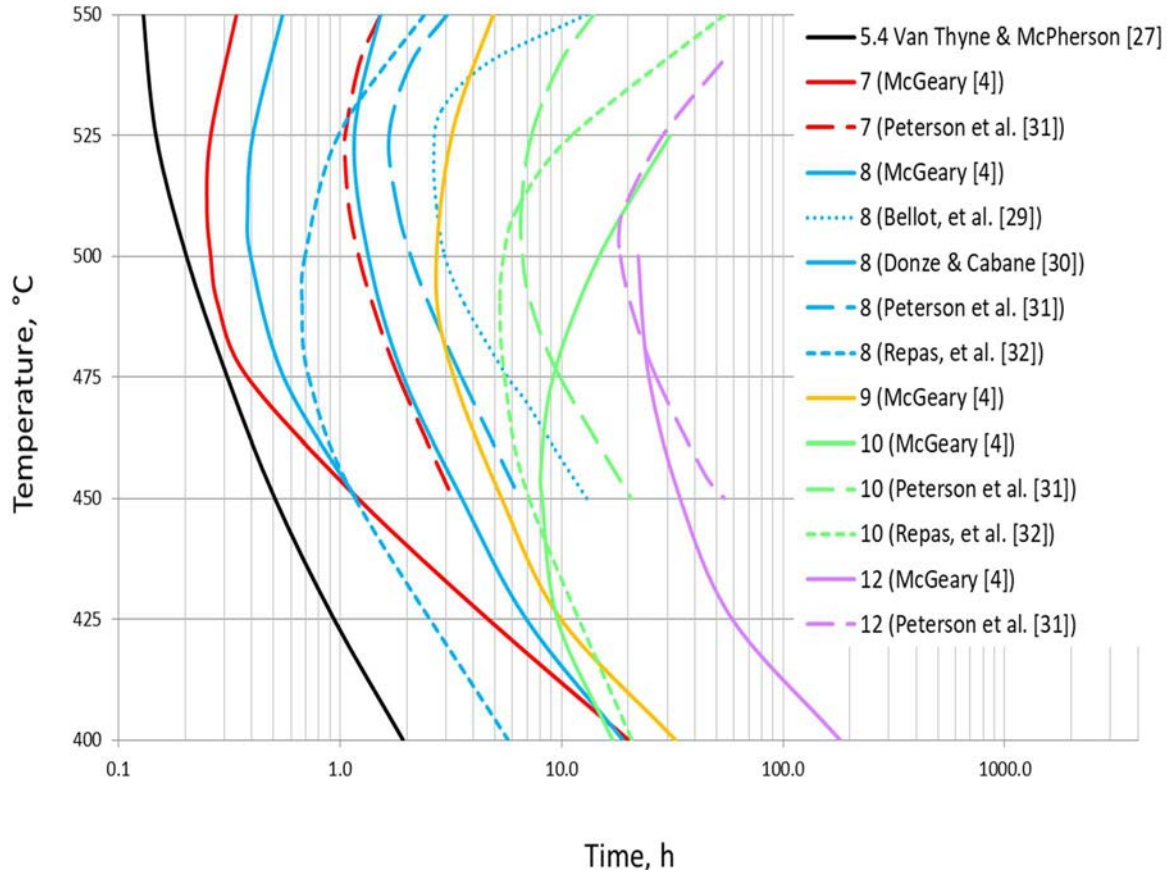

FIG. 2. TTT diagrams developed by various investigators during the 1950s and 1960s. The molybdenum content of the alloy and the investigator are listed in the legend. Note that the diagrams are color-coded by Mo content and investigator-coded by curve type and methodology coded by line type (metallography – solid, resistivity +hardness + metallography – long dashes, metallography + hardness – short dashes dilatometry – dots) coded by line type (courtesy of Argonne National Laboratory).

2.3. ROOM TEMPERATURE DENSITIES OF γ PHASE U–Mo ALLOYS

Two densities can be determined for any crystalline material — its theoretical density and its effective (i.e. 'real world') density. The theoretical density is determined from the formula mass and volume of a unit cell of a perfect crystal of the material, which, in practice, cannot be produced, hence the name, theoretical. The effective density of a crystalline material, either as found in nature or as manufactured, takes into account flaws and defects in the crystal lattice or in the bulk material, such as vacancies, voids, impurities, etc.

Density changes that occur as U–Mo alloys are heated or cooled are also important for fuel design and reactor safety analyses. These changes occur because the volume of the material changes as the temperature changes; therefore, density as a function of temperature will be discussed as part of the thermal expansion topic in Section 2.4. If temperature is not explicitly mentioned, then the properties being discussed are at room temperature.

2.3.1. Theoretical densities of room-temperature U–Mo alloys

Molybdenum, γ–U, and γ phase U–Mo alloy have a bcc crystal structure, comprised of a lattice of unit cells. A bcc unit cell is a cube with side a_0 and contains two 'atoms' of mass equal to the molar mass of the material divided by the Avogadro constant, N_A.; one 'atom' is located at the centre and one-eighth of an 'atom' is located at each corner of the cube. The lattice parameter[7] is measured by either X ray or neutron diffraction. The theoretical density of a bcc material is calculated by using the equation

$$\rho_{\text{theor}} = \frac{2\text{M}}{\text{N}_\text{A}(a_0)^3} \times 10^{24} \tag{8}$$

where ρ_{theor} is the theoretical density in g/cm^3, M is the molar mass of the material in g/mol, N_A is the Avogadro constant, and a is the lattice parameter in Å (1 Å = 10^{-8} cm).

Six sets of lattice parameter data for bulk U–Mo produced by melting and casting are discussed and analysed in Section A.4.2 of the Appendix: Wilson and Rundle in 1949 [33], McGeary in 1955 [4], Dwight in 1960 [22], Nomine et al. in 1974 [34], Burkes et al. in 2009 [35], and Leenaers in 2014 [36]. Note that Burkes et al.'s samples additionally were hot rolled to foils before the lattice parameter measurement.

The lattice parameters obtained from the bulk U–Mo samples are shown in Fig. 3, where one sees that all lattice parameters except those measured by Wilson and Rundle are tightly grouped over the range of Mo content now being considered for LEU U–Mo fuels (7–10 wt%, or 13.7–25/3 at/%). Although the lattice parameters measured by Leenaers are among those that are tightly grouped, a fit to her data exhibits a significantly steeper negative slope than the other datasets. Therefore, as discussed in the Appendix, a lattice-parameter correlation was developed of all the data except those of Wilson and Rundle [33] and Leenaers [36]. As seen in Fig. 3, this correlation and Dwight's [22] correlation are very similar over the plotted range of Mo content; assuming an uncertainty in the measured Mo content of ±0.47 at.%, as discussed in the Appendix, these two correlations substantially overlap. The difference in density calculated using one or the other of these two correlations is only 0.03 g/cm^3 for U–6Mo and 0.01 g/cm^3 for U–12Mo. Because Dwight's published least squares linear fit [22],

[7]The term 'lattice parameter' is commonly used interchangeably with 'lattice constant.' In this publication, 'parameter' has been chosen because the lattice parameter changes with temperature, addition of impurities, introduction of defects in the crystal, etc.

$$a_0^{\gamma UxMo} = 3.4808 - 0.00314x_a^{Mo}, \text{ (equilibrium } \gamma \text{ phase , } 12.7 \le x_a^{Mo} \le 33.3) \quad (9)$$

where $a_0^{\gamma UxMo}$ is the lattice parameter at room temperature in Å and x_a^{Mo} is the Mo content of the U–Mo alloy in at.%, has been used for almost 60 years, it is recommended that it continue to be used for bulk U–Mo.

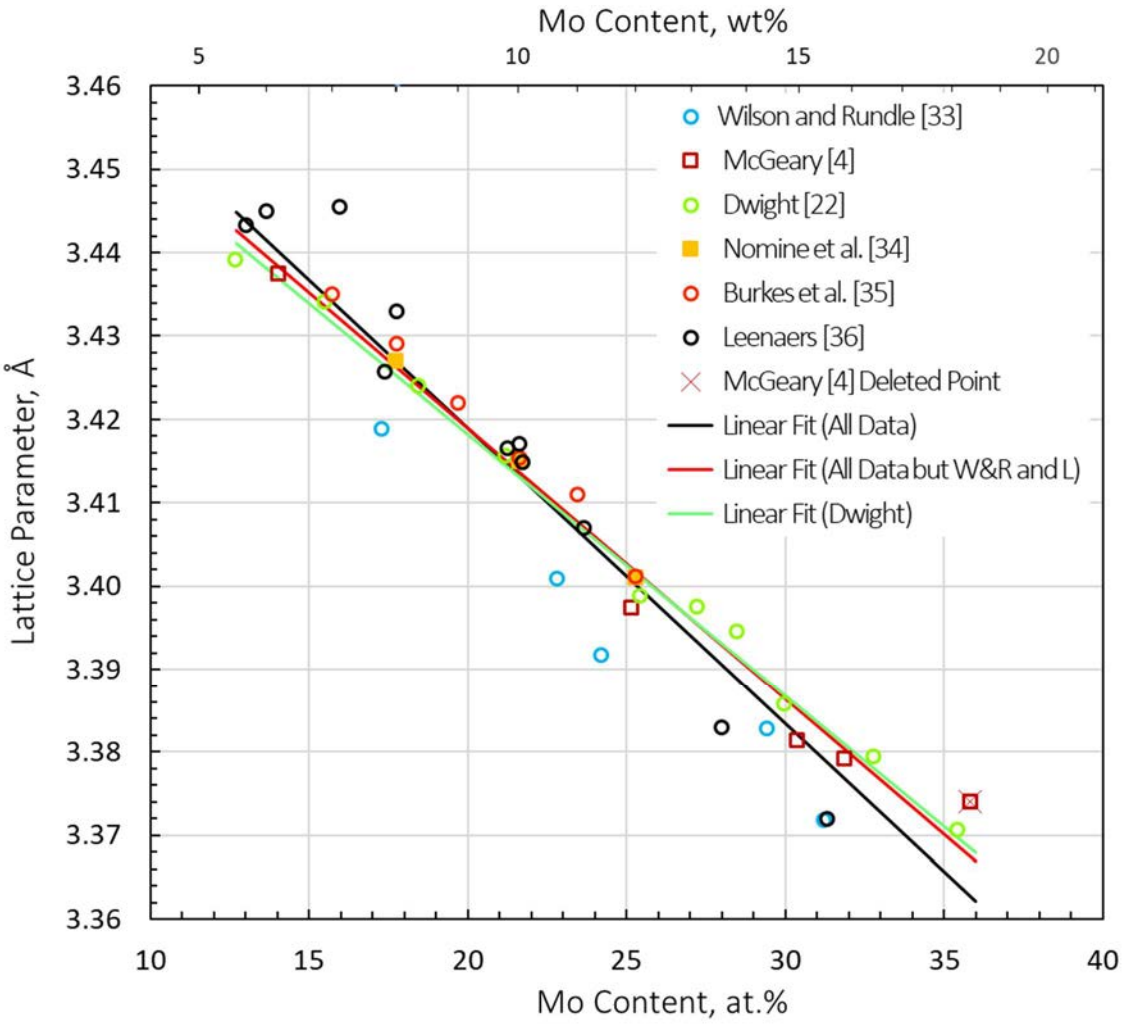

FIG. 3. Measured lattice parameters of gamma phase U–Mo bulk alloys shown with linear least squares fit lines (courtesy of James L. Snelgrove).

The theoretical density of γ phase natural or depleted bulk uranium, based on the lattice parameter from Eq. (9), is 18.74 g/cm^3. A least squares fit of U–Mo theoretical densities calculated using Eq. (8) at ~0.5 at.% Mo intervals between the limits of Mo content that allow formation of metastable γ phase U–Mo (where a is calculated using Dwight's lattice parameter correlation, Eq. (9), and M is calculated using Eq. (5)) yields the following equations:

$$\rho_{theor,Dw}^{\gamma UxMo} = 18.74 - 0.0603x_a^{Mo} - 0.000246(x_a^{Mo})^2, (12.7 \le x_a^{Mo} \le 33.3) \quad (10)$$

$$\rho_{theor,Dw}^{\gamma UxMo} = 18.74 - 0.151x_w^{Mo} - 0.000875(x_w^{Mo})^2, (5.5 \le x_w^{Mo} \le 16.8) \quad (11)$$

where $\rho^{\gamma UxMo}_{theor,Dw}$ is the theoretical density of γU–xMo in g/cm^3 calculated using Dwight's correlation for the lattice parameter and (x_a^{Mo}, x_w^{Mo}) is the Mo content of the alloy in (at.%, wt%).

A rule of mixtures (RoM) formula has often been used to estimate the theoretical density of an alloy; for natural or depleted UxMo, one should use Eq (47), developed in Section A.4.3 of the Appendix and shown here as Eq. (12):

$$\rho^{\gamma UxMo}_{theor,RoM} = (0.05336 + 0.000445x_w^{Mo})^{-1}, (5.5 \leq x_w^{Mo} \leq 16.2) \quad (12)$$

where the quantities are defined as for Eqs (10, 11). It is important to remember to use the extrapolated γ–U density based on its room-temperature lattice parameter (18.74 g/cm^3) presented above when estimating the density of a U–Mo alloy in the metastable γ state.

Thus far, only the theoretical density of bulk U–Mo alloys has been discussed. However, the U–Mo powder now being used in the development of dispersion fuel is being produced by atomization. One set of lattice parameter measurements has been made using atomized powder, but further study is needed to understand these data. They are discussed in the final paragraphs of Section A.4.2. of the Appendix.

2.3.2. Effective densities of room-temperature U–Mo alloys

The effective density of a piece of U–Mo is determined directly from its mass and volume. The most accurate way to determine the volume, generally known as Archimedes' method, is to measure the difference in the weight of a piece of U–Mo alloy in air and in a liquid (usually water) and divide by the density of the liquid at ambient temperature. Most of the densities discussed here were determined on lab-scale specimens of U–Mo alloys cut from arc-melted buttons, castings, or further-processed material. The particle density of a powder sample can be determined using a liquid pycnometer (Archimedes' method) or a gas expansion pycnometer (based on Boyle's law).

The only set of measured room temperature densities covering the full range of metastable γ phase U–Mo alloys appears to be the one published by McGeary [4] for six U–Mo alloys with Mo contents in the range of 6 to 25 wt%, measured in the early to mid-1950s using the Archimedes method. Though not stated explicitly, it has been assumed that the alloys were prepared using natural or depleted uranium. These data are plotted in fig. 8 of Ref. [4], along with theoretical densities calculated from lattice parameters measured for the same alloys; an adaptation of this figure is shown in Section A.4.4 of the Appendix. The measured densities, determined from their Cartesian coordinates on the plot, are shown in Fig. 4 below and listed in Table 13 in Section A.4.4 of the Appendix. The theoretical densities, also plotted in Fig. 4 and listed in Table 13, are on average about 1% higher than the measured densities, suggesting that the samples contained only a small amount of porosity. McGeary reports that the probable errors (standard deviations) in the density and the Mo content are ±0.006 (±0.009) g/cm^3 and ±0.4 (±0.6) at.%, respectively; some additional error has been introduced by digitizing the data in McGeary′s fig. 8. Section A.4.4 of the Appendix contains a more detailed discussion of McGeary′s measured densities. It was concluded that a linear least squares fit of McGeary′s three lowest-Mo-content effective-density data points alone should be most representative of metastable γ phase U–Mo, yielding the following equation:

$$\rho^{UxMo}_{fit,McG} = 18.59 - 0.0674x_a^{Mo} \quad (13)$$

where ρ^{UxMo} is in g/cm^3 and x_a^{Mo} is in at.%.

The constants and coefficients of Eqs (10, 11, 12, and 13) were derived for the U–Mo alloys containing depleted or natural uranium. The process and an equation for converting densities from one uranium assay (or enrichment) to another are discussed in Section A.4.5 of the Appendix. The resulting equation, Eq. (52), is reproduced here as Eq. (14):

$$\rho_{e_2}^{\mathrm{UxMo}} = \frac{\left[238.05+1.421x_a^{\mathrm{Mo}}-0.0301\left(1-0.01x_a^{\mathrm{Mo}}\right)e_2\right]}{\left[238.05+1.421x_a^{\mathrm{Mo}}-0.0301\left(1-0.01x_a^{\mathrm{Mo}}\right)e_1\right]}\rho_{e_1}^{\mathrm{UxMo}} \tag{14}$$

where ρ^{UxMo} is the density (g/cm^3), x_a^{Mo} is the concentration (at.%), and e is the enrichment (at.%).

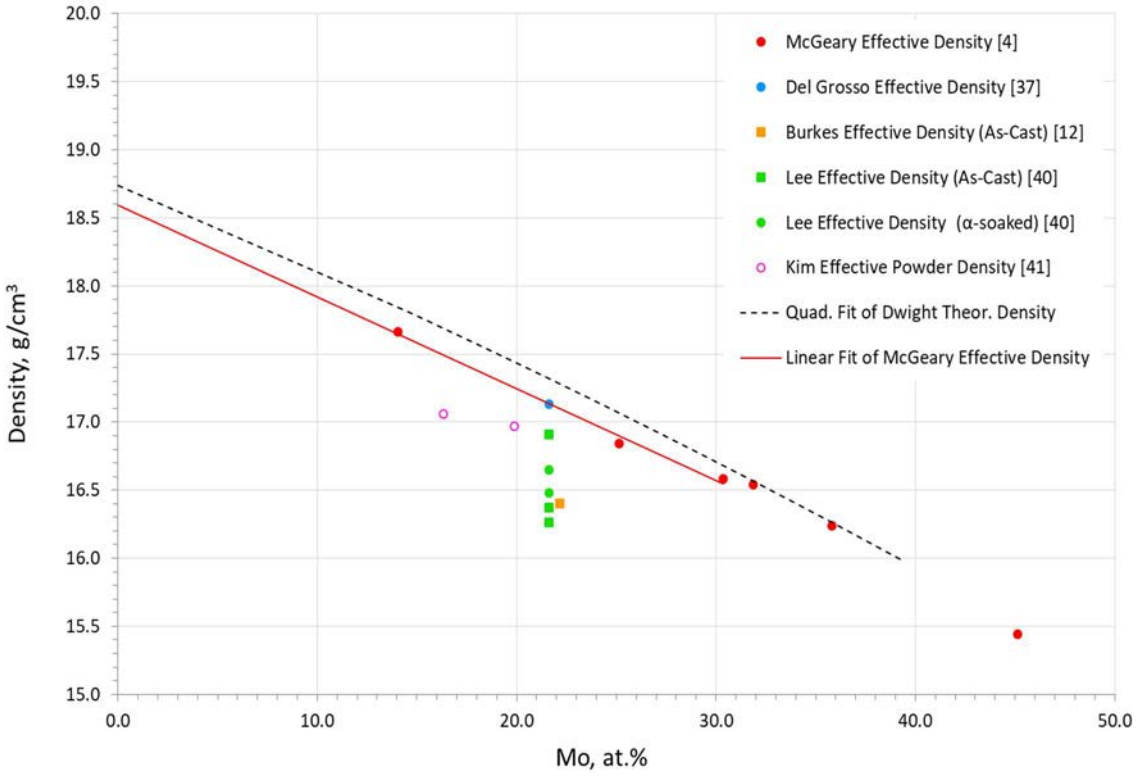

FIG. 4. Measured effective and calculated theoretical densities of U–Mo alloys as a function of molybdenum content (courtesy of Argonne National Laboratory).

Other experimenters have reported room-temperature densities of one or two U–*x*Mo alloys, especially U–10Mo; several of these were reported as the room temperature density obtained during studies of U–Mo density vs. temperature.

Del Grosso [37], in his fig. 4, showed the density of γ quenched U–10Mo, from data obtained by the Southern Research Institute for Atomic Power Development Associates, Inc. (APDA), to be 17.13 g/cm^3. The density data reported graphically by Del Grosso, is reported also in tabular form in Ref. [38], and Section A.5.2.3 of this publication presents further discussions of the APDA density data.

Gates et al. [39] reported the pre-irradiation densities of 14 γ quenched U–10Mo samples prepared by Battelle Memorial Institute (BMI) for APDA; the average density was 17.15 ± 0.05 g/cm^3, consistent with the values reported in Refs [37] and [38].

Burkes et al. [12] reported the density of as-cast 10.3 ± 0.5 wt% U–Mo to be 16.4 ± 0.1 g/cm^3.

Lee et al. [40] reported the densities of two U–10Mo ingots to be 16.26 and 16.91 g/cm^3 in the as-cast condition and 16.48 and 16.65 g/cm^3 in the γ quenched condition; a third ingot had a density of 16.37 g/cm^3 both in the as-cast condition and after being α soaked for 140 h.

Kim et al. [41] reported the theoretical densities of U–7.3Mo and U–9.1Mo to be respectively 17.53 and 17.19 g/cm^3, which are in reasonable agreement with 17.69 and 17.44 g/cm^3 calculated using Eqs. (8) and (9). However, they also reported the actual densities of U–7.3Mo and U–9.1Mo powders, produced by centrifugal atomization, to be 17.06 and 16.97 g/cm^3, respectively; these values are 2.7–3.5% lower than the theoretical values calculated using Eq. (11) owing mainly to central voids contained in many of the particles.

All measured densities discussed above ranged from about 0.2 to 6% lower than the corresponding theoretical density based on Dwight's lattice parameters; they are also shown in Fig. 4. The average deviation of the effective density from theoretical was 4.8 ± 1.7% for the four as-cast samples and 1.9 ± 1.8% for the seven γ quenched samples. The production method and subsequent heat treatment, if any, were likely responsible for most of the differences. Therefore, fabricators should measure density of U–Mo alloys created by their own specific fabrication processes. In the absence of fabrication data, if one needs to estimate the room temperature effective density of a U–Mo alloy with a specific Mo content, one should calculate the theoretical density using Eq. (11) and decrease that value by ~4.5% for as-cast material and by ~1.5% for γ quenched material to account for real world effects that reduce the density.

2.4. THERMAL EXPANSION AND DENSITIES OF U–Mo ALLOYS AT ELEVATED TEMPERATURE

2.4.1. Thermal expansion as a function of temperature

Knowledge of the thermal expansion[8] of a fuel alloy is important in the design of a fuel element and even in the analysis of the results of some fuel development irradiation test results. Hence, it is not surprising that thermal expansion data were obtained during U–Mo fuel development in the 1950s for use in power reactors and again in the current development period beginning in the late 1990s for use as LEU fuel for research reactors.

The definitions of the instantaneous and average coefficients of thermal expansion, as well as the equations associated with the expansion and density change of U–Mo alloys as their temperature changes, are given in Section A.5.1 of the Appendix. The following quadratic functions of temperature were found to be very useful in fitting thermal dilation[9] data:

$$\Delta L(T)/L_0 = a_2T^2 + a_1T + a_0 \tag{15}$$

$$\alpha(T) = 2a_2T + a_1 \tag{16}$$

$$\bar{\alpha}(T_0, T) = a_2(T + T_0) + a_1 \tag{17}$$

where $\Delta L(T) = L(T) - L(T_0)$ $L(T)$ and $L(T_0)$ are the lengths of the specimen at temperature T and T_0, respectively; T_0 and T are the initial and final temperatures in °C; a_2, a_1, and a_0 are coefficients determined during the fitting process; and α and $\bar{\alpha}$ are the instantaneous and average coefficients of linear thermal expansion in 10^{-6}°C^{-1}. It is seen that $\alpha(T)$ is the slope of

[8] The term 'expansion' is used for convenience when discussing both heating or cooling (negative expansion, rather than 'contraction').

[9] The term 'dilation' and $\Delta L(T)/L_0$ are used interchangeably in the text.

the dilation curve at any temperature, and $\bar{\alpha}(T_0, T)$ is the average slope of the dilation curve over the temperature interval of T_0 to T.

Original thermal expansion data for U–Mo alloys have been reported, most often as coefficients of thermal expansion in several previous works, listed in order of publication date: McGeary [4], Saller et al. [42], Del Grosso [37], Konobeevsky et al. [43], Riddle [44], and Burkes et al. [12, 13]. These thermal expansion data are discussed in detail in Section A.5 of the Appendix. In McGeary′s fig. 7, the average coefficients of linear thermal expansion are plotted from 100 to 400°C for γ quenched U–Mo alloys with nominal Mo contents of 3, 6, 9, 10.5, 12, 15, and 18 wt%. It is not reported whether these data were derived only from the heating curve, or from an average of the heating and cooling curves. Equation (56) in Section A.5.1 was used to convert average coefficients of thermal expansion to dilations. Because U–Mo alloys containing less than ~5.4 wt% Mo cannot be retained in the metastable γ state at temperatures less than the eutectoid temperature, a least squares linear fit of the dilation data excluding U–3Mo has been made, resulting in the following equation:

$$\frac{\Delta L}{L_0(100,\,400)}_{\text{fit, McG}} = 0.474 - 0.00705 x_{\text{w}}^{\text{Mo}} \quad (6 \le x_{\text{w}}^{\text{Mo}} \le 18) \tag{18}$$

where $\frac{\Delta L}{L_0}$ is in % and x_{w}^{Mo} is in wt%. Owing to the considerable scatter in the data and there being only one value of ΔT, Eq. (18) likely is of limited value.

The bulk of the data are based on an initial temperature (T_0) ranging from 20 to 30°C (room temperature). As discussed in Section A.5.2.1 of the Appendix, McGeary showed portions of dilation curves between ~20 and ~750°C, for several γ quenched alloys, but the incompleteness of the curves for U–9Mo and U–12Mo did not warrant an effort to digitize them. Saller et al. made measurements both on α soaked and on γ quenched specimens, Burkes et al. used as-cast specimens, and the other three sources reported data only from γ quenched specimens. Saller et al., Del Grosso, and Burkes et al. reported separately dilation data obtained during the heating and cooling portions of a measurement cycle, while Riddle reported that he saw no difference between the dilation curves during heating and cooling; his curve represented an average of the two. Konobeevsky et al. did not identify the portion (or portions) of the cycle from which their data came and reported the instantaneous coefficient of thermal expansion as a linear function of T; for this work, it has been assumed that their data was for heating only. Dilation data from the four remaining sources, determined either directly from dilation curves, or back-calculated from average coefficients of thermal expansion, are tabulated and discussed in the Appendix. Del Grosso also reported the only thermal expansion measurements in the transverse direction found in the literature. A number of other authors have quoted data from the original sources, and the data from secondary (or tertiary) sources have been compared to data from the original sources. In some instances, transcription errors have occurred or the data have been misinterpreted. Again, these are discussed in Section A.5 of the Appendix.

The data reported in [12, 13, 37, 42, 43, 44] and evaluated during this work were for alloys with Mo content ranging from 7.2 to 12.1 wt% and for maximum temperatures ranging from 500 to 1000°C. Least squares fits of the dilation data, using Eq. (15) for single quadratic curves or Eq. (66) from Section A.5.1 of the Appendix for piecewise quadratic curves, yielded coefficients a_2, a_1, and a_0. Values of a_2, a_1, and a_0 are listed in Table 1 and the resulting dilations are plotted in Fig. 5. The solid curves accompanying each set of measured data points shows the dilation calculated using the fit coefficients in Table 1.

Several general observations can be made about U–Mo thermal expansion:

(a) The shape of the dilation curve is dependent on the metallurgical state of the alloy. Phase transitions and other metallurgical changes that occur in U–Mo are often accompanied by

volume changes. Such effects are usually seen during the first heating cycle. Burkes et al.'s measurement of dilation curves during three complete heating and cooling cycles [12, 13], discussed in Section A.5.2.6 of the Appendix, illustrates the complex behaviour of a U–Mo alloy initially in a complex (as-cast) metallurgical state. The shape and slope of each of the cooling curves are very different from those measured by other investigators.

(b) Because the $\alpha + \gamma'$ to γ transformation above 565°C occurs much more rapidly than the reverse transformation below 565ºC, the initial heating curve of a U–Mo alloy that contains a considerable amount of the $\alpha + \gamma'$ phases will look quite different than the following cooling curve and from a subsequent heating curve. Sometimes, as evident in the dilatometer traces shown in fig. 2 of Burkes et al. [12], several complete heating and cooling cycles may be required for the sample to become metallurgically stable.

(c) U–Mo alloys undergo hysteresis when heated from and then cooled back to a given temperature below the γ to $\alpha + \gamma'$ phase transformation temperature. If the alloy undergoes a phase transformation during heating, the alloy when cooled will have expanded; if no phase transformation has occurred, the alloy when cooled will have contracted [4]. The magnitude of this hysteresis was relatively small (~0.02 to 0.04% $\Delta L/L_0$) for test specimens that had been α soaked or γ quenched before testing; however, the magnitude of this effect was about ten times as great for Burkes et al.'s as-cast specimens. No discussion about total hysteresis during repetitive cycles was discovered in the literature; it is assumed that the negative effect once a specimen has been fully converted to γ phase material would eventually reduce the length of the specimen back to its original length. On the other hand, if several cycles are required for the specimen to become fully γ phase material, the total length increase from hysteresis could be equivalent to the effect of heating to high temperatures.

(d) The situation described just above raises a question about how U–Mo thermal expansion measurements should be made and which of the data obtained best represents U–Mo's 'real world' thermal expansion behaviour. For a one-cycle measurement, should the heating curve, the cooling curve, or an average of the two be used? For a multicycle measurement, should data from all cycles be considered, or just the data from the final cycle? Perhaps the differences between heating and cooling data, or cycle-to-cycle data are small enough not to significantly affect the results of analyses using the thermal expansion data. Because the metallurgical state of the alloy does affect its thermal expansion, careful consideration of the particular case being analysed may be necessary to select the best data to use. Use of the thermal expansion during heating is more conservative than using either the data obtained during cooling (least conservative) or an average of the heating and cooling data; however, one should guard against being overly conservative.

TABLE 1. COEFFICIENTS OF QUADRATIC FIT EQUATIONS FOR γ QUENCHED U–Mo DILATIONS DURING HEATING AND COOLING

Data Source	U*x*Mo, x_w, (wt%)	U*x*Mo, x_a, (at.%)	Dilation Direction	Range of Validity, (°C)	Section of Dilation Curve	Eq. No.	a_2, (10^{-7} %/°C^2)	a_1, (10^{-3} %/°C)	a_0, (10^{-2} %)
Saller et al. [42]	7.18	16.1	Long	20–550	H1	(85)	6.160	1.130	−4.10
				550–950	H2	(86)	2.199	1.536	−14.28
				20–550	C1	(87)	6.075	1.166	−12.12
				550–950	C2	(88)	5.942	1.129	-9.40
Saller et al. [42]	9.36	20.4	Long	20–550	H1	(81)	5.286	1.253	-2.84
				550–950	H2	(82)	-2.147	2.076	-25.45
				20–550	C1	(83)	5.378	1.128	−5.97
				550–950	C2	(84)	8.692	0.699	7.53
Saller et al. [42]	12.10	25.5	Long	20–550	H1	(89)	4.032	1.093	-4.59
				550–950	H2	(90)	5.960	0.891	0.86
				20–550	C1	(91)	4.877	1.066	−8.52
				550–950	C2	(92)	6.955	0.802	-0.41
Del Grosso [37]	10 (Nom)	21.6	Long	30–550	H1	(102)	6.085	1.067	−3.85
				550–900	H2	(103)	1.227	1.771	−27.8
				30–550	C1	(104)	5.367	1.071	-0.01
				550–900	C2	(105)	7.547	0.800	8.32
Del Grosso [37]	10 (Nom)	21.6	Trans	30–550	H1	(106)	6.804	1.379	−4.39
				550–900	H2	(107)	−3.342	2.399	−30.03
				30–550	C1	(108)	4.942	1.210	-2.30
				550–900	C2	(109)	9.144	0.949	-0.65
Riddle [44]	10 (Nom)	21.6	Long	25–600	<H, C>[a]	(113)	4.051	1.096	−2.83
Burkes et al. [12, 13]	10.3	22.2	Long	27–250	H1	(116)	7.194	1.095	-3.09
				250–350	H2	(117)	3.524	1.900	-20.92
				350–650	H3	(118)	4.384	1.203	2.15
				650–800	H4	(119)	44.27	-4.098	178.2
				27–250	C1	(120)	-1.490	1.253	34.95
				250–350	C2	(121)	-3.192	1.348	33.63
				350–650	C3	(122)	4.485	0.937	38.61
				650–800	C4	(123)	-8.453	2.440	-4.42
Konobeevsky [43]	9 (Nom)	19.7	Long	20–500	H[b]	(111)	1.4	1.16	−2.33

[a]: Average of heating (H) and cooling (C) curves.

[b] Assumed

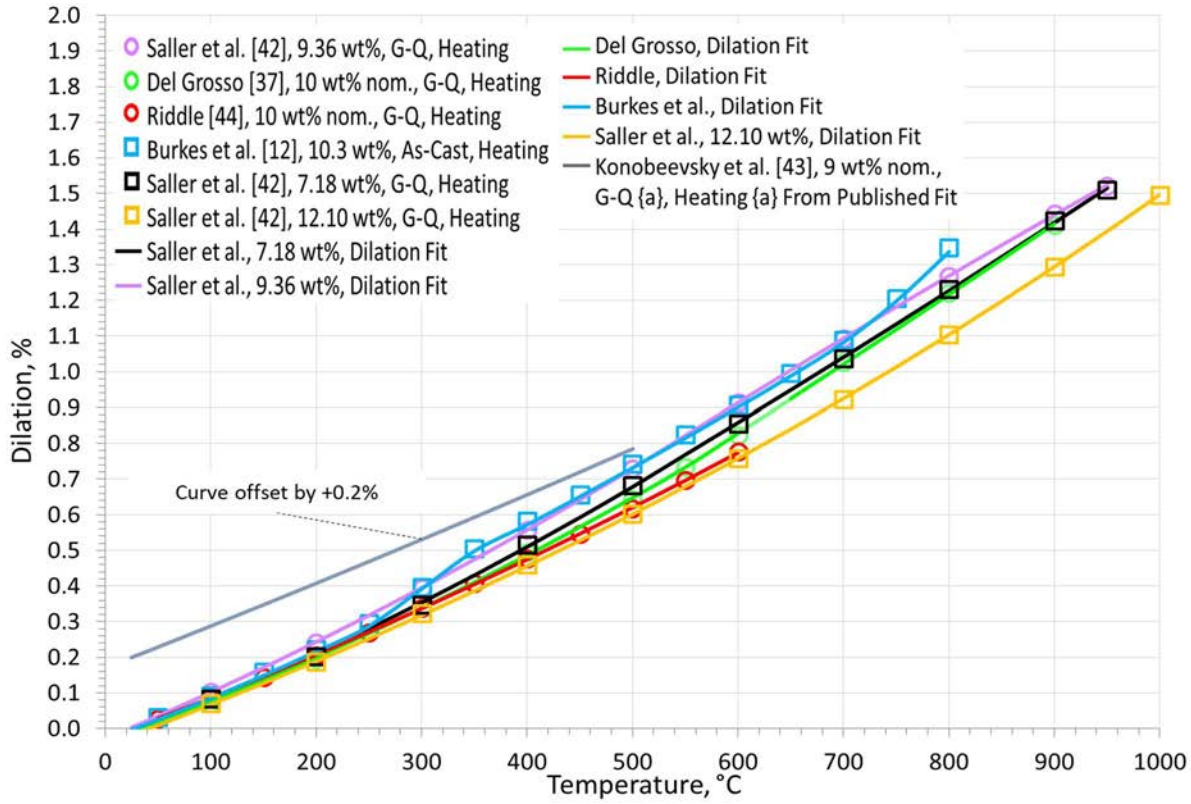

(a) During Heating

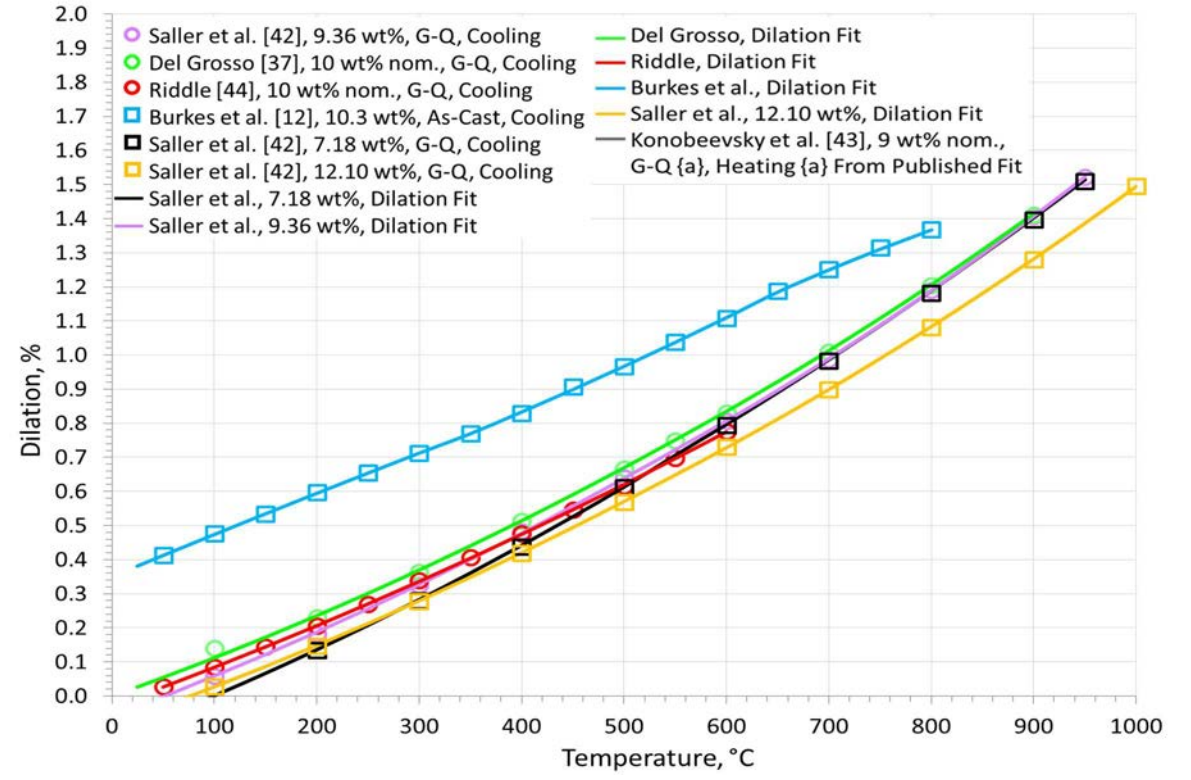

(b) During Cooling

FIG. 5. Dilation from 25 to T*°C of U–Mo alloys with Mo contents between 9 and 11 wt% developed from primary source data. (G-Q: γ quenched; A-C: as-cast; {a}: assumed) (courtesy of Argonne National Laboratory).*

2.4.2. Density change as a function of temperature

The change in density of an alloy as the temperature changes solely owes to the change in its volume, which, of course, is a result of its thermal expansion and metallurgical state. Because the thermal expansion of U–Mo alloys at high temperatures does not exceed 2%, the approximation defined by Eq. (69), shown here as Eq. (19), is perfectly adequate to calculate the change of density as a function of temperature.

$$\rho = \rho_0(1 + 3\Delta L_T / L_0)^{-1} \tag{19}$$

Both Del Grosso [37] and Burkes et al. [12, 13] presented density data as a function of temperature for nominal U–10Mo. These data are discussed briefly in Section A.5.3 of the Appendix.

2.5. HEAT CAPACITY

Knowledge of the heat capacity of a fuel alloy is necessary to calculate the temperature rise in the fuel during a transient heating event. The definitions of, and the symbols commonly associated with, heat capacity, specific heat capacity, and enthalpy change are discussed briefly in Section A.6 of the Appendix, and it is recommended that the reader review that section. Analogous to the relationship between the instantaneous coefficient of thermal expansion and dilation discussed in Section 2.4.1 the specific heat capacity is the instantaneous slope of the enthalpy function of temperature. Also discussed there are equations useful for fitting heat capacity data: Eqs (128) and (129) or, alternatively, enthalpy change data Eqs (130) and (131).

Four independent measurements of the heat capacity or specific heat capacity of U–Mo alloys with Mo content ranging from 8.0 to 10.3 wt% have been found in the literature: Farkas and Eldridge [45], Matsui et al. [46], Parida et al. [47], and Burkes et al. [12]. It is interesting to note that the first of these publications was in 1968, much later than publications containing much of the data discussed in the previous sections. These measurements are discussed in Section A.6 of the Appendix. The specific heat capacity data and least squares fit lines are shown here in Fig. 7; the equations of the fit lines can be found in Section A.6.1 of the Appendix.

Unless the alloy undergoes a phase change, the heat capacity is seen to increase linearly with temperature. Phase changes can add heat to, or absorb heat from, the alloy, producing a rapid change in its heat capacity, as seen in Matsui et al.'s data shown in Fig. 6.

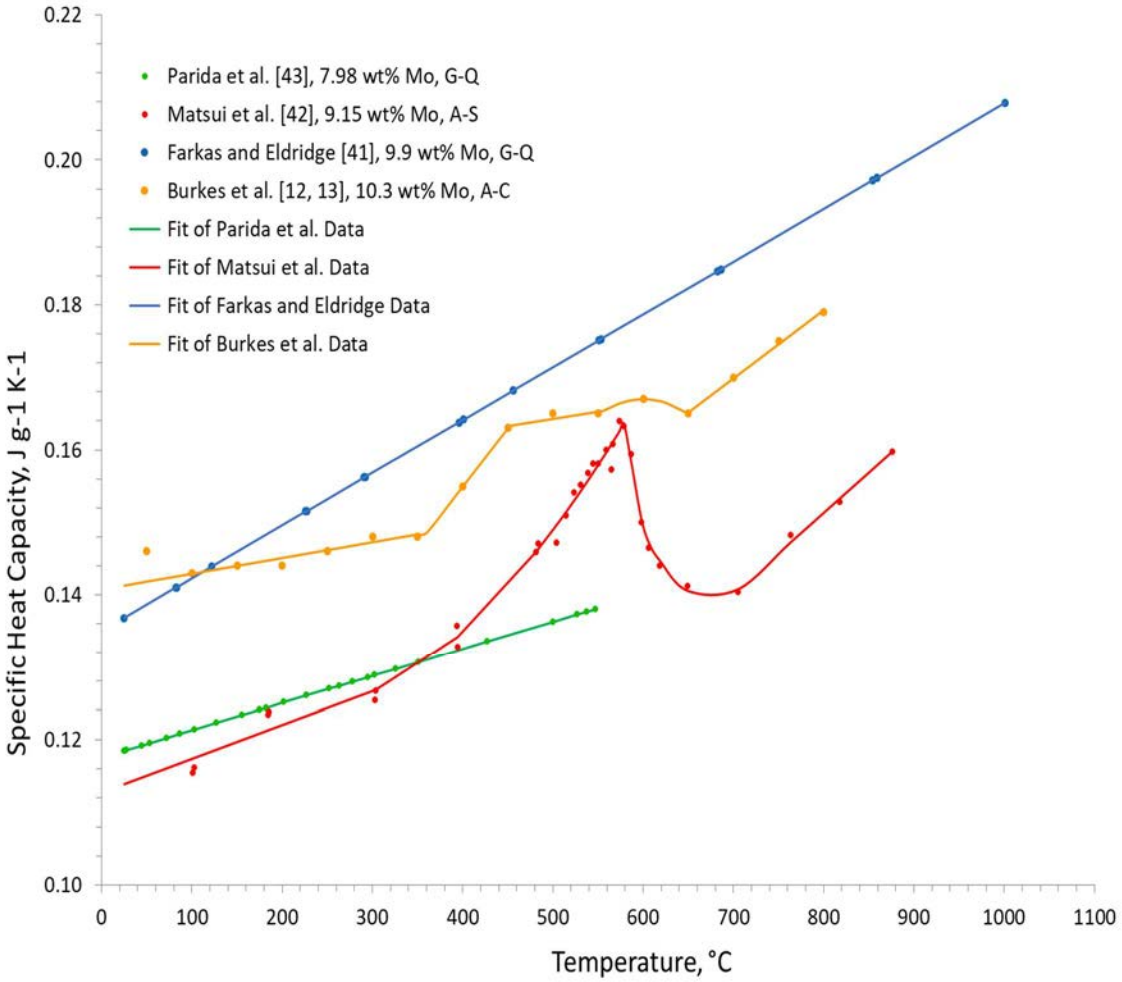

FIG. 6. Specific heat capacity of U–Mo alloys as a function of temperature (A-C: as-cast; A-S: α soaked; G-Q: γ quenched) (courtesy of Argonne National Laboratory).

2.6. THERMAL CONDUCTIVITY

Knowledge of the thermal conductivity of U–Mo fuel as a function of temperature is needed when designing U–Mo fuel plates or pins, particularly for monolithic fuel, because its thermal conductivity is about an order of magnitude lower than that of the aluminium cladding. Eight original sources of thermal conductivity data have been identified and are listed here in order of publication date: Westphal [48], Del Grosso [37], Francis [49], Konobeevsky [43], Roy et al. [50], Lee et al. [40], and Burkes et al. [12, 13]. The data in the two most recent sources were based on laser-flash diffusivity measurements, while the remaining data were based on older temperature drop methods. The data encompasses Mo content ranging from 5.4 to 12 wt% and temperature ranging from 20 to 820°C. The data from the sources listed above are discussed in Sections A.7.1.1and A.7.1.2 of the Appendix and are shown in Fig. 7.

The result of a least squares quadratic fit of all of the data plotted using ‘filled’ symbols is shown by the solid line in the figure; the equation of the fit line is:

$$k_{\mathrm{W,R,DG,L}}^{\mathrm{U-Mo}}(T) = 1.69 \times 10^{-5}T^2 + 0.0210T + 10.52, (20 \leq T < 820) \quad (20)$$

where $k^{\mathrm{U–Mo}}$ is the thermal conductivity in $\mathrm{W \cdot m^{-1} \cdot K^{-1}}$ and T is the temperature in °C and where the subscript to the right of k identifies the lead author of each source. The two datasets shown using 'open' symbols were excluded from the fit, as discussed in Section of the Appendix. Because Lee et al.'s data are significantly lower than the data of the other investigators and because Konobeevsky et al.'s data rise much more rapidly as the temperature increases than do the data of the other investigators, one might wish not to fit all of the data with one curve. A least squares fit of Lee et al.'s data alone yields the equation:

$$k_{\mathrm{L}}^{\mathrm{U-Mo}}(T) = 3.95 \times 10^{-5}T^2 + 0.0438T + 9.20, (25 \leq T < 500) \quad (21)$$

A least squares fit of Westphal's, Roy et al.'s, and Del Grosso's data yields the equation:

$$k_{\mathrm{W,R,DG}}^{\mathrm{U-Mo}}(T) = 6.95 \times 10^{-6}T^2 + 0.0267T + 11.86, (25 \leq T < 820) \quad (22)$$

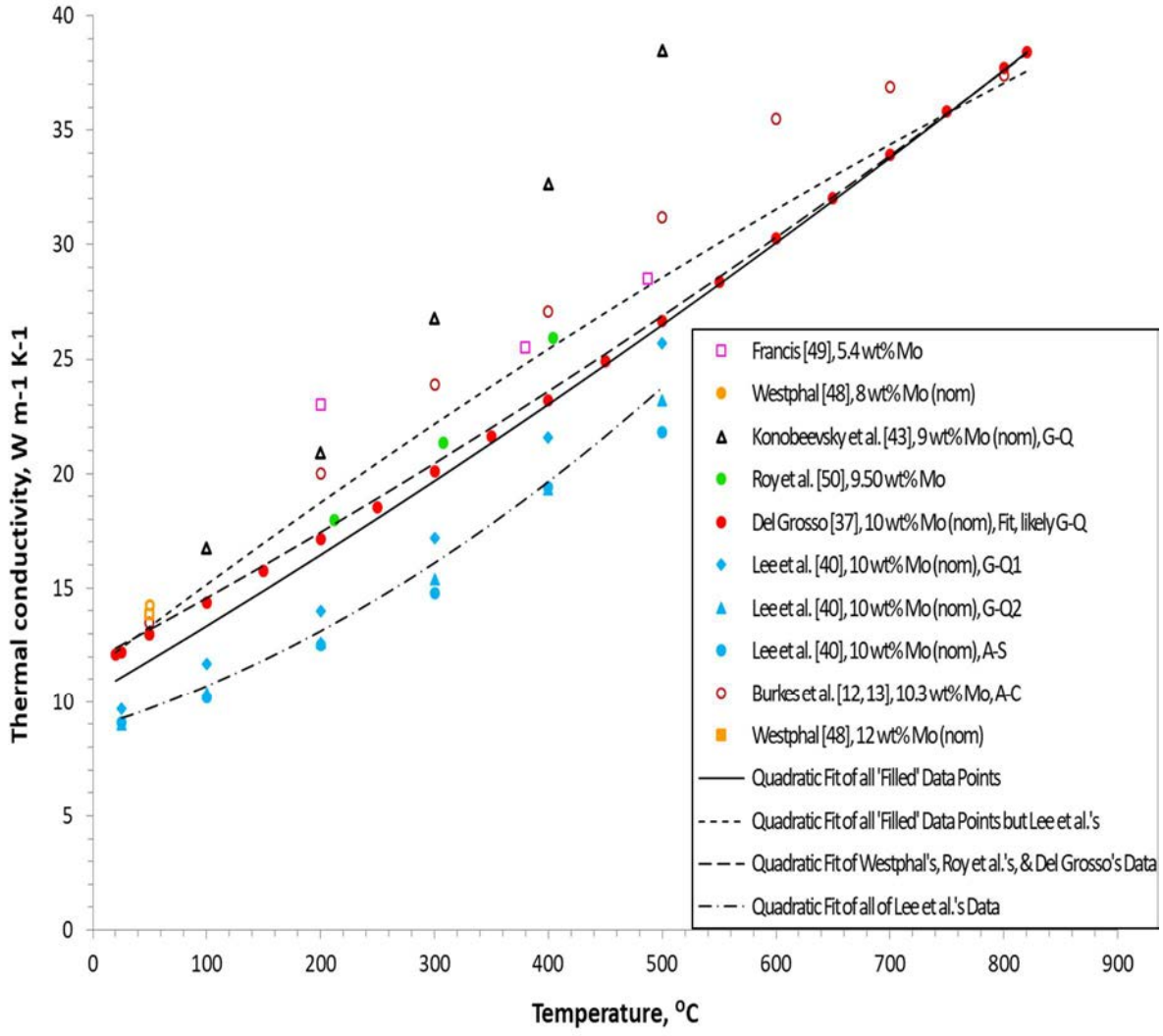

FIG. 7. Thermal conductivity data for U–Mo alloys (A-C: as-cast; A-S: α soaked; G-Q: γ quenched; nom: nominal) (courtesy of Argonne National Laboratory).

2.7. MECHANICAL PROPERTIES

The mechanical properties of U–Mo alloys are important for determining the overall fuel plate properties, and they impact fuel irradiation behaviour, particularly for the monolithic fuel. Mechanical properties data can also be used to model fuel particle irradiation behaviour.

Burkes et al. [14] have reported mechanical properties, obtained from microhardness and quasi-static tensile tests, of six depleted-uranium and molybdenum (DU–Mo) alloy foils. In general, the microhardness, yield strength, Young's modulus, and ultimate tensile strength increased with increasing Mo content from 7 to 12 wt% at room temperature.

Hardness data as a function of temperature from two sources are plotted in Fig. 8 [42, 51]. Hardness at room temperature tends to increase with molybdenum content in the range of 7–12 wt% as shown in Fig. 9 [14, 52]., show that Young's modulus, yield strength, and tensile strength also increase with molybdenum content as shown in Fig. 11, Fig. 12, and Fig. 13 [14]. The ductility increases slightly when the weight fraction of molybdenum in the alloy increases, as shown in Fig. 13 [14].

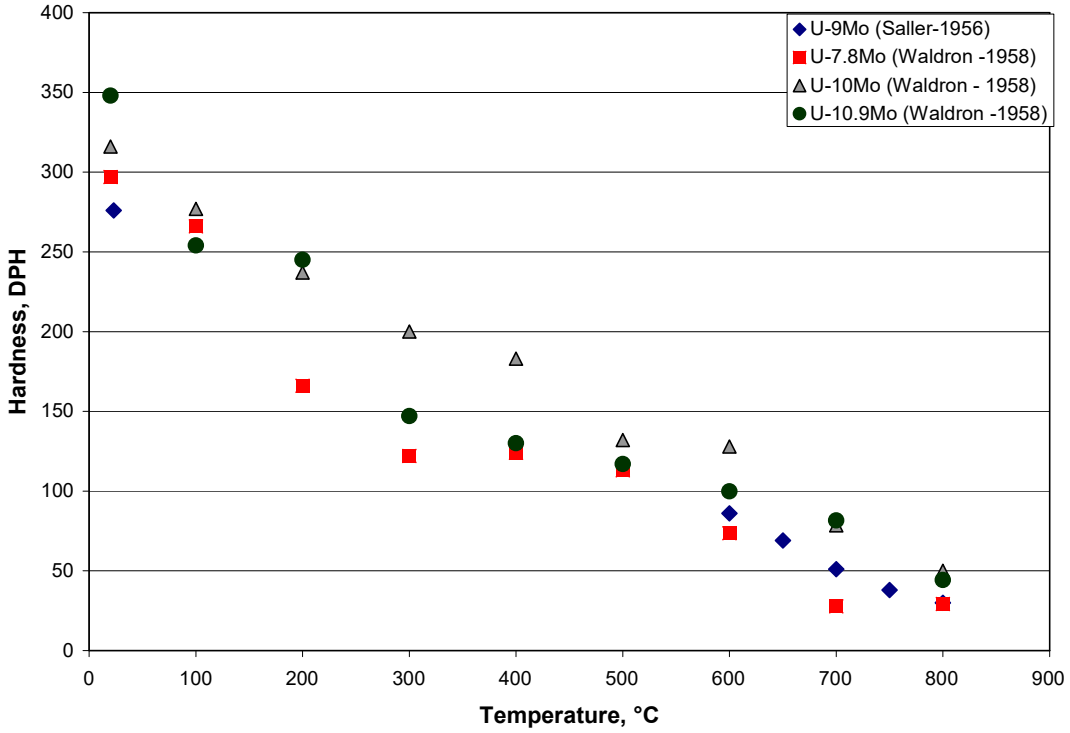

FIG. 8. Hardness data for γ annealed U–Mo alloys as a function of temperature [42, 51] (courtesy of Idaho National Laboratory).

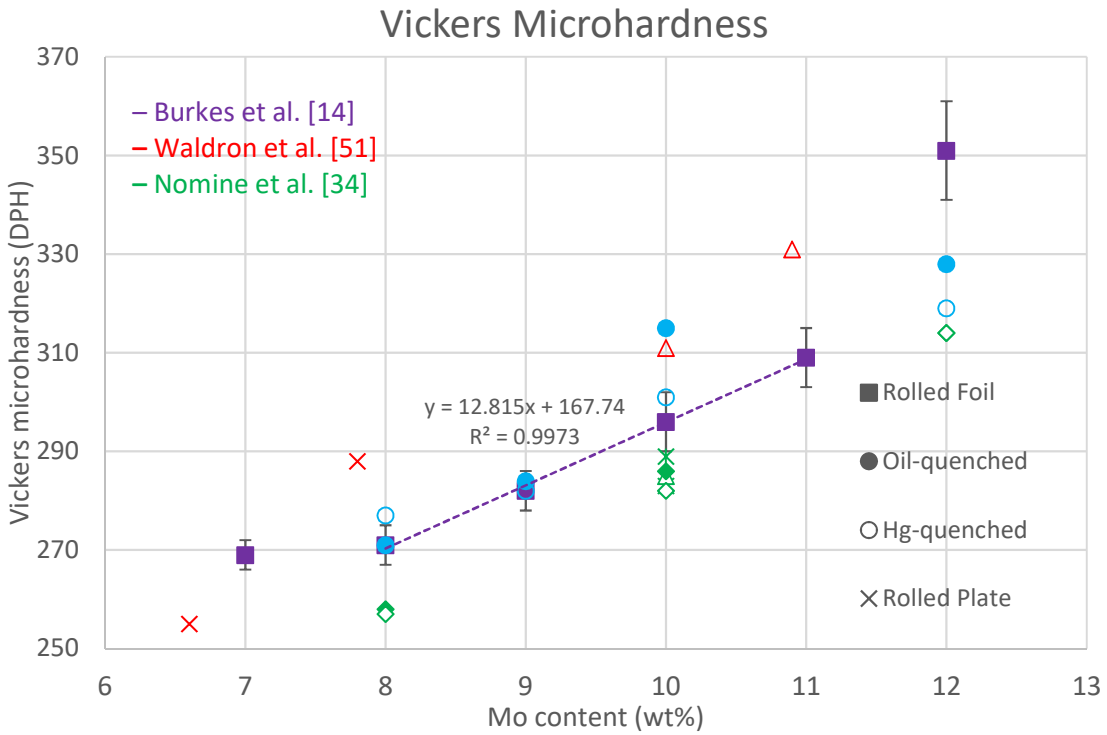

FIG. 9. Average Vickers microhardness values of U–Mo alloys at room temperature as a function of Mo alloying content (adapted from Burkes et al. [14]).

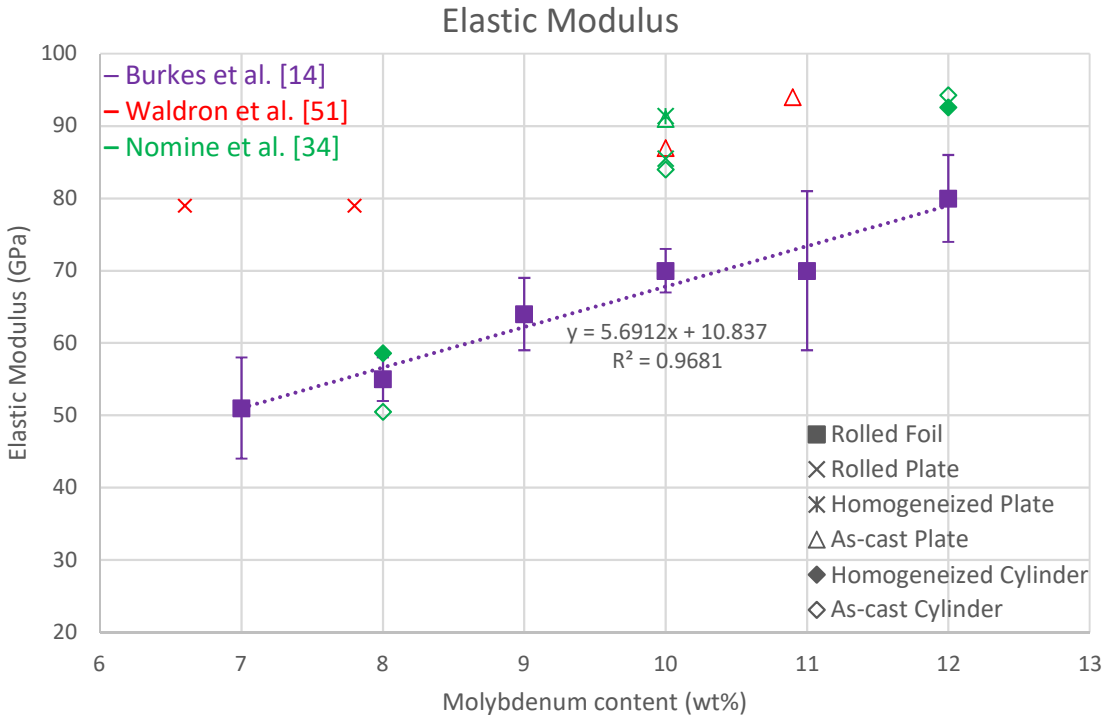

FIG. 10. Average elastic modulus of U–Mo alloys as a function of Mo content (adapted from Burkes et al. [14]).

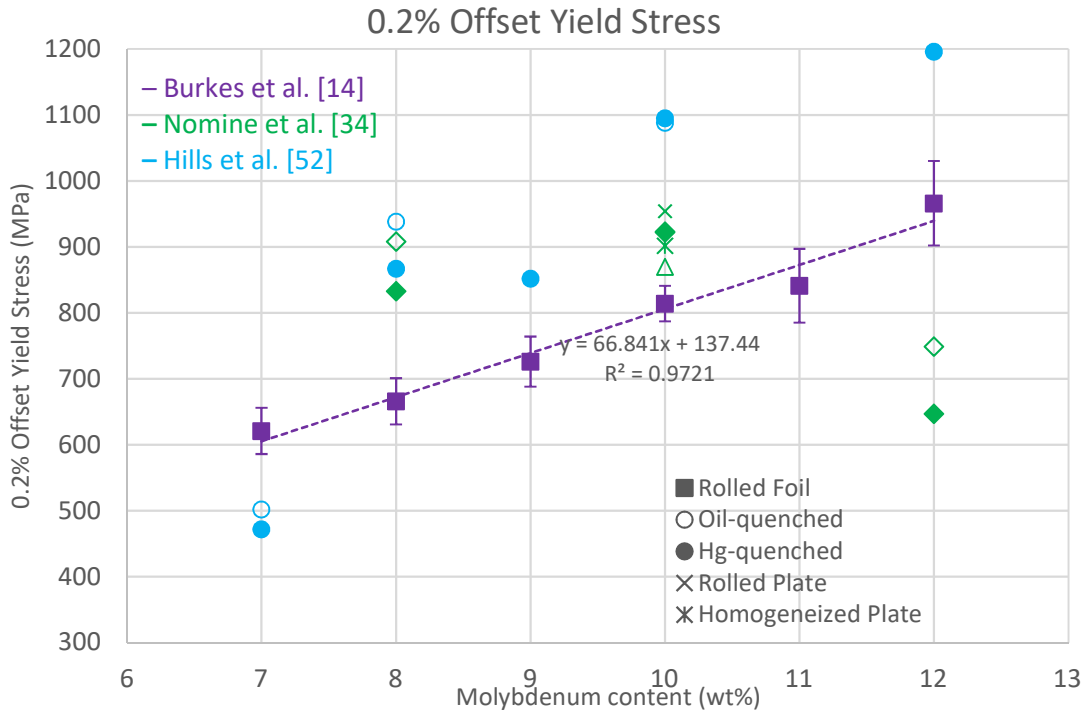

FIG. 11. Average 0.2% offset yield strength of the alloys as a function of Mo content (adapted from Burkes et al. [14]).

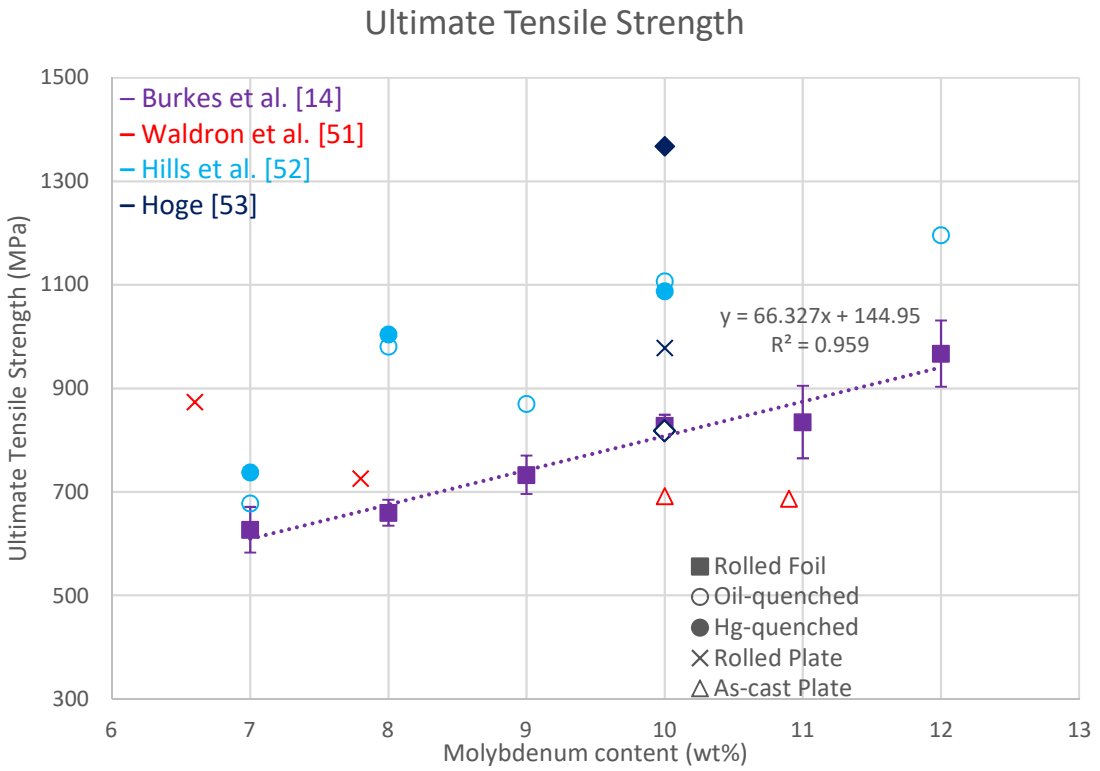

FIG. 12. Average ultimate tensile strength of the alloys as a function of Mo content (adapted from Burkes et al. [14] and [53]).

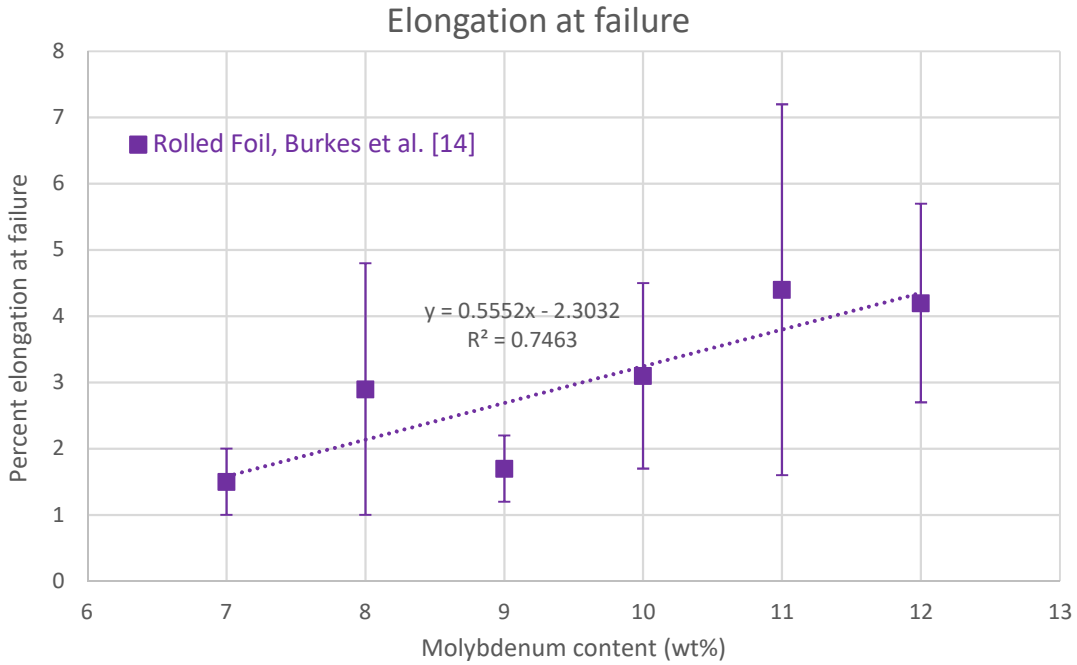

FIG. 13. Average percent of elongation of the alloys as a function of Mo content (adapted from Burkes et al. [14]).

Burkes et al. [14] include a good discussion of possible reasons for the differences in the various investigators' data shown in Fig. 8 – Fig. 12. They derived linear fits to the data they obtained in their experiments using non-homogenized U–Mo foils; their results, taken from Fig. 9 – Fig. 13 and rounded to significant digits, are shown in Eqs (23)–(27), below. Note that, although not discussed in Ref. [14], the error bars accompanying Burkes et al.'s data points appear to represent the standard deviation of the measured values and do not include uncertainties such as that in the Mo content. It is evident from the figures and the discussions in Ref. [14] that the mechanical properties of unirradiated U–Mo alloys vary significantly. The amount of variance can depend on their homogeneity and metallurgical states, which depend on the manufacturing process and conditions. Therefore, the user should use the following fits with caution. All of the equations below represent U–Mo alloy properties at room temperature and $x_{\mathrm{w}}^{\mathrm{Mo}}$ is in wt%:

Hardness in diamond pyramid hardness (DPH):

$$H^{\mathrm{U}x\mathrm{Mo}} = 12.8x_w^{Mo} + 168, (8 \le x_w^{Mo} \le 11) \tag{23}$$

Young's modulus in GPa:

$$E^{\mathrm{U}x\mathrm{Mo}} = 5.69x_w^{Mo} + 10.8, (7 \le x_w^{Mo} \le 12) \tag{24}$$

Yield strength (0.2% offset) in MPa:

$$YS^{\mathrm{U}x\mathrm{Mo}} = 66.8x_w^{Mo} + 137, (7 \le x_w^{Mo} \le 12) \tag{25}$$

Ultimate tensile strength (UTS) in MPa:

$$\mathrm{UTS}^{\mathrm{U}x\mathrm{Mo}} = 66.3x_{\mathrm{w}}^{\mathrm{Mo}} + 145, (7 \le x_w^{Mo} \le 12) \tag{26}$$

Elongation in %:

$$EL^{\mathrm{U}x\mathrm{Mo}} = 0.555x_{\mathrm{w}}^{\mathrm{Mo}} - 2.30, (7 \leq x_w^{Mo} \leq 12) \quad (27)$$

3. PROPERTIES OF OTHER MATERIALS IN U–Mo FUEL SYSTEMS

3.1. INTRODUCTION

U–Mo fuels consist not only of U–Mo alloys but also of many other constituent materials, mostly Al-based alloys. In addition, some new materials are formed as a result of thermally or irradiation-induced reactions between the constituent materials of the fuel system during fuel fabrication and operation in reactors. Understanding the properties of these materials is as important as understanding the properties of the U–Mo alloys themselves in terms of fuel design, fuel performance evaluation, and safety analysis of U–Mo fuel.

This section presents the properties of Al structural materials, Al–Si alloys or dispersions for the matrix, Al alloys for the cladding, fuel–matrix interaction products, diffusion barrier materials for use on fuel particles or foils, and burnable absorber materials.

The properties of composite materials such as the U–Mo/Al and U–Mo/Al–Si dispersion fuel meat are also described here. Some properties of fuel meat can be calculated based on equations using variables such as volume fraction of U–Mo fuel particles, volume fraction of porosity, etc. Fuel–aluminium compatibility and exothermic energy release from the reaction of U–Mo with aluminium in the dispersion matrix or in the cladding (U–Mo/Al reaction) are also important fuel properties.

3.2. PROPERTIES OF CLADDING AND MATRIX MATERIALS

The most commonly used structural materials for research reactor fuel, such as for cladding and for the dispersion matrix, are made of aluminium and its alloys, mainly because of their low neutron capture cross sections, good fabricability, and high thermal conductivity. Table 2 lists basic physical properties of some structural materials found in the U–Mo fuel systems that have been reported. Initial development of U–Mo dispersion fuel, from the mid-1990s to around 2004 was conducted using unalloyed aluminium powder for the matrix, since it was the matrix material used in aluminide, oxide, and silicide dispersion fuels. Currently, Al–Si mixed or alloyed powder is being used as the fuel matrix material to reduce interaction between U–Mo fuel particles and the matrix in irradiation tests supporting development of medium power research reactors. Aluminium alloys are used for the cladding of U–Mo fuel. While AA 6061[10] is widely used in the USA, AA 1060, AG3NE (similar to AA 5754) or AlFeNi (similar to an AA 8000 series alloy) and SAV-1 (Russian abbreviation CAB-1) alloys are used by Canadian, French, and Russian fuel fabricators, respectively.

As noted in Section 2.1.1, the first nuclear power plant in the Soviet Union began operation in 1954 using U–9Mo dispersed in Mg. The use of magnesium as the dispersion fuel matrix has been studied during the present development of reduced enrichment fuels, including limited irradiation tests; post irradiation examination (PIE) indicated the U–Mo/Mg dispersion

[10]AA xxxx is the international designation of wrought aluminium alloys by the Aluminum Association Inc., Arlington, Virginia USA.

fuel had no abnormal swelling under medium power up to 80 at.% burnup. The use of Zircaloy cladding with U–Mo fuel has also been considered. In this publication, magnesium alloys and zirconium alloys are not described in any detail.

TABLE 2. BASIC MATERIAL PROPERTIES OF ALUMINIUM AND OTHER STRUCTURAL MATERIALS [54]

Material	Atomic mass (amu)	Thermal neutron capture cross section (10^{-28} m^2)	Melting point (°C)	Density (Mg/m^3)	Heat capacity (kJ·kg^{-1}·K^{-1})	Thermal conductivity (W·m^{-1}·K^{-1})	Linear expansion coefficient (10^{-6} K^{-1})
Aluminium	26.98	0.215	660	2.70	0.897	220	23.3
Beryllium	9.01	0.09	1288	1.85	1.825	200	11.3
Magnesium	24.3	0.06	650	1.74	1.040	156	24.8
Iron	55.85	2.43	1538	7.87	0.450	74	11.8
Molybdenum	95.95	2.4	2623	10.22	0.249	147	5.2
Nickel	58.7	4.8	1455	8.90	0.440	88	13.5
Niobium	92.91	1.15	2477	8.57	0.265	54	7.3
Chromium	52	3.07	1907	7.15	0.45	95	4.9
Zirconium	91.22	0.185	1855	6.52	0.278	24	5.7

There are well-defined standard specifications for engineering aluminium alloys. The data for compositions, mechanical properties, and thermal properties of the aluminium alloys used for U–Mo fuel can be found in Refs. [55, 56, 57]. Nominal compositions of aluminium alloys typically used for U–Mo fuel are listed in Table 3.

TABLE 3. COMPOSITION OF ALUMINIUM ALLOYS (wt%)

Alloy	Si	Fe	Cu	Mn	Mg	Cr	Ni	Zn	Ti	Others
AA 1050	0.25	0.40	0.05	0.05	0.05	[d]		0.05	0.03	0.03[a]
AA 1060	0.25	0.35	0.05	0.03	0.03	-	-	0.05	0.03	0.03[a1]
AA 6061	0.40–0.8	0.7	0.15–0.40	0.15	0.8–1.2	0.04–0.35	-	0.25	0.15	0.15[b]
AA 4043	4.5–6.0	0.8	0.30	0.05	0.05	-	-	0.10	0.20	0.15[b]
AA 5754	0.40	0.40	0.10	0.50[c]	2.6–3.6	0.30[c]	-	0.20	0.15	0.15[b]
AG3NE	0.3	0.5	-	-	3.0	-	-	-	-	0.2–0.7
AlFeNi	-	0.8–1.2	-	-	0.8–1.2	-	0.8–1.2	-	-	0.2–0.6
SAV-1	0.5	0.15	-	-	1.0	-	-	-	-	0.05
AMG-2	-	0.25	-	0.24	2.8	-	-	-	-	0.05

[a] 0.03 wt% each; except V, with 0.05 wt%; 99.50 wt% min. Al content.

[a1] 0.03 wt% each; except V, with 0.05 wt%; 99.60 wt% min. Al content.

[b] 0.15 wt% in total; 0.05 wt% each.

[c] 0.10–0.6 wt% (Mn + Cr).

[d] If the field is blank, the wt% is negligible.

The properties of several relevant aluminium alloys are shown for comparison in Table 4. Aluminium alloy AA 5754 is included because it has a composition similar to French alloy AG3NE. While AA 6061 is a precipitation-hardening alloy that has a solution temperature of 529°C and an aging temperature around 160°C for rolling, the Al–Mg alloy is a solid solution-hardening alloy, which is not heat treatable.

TABLE 4. MATERIALS PROPERTIES OF AA 1050, AA 6061, AA 5754, AND AA 4043 ALUMINIUM ALLOYS

Properties	AA1050[a]	AA6061	AA5754 (~AG3NE)	AA4043
Melting point (°C)(solidus–liquidus)	646–657	582–652	590–645	574–632
Density (Mg/m^3)	2.705	2.70	2.67	2.69
Elastic (Young's) modulus for annealed alloy (GPa)	69	69	70	70–80
Poisson's ratio	0.33	0.33	0.33	0.34
Thermal expansion coefficient (20–100°C) ($10^{-6}\cdot K^{-1}$)	23.6	23.6	23.9	22.1
Thermal conductivity ($W\cdot m^{-1}\cdot K^{-1}$)	231	167	125	150

[a] No difference of materials properties between AA1050 and AA1060 (except the thermal conductivity of 234 $W\cdot m^{-1}\cdot K^{-1}$ for AA 1060)

As mentioned above, the addition of Si to the Al matrix is now being used to reduce fuel–matrix interaction. The material properties of Al–Si binary alloys are not well identified because binary Al–Si alloys are not easily available on a commercial basis and some commercial Al–Si alloys contain additional alloying elements [58]. In the Al–Si binary system, solid solubility of Si in Al is limited, and hence, hard silicide particles can be precipitated.[11] The conventional fabrication processes of a dispersion fuel optimized for pure Al powder need to be adjusted because the addition of Si to Al increases both the strength and brittleness of the fuel meat.

Figure 14 shows thermal conductivity data for pure aluminium and AA 6061 in several heat-treated conditions. The lower line shows a regression fit of data to a cubic equation. The upper line shows postulated behaviour of powder metallurgy aluminium in dispersion fuel meat as a function of temperature. The data are from Refs. [55, 59] and Argonne National Laboratory (ANL) unpublished data.

The effect of aluminium cladding corrosion must be considered in fuel performance evaluation. The major variables influencing aluminium cladding corrosion are well identified, and detailed information can be found in Refs. [60, 61, 62]. Only the thermal conductivity of the hydrated aluminium layer and its dissolution rate for several aluminium alloys will be discussed briefly here.

Fuel temperature rises during irradiation partly due to the formation of a hydrated aluminium layer ($Al_2O_3\cdot H_2O$) on the cladding surface. This 'boehmite' layer has a much lower thermal conductivity than Al: a value of 2.25 $W\cdot m^{-1}\cdot K^{-1}$ is generally assumed in the literature [63, 64]. However, porous or delaminated oxide layers undoubtedly lower the effective thermal conductivity.

The composition of aluminium alloys affects the dissolution kinetics in water [65]. Juvenelle et al. [66] measured the dissolution kinetics of five aluminium alloys at boiling temperature, as shown in FIG. 15, with the experimental conditions of $[H+]_0$ = 9N. Alloys with significant magnesium content (AG3NE and AG5NE) showed higher initial dissolution rates.

[11] The maximum solubility of Si in Al is less than 2%, so most Al–Si alloys used in U–Mo/Al–Si studies contain primarily eutectic Si and some precipitated Si.

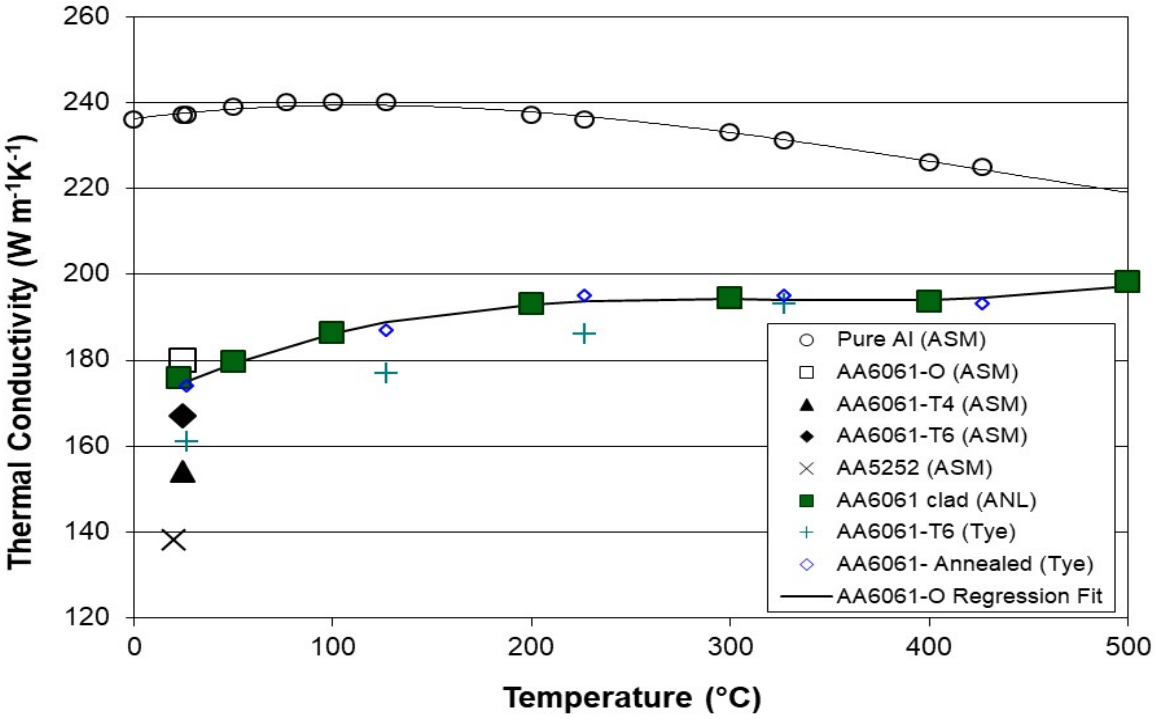

FIG. 14. Thermal conductivity data for pure aluminium and AA6061 in several heat-treated conditions (courtesy of Idaho National Laboratory).

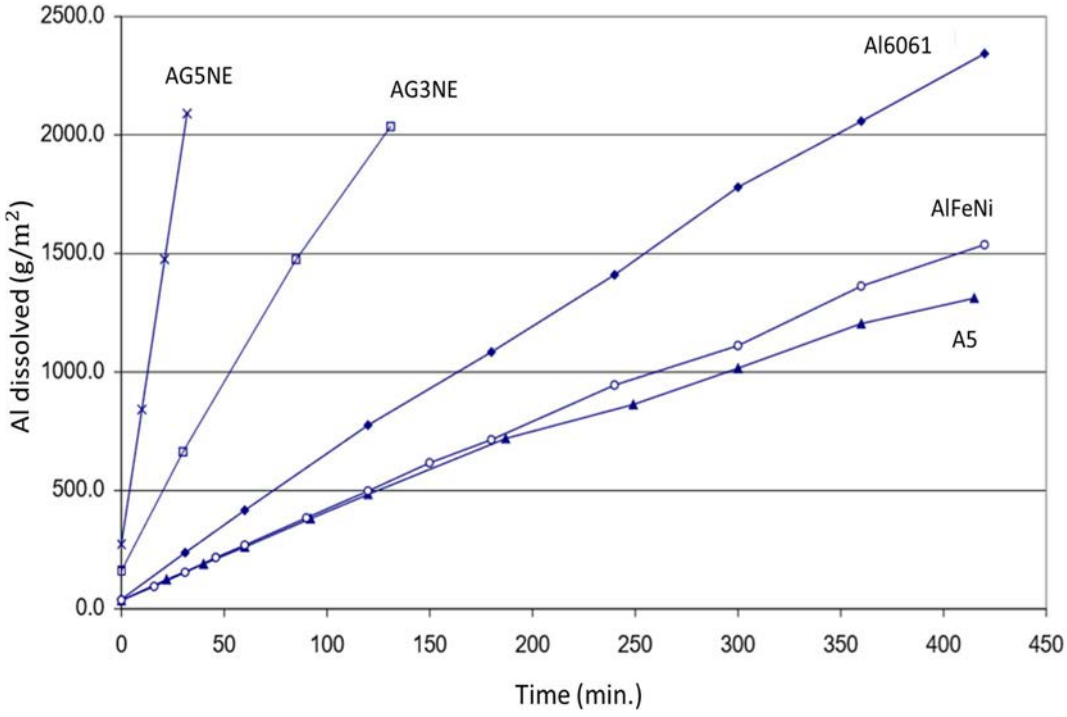

FIG. 15. Dissolution of various Al alloys after immersion in demineralised water at 90°C (Dissolution: $[H+]_0$ = 9N; T is the boiling point) [66]. Note: Aluminium alloy A5 is similar in composition to AA1050. (courtesy of Korean Atomic Institute of Science and Technology).

3.3. PROPERTIES OF DISPERSION FUEL MEATS

The meat of dispersion fuel is a particulate composite material. The composite properties can be deduced from composite theories using the material properties of each constituent. The rule of mixtures is a simple and popular model to predict composite properties. However, the composite properties are not always a linear average of the properties of each material because of the complex interaction of dissimilar materials as well as the effects of the interfaces between the fuel particle and the matrix.

As an example of using the rule of mixtures to estimate an integrated property of dispersion fuel meat, upper and lower bounds for the elastic (Young's) modulus are given by Eqs (28) and (29), respectively.

$$E_c = E_m V_m + E_p V_p \text{ upper bound} \tag{28}$$

$$E_c = \frac{E_m E_p}{V_m E_p + V_p E_m} \text{ lower bound} \tag{29}$$

where E_c is the elastic modulus of the dispersion fuel meat, V is the volume fraction, and the subscripts m and p refer to the matrix and particulate phases.

3.3.1. Elastic modulus of dispersion fuels

The elastic (Young's) modulus of a material is a fundamental material elastic properties that is used in reactor fuel design and safety assessment to characterise the stresses and strains developed during reactor operations. Young's modulus can be measured by various mechanical testing methods, such as tensile testing or ultrasonic techniques. The Young's moduli of three hot-extruded U–Mo/Al dispersion fuel cores, as a function of temperature, were measured using the automated piezoelectric ultrasonic composite oscillator technique by Atomic Energy of Canada Limited (AECL) [67]. The polynomial equation fitted to that experimental data yields the following:

- U–10Mo(64.2 wt%)/Al:

$$E = -2.9956\times10^{-5}T^2 - 2.8964\times10^{-2}T + 72.817 \tag{30}$$

- U–7Mo(61.4 wt%)/Al:

$$E = -2.7950\times10^{-5}T^2 - 3.1415\times10^{-2}T + 73.470 \tag{31}$$

- U–6Mo(62.8 wt%)/Al:

$$E = -3.4999\times10^{-5}T^2 - 3.3456\times10^{-2}T + 76.289 \tag{32}$$

- Al:

$$E = -4.7341\times10^{-5}T^2 - 3.3376\times10^{-2}T + 72.317 \tag{33}$$

where E is in GPa and T is in °C. The values of these fits are shown in Fig. 16.

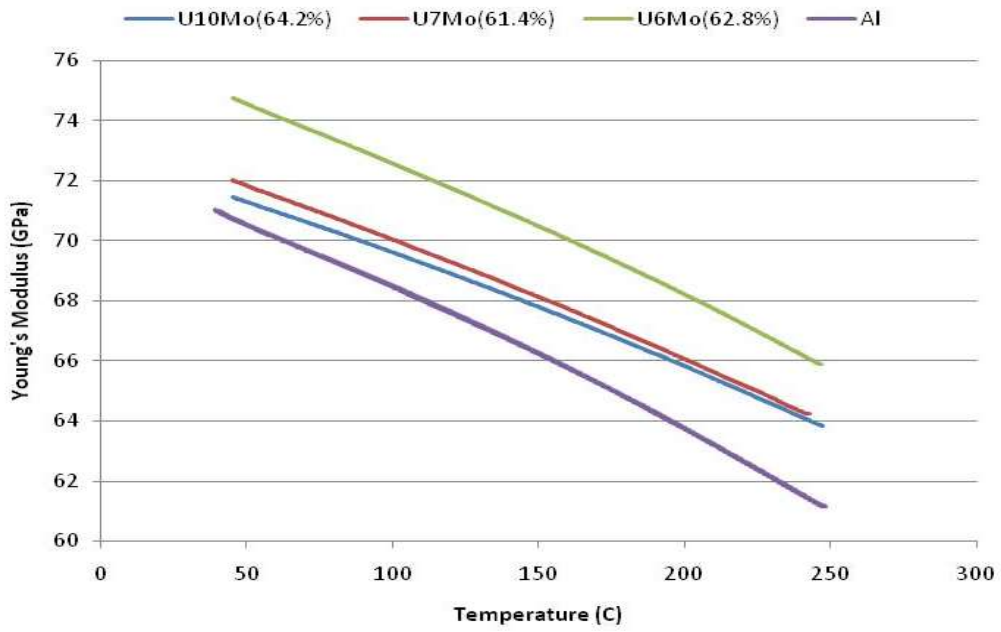

FIG. 16. Young's modulus of U–Mo/Al dispersion fuel meats vs. temperature [67] (courtesy of AECL).

3.3.2. Tensile strength of as-fabricated dispersion fuel meat

Ultimate tensile strength and elongation of U–Mo/Al dispersion fuel meat as a function of the U–Mo volume fraction were measured by Korea Atomic Energy Research Institute (KAERI), as shown in Fig. 17 [41]. The UTS of U–Mo/Al dispersion fuel meats increased with fuel volume fraction, while its elongation decreased with fuel volume fraction.

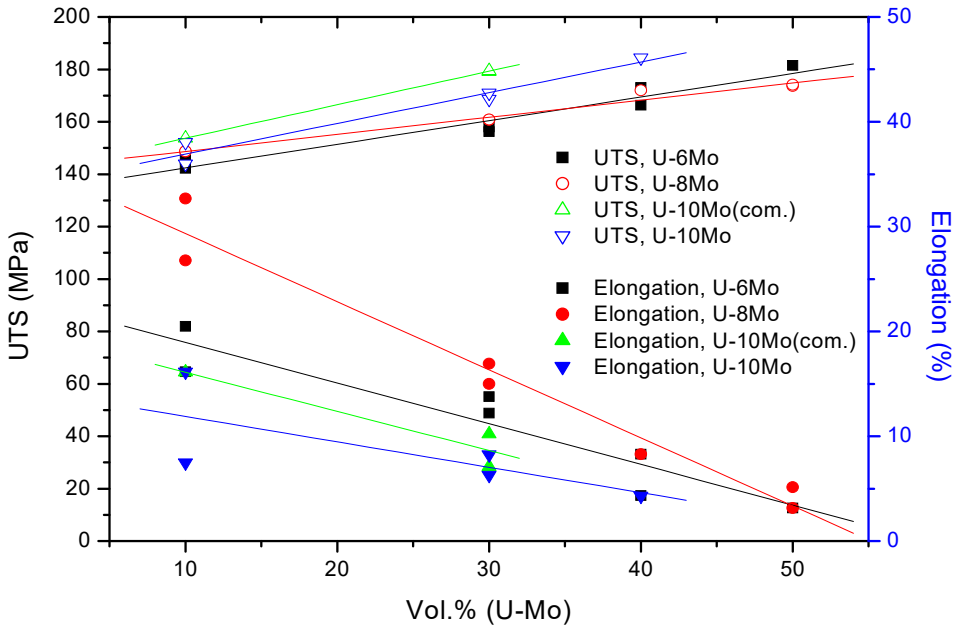

FIG. 17. Tensile strength and elongation data for extruded U–Mo/Al fuel meats as a function of U–Mo volume loading [41](courtesy of KAERI).

3.3.3. Specific heat capacity of U–Mo/Al dispersion fuel meats

Lee et al. measured the specific heat capacity of U–Mo/Al dispersion fuel meats by the differential scanning calorimetry method [68]. The specific heat capacity of the U–Mo/Al dispersion fuel meats increased with temperature for fuel with 30, 40, and 50 vol.% U–Mo, as shown in Fig. 18. As the U–Mo volume fraction increases, the specific heat capacity of the dispersion fuel meat decreases. However, the dependency of the specific heat capacity on the Mo content in the U–Mo alloy was not as significant.

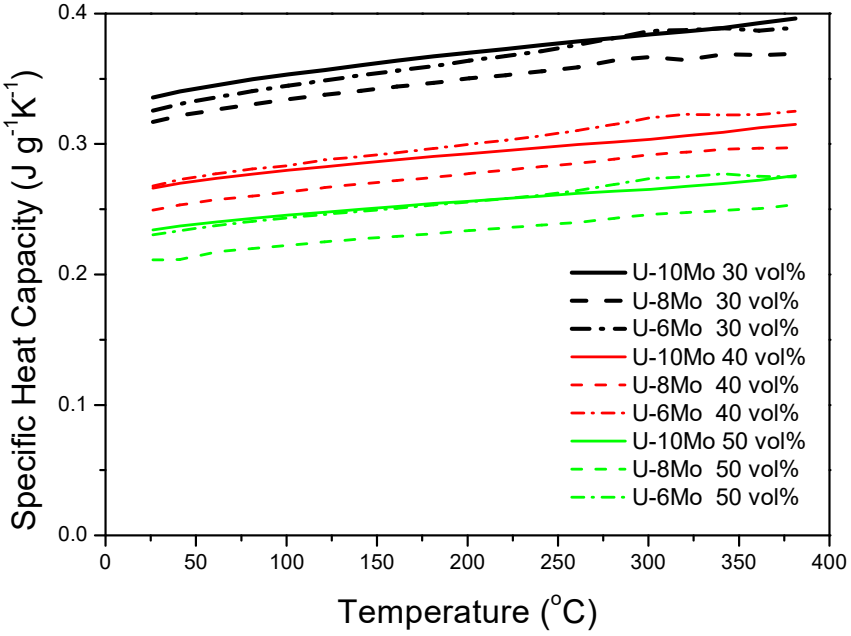

FIG. 18. The variation of the specific heat capacity of U–Mo/Al dispersion fuel meats with temperature, Ref. [68] (courtesy of KAERI).

3.3.4. Thermal conductivity of U–Mo/Al dispersion fuel meats

Lee et al. also measured the thermal conductivities of U–6Mo/Al, U–8Mo/Al, U–10Mo/Al with varying volume fractions of the U–Mo particles in the Al matrix by the laser flash method [40, 68]. The thermal conductivity ($W \cdot m^{-1} \cdot K^{-1}$) can be calculated by using the following expression:

$$k = \rho \alpha C_p \tag{34}$$

where ρ is the density (g/cm^3), α is the thermal diffusivity (cm^2/s) measured by the laser flash method, and C_p is the specific heat capacity ($J \cdot g^{-1} \cdot K^{-1}$). The effects of temperature on the thermal conductivities of U–Mo/Al dispersion fuel meats are not remarkable as shown in Fig. 19. The graph in Fig. 20 shows the temperature dependency of the thermal conductivity of 50 vol.% U–Mo/Al dispersion fuel meats.

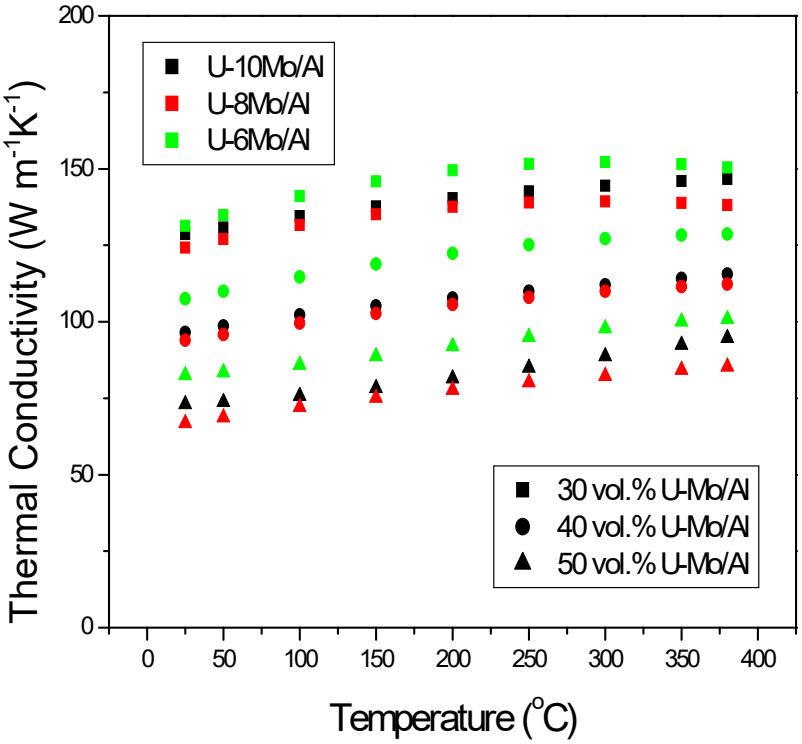

FIG. 19. The variation of the thermal conductivity of U–Mo/Al dispersion fuel meat with temperature [68]. (courtesy of KAERI).

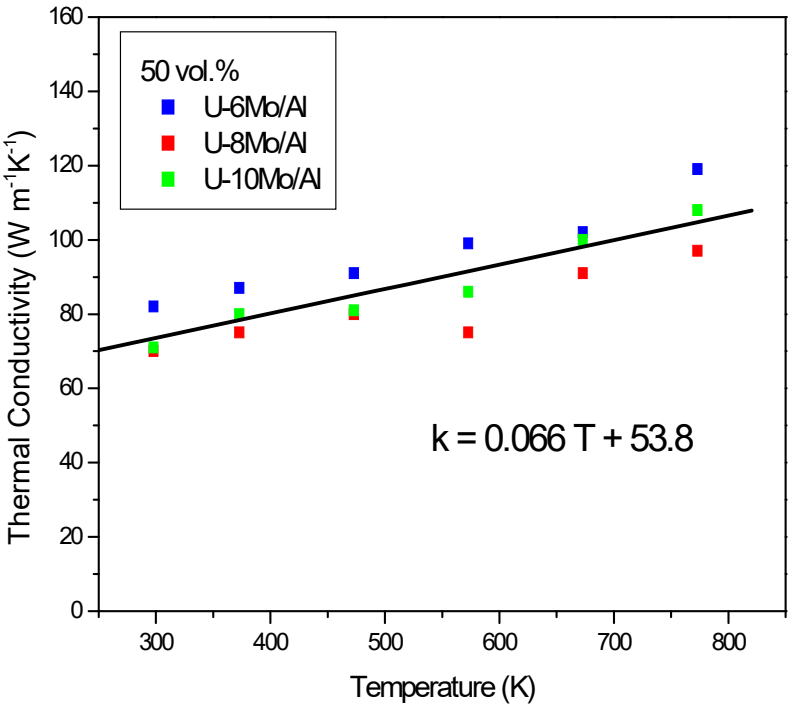

FIG. 20. The variation of the thermal conductivity of 50 vol.% U–Mo/Al dispersion fuel meat with temperature [40](courtesy of KAERI).

Primarily, a modified Hashin and Shtrikman model, shown in Eq (35) has been used for the calculation of the thermal conductivity of dispersion fuel meats [69].

$$k_{meat} = \frac{-k_f + 3V_f k_f + 2k_m - 3V_f k_m + \sqrt{8k_f k_m + (k_f - 3V_f k_f - 2k_m + 3V_f k_m)^2}}{4} \tag{35}$$

where k_{meat} is the effective thermal conductivity of the fully dense fuel meat, k_f is the composite thermal conductivity of the fuel and reaction-product phase, k_m is the thermal conductivity of the matrix phase, and V_f is the sum of the volume fractions of the fuel and reaction-product phases. The composite thermal conductivity of the fuel and reaction product phase, k_f, can be calculated,

$$k_f = \left(\frac{1 - e/r}{k_g} + \frac{e/r}{k_{IL}} \right)^{-1} \tag{36}$$

where e is the thickness of the interaction product, r is the radius of the U–Mo particle, and k_{IL} is the thermal conductivity of the interaction product.

Dispersion fuel meats also contain porosity created during fabrication. Because the porosity reduces the effective thermal conductivity of fuel meats, it is necessary to introduce a correction factor as follows [70]:

$$k_p = k_{100} exp(-2.14 P_m) \tag{37}$$

where k_p is the effective thermal conductivity of fuel meats, k_{100} is the thermal conductivity of the fully dense dispersion meats ($P_m = 0$), and P_m is the fabrication porosity in the fuel meat. This porosity correction factor is valid for porosities below 0.30 [70]. The calculated values as a function of the sum of the volume fractions of the fuel and reaction product show good agreement with measured values for unirradiated U–Mo/Al dispersion fuel meats as shown in Fig. 21.

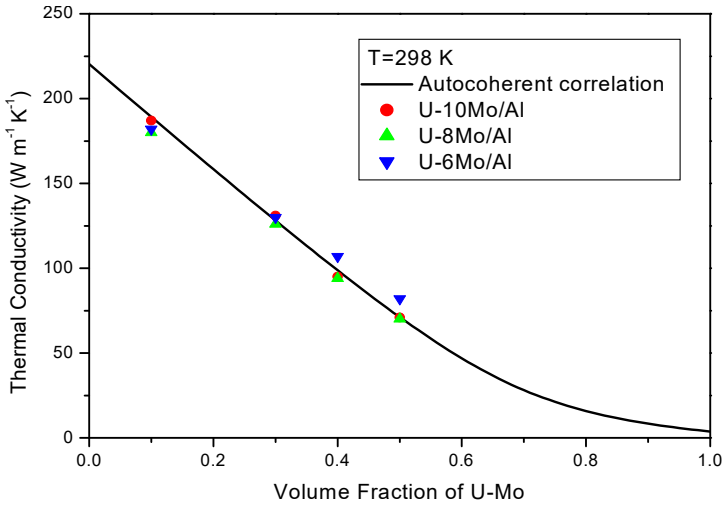

FIG. 21. Dispersion fuel thermal conductivity model compared to measured data, with pure Al matrix [68][12] (courtesy of KAERI).

[12] The data point for U–10Mo/Al, 0.1 volume fraction, is plotted about 10 $W \cdot m^{-1} \cdot K^{-1}$ lower than the 197 $W \cdot m^{-1} \cdot K^{-1}$ listed in table X of Ref. [68].

3.3.5. Properties of fuel–matrix interaction products in U–Mo/Al dispersion fuel meats

The U–Al binary system has three intermetallic compounds, specifically UAl_2, UAl_3, and $U_{0.9}Al_4$. The presence of Mo alloyed with U may introduce a complexity to the interdiffusion behaviour of U–Mo alloy in contact with Al by forming ternary phases such as $U_6Mo_4Al_{43}$ and U–Mo_2Al_{20}.

Fuel–matrix interaction causes one of the most dynamic changes in the material properties of U–Mo fuel — the thermal conductivity of a fuel meat decreases as formation of the interaction product consumes the Al matrix. Although the as-irradiated thermal conductivity of the interaction product, U–Mo/Al_x, has not been measured, it is generally considered to be as low as 6 $W \cdot m^{-1} \cdot K^{-1}$ [71][13]. Porter and Ewh [72] have reviewed results of characterization of fuel–matrix interaction products obtained from out-of-pile annealing tests.

The interaction of the U–Mo alloy fuel and the Al matrix affects the fabrication process, too. In some cases, hot fabrication temperatures had to be changed, e.g. when changing from extrusion of UO_2/Al dispersions to U–Mo/Al dispersions [73], or time at temperature had to be reoptimized when performing a hot isostatic pressing fabrication process (termed hipping) for U–Mo/Al dispersion fuel plates.

3.3.6. Thermal compatibility of U–Mo/Al dispersion fuel meats

Thermal compatibility tests reveal volume changes of U–Mo/Al dispersion fuel owing to interaction of the U–Mo fuel particles and the Al matrix after exposure to high temperatures for long times. Kim et al. measured volume changes of U–6Mo/Al, U–7Mo/Al and U–8Mo/Al dispersion fuel at 400°C and 450°C up to 500 hours. [41] As shown in Fig. 22, the U–Mo/Al dispersion fuel meat with a higher Mo content has more thermal stability at 400°C, while the differences of the thermal compatibility are not large at 450°C.

[13]The thermal conductivity of UAl_4 has been deduced to range from 4–8 $Wm^{-1}K^{-1}$from measurements of UAl/Al dispersions and U–Al alloys — see Ref. [112].

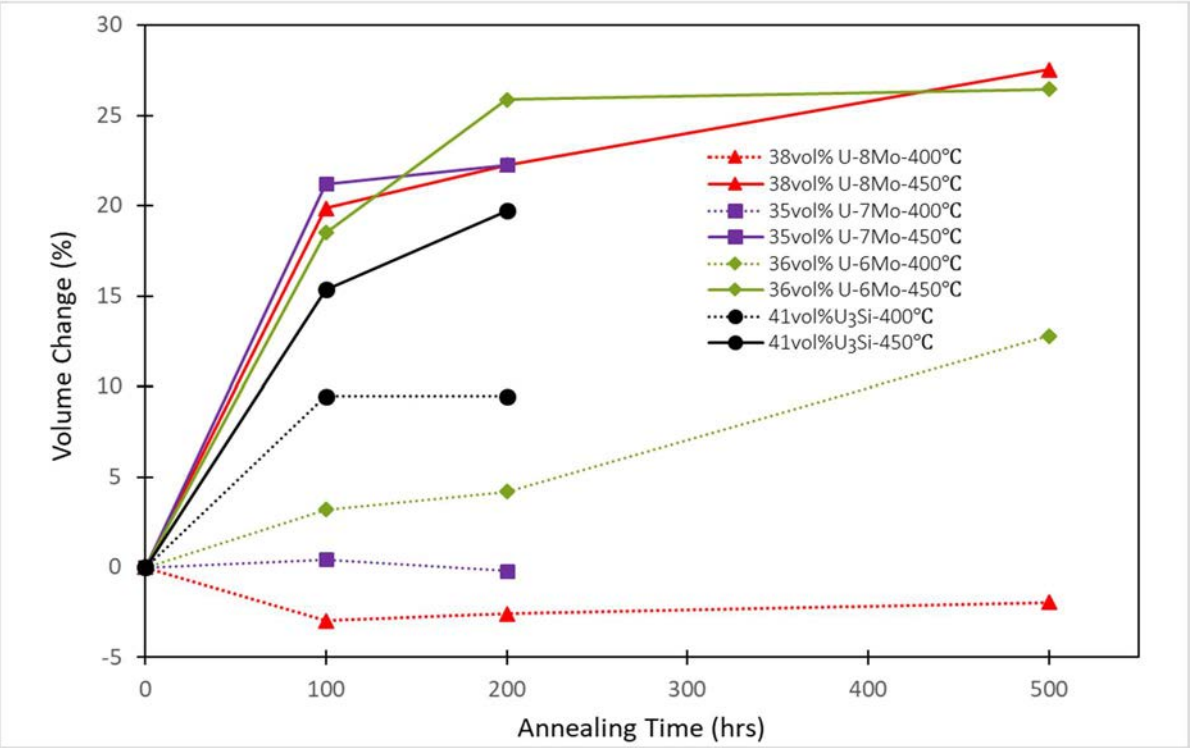

FIG. 22. Thermal compatibility test results for various U–Mo/Al dispersion fuel meats. [41] (courtesy of KAERI).

3.3.7. Exothermic reaction heat release in U–Mo/Al dispersion fuel meats

The reaction between U–Mo and Al is exothermic; Fig. 23 shows that the reaction between U–6Mo and Al took place around 645°C (918 K) [74], while Fig. 24 shows the reaction heat of U–10Mo and Al decreased as the volume fraction of U–Mo fuel increased from 0.3 to 0.5 vol.% [75]. This is understandable since the aluminium matrix ceases to be the continuous phase above 30–35 vol.% fuel, so the amount of fuel alloy surface in contact with the matrix decreases.

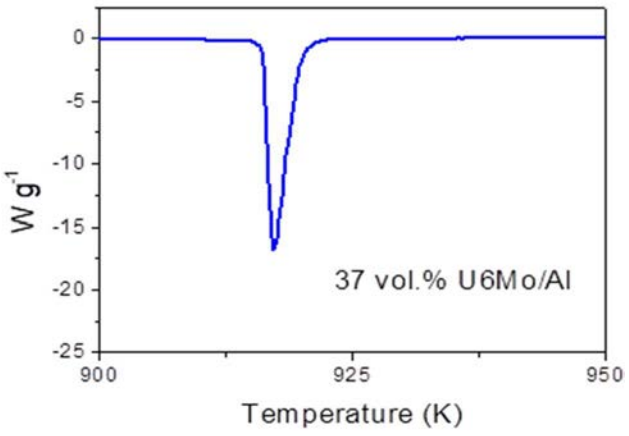

FIG. 23. Calorimeter trace showing heat of reaction of U–6Mo with the aluminium matrix. Ref. [74] (courtesy of KAERI).

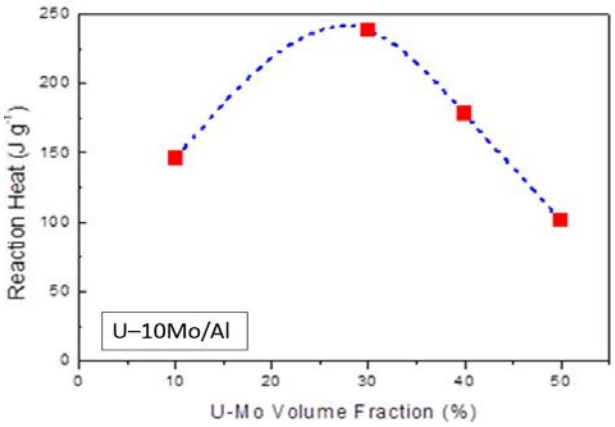

FIG. 24. The variation of reaction heat of U–10Mo/Al dispersion fuel on fraction of fuel volume [75] (courtesy of KAERI).

In addition to determining reaction heats for various volume fractions of spherical U–Mo powder in dispersion fuel, Ryu et al. determined the activation energy for the formation of a (U–10Mo)Al_3 interaction layer between the fuel particle and the Al matrix owing to thermal annealing [75]. Using both the Jander model and the Ginstling-Brounshtein model for a diffusion-controlled reaction in a sphere, they determined the activation energy associated with the reaction to be 277 kJ/mol based on the Jander model and 316 kJ/mol based on the Ginstling-Brounshtein model. Generally, the latter model is considered to be better because it is based on spherical geometry, whereas the Jander model is a planar model expected to hold for only small fraction of the reaction interface.

Leenaers et al. determined the apparent activation energies of a number of (U–Mo)/(Al, Si) interaction products using Kissinger analysis of data obtained by in-situ X-ray diffraction of thin Al or Si layers on a U–Mo substrate (a planar experiment) [76]. The apparent activation energies for the formation of UAl_4, UAl_3, and UAl_2 were 3.6 ± 0.55 eV, 2.74 ± 0.27 eV, and 1.56 ± 0.08 eV, respectively. For USi_2, USi_3, and U_3Si, the apparent activation energies were 3.51 ± 0.53 eV, 3.17 ± 0.3 eV and 2.52 ± 0.26 eV, respectively. Their value for UAl_3, 2.74 eV, converts to 264 ± 26 J/mol in excellent agreement with the Jander model (planar) value obtained by Ryu et al. [75].

The heats of formation of U–Mo/Al_3 intermetallic compounds were obtained by measuring the reaction heats of U–Mo/Al dispersion samples by differential scanning calorimetry [74]. The magnitude of the heat of formation of U–Mo/Al_3 reduces (i.e. less heat is released when the compound is formed) as the Mo content increases, as shown in Fig. 25 [74]. However, the heat of formation of U(Al,$Si)_3$ becomes more negative (i.e. more heat is released when the compound is formed) as the Si content increases, as shown in Fig. 26 [74].

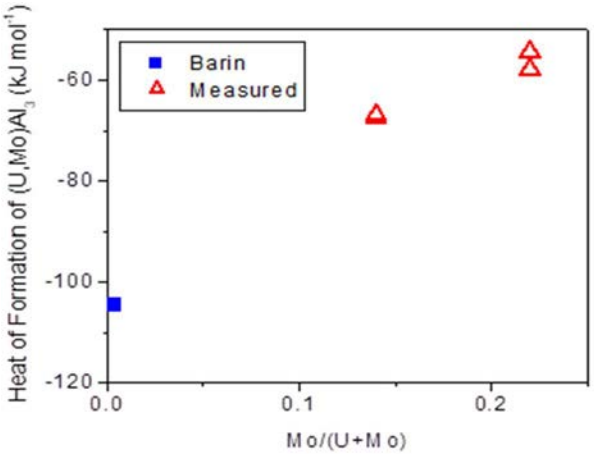

FIG. 25. Heats of formation of U–Mo/Al_3 with Mo/(U + Mo) ratio [74]. Barin's datum comes from Ref. [77].

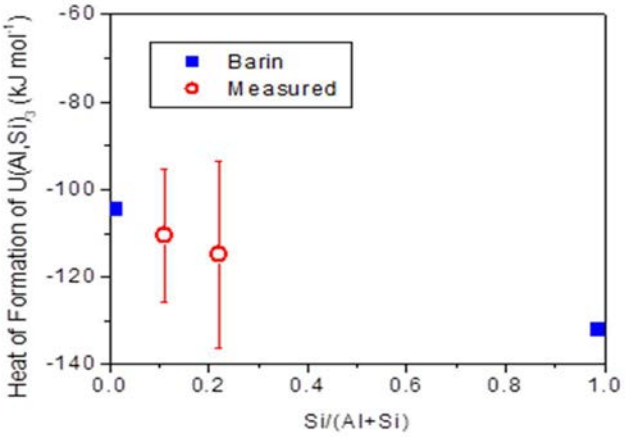

FIG. 26. Heats of formation of U(Al,Si)Al_3 with Si/(Al + Si) ratio, adapted from Ref. [74]. Barin's data come from Ref. *[77]*.

3.3.8. Diffusion barrier coatings in U–Mo/Al dispersion fuel meats

Diffusion barrier coatings applied on U–Mo particles, including silicide, nitride, and oxide, are being tested to assess their effectiveness in suppressing the interaction between the U–Mo particles and the Al matrix. Because the diffusion barrier coatings are very thin, it is believed that material properties of U–Mo powder or U–Mo/Al dispersion fuel do not change much as a result of being coated with diffusion barrier layers. However, if a material with a high neutron capture cross section is being considered, its effect on the neutron economy of the U–Mo fuel should be determined. Because separation of coating layers can occur owing to weak interface bonding or mismatch of thermal expansion between U–Mo and coating materials, it will be useful to have information on the compositions, lattice parameters and thermal expansion coefficients of potential coating materials when their selection is finalized.

3.4. MATERIALS PROPERTIES OF BURNABLE ABSORBERS

Burnable absorbers are used to compensate excess reactivity at the beginning of life of a fuel assembly, to shape the density of heat flux in the core, and to provide optimum burnup. Physical and nuclear properties of chemical elements and their compounds with a high neutron-

absorption cross-section (σ_a) are listed in Table 5 and Table 6. Although selection of proper burnable absorber materials is not specific to U–Mo fuel alone, careful analyses are needed to confirm chemical compatibility with constituent materials like U–Mo and Al–Si.

TABLE 5. PHYSICAL AND NUCLEAR PROPERTIES OF CHEMICAL ELEMENTS WITH HIGH NEUTRON-ABSORPTION CROSS-SECTION [54]

Element	Z	Molecular mass (amu)	Density (g/cm^3)	T_{melt} (°C)	T_{boil} (°C)	Mean σ_a of all stable isotopes (10^{-28} m^2)	Isotope mass number	Molar content in mixture (%)	σ_a (10^{-28} m^2)
B	5	10.81	2.33	2 075	2 550	790	10	19.9	3 990
Ag	47	107.87	10.50	961.9	2 167	63	107	51.8	37.6
							109	48.2	91
Cd	48	112.41	8.65	320.9	766.5	2 550	113	12.36	20 600
In	49	114.52	7.31	156.6	2 024	194	115	95.8	202
Gd	64	157.25	7.895	1 311	3 233	48 900	155	14.8	61 000
							157	15.65	254 000
Dy	66	162.5	8.55	1 412	2 562	948	161	19.0	585
							162	25.5	180
							163	24.9	130
							164	28.1	2 700
Hf	72	178.4	13.31	2 230	3 100	105	177	18.4	1 500
							178	27.0	75
							179	13.8	65
							180	35.4	14
Hg	80	200.5	13.55	−39	356.7	363	199	16.9	2 150
Eu	83	151.96	5.24	822	1597	1 850	151	47.9	9 200
							155	52.1	390

TABLE 6. BASIC THERMO-PHYSICAL PROPERTIES OF BURNABLE ABSORBER MATERIALS [54]

Property	B, nat	B_4C	BN	ZrB_2	TiB_2	HfB_2	Hf	AgInCd	Eu_2O_3	Dy_2O_3	Ta
Molecular mass (amu)	10.811	55.24	24.81	112.85	69.5	200.1	178.5	108.1	352	373	180.9
Melting point (°C)	2075	2450	3000	3050	2920	3240	2220	800	2050	2340	2996
Density (g/cm^3)	2.33	2.51	2.25	6.09	4.52	11.2	13.09	10.17	7.34	8.10	16.65
Heat capacity ($J \cdot kg^{-1} \cdot K^{-1}$)	387	960	848	230	387	396	363	230	413	290	140
Thermal conductivity ($W \cdot m^{-1} \cdot K^{-1}$)	27	92	28.7	23	26	22.6	22.3	60	2.2	2.3	50
Coeff. of linear thermal expansion, α (10^{-6} K^{-1})	5	4.5	2	5.5	7.3	5.3	5.9	22.5	10.1	8.3	6.6

Property values are for temperatures 20 to 200°C

APPENDIX

SUPPLEMENTAL INFORMATION ABOUT URANIUM–MOLYBDENUM ALLOY PROPERTIES, INCLUDING DISCREPANCIES IN THE LITERATURE

Contributed by

J. L. Snelgrove
Argonne National Laboratory, USA

A.1. INTRODUCTION

The purpose of this Appendix is to add depth to the discussions of U–Mo alloy properties that were presented in the main body of this publication, which has been prepared as concisely as possible to facilitate obtaining reliable materials property data of U–Mo alloys. A considerable effort has been made to examine the available literature reporting these properties, as indicated by the extensive list of references.

The principal consideration has been reliability of the data presented here. As might be expected for a fuel whose development began within a very few years of Fermi's demonstration that controlled fission was possible, U–Mo properties data have been included in a number of compilations, some treating only U–Mo and others including data on other uranium alloy fuels. Discrepancies were noted in the reported data that led to extensive studies, including tracing a cited dataset back as close as possible to its original publication, especially of the U–Mo equilibrium phase diagram and of U–Mo thermal expansion data. A number of discrepancies have been found and corrected, to the extent possible, in this Appendix. This work is not intended to be a critical review of the data, in part because some of the properties data are dependent on the manufacturing and thermal history of the test specimens and because the lack of enough information on the test specimens themselves. The mechanical properties of U–Mo alloys have not been considered in this Appendix because they are so dependent on the history of the test specimen.

A secondary, but very important, goal was to make the data examined in this Appendix available in numerical form for those who might wish to examine it in more detail. As will be seen, much of the data were found in the form of plots which had to be digitized to facilitate examination of the data presented. Copious tables of the digitized data will be found in this Appendix. In addition, the tabulated data for a number of properties have been fit using linear or quadratic functions, often in a piecewise manner, to facilitate use of the data and to provide a concise means to present the data in the main body of this publication.

A.2. U–Mo EQUILIBRIUM PHASE DIAGRAM

Generally, equilibrium phase diagrams, or phase diagrams, of binary metal alloys have been developed by a painstaking and time-consuming series of experiments:

(a) Preparation of well-homogenized samples for many different compositions along the composition axis of the diagram.
(b) Determination of phase-change temperatures from room temperature to the liquidus temperature of each alloy by optical pyrometry, dilatometry, hardness measurements, and optical metallography.

(c) Determination of the various phases present in each alloy at various temperatures along the temperature scale for different annealing temperatures and following quenching to different temperatures, using optical metallography and X ray diffraction.

Beginning in the mid to late 1970s, the data from the above listed experiments have been supplemented by calculations based on thermodynamic data, especially to fill in portions of the diagram not covered in the experiments.

A.2.1. Development of the U–Mo equilibrium phase diagram

A brief history of the development of the U–Mo equilibrium phase diagram follows. Unless specifically stated otherwise, the temperature scale used by the various researchers is assumed to be the one existing at the time their work was performed (see discussion in Section 2.1.2 of the main body of this publication). Data for this study of U–Mo phase diagrams were either found printed directly on each diagram, taken from text and tables accompanying the diagram, or derived by manual digitization of the phase boundaries shown on the diagram.

(1) The first phase diagram was reported by Ahmann et al. [3] at Iowa State College in 1945. This paper was classified until 14 December 1955 and was not declared publicly releasable until 16 January 2014. It summarised work undertaken by a number of US laboratories. Their study included U–Mo samples from 0.15–93. 3 at.% (0.06–84.7 wt%) Mo and covered a temperature range from ~500 to ~1500°C. Their measured data and their phase diagram (table 1 and fig. 2 of Ref. [3]), obtained through thermal, annealing/micrographic, dilatometric, and X ray studies, are shown below in Table 7 and Fig. 27 [14]. The U–Mo solidus curve agrees reasonably well with that currently used. Their phase diagram, shown between 400 and 1800°C, indicated that the γ phase was stable to room temperature between Mo contents of ~23 and ~28 at.%. They found no evidence of the $\gamma'(U_2Mo)$ phase. Because the liquidus temperatures in Table 7 for the 1.16 and 2.44 at.% Mo samples seem significantly low, they have been assumed to be solidus temperatures in the present analysis. Also, the liquidus and solidus temperatures for the 19.8 at.% Mo sample in Table 1 seem significantly high (each by approximately the same amount); therefore, they have been excluded from the present analysis.

(2) A similar diagram was published in the open literature in 1950 by Pfeil [78], who was working at Harwell in the United Kingdom. Pfeil reported that the γ phase was stable to room temperature for molybdenum contents above 11.7 at.%. A discussion of Pfeil's paper was published in 1951 in which:
   - Seybolt and McKechnie from the Knolls Atomic Power Laboratory (KAPL) reported that the γ phase was not stable below about 450–650°C and that a distorted γ phase of tetragonal symmetry, called the γ' phase, was seen after a five-day annealing at 450°C [79];
   - Tucker from KAPL reported a set of measurements from which he determined a set of lattice parameters for the γ' phase [80];
   - Pfeil [81] reported that his original experiments had not provided a sufficiently close approach to equilibrium and that he had performed subsequent measurements that gave results in general agreement with those of the KAPL data (Refs [79] and [80]).

[14] A phase boundary shown as a dashed line in any of the following phase diagrams indicates that insufficient data exist to confirm it.

TABLE 7. ADAPTED FROM TABLE 1 OF AHMANN ET AL. [3]

Molybdenum (at.%)	Chemical Analysis (wt%)		Liquidus (°C)	Solidus (°C)	Transformation and Phase Changes
	Mo	U			
0	–	–	1133	–	770, 648
0.15	0.06	97.5	1133	–	770, 648
1.16	0.47	99.3	1130	–	714, 580
1.29	0.524	–	1132	–	721, 568
1.57	0.64	98.2	1135	–	683, 580
2.44	1.00	99.06	1120	–	688 (683), 570
4.70	1.95	96.85	1140	1128	614
4.82	2	–	–	–	(644)
7.13	3	–	–	–	(622)
7.31	3.08	91.5	1150	1136	583
9.37	4	–	–	–	(590)
11.6	5.02	95.14	1160	1123	–
12.1	5.25	–	–	–	(556)
12.8	5.56	89.76	1153	1137	535
14.1	6.20	92.8	1171	1126	–
15.7	7	–	–	–	(588)*
16.2	7.23	90.8	1193	1136	–
17.3	7.76	89.1	1199	1142	–
19.8	9.04	88.3	1232	1177	–
22.2	10.33	88.0	1221	1150	–
27.0	12.95	–	–	–	–
30.4	15.00	–	–	–	–
32.0	15.92	83.25	1300	1277, 1193	–
38.5	20.16	78.5	1480	1285, 1227	1190
51.5	29.94	65.1	(none below 1500)	1291	–
59.5	37.2	59.4	–	1280	–
70.8	49.5	44.8	–	1280	–
81.4	63.9	33.94	–	1295	–
93.3	84.7	15.13	–	–	–

* Heating curve

–: data not available

Note: Temperatures in parenthesis were taken by differential thermocouples.

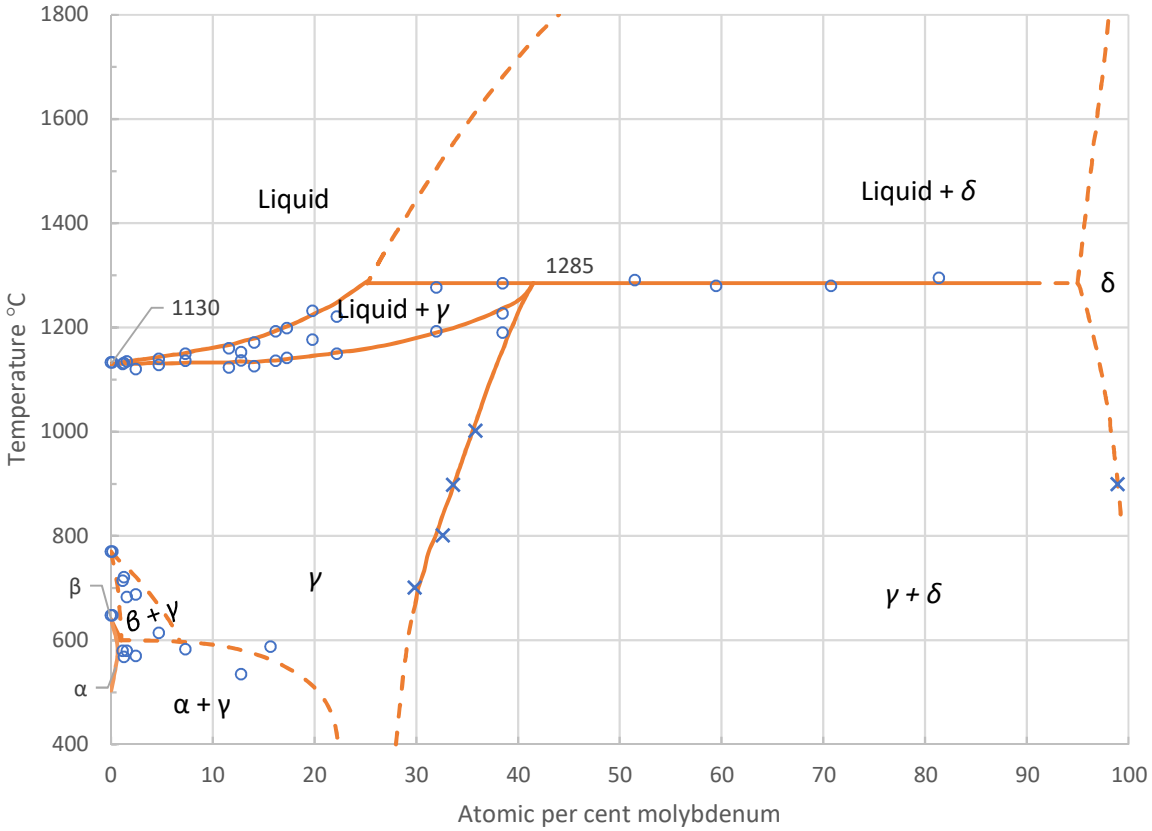

FIG. 27. Ahmann's U–Mo phase diagram (adapted from Ref. [3], fig. 1).

(3) Work at BMI, reported by Saller et al. in 1951 [23] (declassified on 30 November 1955), and by Saller and Rough in 1952 [82] (declassified on 30 July 1957, and declared publicly releasable on 22 March 2006), further defined the structure of the γ' phase and showed the existence of a eutectoid decomposition of the γ phase at 575 ± 10°C and ~26.4 at.% Mo. In addition, the γ' phase was reported to exist between ~28.0 and ~31.3 at.% Mo. The γ' phase was called the ε phase at BMI through at least 1952; the cubic Mo phase found from ~98–100 at.% Mo was called the δ phase, and the designation of these two phases is reversed in Ref. [83], published in 1958. It remained for Halteman, working at the Bettis Laboratory of the Westinghouse Atomic Power Division with an alloy chemically analysed to contain 30.4 at.% Mo, to publicly report the correct crystal structure for the γ' phase (U_2Mo) in 1957 [25].

Rough and Bauer published a U–Mo phase diagram in 1958 showing the eutectoid decomposition of the γ phase at 575°C and ~25.0 at.% Mo and the γ' phase to exist between 31.1 and 32.8 at.% Mo [83]. They also report that Halteman [25] determined the composition range of the γ' phase to be from ~31.5 to ~32.5 at.% Mo; however, Ref. [25] reports work only on the 30.4 at.% alloy. Rough and Bauer's diagram, which contained the best information to that time, is shown in Fig. 28.

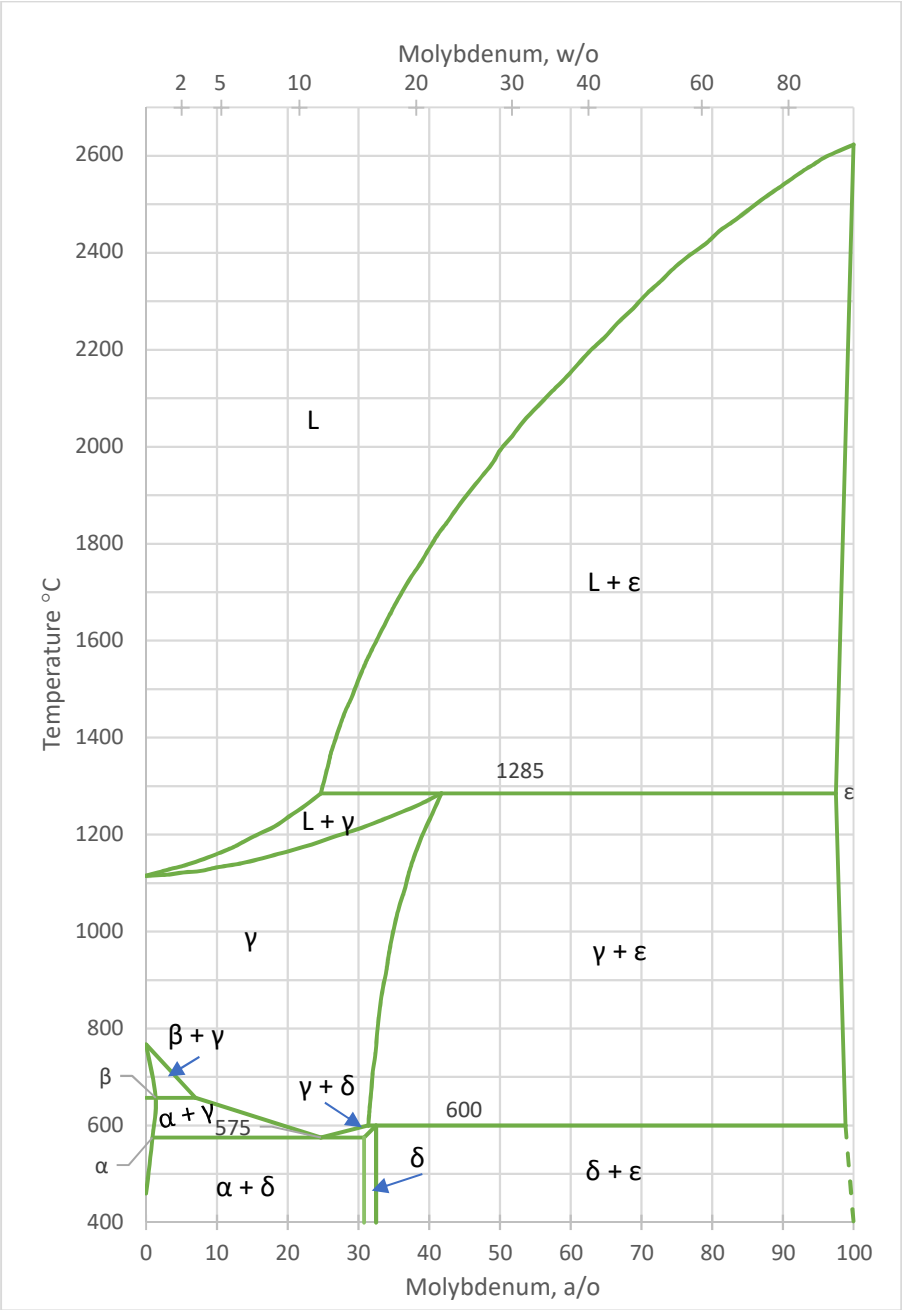

FIG. 28. Rough and Bauer's U–Mo phase diagram of the U–Mo system (adapted from Ref. [83], p. 41).

(4) As stated in Section 2.1.1 of the main body of this publication, the Soviet Union began operation of the world's first nuclear power plant using U–9Mo dispersed in Mg. Konobeevsky et al. presented the then-current Soviet version of the U–Mo equilibrium phase diagram at the Second United Nations International Conference on the Peaceful Uses of Atomic Energy in 1958 [43]. They reported the eutectoid decomposition of the γ phase at 560°C and at ~21.6 at.% Mo.

(5) From 1957 to 1959, Dwight at ANL, and Lehmann at the French Atomic Energy Commission Saclay Research Center performed detailed investigations of U–Mo alloys. Dwight studied alloys containing up to 19 wt% Mo at temperatures below 900°C [22], and Lehmann studied alloys containing up to 4 wt% Mo (below the Mo-content region of

interest for research reactor fuels) at temperatures below 950°C [84]. Both Dwight and Lehmann used metallography and X ray diffraction; Lehmann also performed hardness measurements.

Dwight reported preliminary results in early 1957 showing the $(\alpha + \gamma)/(\beta + \gamma)$ boundary at 637 ± 3°C [85]; his final results placed this boundary at 639 ± 5°C. He employed a sensitive X ray diffraction technique using needle specimens and metallography to show that a prior $\alpha + \gamma$ structure established at 625°C transformed to β at 645°C and that a prior β-structure established at 645°C transformed to $\alpha + \gamma$ at 635°C. Lehmann placed this boundary at 645 ± 5°C, based on metallographic results showing that a U–3Mo sample heated for 3 min. at 950°C and cooled to 640°C over a 1 h period showed growth of α phase lamellae in the γ phase grains. Considering the methods described by each of the authors to determine this boundary, the quality of Dwight's data appears to be at least as high as that of Lehmann. Lehmann also provided a detailed description of the various transformation phenomena seen in the region of the equilibrium phase diagram from 0.5–4 at.% Mo.

Dwight reported the eutectoid decomposition point of the γ phase at 565 ± 5°C and ~10.5 wt% (~22.6 at.%) Mo. He located the γ' phase (called δ phase in his diagram) between ~15.5 and 16.2 wt% (~31.3 to ~32.9 at.%) Mo. Lehmann's phase diagram locates the $(\alpha + \gamma)/(\alpha + \gamma')$ boundary, which is at the eutectoid temperature, at ~557°C. Dwight's phase diagram is shown in Fig. 29. There is an inconsistency in Dwight's reported limit of the $(\beta + \gamma)$ field: 4.5 wt% (10.5 at.%) Mo in the abstract and 4.8 wt% (11.0 at.%) Mo determined during this work from the phase diagram in fig. 2 of Ref. [22].

(6) In 1964, Streets and Stobo published a 'matrix binary' equilibrium U–Mo phase diagram [86] constructed from the data collected during their study of the ternary U–Mo–C system. Their diagram was in good agreement with that of Dwight except: (a) the limit of the $(\beta + \gamma)$ field was placed at 9.3 at.% Mo rather than at Dwight's 10.5 at.%, and (b) the $\gamma/(\gamma' + \text{Mo})$ eutectoid composition was placed at 36at.% Mo at 580°C rather than at Dwight's 34at.% Mo at approximately the same temperature. The limit of the $(\beta + \gamma)$ field attributed to Dwight came from the 4.5 wt% listed in the abstract of Ref. [22]. In Ref. [22] Dwight explicitly stated that no data were available for the $\gamma/(\gamma' + \text{Mo})$ eutectoid composition or temperature; however, the eutectoid point is shown at 34 at.% Mo and 577°C in the phase diagram as seen in Fig. 29. This appears to be the first determination of the temperature of the eutectic line separating the $(\text{Mo} + \gamma')$ and $(\text{Mo} + \gamma)$ phase fields (580 ± 7°C).

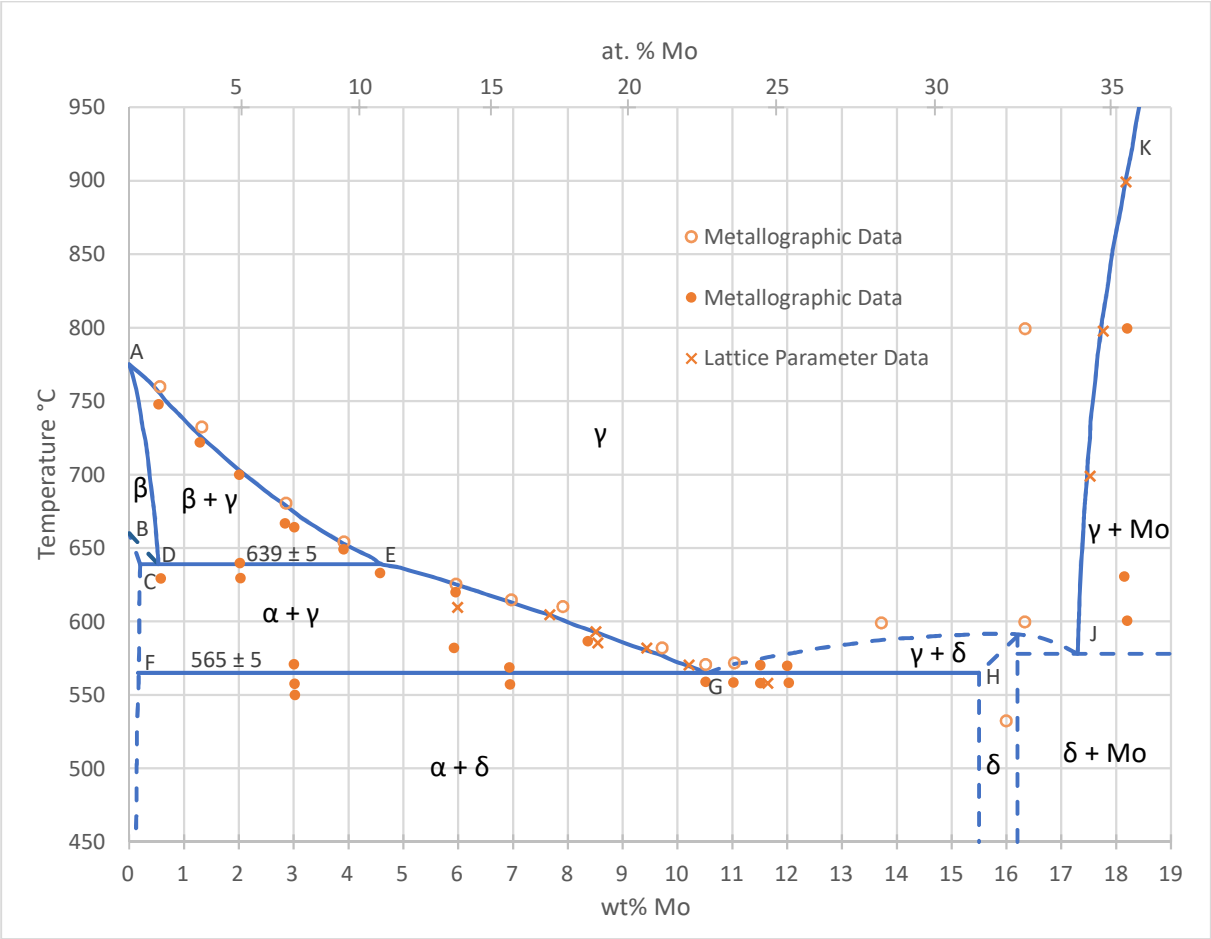

FIG. 29. Dwight's U–Mo Phase Diagram to 19wt% Mo (adapted from Ref. [22], fig. 2).

(7) In 1977 Garg and Ackermann published the results of their study of the high-temperature portion of the U–Mo phase diagram [26], shown in Fig. 30. They used a very sensitive technique based on observing the melting or solidification of the U–Mo in a molybdenum cup viewed by a disappearing-filament optical pyrometer through a small observation hole, described in Ref. [87]. It is not known why they did not measure the U–Mo liquidus temperature during the same experiment.

(8) In 1989, Lundberg published results of work at Los Alamos National Laboratory that indicated the existence of U_2Mo in the temperature range 1127–1252°C [88]; however, he stated that further study was needed to provide a final definition of the high temperature regions of the diagram. No reference to a further study has been found.

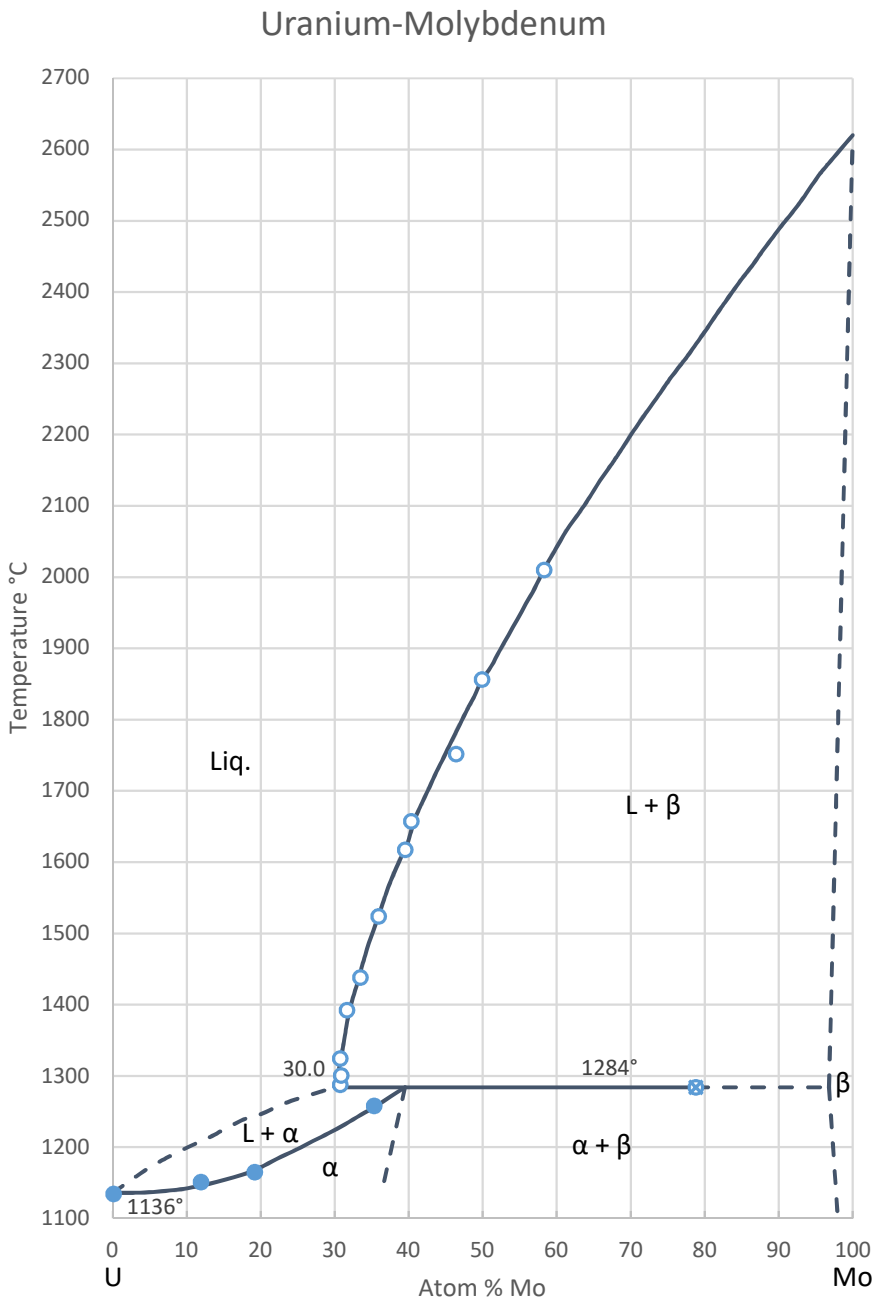

FIG. 30. Garg and Ackermann's U–Mo phase diagram above 1100°C (adapted from Ref. [26], fig. 3).

A.2.2. Compilations of the U–Mo phase diagram

A number of general compilations of binary phase diagrams have been published, beginning in 1958:

(1) In 1958, Hansen and Anderko published the second edition [89] of Hansen's original compilation of binary alloy structures.[15] Their main diagram was constructed using open-

[15] The first edition of Hansen's compilation was published in Germany in 1936 as Der Aufbau der Zweistofflegierungen; of course, U–Mo alloys were not known at that time.

literature data from 1949–1951 discussed in item (2), Section A.2.1. A note added in proof showed a much better diagram of the region between 400 and 800°C, which included some results from work in US laboratories that was being declassified around 1957 (see item (3), Section A.2.1).

(2) Elliott performed a critical review of the literature available through December 1961 pertaining to binary alloys and in 1965 published a first supplement [90] to the work of Hansen and Anderko (see item (1), above). For U–Mo, he stated a preference for Dwight's data (see item (4), Section A.2.1) because of the intensity of Dwight's investigation. Elliott's phase diagram covered the temperature range of 400 to 900°C, and it appears to be essentially identical to Dwight's diagram. He noted that the peritectic decomposition point (mistakenly calling it peritectoid decomposition, which applies only to a reaction of solid phases), at 1290°C and 40 at.% in Konobeevsky's phase diagram (see item (4), Section A.2.1), was in good agreement with that shown by Hansen and Anderko. He did not consider the work of Lehmann [84] during his review.

(3) Shunk published a second supplement [91] to the work of Hansen and Anderko (see item (1), above) in 1969, for which he reviewed primarily the data that became available during 1962–1964. Shunk states that Elliott's diagram (see item (2), above) was confirmed except for minor variances in the solubility of Mo in β–U and in the temperature of the β–U eutectoid reaction; Lehmann had found this to be at 645 ± 5°C rather than at 639 ± 5°C as determined by Dwight (see item (4), Section A.2.1).

(4) In 1973, Hultgren et al. published a U–Mo phase diagram based on those of Hansen and Anderko (see item (1), above) and Elliott (see item (2), above) [92].

(5) In 1973, Hawkins and Hultgren published a detailed U–Mo phase diagram [93] attributed to Hansen and Anderko (see item (1), above), Elliott (see item (2), above), and Shunk (see item (3), above), which is shown below in Fig. 31. Very usefully, this diagram provides a number of explicit temperatures and uranium weight percentages. Indeed, the temperature of the β–U eutectoid reaction had been changed to 645°C, as indicated by Shunk (see item (3), above).

(6) In 1980, Brewer and Lamoreux published a U–Mo phase diagram based on both direct experiment and calculations using thermochemical data [94]. They began with the diagrams of Hawkins and Hultgren (see item(5), above) and Hultgren et al. (see item (4), above), some data on the solubility of Mo in α–U were taken from Gomozov et al. [95], and data on the γ–U solidus and Mo liquidus were taken from Garg and Ackermann (see item (7), Section A.2.1). Brewer and Lamoreux's text accompanying their phase diagram provides equations for a number of the phase boundaries. Their phase diagram is shown below in Fig. 32.

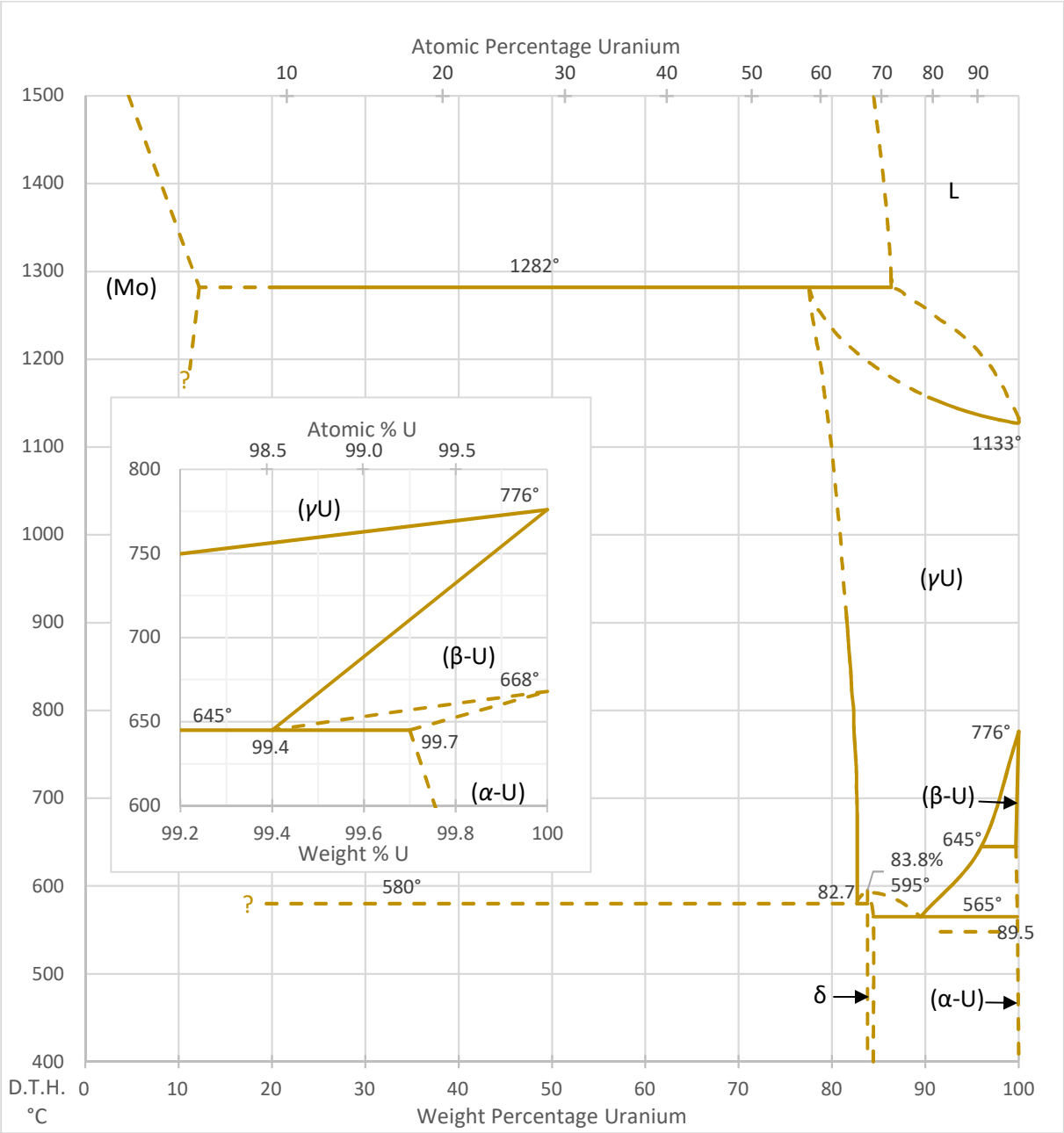

FIG. 31. Hawkins and Hultgren's U–Mo phase diagram (adapted from Ref. [93], p. 321).

(7) The 1998 'paperback version' of the seventh edition of Smithells Metals Reference Book [96] showed a U–Mo phase diagram based on the very old data of Pfeil [78] and the newer data of Streets and Stobo [86].

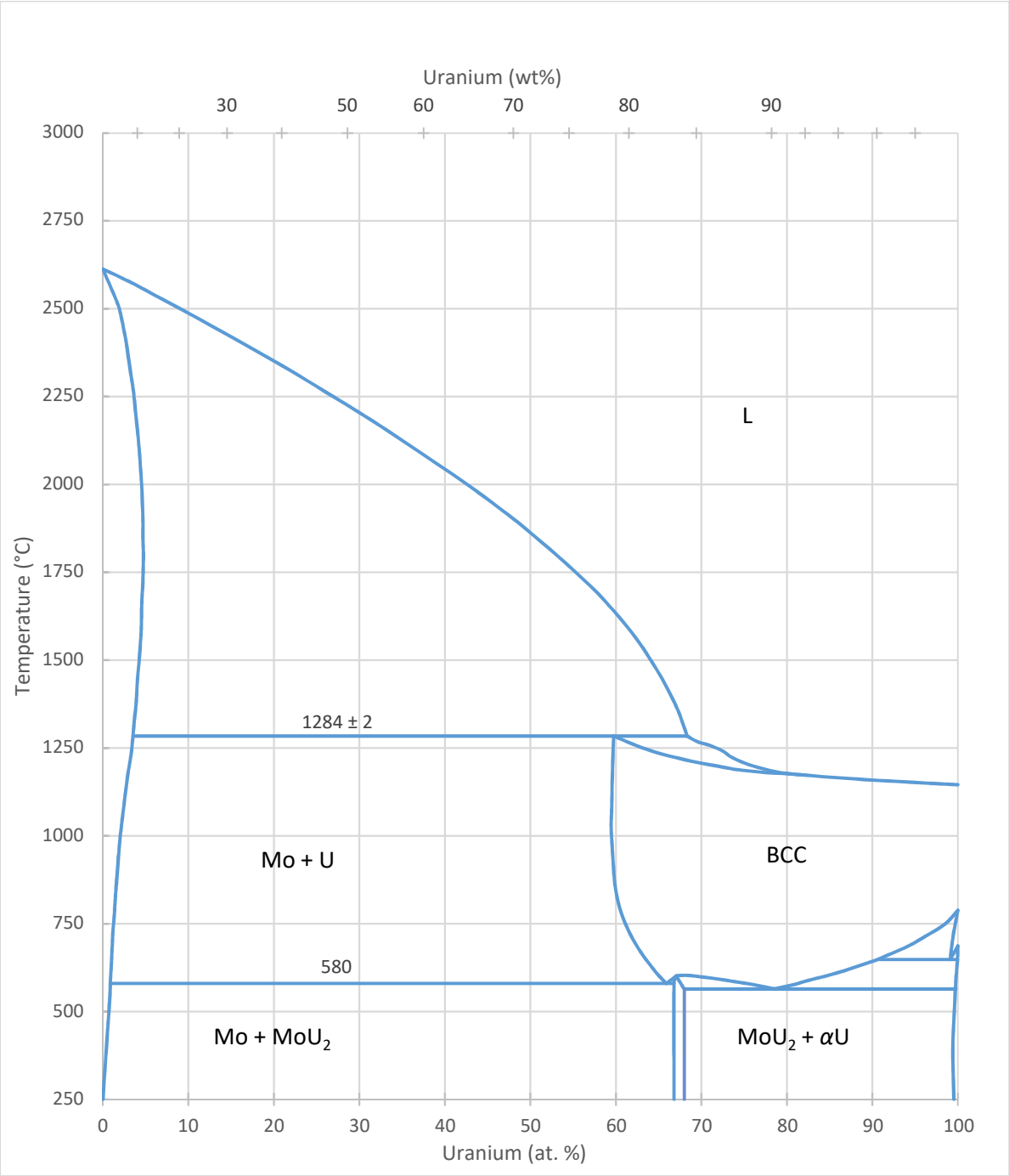

FIG. 32. Brewer and Lamoreaux's U–Mo phase diagram (adapted from Ref. [94], p. 321).

(8) In 1990, Massalski [21] presented a U–Mo phase diagram, shown in Fig. 33, that had been redrawn from that of Brewer and Lamoreaux. (See item (6), above). He has added dashed lines to indicate that Lundberg [88] had found evidence that U_2Mo exists in the temperature range 1127–1252°C (see item (8), Section A.2.1).

(9) In 2004, the 8th edition of Smithells Metals Reference Book [97] changed the U–Mo phase diagram to that of Massalski [21]. (See item (8), above). However, the citations were not updated from those of the seventh edition.

In 2012, Okamoto [98] published a new version of the molybdenum–uranium phase diagram calculated by Berche et al. in 2011 [99] using a Calphad complex thermodynamic database being developed for fourth generation nuclear fuels. Although this phase diagram will not be considered further in the present work, a copy is shown in Fig. 34 to illustrate the differences between this calculated U–Mo phase diagram and those diagrams developed mainly from direct measurements made on U–Mo samples.

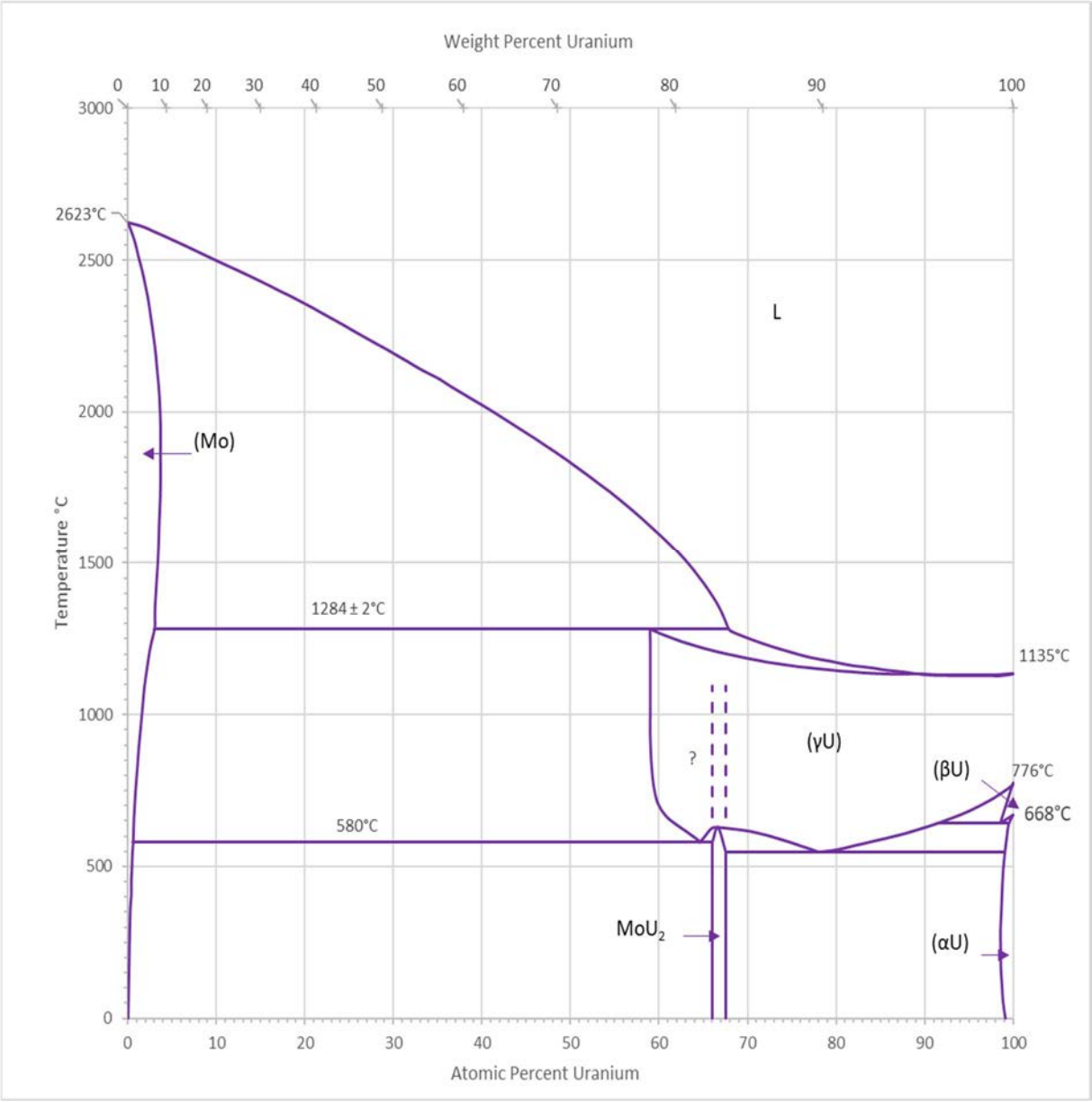

FIG. 33. Massalski's U–Mo phase diagram adapted from Ref. [21], p. 2683).

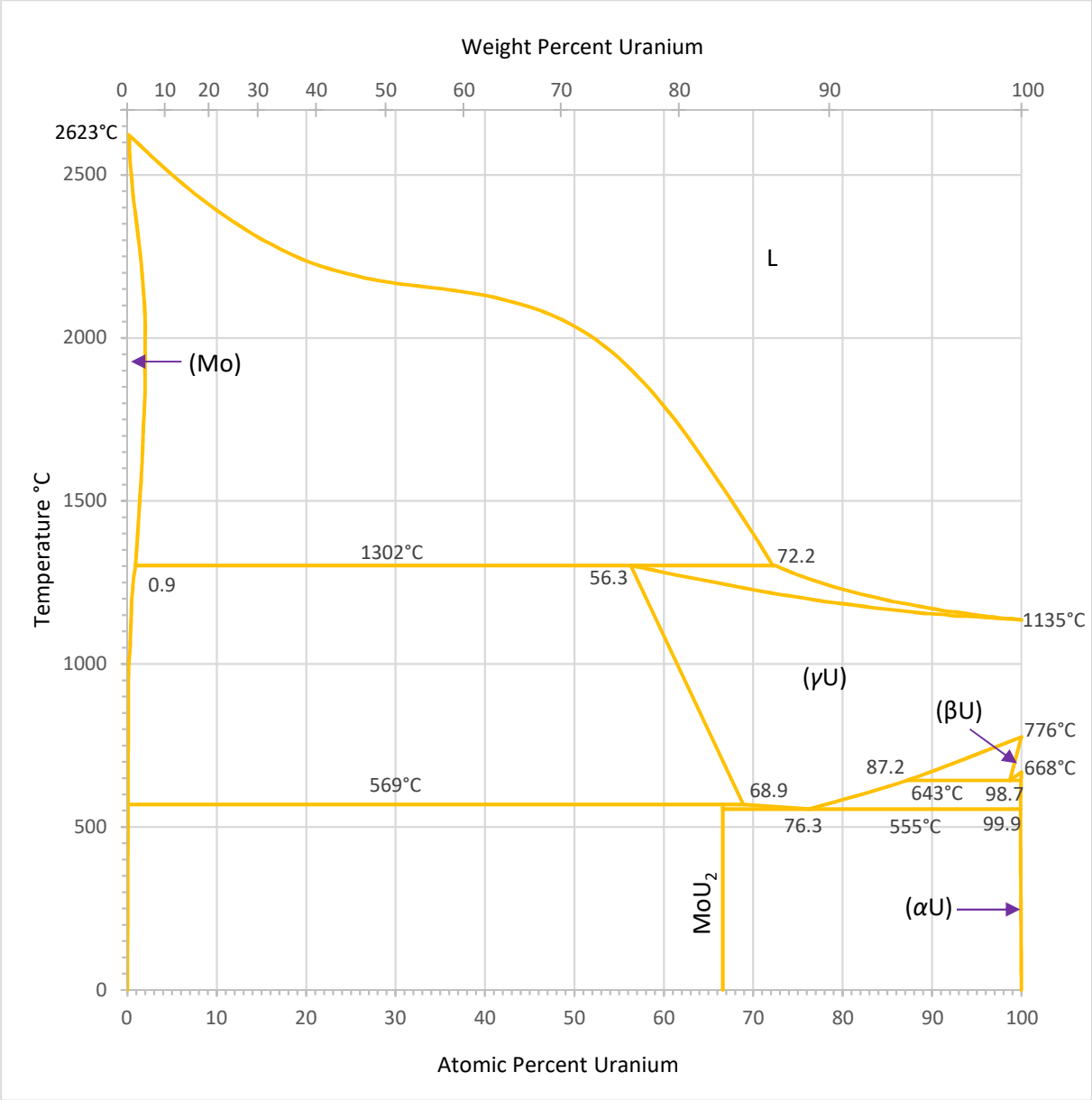

FIG. 34. Berche et al.'s calculated U–Mo phase diagram (adapted from Ref. [98], p. 497).

A.2.3. Discussion of the U–Mo phase diagram and suggested changes

It was necessary to digitize the phase boundary lines in the diagrams shown in the previous section to obtain numerical data. Manual digitization was used to obtain most of the data used to compare the results presented in the various diagrams, although some of the discussions in the references containing the diagrams give the coordinates (composition and temperature) of some points of special interest. Attempts were made to compensate for the varying quality of the diagrams and for some distortion of the diagrams during photocopying; however, the digitization process was not perfect, e.g. some phase boundaries at constant temperature or U content were found to vary by a few pixels from end to end. Such variations, however, represented no more than 3°C or ~0.2 at.%.

In general, the digitized data from a given phase diagram agreed with the data from the references cited as the basis for that diagram. A comparison of (Brewer and Lamoreaux's and Massalski's) diagrams is shown in Fig. 35, along with a number of published data points.[16] Gridlines have been added to aid in seeing the magnitudes of the various differences between the two diagrams. All temperatures have been converted to the ITS-90 scale. See Section 2.1.2 of the main body of this publication for a discussion of temperature scales.

It is interesting to note that most of the experimental data shown in Fig. 35 came either from the earliest (Ref. [3], 1945) or the latest (Ref. [26], 1977) of the publications describing experimental studies of U–Mo phase diagrams. These data appear to be all of the available data between the melting point of U and that of Mo. Gomozov et al.'s three data points showing the solubility limit of Mo in αU between 550 and 630°C are 0.05 at.% Mo at 550°C, 0.12 at.% Mo at 600°C, and 0.19 at.% Mo at 630°C. The many data points used to establish the part of the phase diagram below a straight line from coordinates (64 at.% U, 600°C) to (100 at.% U, 800°C) are not shown — figs 2 and 3 of Ref. [22] and fig. 2 of Ref. [23] show many of these.

Massalski stated that his diagram was redrawn from Brewer and Lamoreaux's diagram, with only the addition of the information from Lundberg; however, no explanation was given for the many differences between the two diagrams. Some differences apparently resulted from plotting mistakes, while others might result from purposeful changes, but the reasons for such changes, if any, were not explained. For example:

- The digitized value of the melting point of γ–U in Brewer and Lamoreaux's diagram (Ref. [94]) was 1148°C, compared to 1134 ± 2°C (on the ITS-90 scale) determined by Dahl and Cleaves [100] as the freezing point of very pure uranium. Dahl and Cleaves found that addition of impurities lowers the freezing (melting) point, so impure U cannot be the cause of the discrepancy; besides, Brewer and Lamoreaux's equation for the U–Mo liquidus line shows it beginning at 1133 ± 2°C. Therefore, the U solidus and liquidus lines in the diagram are considered to be misdrawn;
- In Massalski's diagram [21], the boundary separating the ($\alpha + \gamma'$) from the ($\gamma + \gamma'$) and ($\alpha + \gamma$) phases is shown at 550°C. Because Massalski stated that his diagram was redrawn from Brewer and Lamoreaux's diagram [94], which shows this boundary at 565°C and because Massalski gave no reason for making this change, it is assumed that this is an error in the diagram;
- There are obvious discrepancies between a number of phase boundaries and the measured data points. This is especially evident for the (Mo + γ)/γ phase boundary;
- The two diagrams disagree on the location, width, and height of the γ' phase field;
- It appears that Massalski might have used Ahmann et al.'s measured data to determine his U–Mo solidus line, but it appears that he did not use Ahmann et al.'s liquidus data.

[16] Many more data are available for U–Mo phase equilibria at temperatures below the β-U to γU phase-transformation temperature. Dwight's data shown in Fig. 29 are among the most important.

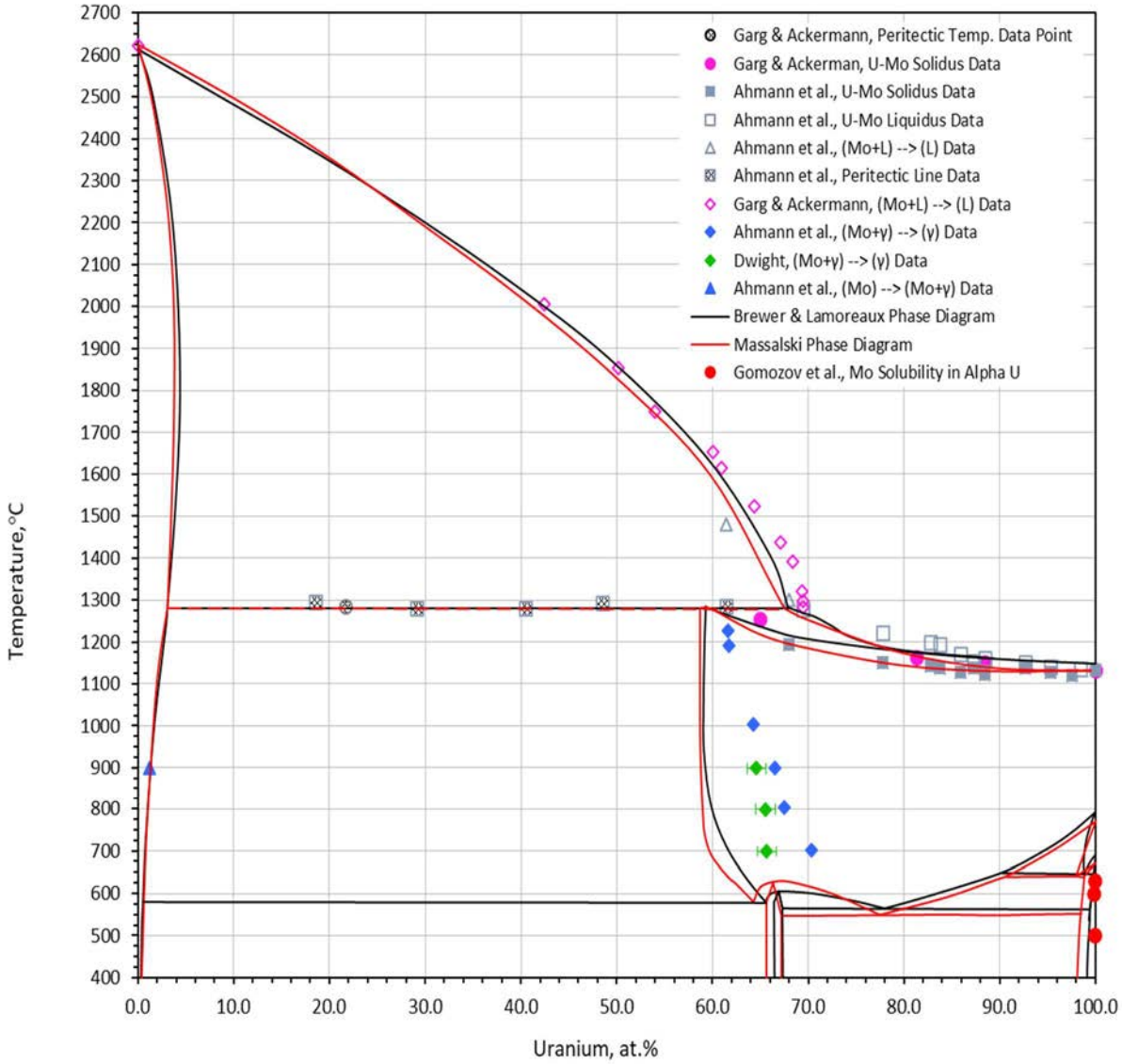

FIG. 35. Comparison of Brewer and Lamoreaux's [94] and Massalski's [21] phase diagrams drawn from digitized points on the phase boundaries shown in FIG. 1 and FIG. 33. The data points are from Refs. [3, 22, 26, 95] (courtesy of Argonne National Laboratory).

A.2.4. Proposed new U–Mo phase diagram

Owing to the wealth of U–Mo phase equilibria (Mo concentration vs. temperature) data available at the higher temperatures and the rather poor agreement of the uranium solidus and liquidus lines, the molybdenum liquidus line, and the (Mo + γ)/γ–U phase boundary with the data, a new diagram is proposed for consideration. The new phase diagram is primarily based on the phase diagrams published by Brewer and Lamoreaux [94] and by Dwight [22], supplemented by other phase boundaries fit to the data shown in Fig. 35. The new diagram was constructed as follows:

- All temperatures have been converted to the ITS-90 scale;
- Temperatures have been rounded to the nearest degree; U contents have been rounded to the nearest tenth of an atomic percent from 0 to 98 at.% and to the nearest hundredth of an atomic percent above 98 at.% U, where large changes in temperature can occur for

small changes in atomic content. The precision of these values bears no relationship to their accuracies. Uncertainties of chemical analyses stated in the literature are typically about ±0.25 wt% (±0.47 at.% for U–10Mo containing natural or depleted U). Temperature uncertainties generally have been stated only for the major isothermal transition lines. The line containing the γU–Mo peritectic point at 1284°C has a ±2°C uncertainty, while the lines containing the γU–Mo eutectoid point at 565°C and the βU–Mo eutectoid point at 639°C have ±5°C uncertainties. Brewer and Lamoreaux place an uncertainty of ±40°C on the 580°C temperature of the transition line separating the (γ' + Mo) and (γ + Mo) phases, based on the high sensitivity of the thermodynamic equations in the region of the γU–Mo eutectoid near 65.5 at.% U and the melting point of the γ' phase. Metallographic and other data in this region indicates a lower uncertainty;

- The melting point of pure U (1134 ± 2°C) was taken from Dahl and Cleaves [100]. The melting point of pure Mo (2622°C) and the α–β and β–γ transition temperatures (668 and 776°C, respectively) of pure U were taken from Massalski [21];
- The lower part of the diagram from the γU–Mo eutectoid point (65.5 at.% U, 580°C) to the uranium β–γ phase transition point (at 100 at.% U and 776°C) and below were taken from Dwight's diagrams (figs. 2 and 3 of Ref. [22]) or from Brewer and Lamoreaux's diagram [94], which were in excellent agreement with each other in this range. The α–U solvus line was adjusted to agree with Gomozov et al.'s data [95]. While adjusting the solvus line, the intersection of the solvus line, the ($\alpha + \beta$) to α transition line, and the ($\alpha + \beta$) to ($\alpha + \gamma$) transition line was set at (99.63 at.% U, 639°C) instead of Dwight's coordinate (99.56 at,% U, 639°C), still in agreement with Dwight's data shown in his fig. 3;
- Two sets of well-separated data exist for the U–Mo solidus line — that of Ahmann et al. in 1945 [3] and that of Garg and Ackermann in 1977 [26]. As mentioned above, it is possible that Massalski drew a smooth curve through Ahmann et al.'s data points to define the solidus line in his diagram. Although Garg and Ackermann measured only four points, the technique they used detects initial melting of the γ(U–Mo) solid solution with high sensitivity [87], so their data should be more accurate. The solidus line in the new diagram is a quadratic fit to these four data points with the constraints that the temperature is 1284°C at 60.5 at.% U and 1134°C at 100 at.% U.

  Because Garg and Ackermann made only four measurements, a true least squares fit with two additional constraints cannot be performed. The curve was artificially adjusted using a fifth data point at 76.5 wt% U, the temperature of which was adjusted to force the curve to meet the constraints. This technique was also used to produce a few of the equations for data extracted from the curves. The equation of the γ phase solidus line is:

$$T_{\text{U–Mo solidus}} = 0.09982(x_a^U)^2 - 19.81(x_a^U) + 2117, (60.5 \le x_a^U \le 100) \quad (38)$$

  where $T_{\text{U–Mo solidus}}$ is the solidus temperature in °C and x_a^U is the uranium content of the alloy in at.%.
- The U–Mo liquidus curve is a quadratic least squares fit of Ahmann et al.'s liquidus data points from Table 7 with the constraints that the temperature is 1284°C at 69.5 at.% U and 1134°C at 100 at.% U. The equation of the γ phase liquidus line is:

$$T_{\text{U–Mo liquidus}} = 0.1236(x_a^U)^2 - 25.87(x_a^U) + 2485, (69.5 \le x_a^U \le 100) \quad (39)$$

  where $T_{\text{U–Mo liquidus}}$ is the liquidus temperature in °C and x_a^U is the uranium content of the alloy in at.%.

- The Mo liquidus curve from 1284 to 2000°C was constructed as a piecewise quadratic curve fit to Garg and Ackerman's data constrained to match the endpoint of the U–Mo liquidus curve at 69.5 at.% U and 1284°C and the pure Mo melting point at 2622°C;
- The (Mo + γ)/γ phase boundary is a quadratic curve drawn through Dwight's three data points and ending at the peritectic point (60.5 at.% U at 1284°C). Although the U content at the peritectic point is ~1.5 at.% higher than shown by Brewer and Lamoreaux or Massalski, the value chosen seems to be more in line with the data. It is interesting to note that Ahmann's three data points at 1000°C and higher for this phase boundary are in quite good agreement with the proposed curve, although they were not considered in its construction. The change in the shape of the curve had they been included would have been negligibly small compared to the uncertainty in the data;
- All of the nonlinear phase boundaries are constructed of single or piecewise quadratic curves, either fit to data as described above or fit to points along phase boundaries determined by manual digitization of phase boundaries in Brewer and Lamoreaux's or Dwight's diagrams;
- Dashed vertical phase boundaries for the γ' phase have been included up to 1252°C to indicate the possibility that this phase exists at higher temperatures as suggested by Lundberg [88]; recall that his experiment covered the temperature range 1127–1252°C.

The proposed U–Mo phase diagram is shown in Fig. 36, with the coordinates (uranium at.%, temperature) of all intersections shown. The coefficients of the quadratic equations for all of the nonlinear phase transition lines are listed in Table 8. In general, four significant digits for the coefficients of the quadratic equations given in Table 8 of the Appendix were sufficient to accurately reproduce the digitized transition line data being fit (to the nearest 0.1 or 0.01 at.% and nearest °C). Occasionally, a fifth significant digit was necessary, especially when the calculated U content was being expressed to the nearest hundredth of an atomic percent. Recall that the number of significant digits shown are required merely to reproduce the data obtained from a previous phase diagram and do not indicate the accuracy of the underlying data.

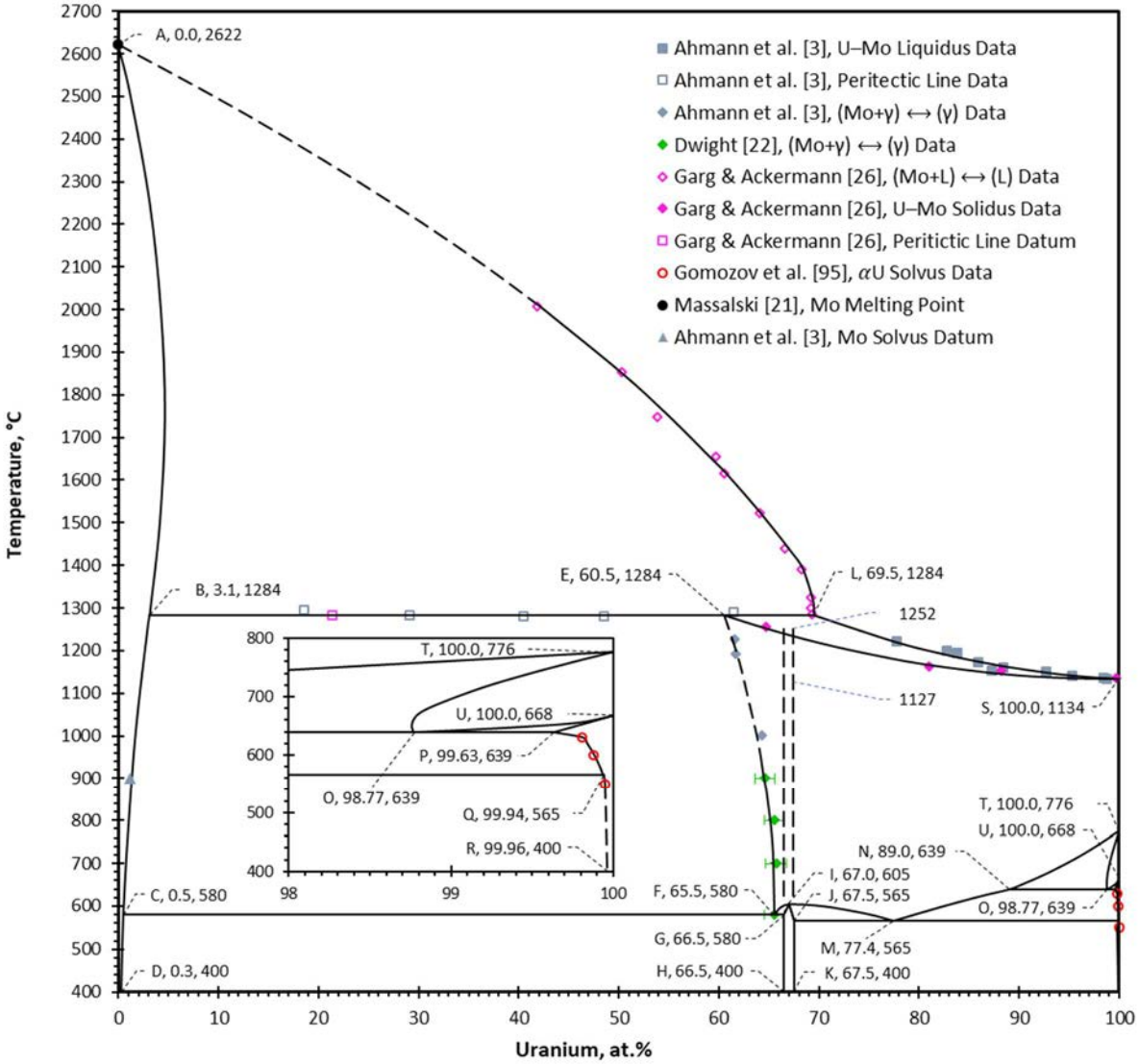

FIG. 36. Full new phase diagram proposed for the U–Mo system showing data points used in its development. Phase-boundary end points (at.% uranium, temperature) are also shown (courtesy of James L. Snelgrove).

TABLE 8. COEFFICIENTS OF EQUATIONS OF PHASE BOUNDARIES IN THE PROPOSED U–Mo PHASE DIAGRAM

Line Label	Independent Variable	Independent Variable Limits of Validity		Coefficients of Quadratic Equations		
		Lower	Upper	a_2	a_1	a_0
BCD	T	400°C	1284°C	2.643E−6	−1.286E−3	3.737E−1
AB	T	1284°C	2622°C	−6.315E−6	2.236E−2	−1.522E+1
AL	T	1284°C	1393°C	−2.089E−5	2.8194E−2	2.8194E−2
		1393°C	2622°C	−9.7051E−5	2.5016E−1	−9.1705E+1
ES	x_a^U	60.5 at.%	100 at.%	9.982E−2	−1.981E+1	2.117E+3
LS	x_a^U	69.5 at.%	100 at.%	1.236E−1	−2.587E+1	2.485E+3
EF	T	580°C	1284°C	−1.070E−5	1.284E−2	6.165E+1
FI	x_a^U	65.5 at.%	67.0 at.%	−1.2965E+1	1.7344E+3	−5.74E+4
IM	x_a^U	67.0 at.%	77.4 at.%	−3.332E−1	4.430E+1	−8.671E+2
MN	x_a^U	77.4 at.%	89.0 at.%	−8.233E−2	2.008E+1	−4.958E+2
NT	x_a^U	89.0 at.%	100.0 at.%	3.489E−1	−5.353E+1	2.64E+3
OT	T	639°C	681°C	1.5387E−4	−2.0064E−1	1.6415E+2
		681°C	776°C	3.488E−5	−3.888E−2	1.0917E+2
OU	T	639°C	668°C	−1.469E−3	8.5E−2	9.877E+1
PU	T	639°C	668°C	0	1.276E−2	9.148E+1
PQ	T	565°C	630°C	−1.122E−5	1.15E−2	9.702E+1
		630°C	639°C	0	−2.0E−2	1.1241E+2
QR	T	400°C	550°C	0	−9.5E−5	1.0E+2
		550°C	565°C	−1.122E−5	1.15E−2	9.702E+1

A.3. TRANSFORMATION KINETICS OF γ PHASE U–Mo ALLOYS

Beghi [2] has summarized the results of 11 investigations made during the 1950s and 1960s of the kinetics of the isothermal decomposition of U–Mo alloys in the metastable γ phase. The results were generally reported as TTT diagrams, often called C curves owing to their shape, which are plots of the sample temperature versus the time at temperature when transformation from the metastable γ phase is first detected. An example, taken from McGeary [4], of a set of TTT diagrams is shown in Fig. 37. The minimum of the C curve with respect to time is called the nose of the curve. It is interesting to note that the time required for initiation of transformation from the metastable γ phase increases for temperatures both below and above the temperature of the nose. Repas et al. [32] concluded that the decomposition of the γ phase "is relatively complex and takes pace by several different mechanisms".

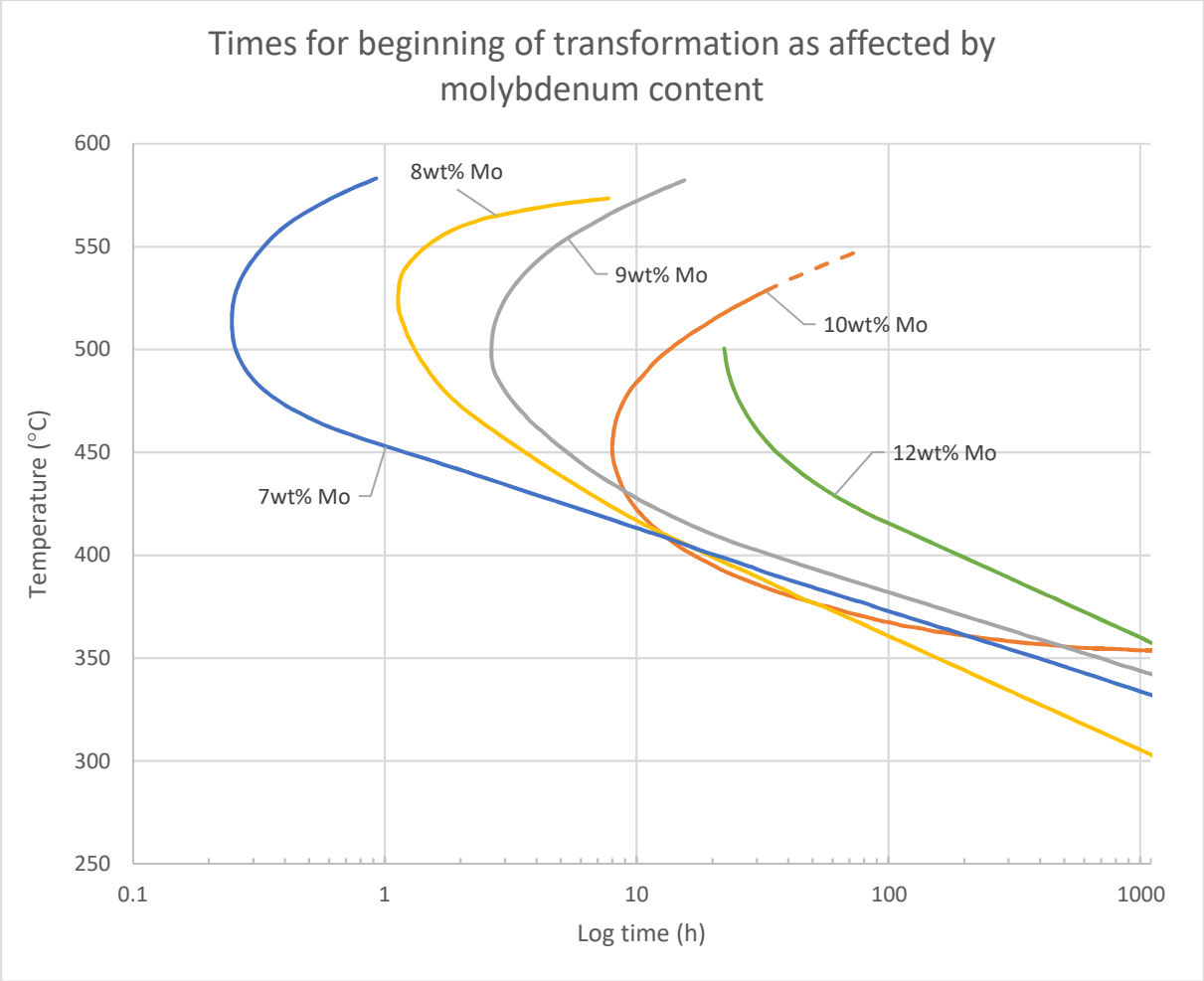

FIG. 37. TTT Diagrams for U–Mo alloys developed by metallographic examination of samples isothermally heated for different lengths of time (adapted from figure 13 of McGeary [4]).

Several methods, either alone or in combination, have been used to detect the initiation of phase change: metallography, resistivity change, hardness change, X ray diffraction, and dilatometry. McGeary used metallography to develop all of the TTT diagrams shown in Fig. 37, and Fig. 38 illustrates how McGeary used this technique to develop the TTT C curve for U–7Mo. Each of the metallographic images is centered at the annealing temperature and time for the sample from which metallographic specimen was taken. The images below the curve show grains and grain boundaries typical of unreacted γ phase U–Mo; the images above and to the right of the curve show changes to the grain boundaries and/or the U–Mo of the grain interior, indicating that transformation has occurred.

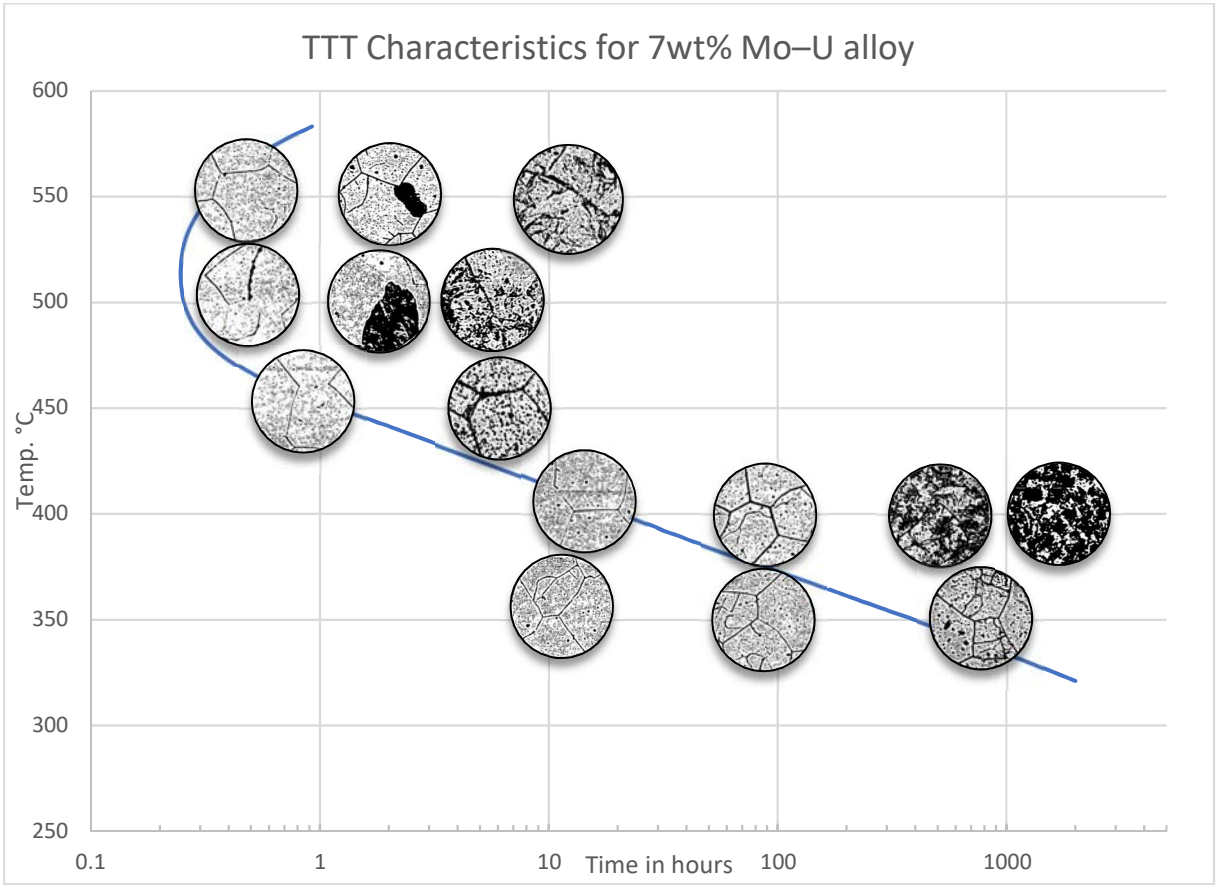

FIG. 38. Use of metallographic images to develop TTT diagram for U–7Mo (adapted from figure 11 of McGeary [4]).

As Fig. 39 illustrates, Van Thyne and McPherson [27] found that the shape of the TTT diagram for U–5.4Mo and the position of its nose was significantly affected by the method of measurement; also, metallography detected the initiation of transformation at an earlier stage than resistivity or hardness measurements. For U–8Mo, U–10Mo and U–12Mo, however, they found that metallography was not completely satisfactory for determining the nose of the TTT diagram. In contrast, McGeary used metallography to develop all of the TTT diagrams shown in Fig. 38. Peterson and his colleagues at the Lawrence Radiation Laboratory [31] concluded that measurement of resistivity change was likely the most sensitive technique across the temperature range of interest and that at high temperatures provided results in good agreement with those obtained by metallography. At lower temperatures, they found metallography to be inferior and found the resistivity change and hardness change techniques to be the most reliable. All seem to agree that metallography is not useful at lower temperatures, but there was obvious disagreement on its use at temperatures near that of the nose of the TTT curves.

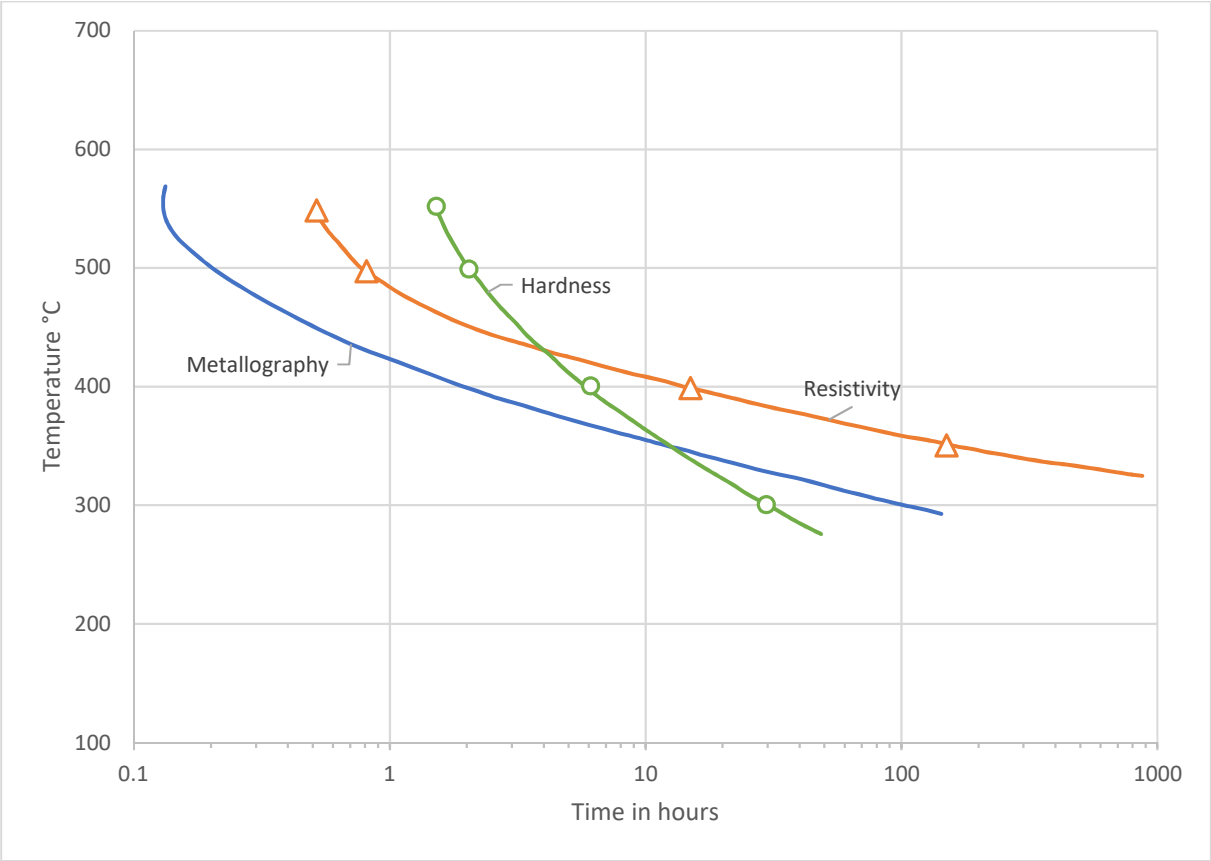

FIG. 39. Differences in the TTT diagrams of U–5.4Mo determined by various techniques (adapted from figure 24 of Van Thyne and McPherson [27]).

The TTT diagrams for six of the 11 investigations discussed by Beghi have been manually digitized to provide the data presented in Table 9 and plotted in Fig. 2 in this publication. Four of the remaining five investigators provided no data for U–Mo alloys of interest for this publication, and data of the final investigator were, again, highly inconsistent with the data in Table 9.

TABLE 9. TRANSFORMATION INITIATION TIMES (h) OBTAINED BY MANUAL DIGITIZATION OF TTT DIAGRAMS REPRODUCED BY BEGHI [2] AND BY FACKELMANN [9]

Mo (wt%)	Source[a]	Technique[b]	Temperature (°C)													
			550	540	525	520	510	505	500	495	490	475	455	450	425	400
5.4	V T	Metall.	**0.13**	–	0.15	–	–	–	0.20	–		0.31		0.51	0.94	1.92
7	McG	Metall.	0.34	–	0.26	–	**0.25**	**–**	0.26	–	0.26	0.38	–	1.2	4.6	20
	P	Resist. +	1.5	1.2	1.1	**1.1**	1.1	–	1.2	–	1.4	1.8	–	3.2	–	–
8	McG	Metall.	1.5	–	**1.2**	**–**	–	–	1.3	–	–	1.9	–	3.5	6.9	19
	B	Dila.	6.0	4.0	–	**2.64**	2.7	–	3.0	–	3.7	5.7	–	13	–	–
	D	Metall.[c]	0.55	–	0.40	–	**0.38**	**–**	0.39	–	–	0.58	–	1.2	–	–
	P	Resist. +	3.1	2.1	**1.7**	**–**	1.8	–	2.1	–	2.5	3.5	–	6.5	–	–
	R	Metall. +	2.4	–	0.98	–	–	–	0.69	–	**0.67**	0.72	–	1.2	–	5.7
9	McG	Metall.	4.9	–	3.2	–	–	–	–	**2.7**	**–**	3.3	–	5.3	9.9	32
10	McG	Metall.	–	–	31	–	–	–	15	–	–	9.2	**8.1**	8.2	9.6	17
	P	Resist. +	14	10	7.3	–	**6.6**	**–**	6.7	–	7.3	9.8	–	21	–	–
	R	Metall. +	55	–	11	–	6.3	–	5.5	–	**5.3**	5.5	–	7.1	–	21
12	McG	Metall.	–	–	–	–	–	–	**22**	**–**	–	25	–	34	59	180
	P	Resist. +	–	53	29	–	**19**	18	18	–	21	27	44	54	–	–

Note: The nose of each curve is indicated by bold-face type.

–: data not available.

[a] The original sources of the TTT diagrams used in the current analysis are: B (J. Bellot et al., Ref [29]); D (G. Donze and C. Cabane, Ref. [30]); McG (R.K. McGeary, Ref. [4]); P (C.A.W. Peterson et al., Ref. [31]); R (P.E. Repas et al., Ref. [32]); and V T (R. J. Van Thyne and D. J. McPherson, Ref. [27].

[b] Technique: Dila. (Dilatometry); Metall (Metallography); Metall. + (Metallography, hardness, and dilatometry); Resist. + (Resistivity, hardness, and metallography).

[c] The metallographic technique is assumed to have been used, based on the title of the article.

A.4. ROOM TEMPERATURE DENSITIES OF γ PHASE U–Mo ALLOYS

A.4.1. Introduction

The density of a crystalline material, such as U–Mo, can be measured at room temperature by two techniques — by the Archimedes method of liquid volume displacement and by measuring the lattice parameters of the crystals forming the material using X ray or neutron diffraction and then calculating the density based on the volume and mass of the crystal's unit cell. The former method measures the 'effective' density of the bulk material, accounting for the presence of voids and contaminants in the material; while, if the contaminant content is sufficiently low, the latter method measures the density of the pure, fully dense material, called its theoretical density. Lattice parameters of materials above room temperature can also be measured. However, the most common method of determining effective densities at elevated temperatures is to measure the dimensional change of the material upon heating; the proportional change in the density is the inverse of the proportional change in the volume.

A.4.2. Determination of the theoretical density of a *γ* phase U–Mo alloy from measured lattice parameters

Theoretical density defined in the first paragraph of Section 2.3. The theoretical density of a bcc material is calculated using Eq. (8). in which the molar mass of the material and its lattice parameter are the independent variables. Measurements of lattice parameters of *γ* phase U–Mo alloys using X ray diffraction by monolithic specimens have been reported by Wilson and Rundle in 1949 [33], McGeary in 1955 [4], Dwight in 1960 [22], Nomine et al. in 1974 [34], Burkes et al. in 2009 [35], and Leenaers in 2014 [36].

Some information about these measurements are presented below.

- Wilson and Rundle made their measurements on five U–Mo alloys specifically to determine the hypothetical lattice parameter of room-temperature *γ* phase uranium by extrapolation to zero molybdenum content. Wilson and Rundle's lattice parameters were taken directly from table 1 of Ref. [33]; they were converted from kX units using 1 kX = 1.00202 Å [101]. The accuracy of the lattice parameters was stated to be ±0.001 kX (equivalent to ±0.001 Å). A least squares linear fit of the measured data yields 3.473 Å for *γ*U, very close to the 3.474 Å Wilson and Rundle determined by graphical extrapolation. (Note that when one converts Wilson and Rundle's lattice parameter for pure *γ*–U from 3.467 ± 0.005 kX to 3.474 ± 0.005 Å using the conversion factor 1.0 kX = 1.00202 Å and uses the then-current value of the Avogadro constant (6.0228×10^{23} mol^{-1}) [102], the extrapolated *γ*–U density is calculated to be 18.85 g/cm^3, rather than their stated value of 18.89 g/cm^3. It is not known why this difference occurs, but it is interesting to note that 18.85 × 1.00202 = 18.89. The value 18.85 g/cm^3 will be assumed to be correct.);
- McGeary [4] measured the lattice parameter of at least five of the six alloys for which he measured effective densities (see Section A.4.4); these theoretical densities are plotted in fig. 8 of Ref. [4]. The data point coordinates were determined by manual digitization. The lattice parameters were calculated using Eq. (8)[17]. McGeary's fig. 8 shows the theoretical density of the 35.8 at.% specimen having a lower value than its effective density, which is impossible if it were in the *γ* phase; therefore, this data point was not considered during the current analysis;
- Dwight's measurements were made as part of an experiment to determine the U–Mo equilibrium phase diagram below 900°C, and Dwight believed them to be the most accurate performed to that time because the alloys were made from high-purity electrolytic uranium. Dwight performed X ray diffraction measurements on 10 specimens with Mo contents ranging from 12.7 to 35.4 at.% (the approximate composition of the *γ*/(*γ* + Mo) phase boundary at 900°C, the highest temperature of his experiment). The resulting lattice parameters are plotted in fig. 1 of Ref. [22]. Even though the quality of the figure was lower than desired, a linear least squares fit of manually digitized data produced coefficients that were very close to those of Dwight's published correlation, which is shown here as Eq. (40):

[17] From 1941-1965the value of the Avogadro constant was determined by a number of investigators, and it ranged between 6.0234×10^{23} and 6.0221×10^{23} mol^{-1}, except for a couple of outliers; since then, its accepted value has been ~6.0221×10^{23} [102]. Although an effort has been made to use the date-appropriate value in Eq. (8), the 0.004 g/cm^3 difference in the calculated theoretical density of uranium resulting from using one or the other of these two values was small enough to be ignored in the analyses performed for this publication.

$$a_0^{\gamma UxMo} = 3.4808 - 0.00314x_a^{Mo}, \text{ (metastable } \gamma \text{ phase , } 12.7 \le x_a^{Mo} \le 33.3) \quad (40)$$

where x_a^{Mo} is the Mo content of the U–Mo alloy in at.% and $a_0^{\gamma UxMo}$ is the lattice parameter at room temperature in Å. The upper limit on the Mo content range is taken as the stoichiometric Mo content of U_2Mo.

- Nomine et al. used γ quenched specimens machined from ingots for their X ray analysis of U–Mo containing, nominally, 8, 10, and 12 wt% Mo. They listed the Mo contents of the as received alloys to be 7.8 to 8.3 wt%, 10.1 to 11.1 wt%, and 11.7 to 12.4 wt%, respectively; however, they used the nominal Mo contents when plotting their data, which is listed in table 3 of Ref. [34]. They showed that the lattice parameters decreased linearly as the atomic Mo content increased; the linearity was not as good when plotted against the midpoint Mo content values, but the fit equations were similar. The nominal Mo contents have been used to analyse their data;
- Burkes et al. [35] measured the lattice parameters of U–Mo alloys with nominal Mo contents of 7, 8, 9, 10, 11, and 12 wt%, a range of 15.7–25.3 at.%. The specimens were cut from hot-rolled foils produced from arc-melted ingots. The foils had been annealed at 650ºC for 2 hr following final rolling. No data were provided on the actual Mo contents of the foils. Burkes et al. displayed their lattice parameter data and their uncertainties in fig. 6 of Ref. [35]; digital data were obtained by manual digitization;

Leenaers [36] measured the lattice parameters of a number of U–Mo alloys with Mo content ranging from 5.7–15.5 wt% (13.0–31.3 at.%). The specimens were prepared from arc-melted coupons; they were given a homogenization anneal at 250ºC for 72 hr before the X ray diffraction measurements. Her data, including uncertainties, are shown graphically in fig. 10 of Ref. [36], along with the data of Burkes et al. [35], just discussed, and those of Park et al. [103], discussed below. Digital data were obtained by manual digitization. The first three authors reported their lattice parameters and derived correlations as functions of Mo content in at.%, while the latter three used wt%. According to Vegard's law [104] [18], the appropriate lattice parameter to use in Eq. (8) to estimate the theoretical density of a U–Mo alloy is the average of the lattice parameters of U and Mo weighted by their molar fractions. Hence, one must correlate the measured lattice parameters with the Mo content in at.% if one wishes to extrapolate to Mo contents outside the measurement range, e.g., to estimate the theoretical density of pure γ–U. Note that if the theoretical density of a γ phase U–Mo alloy is desired, the lattice parameter of γ–U must be used when applying Vegard's law. Therefore, the lattice parameter data from the three most-recent measurements have been refit as a function of the Mo content in at.%.

The Mo contents and the measured lattice parameters reported by these authors are listed in Table 10. The coefficients of a linear least squares fit of each author's data with respect to the Mo content in at.% are listed in Table 11. Although Wilson and Rundle [33], Burkes et al. [35], and Leenaers [36] reported uncertainties with their measured lattice parameters, none provided an explanation of how the uncertainties were calculated; hence, no attempt was made to incorporate the uncertainties into the data analysis. The lattice parameters are plotted in Fig. 40, along with the linear fits for each dataset. Table 10 also lists theoretical densities of pure γ phase U (0 wt% Mo), U–8Mo, U–10Mo, and pure Mo (100 wt% Mo), calculated using lattice parameters obtained from the six lattice parameter correlations in Eq. (8).

[18] Note that Vegard's law is actually an empirical correlation, which does not work for many alloys.

TABLE 10. MEASURED LATTICE PARAMETERS OF ROOM-TEMPERATURE NATURAL OR DEPLETED U–Mo ALLOYS

Mo Content		Lattice parameter (Å)					
(wt%)	(at.%)	Wilson and Rundle [33]	McGeary [4]	Dwight [22]	Nomine et al [34]	Burkes et al. [35]	Leenaers [36]
5.53	12.68	–	–	3.439	–	–	–
5.69	13.02	–	–	–	–	–	3.443
6	13.67	–	–	–	–	–	3.445
6.18	14.04	–	3.437	–	–	–	–
6.88	15.49	–	–	3.434	–	–	–
7	15.74	–	–	–	–	3.435	–
7.11	15.95	–	–	–	–	–	3.445
7.78	17.3	3.419	–	–	–	–	–
7.82	17.38	–	–	–	–	–	3.426
8	17.74	–	–	–	3.427	3.429	3.433
8.35	18.44	–	–	3.424	–	–	–
9	19.7	–	–	–	–	3.422	–
9.77	21.17	–	–	3.416	–	–	–
9.82	21.26	–	–	–	–	–	3.416
10	21.61	–	–	–	3.415	3.415	3.417
10.05	21.71	–	–	–	–	–	3.415
10.64	22.80	3.401	–	–	–	–	–
11.00	23.47	–	–	–	–	3.411	–
11.10	23.65	–	–	–	–	–	3.407
11.40	24.20	3.392	–	–	–	–	–
11.93	25.15	–	3.397	–	–	–	–
12.00	25.28	–	–	–	3.401	3.401	–
12.07	25.41	–	–	3.399	–	–	–
13.10	27.23	–	–	3.398	–	–	–
13.55	28.00	–	–	–	–	–	3.383
13.83	28.48	–	–	3.395	–	–	–
14.37	29.40	3.383	–	–	–	–	–
14.70	29.95			3.386	–	–	–
14.95	30.36	–	3.381	–	–	–	–
15.45	31.20	3.372	–	–	–	–	–
15.53	31.33	–	–	–	–	–	3.372
15.86	31.86	–	3.379	–	–	–	–
16.42	32.77	–	–	3.379	–	–	–
18.10	35.41	–	–	3.371	–	–	–
18.37	35.83	–	3.374	–	–	–	–

–: data not available.

TABLE 11. LATTICE PARAMETER FIT COEFFICIENTS AND THEORETICAL DENSITIES

Author (Publication Date)	Reference	Lattice Parameter Fit Coefficients		Theoretical Density (based on natural U) (g/cm^3)			
		Constant	Slope	γU	U–7Mo	U–10Mo	Mo
Wilson & Rundle (1949)	[33]	3.473	-0.00320	18.87	17.87	17.46	10.17
McGeary (1955)	[4]	3.483	-0.00334	18.71	17.74	17.35	10.20
Dwight (1960)	[22]	3.481	-0.00314	18.74	17.73	17.32	10.03
Nomine et al. (1974)	[34]	3.488	-0.00344	18.63	17.69	17.31	10.25
Burkes et al. (2009)	[35]	3.490	-0.00344	18.60	17.66	17.28	10.23
Leenaers (2014)	[36]	3.504	-0.00417	18.38	17.62	17.31	10.83
All Data		3.490	-0.00355	18.65	17.69	17.32	10.34
All Data but Those of W&R and Leenaers		3.484	-0.00325	18.71	17.71	17.31	10.11

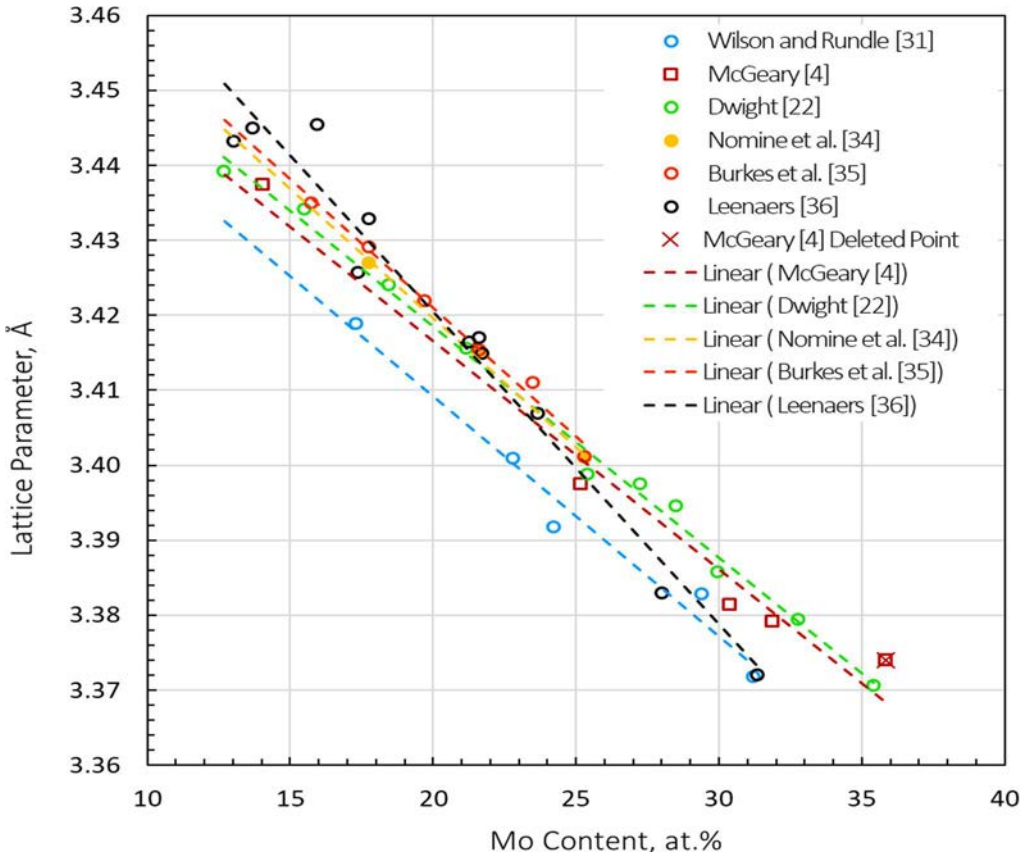

FIG. 40. Measured lattice parameters of gamma phase U–Mo bulk alloys shown with linear least squares fit lines (courtesy of James L. Snelgrove).

Review of the data in Table 10 and Fig. 40 leads to several observations:

— In Fig. 40, the lattice parameters data from McGeary, Dwight, Nomine et al., and Burkes et al. are contained within a relatively narrow band with a range of ~0.04 Å (equivalent

to a density range of ~0.8 g/cm^3) for a given Mo content in the range of about 15.7–21.6 at.% (7–10 wt%), which represents the range of U–Mo alloys under active consideration for LEU fuel. From Table 11 ones sees that the U–7Mo and U–10Mo theoretical densities calculated using the four correlations derived from these datasets are very similar;

- In Fig. 40, the lattice parameters from Wilson and Rundle lie about 0.1 Å below the middle of the band discussed above over the same range of Mo content, so the unit cell volume is predicted to be lower and the theoretical density higher;
- In Fig. 40, Leenaers's data has a significantly steeper negative slope than do the other five datasets so the intersection of its fit with the y-axis will be at a higher value than for the other fits. Consequently, its use in Eq. (8) yields γ–U and Mo densities that are unreasonably low and high, respectively. At this time the difference in slope is unexplained;
- The extrapolated theoretical density of pure Mo is quite close to its actual value, 10.22 g/cm^3, for five of the six correlations shown in Fig. 40, indicating that the extrapolated lattice parameters are close to the measured value of 3.147 Å. This good agreement indicates that γ phase U–Mo closely alloys closely follow Vegard's law;
- Having the correlations extrapolate so well to pure Mo (a lever arm of ~80 at.% Mo) gives one confidence that they also extrapolate very well to pure γ–U (a lever arm of ~20 at.% Mo).

Linear fits have also been made for two combined datasets—one containing all of the data and the other omitting the data of Wilson and Rundle and of Leenaers owing to their differences from the other data, as discussed above. The correlation developed for the latter of these datasets is quite similar to the correlations for the datasets of McGeary and of Dwight. Because each of the lattice parameter correlations listed in Table 11, either for individual or combined datasets, will lead to comparable theoretical densities over the composition range of interest for LEU U–Mo fuels and because Dwight's correlation, Eq. (40), has been used many times over the past 60 years, it is recommended that Dwight's correlation continue to be used.

Even though the uncertainties in the lattice parameter data were not considered in the analysis of the data discussed above, a simple propagation of uncertainties analysis was made based on Eq. (8). Because the Avogadro constant and the uranium and molybdenum molar masses are known to 1 part in 10^4 or better, the largest sources of uncertainty in the calculation of a U–Mo theoretical density using Eq. (8) are in the weight (or molar) fraction of Mo, which for an actual alloy is likely to be measured to an accuracy no better than ±0.25 wt% (or about ±0.47 at.%) over the range of Mo contents in U–Mo fuels. Assuming an uncertainty of ±0.47 at.% in the Mo content of U–10Mo gives an uncertainty of ±0.06 g/cm^3 in the calculated theoretical density as long as the uncertainty in the lattice constant is less than ±0.002 Å, while an uncertainty of ±0.01 Å would give a ±0.16 g/cm^3 uncertainty in the theoretical density.

Because Dwight's U–Mo lattice parameter correlation, Eq. (40), and the molar mass of U–xMo, Eq. (5), are linear functions of x_a^{UxMo}, the theoretical density equation, Eq. (8), contains a linear function of x_a^{UxMo} in the numerator and a cubic function of x_a^{UxMo} in the denominator. Hence, the theoretical density is a nonlinear function of x_a^{UxMo}. Table 11 shows the values of the lattice parameters calculated using Dwight's correlation from Eq. (40) along with the theoretical densities calculated using Eq. (8). Least squares fits of a quadratic function to densities calculated in this manner at ~0.5 wt% intervals, or the equivalent ~1.0–0.7 at.% intervals, result in the following equations, which reproduce the data extremely well. Note that the ranges of validity are equivalent for U–Mo containing natural or depleted U.

$$\rho_{theor,Dw}^{\gamma UxMo} = 18.74 - 0.0603x_a^{Mo} - 0.000246(x_a^{Mo})^2, (12.7 \le x_a^{Mo} \le 395) \quad (41)$$

$$\rho_{\text{theor,Dw}}^{\gamma \text{U}x\text{Mo}} = 18.74 - 0.151x_{\text{w}}^{\text{Mo}} + 0.000875(x_{\text{w}}^{\text{Mo}})^2, (5.5 \le x_{\text{w}}^{\text{Mo}} \le 20.8) \quad (42)$$

Parida et al. [47] in 2001 reported determining the room temperature lattice parameter of 17.7 at.% (7.98 wt%) U–Mo alloy to be 3.4489 Å [47] and stated that this value was very close to the 3.4409 Å reported for the same alloy by Ferro and Marazza [105]. However, the alloy listed by Ferro and Marazza actually contained 12.7 at.% Mo (5.54 wt% Mo). It appears that Parida et al. swapped two digits — 87.3 at.% U (12.7 at.% Mo) was misread (or wrongly transcribed) as 82.3 at.% U (17.7 at.% Mo). Ferro and Marazza cite Dwight [22] as the source of the value 3.4409 Å, which is exactly the value obtained using Dwight's correlation, Eq.(40), with the composition listed by Ferro and Marazza. The value provided by Eq. (40) for the alloy of Parida et al. is 3.4252 Å, significantly farther from their result. (It is interesting to note that the page number in Parida, et al.'s reference to Brewer, et al., is 336 rather than the correct page number 363, also transposed.) Solving Eq. (40) using Parida et al.'s lattice parameter gives a Mo content of 10.2 at.% (4.4 wt%), which is much too small to allow the retention of any γ–U after quenching. Therefore, this datum is considered to be an outlier and was not used in this present evaluation. This error may have led Parida et al. to choose a U–Mo alloy for their heat content experiment that contained far less Mo than was required for retained γ phase metastability, rather than one with Mo content just below that lower limit (see footnote 6 in Section 2.2.3 of the main body of this publication).

All of the discussion of lattice parameters so far has concerned U–Mo alloys produced as bulk buttons or ingots by furnace cooling from the molten state. Because bulk U–Mo cannot be reduced to powder for use in dispersion-type fuels by normal comminution techniques, U–Mo powder is being produced by atomization, resulting in rapid solidification of the molten alloy. In 2010, Park et al. [103] published results of lattice parameter measurements by neutron diffraction on U–Mo powders produced by centrifugal atomization. They observed a microsegregation of Mo at cell boundaries, caused by rapid solidification of Mo from the melt. In this situation, the cells were ~5-micrometre-sized zones of gamma phase U–Mo surrounded by thin boundaries of U–Mo richer in U as a consequence of rapid solidification of molten U–Mo during atomization. Their data are shown in Table 12.

TABLE 12 MEASURED AND FIT LATTICE PARAMETERS FOR CENTRIFUGALLY ATOMIZED U–Mo ALLOYS (REF. [103])

Average Mo Content (Before Solidification)		a_0 (Interior)		a_0 (Boundary)	
		Measured	Linear Fit	Measured	Linear Fit
wt%	at.%	Å	Å	Å	Å
6.0	13.7	3.4546	3.4557	3.4667	3.4646
7.0	15.7	3.4499	3.4432	3.4554	3.4532
8.0	17.7	3.4244	3.4310	3.4365	3.4421
9.0	19.7	3.4164	3.4191	3.4272	3.4313
10.0	21.6	3.4112	3.4075	3.4261	3.4207

Least squares linear fits of the lattice parameters as a function of the average Mo content in atom percent, to remain consistent with the form of Vegard's law, were performed. Because the constant terms of the two equations differed by only 0.0015 Å, the fit was redone using the average of the constant terms and allowing only the two slopes to be fit, yielding the following equations:

$$a_{0,\text{interior}}^{\text{U}x\text{Mo (atomized)}} = 3.540 - 0.00614x_{\text{a}}^{\text{Mo}} \text{ for the } \gamma_{\text{interior}} \text{ phase} \quad (43)$$

$$a_{0,\text{boundary}}^{\text{U}x\text{Mo (atomized)}} = 3.540 - 0.00552x_{\text{a}}^{\text{Mo}} \text{ for the } \gamma_{\text{boundary}} \text{ phase} \quad (44)$$

where x_a^{Mo} is the Mo content of the U–Mo alloy in at.% and $a_0^{\gamma UxMo}$ is the lattice parameter at room temperature in Å.

In their analysis, Parks et al. fit the lattice parameters as a function of the Mo content of the melt in wt.%. Then, assuming that the γ phase U–Mo in the cell interiors and boundary layers have the same characteristics as the bulk γ phase U–Mo discussed above, Parks et al. used Dwight's correlation, Eq.(9) convert their measured lattice parameters for the interior and boundary regions of their particles to Mo content in at.%. Their derived compositions, however, are incompatible with the average compositions of their alloys. This, is evident for the U–6Mo and U–7Mo specimens since the derived Mo contents of both the interior and boundary regions are much smaller than the average composition of the starting material: 8.3 and 4.5 at.% compared to 13.7 at.% for U–6Mo and 9.8 and 8.1 at.% compared to 15.7 at.% for U–7Mo. The volume-averaged Mo content for each of their particles is lower than that of the melt. Therefore, further study is needed to characterize the lattice parameters of atomized U–Mo powders.

A.4.3. Estimating the theoretical density of a γ phase U–Mo alloy using a rule of mixtures formula

The density of an alloy has often been estimated using a rule of mixtures formula. Two formulas for the U–Mo density can be developed starting from mathematical identities involving the two components of density: mass and volume. Starting from the mass identity $m^{\text{U–Mo}} \equiv m^{\text{U}} + m^{\text{Mo}}$, where m represents mass, and dividing each side of the equation by $v^{\text{U–Mo}} \equiv v^{\text{U}} + v^{\text{Mo}}$, where v represents volume, one has:

$$\frac{m^{\text{U–Mo}}}{v^{\text{U–Mo}}} = \rho^{\text{U–Mo}} = \frac{m^{\text{U}}}{v^{\text{U–Mo}}} + \frac{m^{\text{Mo}}}{v^{\text{U–Mo}}} = \left(\frac{m^{\text{U}}}{v^{\text{U}}}\right)\left(\frac{v^{\text{U}}}{v^{\text{U–Mo}}}\right) + \left(\frac{m^{\text{Mo}}}{v^{\text{Mo}}}\right)\left(\frac{v^{\text{Mo}}}{v^{\text{U–Mo}}}\right)$$

$$= \rho_{\text{theor}}^{\gamma\text{U}}\left(\frac{x_v^{\text{U}}}{100}\right) + \rho_{\text{theor}}^{\text{Mo}}\left(\frac{x_v^{\text{Mo}}}{100}\right) \quad (45)$$

where ρ is density and x_v^{U} and x_v^{Mo} are the volume fractions of U and Mo in the alloy in vol%. Applying the identity $x_v^{U} + x_v^{Mo} = 100$, assuming that the theoretical density of γ phase depleted U is 18.74 g/cm^3 and rearranging the terms of the equation, one finds

$$\rho_{\text{theor,RoM}}^{\gamma\text{U}x\text{Mo}} = \rho_{\text{theor}}^{\gamma\text{U}} - \left(\rho_{\text{theor}}^{\gamma\text{U}} - \rho_{\text{theor}}^{\text{Mo}}\right)\left(\frac{x_v^{\text{Mo}}}{100}\right) = 18.74 - 0.0852x_v^{\text{Mo}} \quad (46)$$

Starting instead from the volume identity, substituting m/ρ for v and assuming that the theoretical density of γ phase depleted U is 18.74 g/cm^3, one can derive

$$\frac{1}{\rho_{\text{theor,RoM}}^{\gamma\text{U}x\text{Mo}}} = \frac{\left(1 - 0.01x_{\text{w}}^{\text{Mo}}\right)}{\rho_{\text{theor}}^{\gamma\text{U}}} + \frac{0.01x_{\text{w}}^{\text{Mo}}}{\rho_{\text{theor}}^{\text{Mo}}} = 0.05336 + 0.000445x_{\text{w}}^{\text{Mo}} \quad (47)$$

Values of the densities of uranium $\rho_{\text{theor}}^{\gamma\text{U}}$ and molybdenum $\rho_{\text{theor}}^{\text{Mo}}$ vary among literature reference sources; for instance, the molybdenum density is given as 10.2, 10.22, or 10.28 g/cm^3 by various sources. The room-temperature theoretical densities (i.e. the density based on the crystal structure and lattice parameters) of natural or depleted γ phase uranium (if it could be produced) and natural molybdenum are 18.74 and 10.22 g/cm^3, respectively. The densities of uranium of various enrichments vary proportionately to their molar masses. And the actual density of a piece of metal depends upon its processing history.

Equation (46) is not particularly useful because one rarely knows the volume fraction in advance, but Eq. (47) can be applied directly to any U–Mo alloy, using the notation adopted in this publication. For all practical purposes, the rule of mixtures Eq. (47) and Eqs (41) and (42) based on Dwight's lattice parameter correlation for γ phase U–Mo alloys provide equivalent densities (within 0.02 g/cm^3 of each other) throughout the range of interest for U–Mo fuels.[19]

A.4.4. Directly measured room-temperature densities using the Archimedes method

Relatively few direct measurements of U–Mo alloy densities have been reported. The first measurements using the Archimedes method to be openly reported were provided by McGeary [4], from work performed at the Westinghouse Atomic Power Division's Bettis Laboratory in the early to mid-1950s, for six γ quenched alloys with Mo contents in the range of 6–25 wt% (14–45 at.%). According to the phase diagram of Fig. 41, the 25 wt% alloy would contain a mixture of γ–U and some pure bcc Mo. Lattice parameters for the five samples quenched from the γ–U field were also measured by X ray diffraction by McGeary, as discussed above in Section A.4.2. These data appear only in graphical form in fig. 8 of McGeary's report, which is reproduced here as Fig. 41, and no reference to a previous report is given. Each measured density data point represents the average of measurements made on four separate samples taken from the arc-melted button of that alloy.

Data derived from the figure are listed in Table 13. The linear fit line shown in Fig. 41 for the measured effective densities is represented by Eq. (48), which is consistent with a least squares fit of the measured densities plus the γ–U density, 18.79 g/cm^3, plotted in the figure.

$$\rho^{\gamma \mathrm{U}x\mathrm{Mo}}_{\mathrm{effective,McG}} = 18.74 \; - \; 0.0719 x_{\mathrm{a}}^{\mathrm{Mo}} \tag{48}$$

The γ–U density of 18.79 g/cm^3 was reported by McGeary to be from Wilson and Rundle [33]; however, Wilson and Rundle state that the γ–U theoretical density is 18.89 ± 0.05 g/cm^3, rather than the plotted value of 18.79 g/cm^3. It is quite possible that the point is misplotted in the figure, since a fit to the five data points plus a γ–U density of 18.89 g/cm^3 matches the equation of the plotted theoretical density fit line.

The sixth alloy (45.1 at.%, 24.9 wt%) definitely would not have been in the metastable γ phase at room temperature because that composition is on the Mo-rich side of the $\gamma/(\gamma + \mathrm{U})$ phase boundary; this would explain the absence of a theoretical density for this alloy in Fig. 41 That the fifth alloy (35.8 at.%, 18.4 wt%) has a Mo content higher than that of the γ' phase and that its theoretical density is lower than its effective density might indicate that it is not pure γ phase material. The fourth alloy is also quite close to γ' phase boundary, and its theoretical and effective densities are nearly the same. Consequently, a linear fit of the three lower-Mo-content effective-density data points alone should be most representative of metastable γ phase U–Mo; the result is shown as Eq. (49).

$$\rho^{\gamma \mathrm{U}x\mathrm{Mo}}_{\mathrm{actual,McG}} = 18.59 \; - \; 0.0674 x_{\mathrm{a}}^{\mathrm{Mo}} \tag{49}$$

[19]Note that Burkes et al. used a rule of mixtures equation having the form of Eq. (46) as their eq. (3) of Ref. [13] but mistakenly used molar fractions rather than volume fractions.

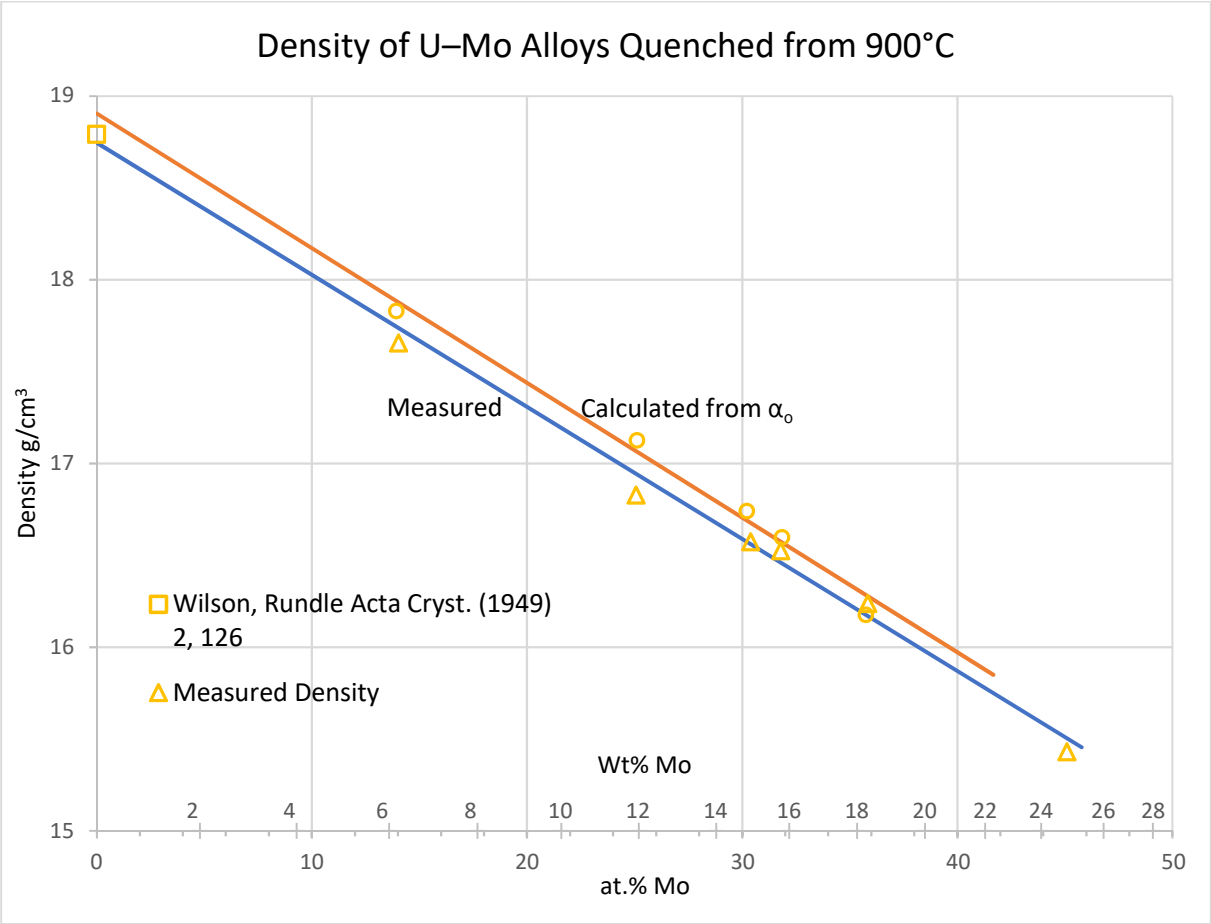

FIG. 41. Density of U–Mo alloys, adapted from McGeary's fig. 8 [4].

TABLE 13. DATA DERIVED FROM McGEARY'S FIG. 8

Mo Content		Density (g/cm³)[a]		Lattice parameter[b] (Å)
(at.%)[a]	(wt%)	Effective	Theoretical	
0.0	0.0	–	18.79[c]	3.472
14.0	6.18	17.66	17.83	3.438
25.2	11.9	16.84	17.13	3.398
30.4	14.9	16.58	16.74	3.382
31.9	15.9	16.54	16.59	3.380
35.8	18.4	16.24	16.18	3.375
45.1	24.9	15.44	–	–

[a]Digitized values from fig. 8, p. 98 of [4].

[b]Calculated from the theoretical density based upon Mo atomic weight, 95.95 g/mol (1938–1961 value) and depleted U atomic weight, 238.04 g/mol. Resulting values show good agreement with lattice parameters from McGeary [4] listed in Table 10.

[c]Wilson and Rundle mistakenly stated that this density is 18.89 g/cm³ and that it corresponds to a lattice parameter of 3.474 Å.

–: data not available.

Klein [7] in his table 3-38, Beghi [2] in his table 2, and Rest et al. [11] in his fig. 2.3 cite McGeary [4] as their primary source of density data as a function of Mo content; these data are listed in Table 14. However, the quoted densities undoubtedly were derived from the linear fit

line shown in McGeary's fig. 8. Fackelmann et al. [9] in his table A-7 also cited McGeary as the source of their data for 0, 2.5, 5, 7.5, 10 wt% Mo, but his values, though similar to those of the others citing McGeary, did not come from the same fit; it appears that Fackelmann et al. may have used a linear fit only to McGeary's five lowest-Mo measured points. These authors should have listed the zero-Mo (γ–U) density from the fit (18.74 g/cm^3), since that would represent the best estimate for a pure γ–U sample manufactured in the same manner as the U–Mo samples if γ–U could exist at room temperature.

TABLE 14. DENSITIES LISTED BY OTHER AUTHORS WHO CITED McGEARY AS THEIR SOURCE

Mo Content		Density (g/cm^3)	
at.%	wt%	Klein, Beghi, Rest	Fackelmann [9]
0.0	0.0	18.7–19.0[a] 19.05[b]	18.8
5.6	2.5	18.3	18.1
11.5	5.0	18.0	17.7
16.7	7.5	17.6	17.4
21.6	10.0	17.2	17.2
30.4	15.0	16.6	–
38.3	20.0	16.0	–
45.3	25.0	15.5	–

[a] Klein [7] and Beghi [2].

[b] Rest et al. [11].

–: data not available.

A.4.5. Converting γ phase (depleted- or natural-U)–Mo densities to (enriched-U)–Mo densities

The U–Mo densities and equations for calculating them discussed in Sections A.4.2-A.4.4 apply to alloys containing depleted or natural uranium. Such alloys were generally used for measurement of unirradiated U–Mo properties. Of course, enriched U is used in alloys for fabricating irradiation test samples and reactor fuel elements. A simple procedure can be used to calculate densities for alloys containing enriched U.

Equation (8) shows that the theoretical density of γ phase U–Mo, a bcc material, is proportional to the molar (atomic) mass of the alloy's unit cell, which, as shown in Eq. (5), is a linear combination of the U and Mo molar masses, each weighted by its molar fraction in the alloy. Equation 5 can also be used to find the molar mass of enriched uranium, by replacing M^{UxMo} by M^U, M^U by M^{U8}, M^{Mo} by M^{U5}, and x_a^{Mo} by e, the uranium enrichment in at.%, yielding

$$M^U = M^{U8} - 0.01e\left(M^{U8} - M^{U5}\right) = 238.051 - 0.03007e \quad (50)$$

Substituting the results of Eq.(50) in Eq. (5) yields Eq. (51) for the molar mass of U–Mo as a function of the uranium enrichment (e) and the molar content of molybdenum in the alloy:

$$M_e^{UxMo} = 238.05 - 1.421x_a^{Mo} - 0.0301(1 - 0.01x_a^{Mo})e \quad (51)$$

Rounding the constants from Eq. (50) in Eq. (51) changes the calculated U–Mo molar mass by less than 0.001 g/mol for LEU fuel.

Looking again at Eq (8), since the lattice parameter is independent of the uranium enrichment, only the molar mass of U–Mo, given by Eq. (5), is a function of the enrichment. Therefore, the ratio of the theoretical densities of two alloys that differ only in their uranium enrichment is the ratio of the molar masses of these alloys. It is reasonable to assume that the ratio of the actual and theoretical densities of any given alloy do not depend on the uranium enrichment, so the preceding statement also holds for actual densities. Hence, if one knows the density of a U–Mo alloy of a given Mo molar fraction (x_a^{Mo}) and enrichment (e_1), the density of another alloy differing only in its enrichment (e_2) is given by Eq. (52) as

$$\rho_{e_2}^{UxMo} = \frac{\left[238.05+1.421x_a^{\mathrm{Mo}}-0.0301\left(1-0.01x_a^{\mathrm{Mo}}\right)e_2\right]}{\left[238.05+1.421x_a^{\mathrm{Mo}}-0.0301\left(1-0.01x_a^{\mathrm{Mo}}\right)e_1\right]}\rho_{e_1}^{\mathrm{U}x\mathrm{Mo}} \tag{52}$$

A.5. THERMAL EXPANSION AND DENSITY CHANGE OF U–Mo ALLOYS DURING HEATING AND COOLING

Thermal expansion (or thermal dilation) and density change during heating and cooling of U–Mo alloys are discussed together in this section because the change in density of an alloy as its temperature changes is a direct result of its change in volume owing to thermal expansion. Thermal expansion is a three dimensional phenomenon (volumetric thermal expansion), but if an alloy expands isotropically (as is usually assumed), the volumetric expansion can be calculated from a measurement of its expansion in only one direction (linear thermal expansion). Linear thermal expansion test specimens are typically rods or bars whose cross-sectional dimensions are considerably smaller than their length to facilitate rapid and uniform heating during testing; hence, expansion in the length direction (longitudinal thermal expansion) of the specimen is typically measured, usually by dilatometry.

Since the earliest measurements on U–Mo alloys in the 1940s, the data of length change (ΔL) and temperature (T) have been recorded simultaneously, first using X–Y recorders and more recently using digital recorders. The shapes of the ΔL vs. T curves vary significantly, depending on the metallurgical state of the material at the beginning of the measurement and on changes of the metallurgical state during the course of the measurement. In the 7–12 wt% Mo content range of interest for U–Mo fuels, the phase diagram (Fig. 1) shows that, upon heating, a U–Mo alloy at equilibrium undergoes a change from a mixture of the α (U) and γ' (U_2Mo) phases to the γ phase at 565°C, with an attendant volume (length) increase, or decrease (if the alloy is being cooled). Under the non-equilibrium conditions of a thermal expansion measurement, the phase-transition temperatures appear to be somewhat higher owing to the time required for heat to reach the inner part of the test specimen and for the solid state transition reaction to occur. The $\alpha + \gamma'$ to γ transition occurs much more rapidly than the γ to $\alpha + \gamma'$ transition; therefore, for temperature-change rates ≥100°C/h (0.028°C/s) and maximum temperatures above 565°C, no discontinuities are seen in the heating or cooling curves after the first heating run for a relatively homogeneous U–Mo alloy because very little of the γ phase material has time to transform back to the $\alpha + \gamma'$ phases during the cooling part of the measurement cycle [4].

A.5.1. Definitions and equations

The instantaneous coefficient of volumetric thermal expansion, α_v, is defined as

$$\alpha_v(T) = \frac{1}{V(T_0)}\frac{dV(T)}{dT} \tag{53}$$

where V is the volume, T is the temperature and T_0 is an arbitrarily chosen baseline temperature (usually room temperature). Therefore, the instantaneous coefficient of volumetric thermal expansion is the slope of the function $V(T)/V(T_0)$ at temperature T. The term 'instantaneous' indicates that $\alpha(T)$ is applicable only at the instant in time when a material undergoing a change in temperature is at temperature T. One assumes that the pressure on the sample remains constant during the expansion (or contraction).

The average coefficient of volumetric thermal expansion is defined as

$$\bar{\alpha}_v(T_0, T) = \frac{\int_{T_0}^{T}\alpha(T)\,du}{\int_{T_0}^{T}du} = \frac{\frac{1}{V_0}\int_{T_0}^{T}\left(\frac{\partial V}{\partial T}\right)du}{\int_{T_0}^{T}du} = \frac{\frac{1}{V_0}V\big|_{T_0}^{T}}{u\big|_{T_0}^{T}} = \frac{\frac{1}{V_0}(V_T - V_0)}{T - T_0} = \left(\frac{\Delta V_T/V_0}{T - T_0}\right) \tag{54}$$

where $V(T) \equiv V_T$ and $V(T_0) \equiv V_0$ are the volumes of the specimen at temperatures T and T_0 and where $\Delta V_T = V(T) - V(T_0)$. The instantaneous and average coefficients of linear thermal expansion are analogously defined as

$$\alpha_l(T) = \frac{1}{L_0}\left(\frac{dL(T)}{dT}\right) \tag{55}$$

$$\bar{\alpha}_l(T_0, T) = \frac{1}{L_0}\left(\frac{\Delta L_T}{T - T_0}\right) \tag{56}$$

where $L(T) \equiv L_T$ and $L(T) \equiv L_0$ are the lengths of the specimen at temperatures T and T_0, respectively and $\Delta L_T = L(T) - L(T_0)$. For clarity, sometimes the subscript of L_0 will be replaced with the specific reference temperature in °C, e.g. L_{27}. Because $\Delta V_T/V_0$ and $\Delta L_T/L_0$ are dimensionless quantities, the unit associated with the instantaneous and average coefficients of thermal expansion is inverse temperature ($°C^{-1}$ in this document). [20] Also, because $\Delta L_T/L_0$ for U–Mo alloys ranges from ~1×10^{-5} to ~1.6×10^{-2}, for temperature changes of 1–900°C above room temperature, in this document $\Delta L_T/L_0$ often is specified in % for convenience. If one assumes that the linear thermal expansion of a material is represented by a quadratic function of T, one arrives at Eqs (57), (58), and (59):

$$\Delta L(T)/L_0 = a_2T^2 + a_1T + a_0 \tag{57}$$

$$\alpha(T) = 2a_2T + a_1 \tag{58}$$

$$\bar{\alpha}(T_0, T) = a_2(T + T_0) + a_1 \tag{59}$$

where a_2, a_1, and a_0 are coefficients determined during the fitting process. Hereinafter, α written with no subscript denotes linear thermal expansion, per standard practice. A subscript will be added to indicate, e.g. volumetric thermal expansion. Because a_0 is not contained in the equations for either of the coefficients of thermal expansion, one can normalize the ΔL_T's (e.g.

[20] In many publications, the unit is written as 'length/length per temperature unit'.

to zero at T_0) without affecting either of the coefficients of thermal expansion. Using Eqs (58) and (59), one can show that

$$\alpha(T_0) = 2a_2(T_0) + a_1 = \bar{\alpha}(T_0, T_0) \tag{60}$$

and

$$\alpha(T_{\text{mean}}) = \frac{1}{2}[\alpha(T_0) + \alpha(T)] = \bar{\alpha}(T_0, T) \tag{61}$$

where T_{mean} is the mean (average) temperature over the temperature interval (T_0, T).

The importance of clearly distinguishing between the instantaneous and the average coefficient of thermal expansion cannot be overemphasized. A definite temperature range, most often with room temperature as the lower end of the range, is always associated with the average coefficient of thermal expansion; unless the temperature range over which a coefficient is evaluated is clearly stated, most likely it is an instantaneous coefficient.

Quadratic functions have been used extensively in this work to fit $\Delta L/L_0$ data. When $T - T_0$ is less than 600°C and no phase changes or other changes have occurred in the U–Mo during heating, $\Delta L/L_0$ has been fit sufficiently well by a single quadratic function of T. Many times, however, it has been useful to use a piecewise quadratic function to provide a sufficiently accurate fit of $\Delta L/L_0$:

$$\Delta L(T_n)/L_0 = \sum_{i=1}^{n}[\Delta L_i(T_{i\text{-}1}, T_i)/L_0] \tag{62}$$

where n is the number of intervals into which the thermal expansion dataset is divided, T_0 is the reference temperature, T_i, $i = 1, 2, \ldots n$, is the upper temperature limit of each interval, and:

$$\Delta L_i(T_{i\text{-}1}, T_i)/L_0 = L(T_i)/L_0 - L(T_{i\text{-}1})/L_0 \tag{63}$$

$$\Delta L(T_i)/L_0 = a_{2,i}T_i^2 + a_{1,i}T_i + a_{0,i} \tag{64}$$

The following expression applies for all temperatures T such that $T_0 \le T \le T_n$:

$$\Delta L(T)/L_0 = \sum_{i=1}^{m\text{-}1}[\Delta L_i(T_{i\text{-}1},T_i)/L_0] + \Delta L_m(T_{m\text{-}1}, T)/L_0 \tag{65}$$

where m is the index number of the interval containing temperature T. The two coefficients of linear thermal expansion are given by

$$\alpha(T) = 2a_{2,m}T + a_{1,m}, \ (T_{m-1} \le T \le T_m) \tag{66}$$

$$\bar{\alpha}(T_0, T) = \frac{\Delta L(T)/L_0 - \Delta L(T_0)/L_0}{T - T_0} = \frac{(a_{2,m}T^2 + a_{1,m}T + a_{0,m}) - (a_{2,1}T_0^2 + a_{1,1}T_0 + a_{0,1})}{T - T_0}, \ (T_{m\text{-}1} \le T \le T_m) \tag{67}$$

The fitting process was carried out in the following manner:

- All fitting was performed on dilation data using the least squares method; when data were reported as average coefficients of linear thermal expansion, they were converted to dilations using Eq.(54);
- If a single quadratic function did not adequately fit the data, the dilation curve was divided into temperature intervals according to features seen in the curve and guided by phase-change temperatures. For example, the $\alpha + \gamma'$ to γ phase-transition occurs at 565°C according to the phase diagram, however, because of the time required for heat to be transferred through the test specimen and for the solid-state transition to occur, the

specimen usually has reached a recorded temperature of ~600°C before the volume change associated with the transition has become evident. At typical heating rates, the specimen will have reached ~650°C before the transition has been completed. For specimens that contain a substantial quantity of α phase material, a rapid increase in volume occurs over this narrow temperature interval and a linear function has been used over the interval, i.e. the coefficient a_2 of the quadratic function is zero;

- A least squares fit of each dilation function was performed individually over each temperature interval. In cases where the slope of the dilation curve did not change sharply in the vicinity of the boundary, fits were overlapped at the boundary for one or more next higher or lower temperature data point(s) to decrease the amount of discontinuity at the boundary. The highest temperature interval was fit first. If the available data were for the heating part of the temperature cycle only or for an average of the heating and cooling parts of the cycle, the fit for the highest temperature interval was unconstrained. When separate data were also available for the heating and cooling parts, the fit for the highest temperature interval of the cooling curve was normalized by adjusting coefficient $a_{0,n}$ so that the dilation at the maximum temperature equalled that of the heating curve. Then the data in the lower temperature intervals were successively fitted and normalized so that dilations calculated for adjoining intervals were the same at the interval-boundary temperature. Dilation differences at the interval-boundary temperatures, $T_{n-1}, \ldots T_1$, were $< 5 \times 10^{-5}$%, which was well within the accuracy of the data and made the overall function effectively continuous at the interval boundaries;
- Equations (66) and (67) were used to calculate the two coefficients of linear thermal expansion listed in tables in Section A.5.2. Because the instantaneous coefficient of linear thermal expansion, the slope of the dilation curve, is usually discontinuous at an interval boundary, the average of the slopes at temperatures infinitesimally above and below the interval-boundary temperature was calculated at each boundary.

The density of a cube of isotropically expanding material at temperature T, ρ_T, relative to its density at temperature T_0, ρ_0, is

$$\frac{\rho_T}{\rho_0} = \frac{V_0}{V_T} = \frac{L_0^3}{L_T^3} = \frac{L_0^3}{(L_0 + \Delta L_T)^3} = \left(1 + \frac{\Delta L_T}{L_0}\right)^{-3} = \left(1 + 3\frac{\Delta L_T}{L_0} + 3\left(\frac{\Delta L_T}{L_0}\right)^2 + \left(\frac{\Delta L_T}{L_0}\right)^3\right)^{-1} \tag{68}$$

and

$$\frac{\rho_T}{\rho_0} \approx \left(1 + 3\frac{\Delta L_T}{L_0}\right)^{-1} \text{ when } \left(\frac{\Delta L_T}{L_0} \ll 1\right) \tag{69}$$

If one has an anisotropic material for which expansion in the transverse direction is different than that in the longitudinal direction, it is easy to show that

$$\frac{\rho_T}{\rho_0} \approx \left(1 + \frac{\Delta L_T}{L_0} + 2\frac{\Delta R_T}{R_0}\right)^{-1} \text{ when } \left(\frac{\Delta L_T}{L_0} \ll 1,\ \frac{\Delta R_T}{R_0} \ll 1\right) \tag{70}$$

for a specimen having a circular cross section with radius R, and

$$\frac{\rho_T}{\rho_0} \approx \left(1 + \frac{\Delta L_T}{L_0} + \frac{\Delta W_T}{W_0} + \frac{\Delta H_T}{H_0}\right)^{-1} \text{ when } \left(\frac{\Delta L_T}{L_0} \ll 1,\ \frac{\Delta W_T}{W_0} \ll 1,\ \frac{\Delta H_T}{H_0} \ll 1\right) \tag{71}$$

for a specimen having a rectangular cross section with width W and height H. For U–Mo alloys, the maximum error from using any of these density ratio approximations is <0.1%, within the

experimental uncertainty of ρ_0. If a 'volume-equivalent' $\Delta L_{T\text{-ve}}/L_0$ is desired that would accurately reproduce the volume change of an anisotropic material in one dimensional calculations, one can see from Eqs (58), (62), and (63) that

$$\frac{\Delta L_{T\text{-ve}}}{L_0} = \left(\frac{\Delta L_T}{L_0} + 2\frac{\Delta R_T}{R_0}\right)/3 \text{ when } \left(\frac{\Delta L_T}{L_0} \ll 1,\ \frac{\Delta R_T}{R_0} \ll 1\right) \tag{72}$$

or

$$\frac{\Delta L_{T\text{-ve}}}{L_0} = \left(\frac{\Delta L_T}{L_0} + \frac{\Delta W_T}{W_0} + \frac{\Delta H_T}{H_0}\right)/3 \text{ when } \left(\frac{\Delta L_T}{L_0} \ll 1,\ \frac{\Delta W_T}{W_0} \ll 1,\ \frac{\Delta H_T}{H_0} \ll 1\right) \tag{73}$$

Hence, the volume-equivalent $\Delta L_{T\text{-ve}}/L_0$ is the weighted average of the individual expansions for the stated conditions. One would need to carefully consider if use of a volume-equivalent $\Delta L_{T\text{-ve}}/L_0$ were appropriate for stress–strain calculations, however.

A.5.2. Sources of thermal expansion data in the literature

Six primary sources of U–Mo thermal expansion data have been identified; three of these provide thermal expansion data well into the γ phase region. The U–Mo used by three of these sources contained nominally 10 wt% Mo, while that of the other sources included a series of U–*x*Mo alloys. These sources are discussed individually below in the order that they were published.

None of the sources of dilation data or coefficients of thermal expansion used in this work have discussed the accuracy of the data. Coefficients of thermal expansion tabulated by five of the sources contained three significant digits (~1 part in 100–170) and by one source contained four significant digits (~1 part in 1000–1700), regardless of the measurement temperature. Because both the temperatures and the dilations were determined from strip charts, it is unlikely that any more than three significant digits is justified for temperatures above 500°C and no more than two below 500°C. In the analysis and discussion of the available data, the emphasis will be on the measured dilations rather than on the coefficients of thermal expansion because the dilations were the quantities measured.

A.5.2.1 McGeary (1955) [4]

At the Westinghouse Electric Company Atomic Power Division's Bettis Laboratory, McGeary measured the linear thermal expansion of α soaked U–Mo alloys with nominal molybdenum contents of 3, 6, 9, 10.5, 12, 15, and 18 wt%; he states that the Mo content is within ±0.25 wt% of the stated values. The test specimens were most likely made by induction melting and casting; they were heated at 525–550°C for 15 or 16 days before testing. In fig. 6 of Ref. [4], McGeary reported that thermal dilations were measured up to 900°C, and he showed a composite of the dilatometer traces for these U–Mo alloys from ~20 to ~750°C. Because the lower temperature part of the curve was missing for the 9 and 12 wt% alloys, no attempt was made to digitize these curves. From the text of Ref [4], it appeared that McGeary's main interest in these data in his fig. 6 was to determine the magnitude of the dilation owing to the $\alpha + \gamma'$ to γ phase change upon heating past the eutectoid temperature.

McGeary's fig. 7 shows the average coefficients of thermal expansion ($\bar{\alpha}$) over the temperature range 100–400°C plotted vs. the Mo content of γ quenched alloys containing nominally 3, 6, 9, 10.5, 12, 15 and 18 wt% Mo. The values of $\bar{\alpha}$ and Mo content of each data point were determined by manual digitization, and an adapted version of the original figure is shown in Fig. 42, with the value of $\bar{\alpha}$ listed beside each data point. Because U–Mo alloys containing less than ~5.4 wt% Mo cannot be retained in the metastable γ state at temperatures

less than the eutectoid temperature, a fit has been made excluding U–3Mo, resulting in the following equation:

$$\bar{\alpha}(100, 400)_{\text{fit, McG}} = 15.8 \; - \; 0.235x_{\text{w}}^{\text{Mo}}, (6 \leq x_{\text{w}}^{\text{Mo}} \leq 18) \tag{74}$$

where $\bar{\alpha}$ is in units of 10^{-6}°C^{-1} and x_{w}^{Mo} is in wt%. This fit line is shown as a solid line in Fig. 42 and is representative of McGeary's data for γ phase U–Mo alloy. Multiplying both sides of Eq. (75) by $\Delta T = 300$ºC leads to the equation

$$\Delta L/L_0\,(100, 400)_{\text{fit, McG}} = 0.474 \; - 0.0071x_{\text{w}}^{\text{Mo}}, (6 \leq x_{\text{w}}^{\text{Mo}} \leq 18) \tag{75}$$

where $\Delta L/L_0$ is in % and x_{w}^{Mo} is in wt%. Owing to the large amount of scatter in the data and to their limited temperature range, McGeary's data are of limited use.

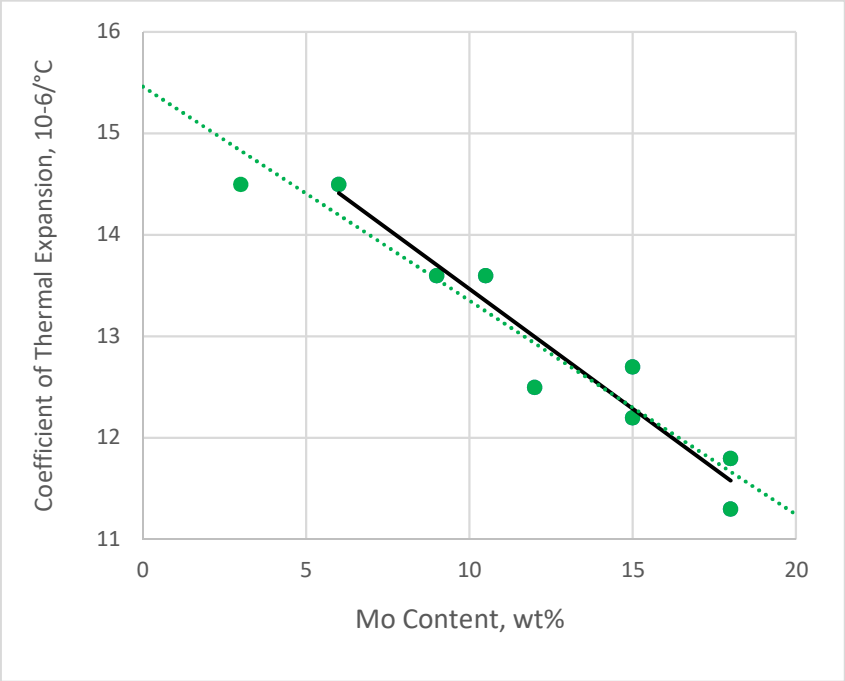

FIG. 42. Average coefficient of linear thermal expansion of U–xMo alloys over the temperature range 100–400°C vs. the Mo content (x) of the alloy; the dotted fit line is McGeary's, shown in fig. 7; the solid fit line excludes the data point at 3 wt% Mo of Eq. (75) (adapted from McGeary's fig. 7 [4]).

A.5.2.2 Saller et al. (1956) [42]

At BMI, Saller et al. measured the linear thermal expansion up to either 950 or 1000°C of five U–Mo alloys ranging in nominal Mo content from 3.5 to 12.0 wt%. The maximum heating and cooling rates used were ~5°C/min (0.083°C/s). The specimens were produced by casting an ingot, forging, rolling, and swaging to a 9.8-mm-diameter cylinder, and vacuum annealing at 593°C to eliminate cracking. One specimen of each alloy was annealed for 1 h at 800°C and then γ quenched prior to measurement, and a second specimen was annealed for 1 h at 800°C, furnace cooled, and then annealed at 500°C for 100–340 h prior to measurement; these latter specimens will be referred to as α soaked.

Saller et al. presented average coefficients of thermal expansion in their table 5 and in plotted dilation curves (i.e. not photocopies of original chart recorder traces) in Figs A-1 through A-5 of Ref. [42]. Saller et al.'s fig. A-4 (specimens of nominal composition 9 wt% Mo and the measured 9.36 wt%, which is the alloy of most interest for comparison in this report) is reproduced below as Fig. 43.

Dilation data for the U–Mo alloys of interest were calculated from the $\bar{\alpha}$'s listed in Saller et al.'s table 5 [42] using Eq. (54), and by manual digitization from the dilations plotted in his figure A-4 shown in Fig. 43. Table 15 compares the dilations of U–9.36Mo based on tabulated $\bar{\alpha}$'s with those obtained from the figure; the agreement is quite good, though the differences for the γ quenched specimen are noticeably larger than for the α soaked specimen. Therefore, it is apparent that the dilation curves in the figure are reasonable representations of the original chart recorder traces.

Figure. 43 shows that the α soaked U–9.36Mo specimen containing a significant amount of $\alpha + \gamma'$ material (heat treatment L: 1 h at 800°C followed by 200 h at 500°C) underwent a rapid increase in its rate of expansion between measured specimen temperatures of 595 and 650°C, primarily because of the $\alpha + \gamma'$ to γ transition[21], while the γ quenched material (heat treatment G) did not because it was already in the γ phase. Saller et al. used heating–cooling rates up to 300°C/h, which were rapid enough that no detectable transformation back to α (U) + γ' material occurred during cooling. This confirms that the $\alpha + \gamma'$ to γ transformation is much more rapid than the reverse transformation. A small, unexplained increase in length occurred during heating of the γ quenched sample between ~400 and ~500°C, well below the phase-transition temperature.

[21]McGeary [4] measured the fractional length increases associated with this transition for nominal 9 and 12wt% U–Mo to be 0.068% over a temperature range of 575–625°C for U–9Mo and 0.053% over a temp. range of 575–615°C for U–12Mo.

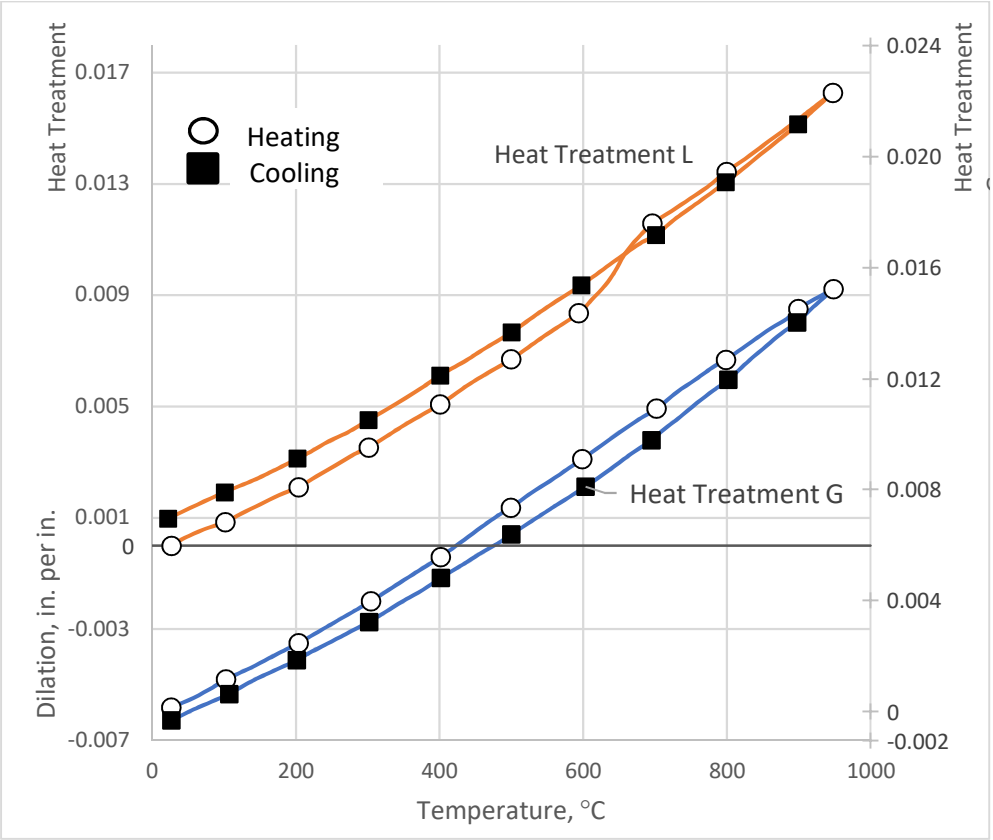

FIG. 43. Linear thermal expansion vs. temperature for U–9.36Mo (adapted from fig. A-4 of Saller et al. [42]). Heat treatment G produces γ quenched U–Mo and heat treatment L produces α soaked U–Mo.

TABLE 15. DILATION DATA FOR U–9.36Mo FROM SALLER ET AL. [42]

	α Soaked				*γ* Quenched			
T	Upon Heating		Upon Cooling		Upon Heating		Upon Cooling	
(°C)	$\frac{\Delta L_{T_a}}{L_{20}}$ (%)	$\frac{\Delta L_{T_b}}{L_{20}}$ (%)	$\frac{\Delta L_{T_a}}{L_{20}}$ (%)	$\frac{\Delta L_{T_b}}{L_{20}}$ (%)	$\frac{\Delta L_{T_a}}{L_{20}}$ (%)	$\frac{\Delta L_{T_b}}{L_{20}}$ (%)	$\frac{\Delta L_{T_a}}{L_{20}}$ (%)	$\frac{\Delta L_{T_b}}{L_{20}}$ (%)
20	0.000	0.000	0.093	0.095	0.000	0.016	-0.035	-0.031
100	0.080	0.081	0.188	0.191	0.103	0.121	0.059	0.063
200	0.207	0.208	0.319	0.313	0.242	0.250	0.182	0.189
300	0.354	0.347	0.457	0.452	0.395	0.405	0.325	0.327
400	0.508	0.508	0.608	0.611	0.558	0.562	0.482	0.482
500	0.674	0.668	0.769	0.765	0.731	0.737	0.641	0.642
600	–	0.825	0.938	0.932	0.913	0.913	0.807	0.810
700	1.151	1.157	1.119	1.112	1.093	1.087	0.987	0.978
800	1.336	1.345	1.311	1.302	1.269	1.271	1.190	1.194
900	1.535	–	1.524	1.509	1.442	1.452	1.408	1.403
950	1.628	1.628	1.628	1.628	1.521	1.521	1.521	1.521

[a] Calculated from $\bar{\alpha}$'s in table 5 of Ref [42]

[b] Digitized from fig. A-4 of Ref [42]

–: data not available

Dilation data have been derived from the $\bar{\alpha}$'s in Saller et al.'s table 5, using Eq. (54), for the nominal 7.0, 9.0, and 12.0 wt% (measured 7.18, 9.36, and 12.10 wt%) Mo γ quenched specimens and the 9.36 wt% α soaked specimen. Results for the α soaked and γ quenched 9.36 wt% specimens are presented in Table 16 and Table 17, respectively, and results for the γ quenched 7.18 and 12.10 wt% specimens are presented in Table 18 and Table 19, respectively.[22, 23] Most of the specimens underwent only one heating–cooling cycle. In these tables, the dilation curves produced upon cooling have been normalized to have the same value of $\Delta L_T/L_{20}$ at 950°C (1000°C for U–12.10Mo) as the corresponding heating curve to make it easy to follow the dilation curve for each heating–cooling cycle.

TABLE 16. LINEAR THERMAL EXPANSION DATA OF SALLER ET AL. [42] FOR α SOAKED U–9.36Mo

T (°C)	Upon Heating				Upon Cooling			
	$\bar{\alpha}(20,T)$[a] (10^{-6}°C^{-1})	$\Delta L_T/L_{20}$[b] (%)	$\Delta L_T/L_{20}$, fit[c] (%)	$\bar{\alpha}(20,T)$[d] (10^{-6}°C^{-1})	$\bar{\alpha}(20,T)$[a] (10^{-6}°C^{-1})	$\Delta L_T/L_{20}$[e] (%)	$\Delta L_T/L_{20}$, fit[f] (%)	$\bar{\alpha}(20,T)$[g] (10^{-6}°C^{-1})
20	–	0.000	-0.029	12.75	–	0.093	0.091	11.62
100	9.99	0.080	0.076	13.04	11.86	0.188	0.188	12.03
200	11.49	0.207	0.212	13.39	12.57	0.319	0.319	12.54
300	12.63	0.354	0.356	13.74	13.00	0.457	0.457	13.05
400	13.36	0.508	0.507	14.10	13.56	0.608	0.607	13.56
500	14.05	0.674	0.665	14.45	14.08	0.769	0.767	14.08
600	–	0.825[h]	0.830	14.81	14.57	0.938	0.937	14.59
650	–	–	1.057	17.23	–	–	1.026	14.84
700	16.92	1.151	1.150	17.33	15.09	1.119	1.119	15.11
800	17.13	1.336	1.338	17.52	15.62	1.311	1.313	15.67
900	17.44	1.535	1.532	17.73	16.26	1.524	1.521	16.25
950	17.51	1.628	1.630	17.84	16.51	1.628	1.630	16.55

[a] From Ref. [42], table 5, Heat Treatment L.

[b] Derived from $\bar{\alpha}(20,T)$, Heating, using Eq. (56) and, assuming that $\Delta L_T/L_{20} = 0$ at $T = 20$°C.

[c] Calculated using Eqs (76)–(79).

[d] Calculated using Eq. (64) and the coefficients of the piecewise fit of $\Delta L_T/L_{20}$ (Heating) shown in Eqs (76)– (79), except for the value at 20°C, which was calculated using Eqs (60). and (66) and the coefficients of Eq. (76).

[e] Derived from $\bar{\alpha}(20,T)$, Cooling, using Eq. (56) and normalized to the value of $\Delta L_T/L_{20}$ (Heating), at 950°C for the corresponding dilation curve.

[f] Calculated using Eqs (79) and (80).

[g] Calculated using Eq. (64) and the coefficients of the piecewise fit of $\Delta L_T/L_{20}$ (Cooling) shown in Eq. (79) and (80), except for the value at 20°C, which was calculated using Eqs (60) and (66) and the coefficients of Eq. (79).

[h] From Ref. [42], fig. A-4, Heat Treatment L, Heating, because the value was missing from Ref. [42], table 5.

–: data not available.

[22] One apparent (likely typographical) error was discovered while plotting the 7.18 g/cm^3 data given by Saller et al. in their table 5 — the value listed for $\bar{\alpha}$(20–500°C), 12.66 × 10^{-6} °C^{-1}, fell well below the curve of the other points. However, the value 13.66 × 10^{-6} °C^{-1} fits very well with the other data; hence, the latter value has been used in all analyses in this report.

[23] Touloukian et al. [113] have converted the $\bar{\alpha}$'s in Saller, et al.'s Table 5 to dilations, tabulated them in data table 207, and plotted them in fig. 207 of Ref. [109]. Two mistakes were spotted in Touloukian et al.'s data table 207: $\Delta L_T/L_0$ at 873 K for curve 10 should be 0.896% rather than 0.837%; $\Delta L_T/L_0$ at 1073 K for curve 14 should be 1.225% rather than 1.382%. Also, to correct for the apparent error discussed in the previous footnote, $\Delta L_T/L_0$ at 573 K in Touloukian et al.'s curve 10 should be changed from 0.354% to 0.382%.

The dilation curve upon heating for the α soaked specimen was fit using quadratic functions below and above the $\alpha + \gamma'$ to γ transition. Because $\bar{\alpha}(20, 600)$ was missing in Saller et al.'s table 5 of Ref. [42], the digitized value of $\Delta L_{600}/L_{20}$ from Saller et al.'s fig. A-4 (0.825%) was used (because the difference between the dilation calculated from $\bar{\alpha}$ in Saller et al.'s table 5 and from their fig. A-4 switches sign between 500 and 700°C, it is likely that the dilations closely agree at 600°C). The two quadratic functions are connected by a straight line between 600 and 650°C. The fit equations for α soaked U–9.36Mo during heating are:

$$\Delta L_T/L_{20}\ (\text{Heating}) = (6.204 \times 10^{-7})T^2 + (1.118 \times 10^{-3})T + (-3.902 \times 10^{-2}), \quad (20 \le T \le 550) \quad (76)$$

$$\Delta L_T/L_{20}\ (\text{Heating}) = (4.060 \times 10^{-3})T + (-1.470), \quad (550 \le \text{T} \le 600) \quad (77)$$

$$\Delta L_T/L_{20}\ (\text{Heating}) = (2.507 \times 10^{-7})T^2 + (1.507 \times 10^{-3})\,T + (2.785 \times 10^{-2}), \quad (600 \le T \le 950) \quad (78)$$

where $\Delta L/L$ is in % and T is in °C[24].

The dilation owing to the volume change of the transition alone is estimated by the difference between the values of Eqs (76) and (78) evaluated at 625°C (0.139%). Note that this value is twice the value given by McGeary in his table III for U–9Mo (0.068%), implying that Saller et al.'s α soaked specimen contained twice the fraction of $\alpha + \gamma'$ material as that of McGeary's α soaked specimen. The reason for this difference is not clear. McGeary did not state that his specimens were γ quenched prior to the 15–16 day α soak, so they might have contained some α phase material prior to the α soak and might have been expected to contain even more α phase material when tested. Saller et al.'s specimen was first γ quenched before being α soaked for 200 h at 500°C, closer to the nose of the TTT curve than the 525–550°C used by McGeary, so perhaps the higher transition rate, even for a shorter time, was enough to produce the difference.

Because all of the $\alpha + \gamma'$ material is converted to γ during the heating portion of the temperature cycle and because the γ to $\alpha + \gamma'$ transition is very slow, during cooling the test specimen remains in the γ phase and the cooling curve is smooth.

$$\Delta L_T/L_{20}\ (\text{Cooling}) = (5.106 \times 10^{-7})T^2 + (1.142 \times 10^{-3})T + (6.950 \times 10^{-2}), \quad (20 \le T \le 550) \quad (79)$$

$$\Delta L_T/L_{20}\ (\text{Cooling}) = (6.560 \times 10^{-7})T^2 + (9.614 \times 10^{-4})T + (1.247 \times 10^{-1}), \quad (550 \le T \le 950) \quad (80)$$

where $\Delta L/L$ is in %°C^{-1} and T is in °C. The dilation data and their fits for the α soaked U–9.36Mo specimen are shown in Fig. 44 (cf. Fig. 43).

[24] Many of the equations in this publication are displayed in an unconventional manner in order to minimize the possibility of making mistakes in the sign of the coefficient when making use of the equation: each coefficient is enclosed in parentheses; if it has a negative value, the sign is included with the coefficient.

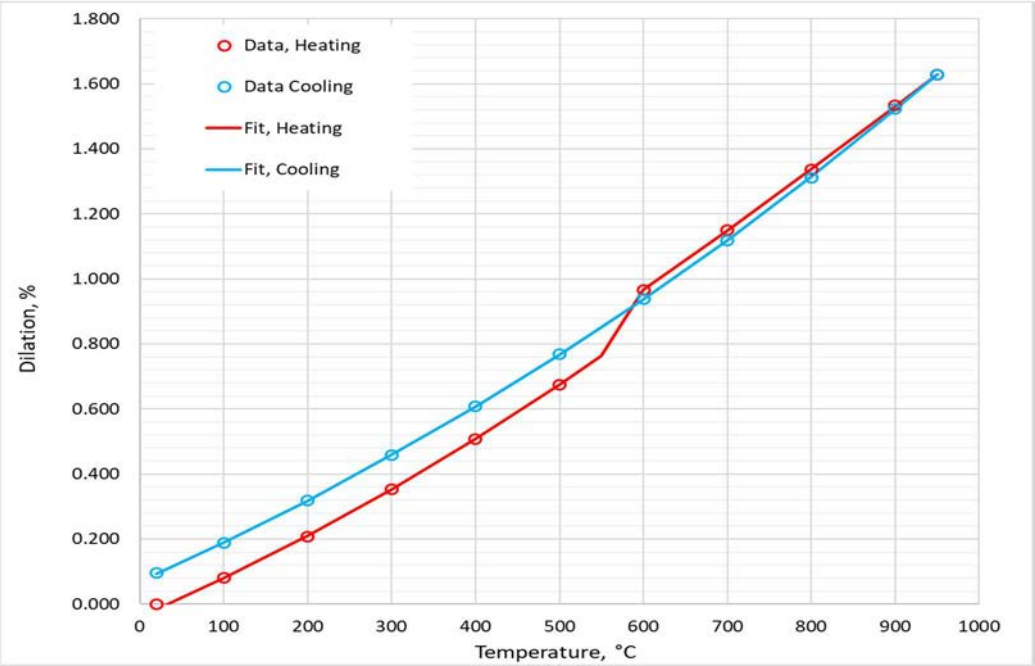

FIG. 44. Linear thermal expansion of α soaked U–9.36Mo over the temperature range 20–950°C from Saller et al. (Ref. [42] illustrating the fits of Eqs (76)– (78) (courtesy of Argonne National Laboratory).

Piecewise functions consisting of two quadratics were used to fit Saller et al.'s dilation data for both the heating portion and the cooling portion of the measurement cycle for γ quenched U–7.18Mo, U–9.36Mo, or U–12.10U–Mo; the temperature boundary between the two pieces of the function was chosen to be 550 ºC. The results of the fits are shown in Table 17–Table 19.

TABLE 17. LINEAR THERMAL EXPANSION DATA OF SALLER ET AL. [42] FOR γ QUENCHED U–9.36Mo

T (°C)	Upon Heating				Upon Cooling			
	$\bar{\alpha}(20,T)$[a] (10^{-6}°C^{-1})	$\Delta L_T/L_{20}$[b] (%)	$\Delta L_T/L_{20}$, fit[c] (%)	$\bar{\alpha}(20,T)$[d] (10^{-6}°C^{-1})	$\bar{\alpha}(20,T)$[a] (10^{-6}°C^{-1})	$\Delta L_T/L_{20}$[e] %	$\Delta L_T/L_{20}$, fit[f] (%)	$\bar{\alpha}(20,T)$[g] (10^{-6}°C^{-1})
20	–	0.000	-0.004	12.74	–	–0.035	-0.039	11.48
100	12.88	0.103	0.102	13.16	11.80	0.059	0.056	11.91
200	13.42	0.242	0.102	13.16	12.09	0.182	0.185	12.44
300	14.11	0.395	0.243	13.69	12.86	0.325	0.324	12.98
400	14.68	0.558	0.395	14.22	13.61	0.482	0.474	13.52
500	15.22	0.731	0.557	14.75	14.08	0.641	0.635	14.06
600	15.74	0.913	0.730	15.28	14.52	0.807	0.807	14.60
700	16.07	1.093	0.914	15.82	15.04	0.987	0.990	15.14
800	16.27	1.269	1.093	16.13	15.71	1.190	1.190	15.77
900	16.39	1.442	1.440	16.40	16.40	1.408	1.408	16.45
950	16.36	1.521	1.523	16.42	16.74	1.521	1.523	16.80

[a] From Ref. [42], table 5, Heat Treatment G.

[b] Derived from $\bar{\alpha}(20,T)$, Heating, using Eq. (56) and assuming that $\Delta L_T/L_{20} = 0$ at $T = 20$°C.

[c] Calculated using Eqs (76) and (78).

[d] Calculated using Eq. (64) and the coefficients of the piecewise fit of $\Delta L_T/L_{20}$ (Heating) shown in Eqs (76) and (78), except for the value at 20°C, which was calculated using Eqs (60) and (66) and the coefficients of Eq. (81).

[e] Derived from $\bar{\alpha}(20,T)$, Cooling, using Eq. (56) and normalized to the value of $\Delta L_T/L_{20}$ (Heating) at 950°C for the corresponding dilation curve.

[f] Calculated using Eqs (79) and (84).

[g] Calculated using Eq. (64) and the coefficients of the piecewise fit of $\Delta L_T/L_{20}$ (Cooling) shown in Eqs (83) and (84), except for the value at 20°C, which was calculated using Eqs (60) and (66)and the coefficients of Eq. (83).

–: data not available.

The equations of the fits of Saller et al.'s linear thermal expansion data for γ quenched U–9.36Mo are:

$$\Delta L_T/L_{20}\,(\text{Heating}) = (5.286 \times 10^{-7})T^2 + (1.253 \times 10^{-3})T + (-2.84 \times 10^{-2}), \quad (20 \le T \le 550) \quad (81)$$

$$\Delta L_T/L_{20}\,(\text{Heating}) = (-2.147 \times 10^{-7})T^2 + (2.076 \times 10^{-3})T + (-2.545 \times 10^{-1}), \quad (600 \le T \le 950) \quad (82)$$

$$\Delta L_T/L_{20}\,(\text{Cooling}) = (5.378 \times 10^{-7})T^2 + (1.128 \times 10^{-3})T + (5.97 \times 10^{-2}), \quad (20 \le T \le 550) \quad (83)$$

$$\Delta L_T/L_{20}\,(\text{Cooling}) = (8.692 \times 10^{-7})T^2 + (6.990 \times 10^{-4})T + (7.53 \times 10^{-2}), \quad (600 \le T \le 950) \quad (84)$$

where $\Delta L/L$ is in % and T is in °C.

TABLE 18. LINEAR THERMAL EXPANSION DATA OF SALLER ET AL. [42] FOR γ QUENCHED U–7.18Mo

T (°C)	Upon Heating				Upon Cooling			
	$\bar{\alpha}(20,T)$[a] (10^{-6}°C^{-1})	$\Delta L_T/L_{20}$[b] (%)	$\Delta L_T/L_{20}$, fit[c] (%)	$\bar{\alpha}(20,T)$[d] (10^{-6}°C^{-1})	$\bar{\alpha}(20,T)$[a] (10^{-6}°C^{-1})	$\Delta L_T/L_{20}$[e] %	$\Delta L_T/L_{20}$, fit[f] (%)	$\bar{\alpha}(20,T)$[g] (10^{-6}°C^{-1})
20	–	0.000	-0.019	11.55	–	-0.102	-0.098	11.90
100	10.43	0.083	0.077	12.04	12.78	0.000	0.001	12.39
200	11.26	0.203	0.209	12.66	13.13	0.134	0.136	13.00
300	12.42	0.348	0.352	13.27	13.66[h]	0.280	0.283	13.60
400	13.60	0.517	0.508	13.89	14.18	0.437	0.442	14.21
500	14.23	0.683	0.677	14.50	14.88	0.612	0.614	14.82
600	14.73	0.854	0.858	15.12	15.45	0.794	0.797	15.43
700	15.26	1.038	1.040	15.58	15.96	0.983	0.987	15.95
800	15.78	1.231	1.226	15.97	16.45	1.181	1.189	16.50
900	16.17	1.423	1.417	16.33	17.04	1.397	1.403	17.05
950	16.24	1.510	1.515	16.49	17.34	1.510	1.515	17.34

[a] From Ref. [42], table 5, Heat Treatment G.

[b] Derived from $\bar{\alpha}(20,T)$, Heating, using Eq. (56), assuming that $\Delta L_T/L_{20} = 0$ at $T = 20$°C.

[c] Calculated using Eqs (85) and (86).

[d] Calculated using Eq. (64) and the coefficients of the piecewise fit of $\Delta L_T/L_{20}$ (Heating) shown in Eqs (85) and (86), except for the value at 20°C, which was calculated using Eq.(60).

[e] Derived from $\bar{\alpha}(20,T)$, Cooling, using Eq. (56) and normalized to the value of $\Delta L_T/L_{20}$ (Heating), at 950°C for the corresponding dilation curve.

[f] Calculated using Eqs (79) and (88).

[g] Calculated using Eq.(64) and the coefficients of the quadratic fit of $\Delta L_T/L_{20}$ (Cooling) shown in Eq. (87), except for the value at 20°C, which was calculated using Eq.(60).

[h] Replaces the apparently erroneous value in Ref. [42], table 5, as explained in footnote 22.

–: data not available.

The equations of the fits of Saller et al.'s linear thermal expansion data for γ quenched U–7.18Mo are:

$$\Delta L_T/L_{20}\,(\text{Heating}) = (6.160 \times 10^{-7})T^2 + (1.130 \times 10^{-3})T + (-\ 4.10 \times 10^{-2}) \quad (20 \le T \le 550) \quad (85)$$

$$\Delta L_T/L_{20}\,(\text{Heating}) = (2.199 \times 10^{-7})T^2 + (1.536 \times 10^{-3})T + (-\ 1.428 \times 10^{-1}) \quad (550 \le T \le 950) \quad (86)$$

$$\Delta L_T/L_{20}\,(\text{Cooling}) = (6.075 \times 10^{-7})T^2 + (1.166 \times 10^{-3})T + (-\ 1.212 \times 10^{-1}) \quad (20 \le T \le 550) \quad (87)$$

$$\Delta L_T/L_{20}\,(\text{Cooling}) = (5.942 \times 10^{-7})T^2 + (1.129 \times 10^{-3})T + (-\ 9.40 \times 10^{-2}) \quad (550 \le T \le 950) \quad (88)$$

where $\Delta L/L$ is in % and T is in °C.

TABLE 19. LINEAR THERMAL EXPANSION DATA OF SALLER ET AL. [42] FOR γ QUENCHED U–12.10Mo

T (°C)	Upon Heating				Upon Cooling			
	$\bar{\alpha}(20,T)$[a] (10^{-6}°C^{-1})	$\Delta L_T/L_{20}$[b] (%)	$\Delta L_T/L_{20}$, fit[c] (%)	$\bar{\alpha}(20,T)$[d] (10^{-6}°C^{-1})	$\bar{\alpha}(20,T)$[a] (10^{-6}°C^{-1})	$\Delta L_T/L_{20}$[e] %	$\Delta L_T/L_{20}$, fit[f] (%)	$\bar{\alpha}(20,T)$[g] (10^{-6}°C^{-1})
20	–	0.000	-0.023	11.1	–	-0.064	-0.065	10.86
100	8.95	0.072	0.069	11.46	11.34	0.027	0.025	11.25
200	10.45	0.188	0.191	11.86	11.70	0.147	0.146	11.73
300	11.59	0.325	0.320	12.26	12.22	0.278	0.277	12.22
400	12.11	0.460	0.458	12.65	12.73	0.420	0.418	12.71
500	12.56	0.603	0.603	13.05	13.19	0.569	0.568	13.20
600	13.08	0.759	0.757	13.44	13.69	0.730	0.729	13.68
700	13.56	0.922	0.923	13.91	14.14	0.898	0.899	14.18
800	14.14	1.103	1.102	14.41	14.69	1.082	1.084	14.73
900	14.71	1.294	1.292	14.94	15.27	1.280	1.282	15.31
1000	15.25	1.495	1.495	15.48	15.90	1.495	1.495	15.91

[a] From Ref. [42], table 5, Heat Treatment G.

[b] Derived from $\bar{\alpha}(20,T)$, Heating, using Eq. (56), assuming that $\Delta L_T/L_{20} = 0$ at $T = 20$°C.

[c] Calculated using Eqs(89) and (90).

[d] Calculated using Eq. (65) and the coefficients of the piecewise fit of $\Delta L_T/L_{20}$ (Heating) shown in Eqs (89) and (78) , except for the value at 20°C, which was calculated using Eqs (60) and (66) and the coefficients of Eq. (89).

[e] Derived from $\bar{\alpha}(20,T)$, Cooling, using Eq. (56) and normalized to the value of $\Delta L_T/L_{20}$ (Heating) at 950°C for the corresponding dilation curve. (91) and (95).

[g] Calculated using Eq. (65) and the coefficients of the piecewise fit of $\Delta L_T/L_{20}$ (Cooling) shown in Eqs (91) and (95)., except for the value at 20°C, which was calculated using Eqs (60) and (66) and the coefficients of Eq. (91).

–: data not available.

The equations of the fits of Saller et al.'s linear thermal expansion data for γ quenched U–12.10Mo are:

$$\Delta L_T/L_{20}\ (\text{Heating}) = (4.032 \times 10^{-7})T^2 + (1.093 \times 10^{-3})T + (4.59 \times 10^{-2}) \quad (20 \le T \le 550) \quad (89)$$

$$\Delta L_T/L_{20}\ (\text{Heating}) = (5.960 \times 10^{-7})T^2 + (8.91 \times 10^{-4})T + (8.60 \times 10^{-3}) \quad (550 \le T \le 1000) \quad (90)$$

$$\Delta L_T/L_{20}\ (\text{Cooling}) = (4.877 \times 10^{-7})T^2 + (1.066 \times 10^{-3})T + (-8.52 \times 10^{-2}) \quad (20 \le T \le 550) \quad (91)$$

$$\Delta L_T/L_{20}\ (\text{Cooling}) = (6.955 \times 10^{-7})T^2 + (8.02 \times 10^{-4})T + (-4.10 \times 10^{-3}) \quad (550 \le T \le 1000) \quad (92)$$

where $\Delta L/L$ is in % and T is in °C.

Except for normalization, the cooling curves for the α soaked and γ quenched U–9.36Mo specimens shown in Table 14, are very similar, indicating that both specimens were in essentially the same metallurgical state following one heating cycle. Therefore, one could argue that thermal expansion data obtained during cooling are more representative of γ phase U–Mo, while those obtained during heating, especially of α soaked U–Mo, might well be more

representative of as-fabricated U–Mo fuel meat. Over the range of Saller et al.'s data examined during this work, there is generally good agreement between the average coefficients of linear thermal expansion calculated from the measured dilations and those calculated from the quadratic fit. Finally, for the 7–12 wt% Mo range of interest for U–Mo fuels, Saller et al.'s data show that if an α phase transition occurs during the heating portion of a heating–cooling cycle, the specimen's length will have increased slightly upon its return to room temperature; conversely, if no phase transition occurs, the specimen's length will have decreased slightly. Consequently, for γ phase U–Mo, as U–Mo would be if it had been under irradiation, the dilation during cooling is greater than that during heating, so use of the cooling data would be slightly more conservative than use of the heating data.

Saller et al.'s dilation data and the fits represented by Eqs (81)–(92) for γ quenched U–Mo having Mo contents of 7.18, 9.36, and 12.10 wt% are shown in Fig. 45. Notice the cooling curve for the U–9.36Mo specimen changes shape around 500°C, while the cooling curves for the U–7.18Mo and U–12.10Mo specimens remained convex throughout the entire temperature range. It is not known why this happened.

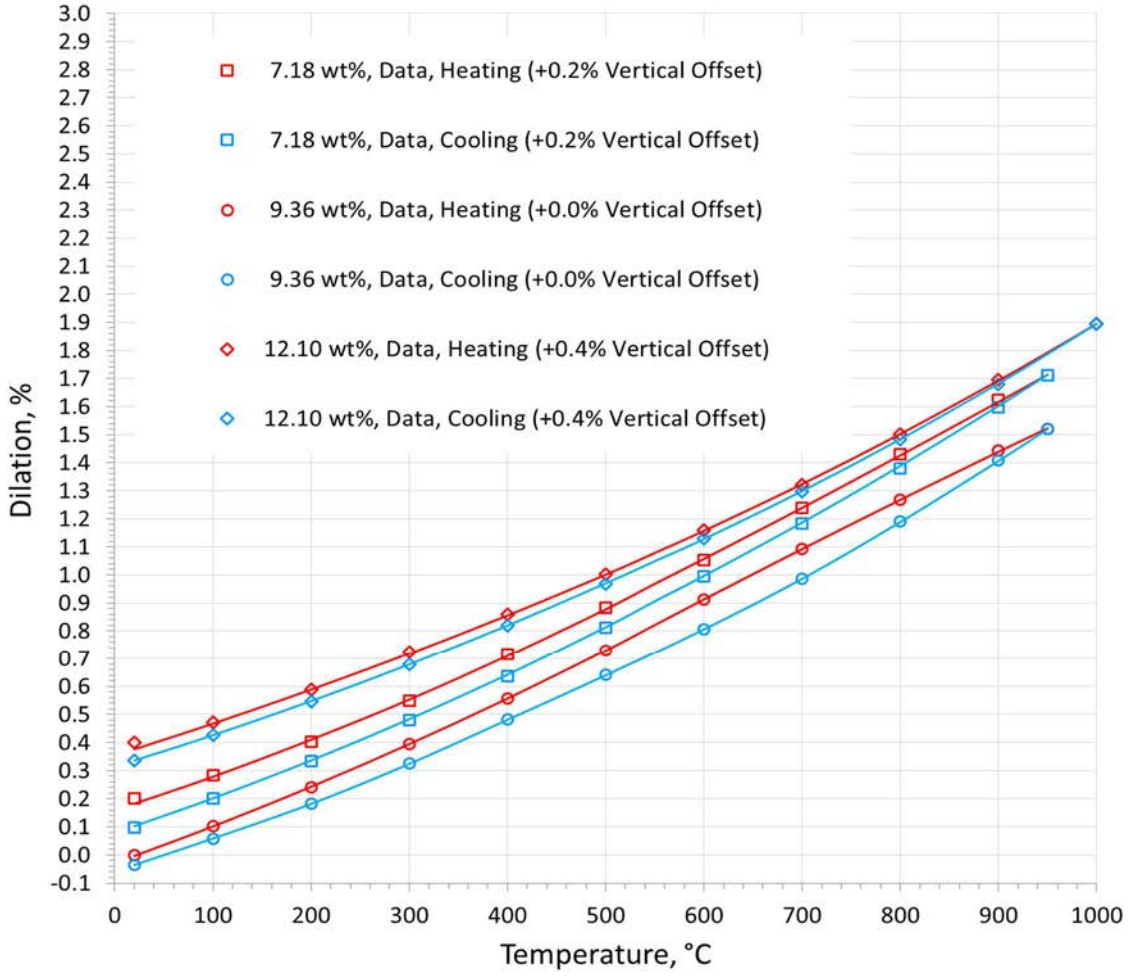

FIG. 45. Dilation of γ quenched U–7.18Mo, U–9.36Mo, and U–12.10Mo during heating and cooling as measured by Saller et al. (Ref [42]. The curves are the least squares fits represented by Eqs (81)–(92). Note that the U–7.18Mo and U–12.10Mo data are offset vertically to avoid overlapping of the curves. (courtesy of Argonne National Laboratory).

A.5.2.3 Del Grosso (1957) [37]

In December 1955, the decision was taken to use U–10Mo as the reference fuel alloy for the Enrico Fermi Nuclear Power Plant to be built near Detroit [106]. APDA, lead nuclear designer, contracted with a number of research organizations to produce the materials properties data needed for the fuel design. Southern Research Institute, in two unpublished reports, provided the coefficient of thermal expansion data[25] reported by Del Grosso in Ref. [37]. The measurements were made on extruded specimens that had been heat treated at 900°C for an unspecified time and then water quenched.

Dilation measurements were made in both the longitudinal and transverse directions (this appears to be the only investigation in which dilation in the transverse direction has been measured). The heating and cooling rates used were not specified. The magnitude of the longitudinal or transverse ΔL_T was recorded at the end of each temperature increment, divided by the room-temperature longitudinal or transverse dimension of the test specimen and by $(T_e - T_b)$ to produce $\bar{\alpha}_{Long}(T_b, T_e)$ or $\bar{\alpha}_{Trans}(T_b, T_e)$ where T_b and T_e are the beginning and ending temperatures of each temperature interval, respectively.

Knowing that the U–Mo equilibrium $\alpha + \gamma'$ phase-transition occurs at 550°C or higher, measurements were made at 10°C intervals between 550 and 600°C in order to define the approximate temperature at which dilation changes owing to the phase transition occurred. Saller et al.'s [42] data for α soaked specimens discussed in the previous section showed that the effect of the transition did not become apparent until the specimen had reached a temperature about 30°C above the transition temperature (cf. Fig. 43), because heat requires time to transfer throughout the test specimen and a solid-state transition requires time for diffusion of the material phases to occur.

The data contained in Del Grosso's tables 1–3 are listed below in Table 20–Table 22, respectively. Since $\Delta L_T/L_0$ was found to be a quadratic function of T, Eq. (60) shows that for each temperature interval, Del Grosso's coefficients of thermal expansion represent both the instantaneous coefficient at the centre of the interval and the average coefficient over the interval, as shown by Eq. (61).

[25] No reason is apparent why the Southern Research Institute presented its data as coefficients of thermal expansion instead of dilations.

TABLE 20. COEFFICIENTS OF THERMAL EXPANSION OF γ QUENCHED U–10Mo IN THE LONGITUDINAL DIRECTION, SPECIMEN NO. 1 (ADAPTED FROM DEL GROSSO'S TABLE 1 IN REF. [37])

Heating Temperature (°C)		$\alpha(T_{mean})$ (10^{-6}°C^{-1})		Cooling Temperature (°C)		$\alpha(T_{mean})$ (10^{-6}°C^{-1})	
T_b, T_e	T_{mean}	Run 1	Run 2	T_b, T_e	T_{mean}	Run 1	Run 2
30, 100	65	7.4	11.0	900, 800	850	19.8	20.3
100, 200	150	12.9	12.1	800, 700	750	19.8	18.3
200, 300	250	14.6	14.3	700, 600	650	17.1	18.6
300, 400	350	15.8	15.1	600, 590	595	17.3	17.3
400, 500	450	15.6	14.4	590, 580	585	17.3	14.9
500, 550	525	16.8	18.9	580, 570	575	17.3	17.3
550, 560	555	19.8	17.3	570, 560	565	14.9	14.9
560, 570	565	17.3	14.9	560, 550	555	14.9	14.9
570, 580	575	17.3	22.2	550, 500	525	16.8	15.9
580, 590	585	17.3	14.9	500, 400	450	15.4	15.4
590, 600	595	19.8	19.8	400, 300	350	14.6	14.9
600, 700	650	17.4	24.8	300, 200	250	14.6	13.4
700, 800	750	20.6	19.6	200, 100	150	–	13.4
800, 900	850	17.6	17.8	100, 30	65	–	14.5

–:data not available

TABLE 21. COEFFICIENTS OF THERMAL EXPANSION OF γ QUENCHED U–10Mo IN THE LONGITUDINAL DIRECTION, SPECIMEN NO. 2 (ADAPTED FROM DEL GROSSO'S TABLE 2 IN REF. [37])

Heating Temperature (°C)		$\alpha(T_{mean})$ (10^{-6}°C^{-1})		Cooling Temperature (°C)		$\alpha(T_{mean})$ (10^{-6}°C^{-1})	
T_b, T_e	T_{mean}	Run 1	Run 2	T_b, T_e	T_{mean}	Run 1	Run 2
30, 100	65	10.6	11.4	900, 800	850	21.0	21.4
100, 200	150	12.4	12.7	800, 700	750	20.3	19.7
200, 300	250	14.4	14.2	700, 600	650	17.3	18.1
300, 400	350	15.6	15.4	600, 590	595	17.3	17.4
400, 500	450	15.1	14.7	590, 580	585	17.3	17.4
500, 550	525	17.4	18.9	580, 570	575	17.3	17.4
550, 560	555	12.4	17.4	570, 560	565	14.9	14.9
560, 570	565	17.3	17.4	560, 550	555	17.3	14.9
570, 580	575	19.8	19.9	550, 500	525	16.9	16.9
580, 590	585	17.3	17.4	500, 400	450	15.4	15.2
590, 600	595	17.3	19.9	400, 300	350	14.7	15.2
600, 700	650	19.1	20.2	300, 200	250	11.7	14.2
700, 800	750	18.8	18.9	200, 30	115	11.8	11.7
800, 900	850	19.6	20.6				

TABLE 22. COEFFICIENTS OF THERMAL EXPANSION OF γ QUENCHED U–10Mo IN THE TRANSVERSE DIRECTION, SPECIMEN NO. 1 (ADAPTED FROM DEL GROSSO'S TABLE 3 IN REF. [37])

Heating Temperature (°C)		$\alpha(T_{mean})$ (10^{-6}°C^{-1})		Cooling Temperature (°C)		$\alpha(T_{mean})$ (10^{-6}°C^{-1})	
T_b, T_e	T_{mean}	Run 1	Run 2	T_b, T_e	T_{mean}	Run 1	Run 2
30, 100	65	13.4	13.0	900, 800	850	25.4	25.4
100, 200	150	14.5	16.4	800, 700	750	23.6	21.8
200, 300	250	–	18.2	700, 600	650	21.8	21.8
200, 317	259	17.1	–	600, 575	588	21.8	14.6
300, 400	350	–	18.2	575, 550	563	21.8	21.8
317, 400	359	21.9	–	550, 500	525	21.8	14.5
400, 500	450	23.6	16.4	500, 400	450	16.4	10.9
500, 550	525	21.8	18.2	400, 317	359	15.3	–
550, 575	563	21.8	21.8	400, 300	350	–	16.4
575, 600	588	14.6	14.6	317, 200	259	15.6	–
600, 700	650	18.2	21.8	300, 200	250	–	21.8
700, 800	750	21.8	20.0	200, 100	150	10.9	–
800, 900	850	16.4	16.4	200, 30	115	–	11.8
				100, 30	65	10.9	–

–:data not available

The instantaneous coefficients of thermal expansion in the longitudinal direction in Table 20 and Table 21 are plotted vs. the mean temperature of each temperature interval in Fig. 46, along with the piecewise-linear least squares fit line from Del Grosso's fig. 2. Del Grosso's piecewise linear fit line for his instantaneous coefficients of linear thermal expansion in the longitudinal direction in Fig. 46 are described by the following equations:

$$\alpha_{Long} = 0.0985T + 11.22, (30 < T < 550) \quad (93)$$

$$\alpha_{Long} = 16.64, (550 \leq T < 600) \quad (94)$$

$$\alpha_{Long} = 0.0128T + 8.96, (600 \leq T \leq 900) \quad (95)$$

where α_{Long} is in 10^{-6}°C^{-1}. The scatter-band limits are ±1.7 10^{-6}°C^{-1} with respect to the fit line value. A linear least squares fit of all data points yields:

$$\alpha_{Long} = 0.0119T + 10.6, (30 \leq T \leq 900) \quad (96)$$

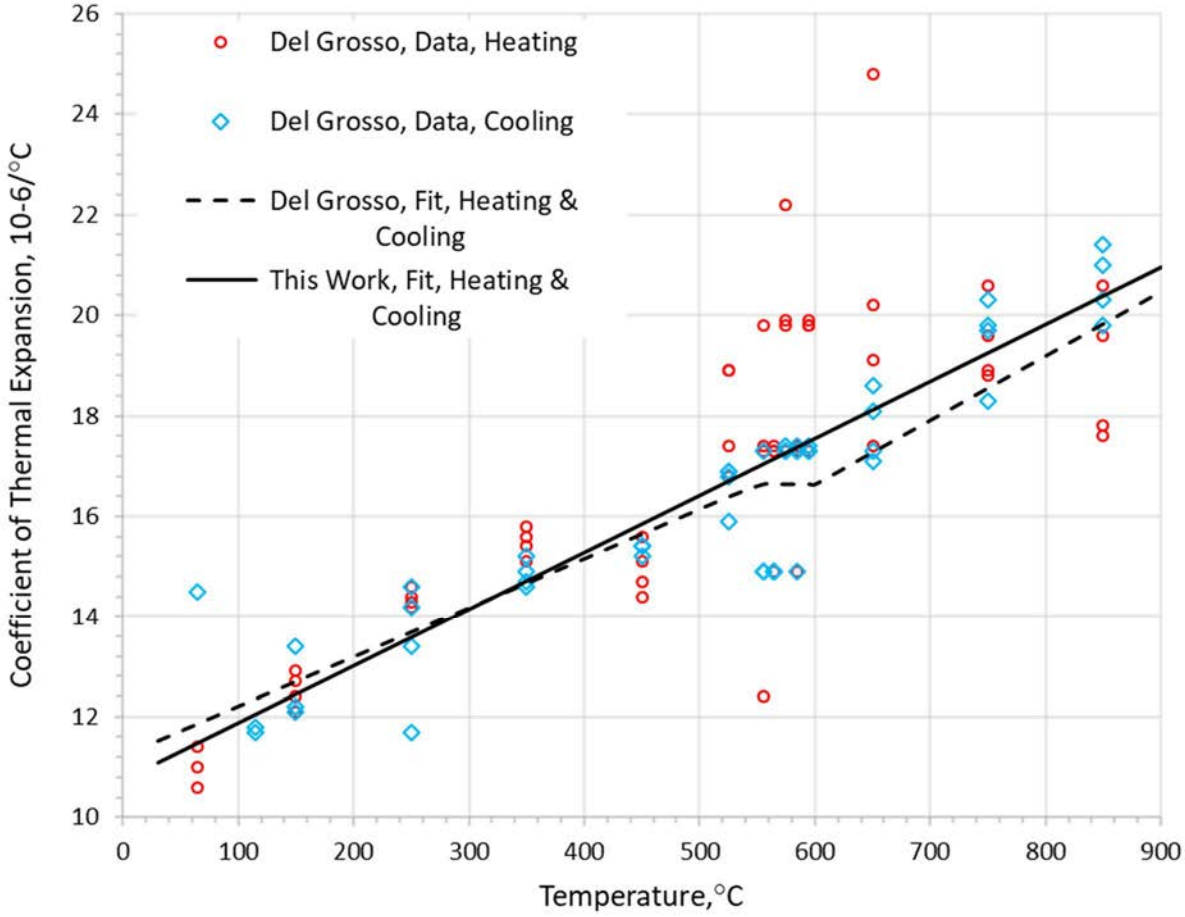

FIG. 46. Instantaneous coefficients of linear thermal expansion in the longitudinal direction during both heating and cooling of γ quenched U–10Mo from Del Grosso (Ref. [37]). Del Grosso's piecewise linear fit (dashed line) and a linear fit of all data points (solid line) are shown (courtesy of Argonne National Laboratory).

As shown in Fig. 46, Del Grosso assumed that the 550–600°C portion of his piecewise fit was flat, apparently influenced by the flat appearance of the closely spaced data taken at 10°C increments over that temperature range; however, this was just a visual artefact of the data owing to small temperature intervals and the difficulty in reading the small changes in the dilation over those intervals. Since the instantaneous coefficient of linear thermal expansion is the slope of the dilation curve at a given temperature, Del Grosso's model implies that the physical process causing the slope to increase with increasing temperature is suspended during the time that the specimen temperature is passing through the transition temperature and then is resumed following the transition. There are two reasons to reject this model. First, having been γ quenched, the specimen would already have consisted primarily of γ phase material whose behaviour should not be affected by passing through the transition temperature. Second, any $\alpha + \gamma'$ material would continue to expand at its own rate until it transforms, and the newly formed γ material would begin to expand as soon as it is created. The single straight line shown in Fig. 46 is a better fit of Del Grosso's instantaneous coefficients of linear thermal expansion.

A similar figure could be produced from the data for the transverse direction in Table 22, along with the piecewise-linear fit of the data and the scatterband Del Grosso shows in his fig. 3. Del Grosso's piecewise linear fit line for his transverse instantaneous coefficients of thermal expansion in his table 3 are described by the following equations:

$$\alpha_{Trans} = 0.015T + 11.55, (30 \leq T \leq 550) \quad (97)$$

$$\alpha_{Trans} = 19.80, (550 \leq T \leq 600) \quad (98)$$

$$\alpha_{Trans} = 0.010T + 13.80, (600 \leq T \leq 900) \quad (99)$$

where α_{Trans} is in 10^{-6}°C^{-1}. The scatterband limits are ±1.7 10^{-6}°C^{-1} with respect to the fit line value. A linear least squares fit of all data points yields:

$$\alpha_{Trans} = 0.0107T + 13.3, (30 < \text{T} < 900) \quad (100)$$

However, even better fits of the data are possible. Recall that the α at the midpoint temperature of each interval in Table 20–Table 22 is equal to the $\bar{\alpha}$'s over the temperature interval. Since these coefficients are very scattered, even more so for the transverse than for the longitudinal measurements, it makes sense to reconstruct the original $\Delta L_T/L_0$ curves to see if the scatter can be reduced. Summing a series of incremental measurements usually reduces the uncertainty — if one increment is too low, the next is likely to be too high, leaving a smaller uncertainty for the sum. The length increase during each temperature interval is

$$\Delta L(T_b, T_e)/L_{30} = \bar{\alpha}(T_b, T_e) \times (T_e - T_b). \quad (101)$$

The cumulative sums of the $\Delta L(T_b, T_e)/L_{30}$'s for each individual run, derived from the data in Table 20–Table 22, are listed in Table 23 and shown in Fig. 47. Except for roundoff and any errors in Del Grosso's tabulated coefficients, these are the dilations originally measured during the experiment, i.e. the original data. Note that, indeed, the dilation data is much less scattered than the coefficient of thermal expansion data.

TABLE 23. DILATIONS OF γ QUENCHED U–10Mo SPECIMENS (DERIVED FROM LONGITUDINAL AND TRANSVERSE COEFFICIENTS OF LINEAR THERMAL EXPANSION FROM DEL GROSSO (REF. [37])

T_e (°C)	Longitudinal $\Delta L_T/L_{30}$ (%)				Transverse $\Delta R_T/R_{30}$ (%)	
	Specimen No. 1		Specimen No. 2		Specimen No. 1	
	Run 1	Run 2	Run 1	Run 2	Run 1	Run 2
30	0.000	0.000	0.000	0.000	0.000	0.000
100	0.052	0.077	0.074	0.080	0.091	0.091
200	0.181	0.198	0.198	0.207	0.236	0.255
300	0.327	0.341	0.342	0.349	–	0.437
317	–	–	–	–	0.436	–
400	0.485	0.492	0.498	0.503	0.618	0.619
500	0.641	0.636	0.649	0.650	0.854	0.783
550	0.725	0.731	0.736	0.744	0.963	0.874
560	0.745	0.748	0.749	0.762	–	–
570	0.762	0.763	0.766	0.779	–	–
575	–	–	–	–	1.017	0.928
580	0.779	0.785	0.786	0.799	–	–
590	0.797	0.800	0.803	0.816	–	–
600	0.816	0.820	0.820	0.836	1.054	0.965
700	0.990	1.068	1.011	1.038	1.236	1.183
800	1.196	1.264	1.199	1.227	1.454	1.383
900	1.372	1.442	1.395	1.433	1.618	1.547
800	1.174	1.239	1.185	1.219	1.364	1.293
700	0.976	1.056	0.982	1.022	1.128	1.075
600	0.805	0.870	0.809	0.841	0.910	0.857
590	0.788	0.852	0.792	0.824	–	–
580	0.771	0.837	0.775	0.807	–	–
575	–	–	–	–	0.855	0.820
570	0.753	0.820	0.757	0.789	–	–
560	0.739	0.805	0.743	0.774	–	–
550	0.724	0.790	0.725	0.759	0.801	0.766
500	0.640	0.711	0.641	0.675	0.692	0.693
400	0.486	0.557	0.487	0.523	0.528	0.584
317	–	–	–	–	0.401	–
300	0.340	0.408	0.340	0.371	–	0.420
200	0.194	0.274	0.223	0.229	0.218	0.202
100	–	0.140	–	–	0.109	–
30	–	0.038	0.022	0.030	0.033	0.002

–: data not available.

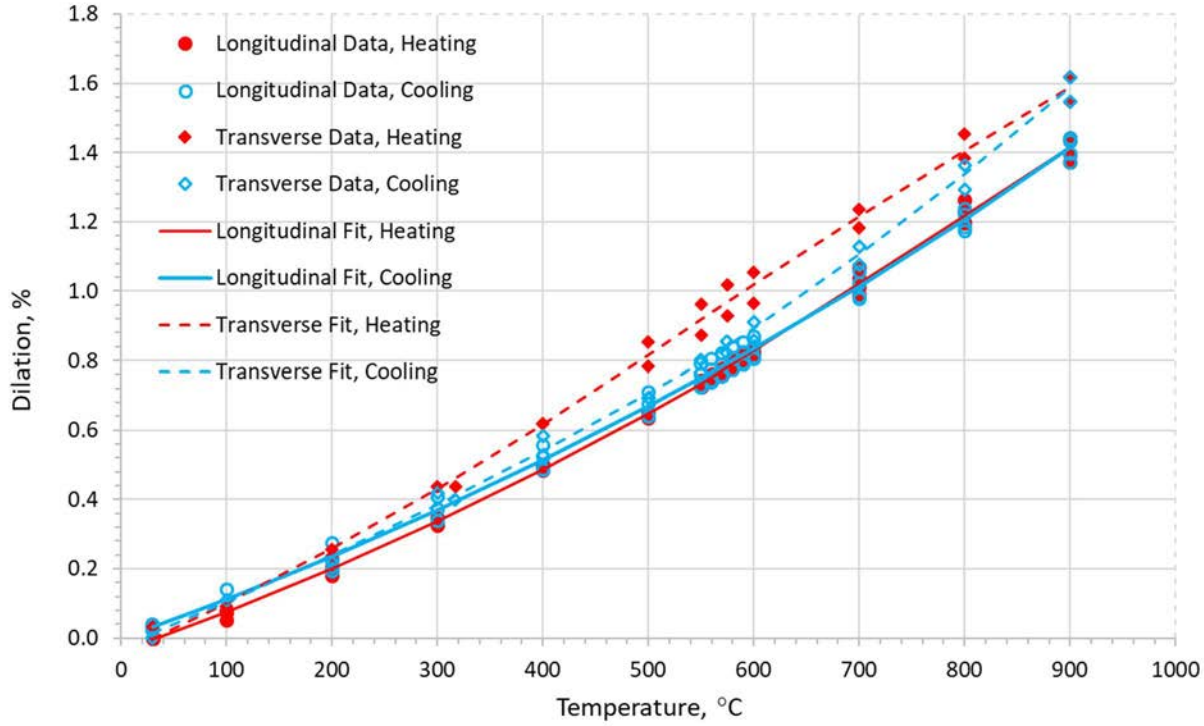

FIG. 47. Dilation in the longitudinal and transverse directions vs. temperature of γ quenched U–10Mo from Del Grosso [37]. The lines represent quadratic least squares fits of the data from Eqs (102)–(109). (courtesy of Argonne National Laboratory).

The heating and cooling dilation data listed in Table 23 have been analysed separately for both the longitudinal and transverse measurements. As seen in Fig. 47, the heating and cooling curves are very similar in the longitudinal direction. The dilation data are more scattered in the transverse direction, and the dilations during heating are considerably larger than the longitudinal dilations at temperatures above 200ºC; the dilations during cooling in the transverse direction are also considerably larger than the longitudinal dilations at temperatures above 500ºC. It is conjectured that Del Grosso's specimens were cylindrical in cross section since the fuel was being developed for the Fermi-1 reactor; hence, it might have been more difficult to keep the opposing measuring points aligned, resulting in more scatter, and differences owing to the presumed longitudinal manufacturing direction might have caused a directional effect in the dilation of the specimen. Piecewise least squares fits of Del Grosso's γ quenched U–10Mo longitudinal data yielded the equations:

$$\Delta L_T/L_{30}\ (\text{Heating}) = (6.085 \times 10^{-7})T^2 + (1.067 \times 10^{-3})T + (-3.85\times10^{-2}), \quad (30 \le T \le 550) \qquad (102)$$

$$\Delta L_T/L_{30}\ (\text{Heating}) = (1.227 \times 10^{-7})T^2 + (1.771 \times 10^{-3})T + (-2.787\times10^{-1}), \quad (550 \le T \le 900) \qquad (103)$$

$$\Delta L_T/L_{30}\ (\text{Cooling}) = (5.367 \times 10^{-7})T^2 + (1.071 \times 10^{-3})T + (-1.0 \times 10^{-4}), \quad (30 \le T \le 550) \qquad (104)$$

$$\Delta L_T/L_{30}\ (\text{Cooling}) = (7.547 \times 10^{-7})T^2 + (8.00 \times 10^{-4})T + (8.32 \times 10^{-2}), \quad (550 \le T \le 900) \qquad (105)$$

where $\Delta L_T/L_{30}$ is in % and T is in °C. Piecewise least squares fits of the transverse data yielded the equations:

$$\Delta R_T/R_{30}\ (\text{Heating}) = (6.804 \times 10^{-7})T^2 + (1.379 \times 10^{-3})T + (-4.39 \times 10^{-2}), \quad (30 \le T \le 550) \qquad (106)$$

$$\Delta R_T/R_{30}\ (\text{Heating}) = (-3.342 \times 10^{-7})T^2 + (2.399 \times 10^{-3})T + (-3.003 \times 10^{-1}), \quad (550 \le T \le 900) \qquad (107)$$

$$\Delta R_T/R_{30}\ (\text{Cooling}) = (4.942 \times 10^{-7})T^2 + (1.210 \times 10^{-3})T + (2.30 \times 10^{-2}), \quad (30 \le T \le 550) \qquad (108)$$

$$\Delta R_T/R_{30}\ (\text{Cooling}) = (9.144 \times 10^{-7})T^2 + (9.490 \times 10^{-4})T + (-6.5 \times 10^{-3}), \quad (550 \le T \le 900) \qquad (109)$$

where $\Delta R_T/R_{30}$ is in % and T is in °C. Equations for volume-equivalent dilations can be developed by applying Eq. (73) to the dilations described by Eqs (99-105).

Results obtained from the least squares fits of the longitudinal and transverse dilations are also shown in Table 24 along with the instantaneous and average coefficients of expansion calculated using Eqs (58) and (59); the fits are shown graphically in Fig. 47. The instantaneous coefficients of expansion published by Del Grosso are also shown in Table 24 for comparison. The values in the table were derived from the average of the heating and cooling curves in the longitudinal direction (Eqs (102)–(105)) and in the transverse direction (Eqs (106)–(109) of U–10Mo from Del Grosso). It is recommended that the newly calculated values be adopted.

TABLE 24. LINEAR THERMAL EXPANSION DATA OF DEL GROSSO [37] FOR γ QUENCHED U–10Mo

(a) DURING HEATING

T (°C)	Longitudinal Direction				Transverse Direction			
	$\Delta L/L_{30}$	$\Delta L/L_{30}$	α	$\bar{\alpha}(25, T)$	$\Delta R/R_{30}$	$\Delta R/R_{30}$	α	$\bar{\alpha}(25, T)$
	Measured[a] (%)	Fit (%)	From Fit (10^{-6}°C^{-1})	From Fit (10^{-6}°C^{-1})	Measured[a] (%)	Fit (%)	From Fit (10^{-6}°C^{-1})	From Fit (10^{-6}°C^{-1})
30	0.000	-0.007	11.0	11.0	0.000	-0.002	14.2	14.2
100	0.071	0.073	11.9	11.5	0.091	0.100	15.2	14.7
200	0.196	0.198	13.1	12.1	0.245	0.259	16.5	15.4
300	0.340	0.336	14.3	12.7	0.437	0.430	17.9	16.0
400	0.494	0.485	15.5	13.3	0.618	0.616	19.2	16.7
500	0.644	0.646	16.8	13.9	0.818	0.815	20.6	17.4
550	0.734	0.732	18.2	14.2	0.918	0.918	20.8	17.7
600	0.823	0.827	19.2	14.6	1.009	1.018	20.0	17.9
700	1.027	1.020	19.4	15.3	1.209	1.215	19.3	18.2
800	1.222	1.216	19.7	15.9	1.418	1.405	18.6	18.3
900	1.411	1.414	19.9	16.3	1.582	1.588	18.0	18.3

[a] Average at each temperature of the dilations during heating listed in Table 23.

(b) DURING COOLING

T (°C)	Longitudinal Direction				Transverse Direction			
	$\Delta L/L_{30}$	$\Delta L/L_{30}$	α	$\bar{\alpha}(25, T)$	$\Delta R/R_{30}$	$\Delta R/R_{30}$	α	$\bar{\alpha}(25, T)$
	Measured[a] (%)	Fit (%)	From Fit (10^{-6}°C^{-1})	From Fit (10^{-6}°C^{-1})	Measured[a] (%)	Fit (%)	From Fit (10^{-6}°C^{-1})	From Fit (10^{-6}°C^{-1})
30	0.030	0.032	11.0	11.0	0.018	0.013	12.4	12.4
100	0.140	0.112	11.8	11.4	0.109	0.102	13.1	12.7
200	0.230	0.235	12.9	11.9	0.210	0.238	14.1	13.2
300	0.364	0.369	13.9	12.5	0.420	0.384	15.1	13.7
400	0.513	0.513	15.0	13.0	0.556	0.540	16.1	14.2
500	0.666	0.669	16.1	13.6	0.693	0.696	17.8	14.5
550	0.750	0.751	16.5	13.8	0.783	0.791	18.5	15.0
600	0.831	0.834	17.1	14.1	0.883	0.891	20.5	15.4
700	1.009	1.012	18.6	14.6	1.101	1.105	22.3	16.3
800	1.204	1.205	20.1	15.2	1.328	1.337	24.1	17.2
900	1.411	1.414	21.6	15.9	1.582	1.588	25.9	18.1

[a] Average at each temperature of the dilations during COOLING listed in Table 21.

Numerous authors have published Del Grosso's instantaneous thermal expansion data, although Ref. [37] was never explicitly cited as the source:

— APDA reported Del Grosso's data in Ref. [38], table XVIII; since these data are consistent with the data read from the graphs shown in Del Grosso's figures, this work uses them as Del Grosso's values;

- Both Farkas [8] and Fackelmann et al. [9] cited APDA [38], but only listed values up to 550°C, and Farkas mistakenly listed 500°C, rather than 550°C, for the last entry in his table;
- Klein [7] cited a personal communication with APDA; his longitudinal data match those of APDA [38], but four of his transverse values appear to have been rounded differently (it is likely that all APDA documents were still proprietary when Klein produced his document);
- Beghi [2] cited Klein and exactly copied his tabulated values;
- Burkes et. al. [12] also cited Klein, but six of their values vary by ±1 in the least-significant digit from those of Klein, suggesting that they did not come directly from Klein's table;
- Rest et al. [11] compared Klein's data to those from other sources in their fig. 2.2. They plotted the unweighted average of the longitudinal and transverse values, which range from 1–3% lower than the weighted average (preferred) values derived using Eq. (72).

Some clarification is needed concerning Rest et al.'s discussion of the thermal expansion of U–Mo alloys measured by various experimenters, and one misplotted point in their figure 2.2 should be noted. First, the reader may be confused about which coefficient is being discussed. Rest et al.'s figure caption rightly states that Klein's values are instantaneous coefficients; however, the statement that the data from other sources plotted in the figure "represent mean values of expansion reported over a temperature range" could be interpreted to signify that the other data are average coefficients of thermal expansion. While it is true that the data of McGeary [4] and Saller [42] are average coefficients of thermal expansion, Rest et al. have used Eq.(61) to convert average coefficients over temperature intervals to instantaneous coefficients at the mean temperature of the interval; this is only true if the dilation curve is a quadratic function, but here this assumption is close to being true. Although Repas et al. [32] did not say which of the two thermal expansion coefficients they were reporting in their table 2, one can conclude that they are instantaneous coefficients, since, based on the described experiment procedure, dilatometer measurements were taken at 10°C intervals, starting at 500°C. Also, it was determined during this work that Saller et al.'s data listed by Repas et al. for comparison had also been converted to instantaneous coefficients under the assumption Saller et al.'s dilation curves were quadratic. Even though two piecewise quadratic functions were used in this work to fit Saller et al.'s dilation data, a single quadratic did fit reasonably well. Although Rest et al. interpreted Repas et al.'s data correctly, they mistakenly plotted their data at the numerical value of the temperature in degrees Celcius instead of at 811 K, which would have brought Repas et al.'s data close to the other plotted data. Second, the vertical axis title is incorrect in Rest et al.'s figure — as written (thermal expansion, ppm) it could be interpreted to mean dilation; a correct unit for thermal expansion would be ppm/°C. Finally, Rest et al.'s comparison of the U–Mo instantaneous coefficients in their figure to the average coefficient of thermal expansion of aluminium adds to the potential for confusion.

A.5.2.4 Konobeevsky et al. (1958) [43]

Konobeevsky et al. presented the following equation for the instantaneous coefficient of linear thermal expansion of U–9Mo:

$$\alpha(T) = (2.8 \times 10^{-7})T + (1.16 \times 10^{-3}), (20 < \mathrm{T} \leq 500°\mathrm{C}) \quad (110)$$

where α is in %/°C and T is in °C. Using Eqs (55) and (56), one finds that:

$$\Delta L(T)/L_{20} = (1.4 \times 10^{-7})T^2 + (1.16 \times 10^{-3})T + (-2.33 \times 10^{-2}) \quad (111)$$

$$\bar{\alpha}(20, T) = (1.4 \times 10^{-7})(T + 20) + (1.16 \times 10^{-3}) \approx (1.4 \times 10^{-7})T + (1.16 \times 10^{-3}) \quad (112)$$

where α and $\bar{\alpha}$ are in %/°C and T is in °C. The authors give no information about the metallurgical state of the test specimens, although they had stated earlier that both γ quenched and α soaked specimens had been used for Young's modulus measurements as a function of temperature. Therefore, it is reasonable to assume that they used γ quenched specimens for the thermal expansion measurements. It is unknown whether Eq. (110) represents data from only the heating portion of the temperature cycle or from an average of the heating and cooling portions.

A.5.2.5 Riddle (1958) [44]

At Oak Ridge National Laboratory (ORNL), Riddle measured the linear thermal expansion over a temperature range of 25–600°C of two γ quenched U–10Mo samples prepared from a single casting. The samples were annealed at 900°C for 24 h in vacuum and then water-quenched. Fig. 48 adapted from fig 19.18 of Ref. [44], shows the results obtained from an average of ten heating and cooling curves using the two samples. The data obtained by manual digitization of the three curves presented in the fig.19.18 are listed in Table 25.

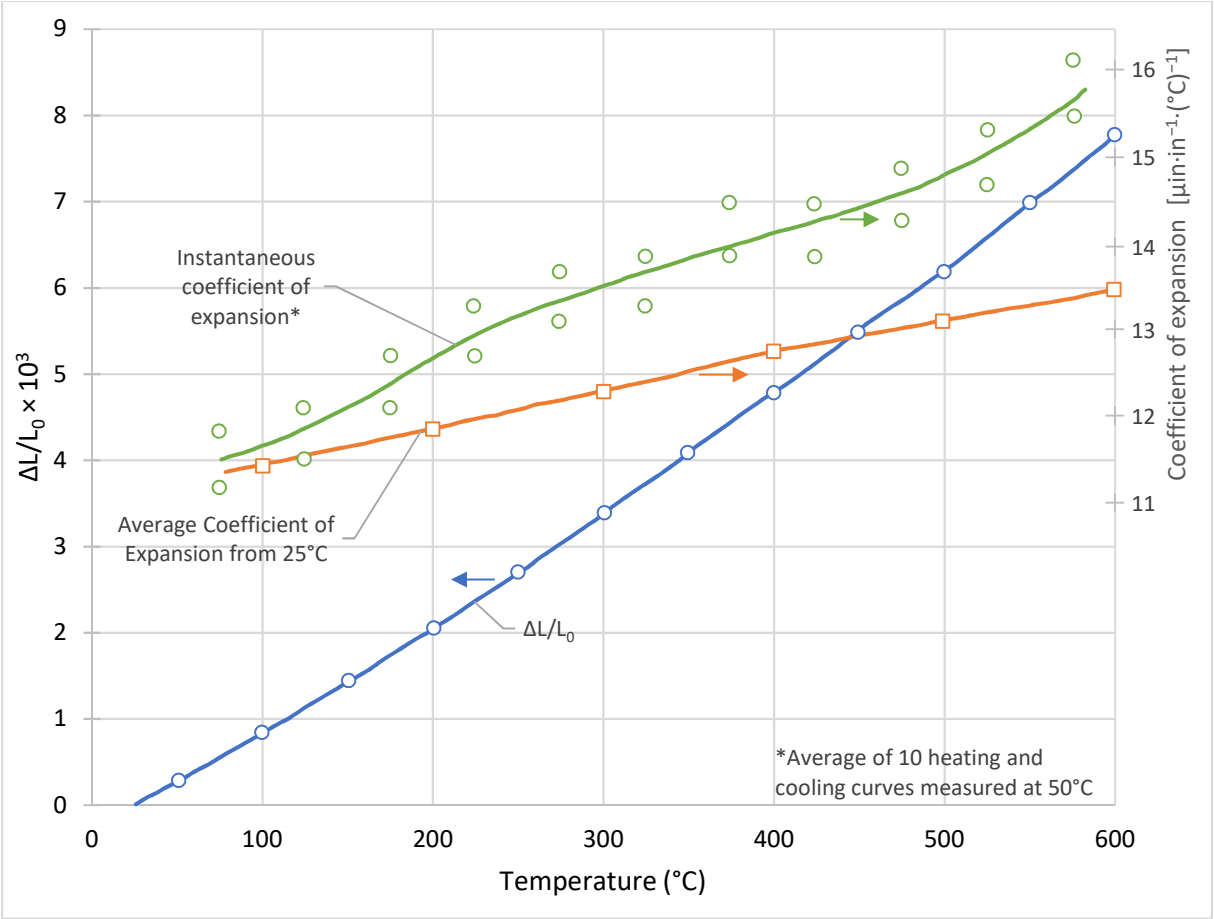

FIG. 48. Linear thermal expansion of a γ quenched U–10Mo casting (adapted from fig. 19.18 of Ref. [44]).

A quadratic least squares fit to Riddle's $\Delta L_T/L_{25}$ data leads to the following equations:

$$\Delta L_T/L_{25} = (4.051 \times 10^{-7})T^2 + (1.096 \times 10^{-3})T + (-2.83 \times 10^{-2}), \ (25 < T \leq 600°C) \quad (113)$$

$$\alpha(T) = (8.102 \times 10^{-7})T + (1.096 \times 10^{-3}) \quad (114)$$

$$\bar{\alpha}(25, T) = (4.051 \times 10^{-7})(T + 25) + (1.096 \times 10^{-3}) \quad (115)$$

where $\Delta L/L_0$ is in % and T is in ºC.

TABLE 25. LINEAR THERMAL EXPANSION DATA OF γ QUENCHED U–10Mo OBTAINED FROM RIDDLE'S FIGURE 19.18 (REF. [44])

	$\Delta L_T/L_{25}$ (%)		$\bar{\alpha}(25, T)$ (10^{-6}°C^{-1})		α (10^{-6}°C^{-1})	
T (°C)	Digitized from Fig . 19.18 of Ref. [44]	From $\Delta L_T/L_{25}$ fit per Eq. (113)	Digitized from fig 19.18 of Ref [44]	From $\Delta L_T/L_{25}$ fit per Eq. (115)	Digitized from Fig . 19.18 of Ref. [44]	From $\Delta L/_T L_{25}$ fit per Eq. (114)
25	0.000	-0.001	–	11.2	–	11.2
50	0.028	0.028	–	11.3	–	11.4
100	0.085	0.085	11.4	11.5	11.6	11.8
150	0.144	0.145	–	11.7	12.1	12.2
200	0.205	0.207	11.8	11.9	12.7	12.6
250	0.269	0.271	–	12.1	13.2	13.0
300	0.339	0.337	12.3	12.3	13.5	13.4
350	0.408	0.405	–	12.5	13.9	13.8
400	0.477	0.475	12.8	12.7	14.1	14.2
450	0.547	0.547	–	12.9	14.4	14.6
500	0.617	0.621	13.1	13.1	14.9	15.0
550	0.697	0.697	–	13.3	15.3	15.4
600	0.777	0.775	13.5	13.5	–	15.8

–: data not available.

As seen in Table 25, the values of $\Delta L_T/L_0$ calculated using Eq. (113) agree very well with the digitized data from Riddle's $\Delta L_T/L_0$ curve in Fig. 48, showing that his dilation curve was, indeed, quadratic. Because Riddle's α data points are plotted midway between his data points for $\Delta L_T/L_0$ and because two points are plotted at each temperature, it appears that Riddle analysed his data in a manner similar to that used by Del Grosso (see Section A.5.2.3); the two points would then represent the scatterband of the data. It is seen that the two coefficient curves shown in Riddle's plot deviate from the expected linear shape. It is recommended that Eqs (113)– (115) be used to represent Riddle's data.

Both Farkas [8] and Fackelmann [9] reported Riddle's $\bar{\alpha}$'s to be: 11.5, 11.75, 12.1, 12.7, 13.0, and 13.5 in units of 10^{-6}°C^{-1} at 100, 200, 300, 400, 500, and 600°C, respectively, in reasonable agreement with the digitized values listed in Table 25.

A.5.2.6 Burkes et al. (2010) [12, 13]

Burkes et al. measured the linear thermal expansion from 27 to 800°C of a 6.35-mm-dimeter as-cast sample of U–10.3Mo alloy produced for their thermal diffusivity and dilation measurements. The heating and cooling rate was 0.042°C/s (2.5°C/min). The Mo content of the casting was determined using inductively coupled plasma–mass spectrometry, and the average density of three samples cut from the first casting was determined using the Archimedes method to be 10.4 ± 0.1 g/cm^3. That the sample was not heat treated prior to the measurement is unique among all of the measurements reported above and suggests that the resulting data may not be directly comparable to data from the other thermal expansion studies of U–Mo discussed above.

Burkes et al. characterized the phase composition of their as-cast sample before and after the dilatometry experiment using X ray diffraction. The phase composition prior to thermal cycling in the dilatometer was 90.5 wt% γ, 2.8 wt% α, and 6. 8wt% γ'; after the dilatometer runs, the composition values had changed to 93.5, 1.1, and 4.9 wt%, respectively, indicating that some of the $\alpha + \gamma'$ material had transformed to γ. Insufficient information was available to assess whether the X ray diffraction results reflected the composition throughout the specimen or just the volume close to the surface of the specimen.

Typical heating and cooling traces of three consecutive runs on a dilatometry sample are shown in fig. 2 of Ref. [12]; an adaptation of this figure is shown below as Fig. 49. Table 26 lists values of $\Delta L_T/L_{27}$ obtained by manual digitization of these traces. using a photocopy of the figure from the referenced journal article. The three values of the heating dilations have been averaged at each temperature to represent the average response of the specimen during the three heating runs, and the same has been done for the cooling runs. The average dilations during heating and during cooling have been adjusted and normalized as will be discussed below. These dilations are also listed in Table 26.

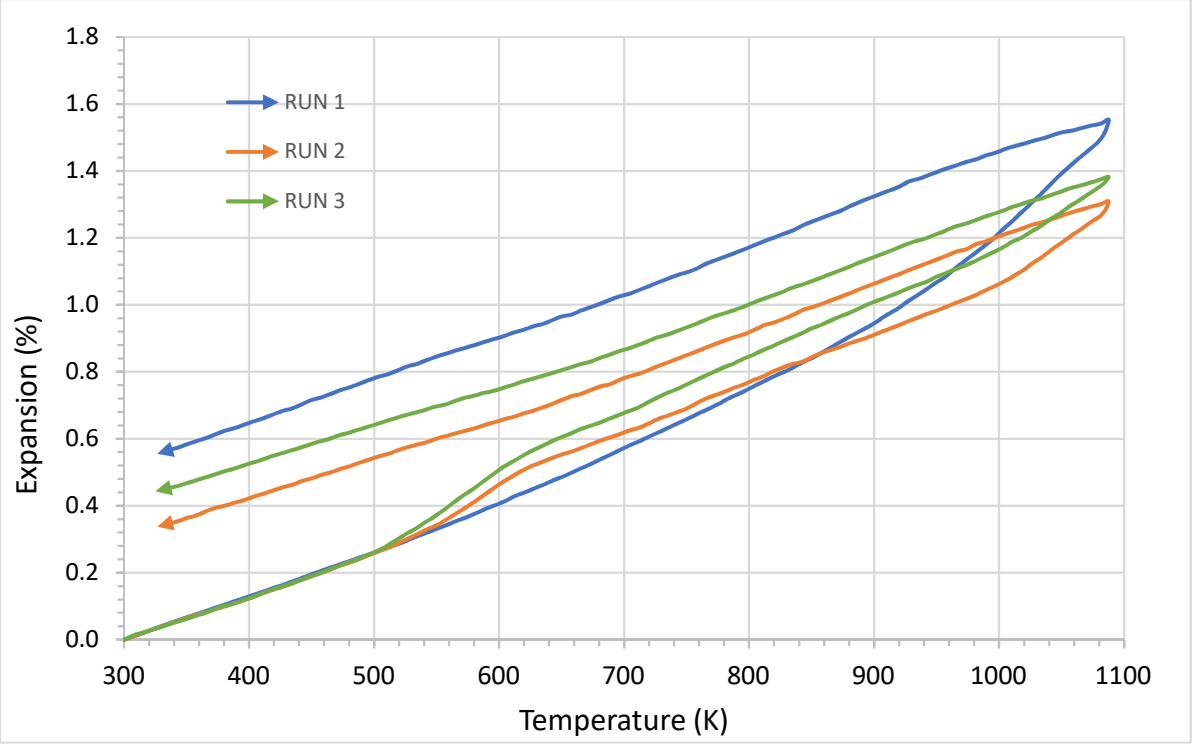

FIG. 49. Dilatometer traces from three heating–cooling cycles of as-cast U–10.3Mo (adapted from fig. 2 of Burkes et al. [12]).

TABLE 26. COMPARISON OF DILATIONS OF BURKES ET AL.'S AS-CAST U–10.3Mo SPECIMENS (DERIVED FROM THE INDIVIDUAL HEATING–COOLING CURVES SHOWN IN FIG. 2 OF REF. [12])

T (°C)	$\Delta L_T/L_{27}$ During Heating (%)					$\Delta L_T/L_{27}$ During Cooling (%)				
	Run 1	Run 2	Run 3	Av.	Norm.[a] Av.	Run 1	Run 2	Run 3	Av.	Norm.[a] Av.
27	0.000	0.000	0.000	0.000	0.000	0.515	0.301	0.381	0.399	0.367
50	0.032	0.032	0.032	0.032	0.025	0.546	0.330	0.438	0.438	0.406
100	0.092	0.092	0.092	0.092	0.085	0.613	0.394	0.495	0.501	0.469
150	0.159	0.159	0.159	0.159	0.152	0.676	0.448	0.552	0.559	0.527
200	0.222	0.222	0.222	0.222	0.215	0.746	0.511	0.610	0.622	0.590
250	0.292	0.292	0.302	0.295	0.288	0.806	0.565	0.667	0.679	0.647
300	0.362	0.394	0.438	0.398	0.391	0.870	0.622	0.721	0.738	0.706
330	0.413	0.470	0.514	0.466	0.459	0.908	0.657	0.752	0.772	0.741
350	0.441	0.514	0.559	0.505	0.498	0.930	0.679	0.775	0.795	0.763
400	0.524	0.584	0.638	0.582	0.575	0.990	0.743	0.832	0.855	0.823
450	0.610	0.648	0.711	0.656	0.649	1.057	0.841	0.895	0.931	0.899
500	0.695	0.733	0.800	0.743	0.736	1.130	0.883	0.959	0.990	0.959
550	0.794	0.800	0.883	0.825	0.818	1.200	0.952	1.035	1.062	1.030
600	0.889	0.876	0.959	0.908	0.901	1.276	1.022	1.098	1.132	1.100
650	1.003	0.943	1.044	0.997	0.990	1.359	1.098	1.181	1.213	1.181
700	1.130	1.016	1.117	1.088	1.081	1.422	1.168	1.238	1.276	1.244
750	1.295	1.111	1.213	1.206	1.199	1.483	1.232	1.305	1.340	1.308
800	1.467	1.244	1.333	1.348	1.341	1.533	1.295	1.365	1.393	1.361
815	1.549	1.308	1.378	1.412	1.380	1.549	1.308	1.378	1.412	1.380

[a] Corrected for time lag effect at 815°C and normalized as explained in the text.

The dilatometer traces shown in Fig. 49 are significantly different from those shown for γ quenched samples by Riddle in Ref. [44] or by Saller et al. in Ref. [42] Fig. 43. Consequently, the behaviour of the average coefficient of linear thermal expansion $\bar{\alpha}$ as a function of temperature is also quite different. In particular:

(a) The heating curves from runs 1, 2, and 3 for Burkes et al.'s as-cast sample exhibit a marked increase in slope beginning at ~600, ~730, and ~750°C, respectively, presumably as a result of the $\alpha + \gamma'$ to γ transition. Although the transition occurs at ~565°C, there is a time (temperature) lag before the effect is seen in the dilatometer trace. Recall that this phase transformation also is seen beginning at ~600°C in Saller et al.'s α soaked U–9.36Mo specimen, as shown in Fig. 43; however, in Burkes et al.'s specimen, the expansion occurs much more slowly and is still seen in runs 2 and 3. Apparently, the transformation in the much-more-complex metallurgical structure of the as-cast specimen occurs at a significantly slower rate than in a well-homogenized γ quenched specimen. The relatively large increase in the slope of the heating curve between 810 and 815°C, seen in each heating trace, likely indicates that there was a small temperature overrun and some lag time before the specimen began to cool. It will be assumed that this is the case, so the effect of the lag time, estimated to average ~0.025%, has been subtracted from the average dilation at 815°C during heating. Renormalization of the average dilation at the

start of cooling results in the dilation curve during cooling being lowered by 0.025% at each temperature.

(b) The slopes of the heating curves of runs 2 and 3 are noticeably larger over the temperature range of about 250 to 350°C than the slopes above and below this temperature range. It is interesting that the increase in $\Delta L/L_0$ over this temperature range is larger during run 3 than during run 2. Burkes et al. suggest the effect could result from better homogenization of the alloy during each thermal cycle; it is likely that relaxation of mechanical stresses is occurring.

(c) The shapes of the three cooling curves are very similar to each other, and the slope of the average cooling curve is significantly smaller than that of the average heating curve for temperatures above ~250°C. This coefficient, $\sim 1.3 \times 10^{-3}$ %/°C , is smaller than Saller et al.'s value for either α soaked or γ quenched U–9.36Mo cooled from 800 to 250°C, $\sim 1.7 \times 10^{-3}$ %/°C. One can see a change in the slope of the cooling curves between ~350 and 300°C, which is likely related to the phenomenon causing the slope change in the heating curves described in item (b) immediately above.

(d) The lower average coefficient for the cooling portion of the test cycle means that the hysteresis effect at the end of a cycle for the as-cast U–10.3Mo sample, averaging about 0.4% $\Delta L/L_0$, is much larger than that experienced by investigators using heat-treated samples; e.g. for Saller et al.'s U–9.36Mo, the hysteresis effect was about 0.09% $\Delta L/L_0$ for the α soaked specimens and about −0.04% $\Delta L/L_0$ for the γ quenched specimens.

The differences between the heating–cooling curves of Burkes et al.'s as-cast U–Mo and those of Saller et al.'s γ quenched U–Mo shows that the metallurgical state of U–Mo is important when considering thermal expansion effects. Also, one sees the importance of performing more than one thermal cycling run during a thermal expansion measurement if the metallurgical state of the sample might be complex.

The normalized average dilations for heating and for cooling derived from Fig. 49 are shown in Fig. 50, along with least squares fits to the heating and cooling data. Owing to the character of the curves, four quadratic equations each were used to fit the heating data and the cooling data:

$$\Delta L_T/L_{27}\ (\text{Heating}) = (7.194 \times 10^{-7})T^2 + (1.095 \times 10^{-3})T + (-3.09 \times 10^{-2}), \quad (27 \le T \le 250) \tag{116}$$

$$\Delta L_T/L_{27}\ (\text{Heating}) = (3.524 \times 10^{-7})T^2 + (1.900 \times 10^{-3})T + (-2.092 \times 10^{-1}), \quad (250 \le T \le 350) \tag{117}$$

$$\Delta L_T/L_{27}\ (\text{Heating}) = (4.384 \times 10^{-7})T^2 + (1.203 \times 10^{-3})T + (2.15 \times 10^{-2}), \quad (350 \le T \le 650) \tag{118}$$

$$\Delta L_T/L_{27}\ (\text{Heating}) = (4.427 \times 10^{-6})T^2 + (-4.098 \times 10^{-3})T + (1.782) \quad (650 \le T \le 800) \tag{119}$$

$$\Delta L_T/L_{27}\ (\text{Cooling}) = (-1.490 \times 10^{-7})T^2 + (1.253 \times 10^{-3})\text{T} + (3.495 \times 10^{-1}) \quad (27 \le T \le 250) \tag{120}$$

$$\Delta L_T/L_{27}\ (\text{Cooling}) = (-3.192 \times 10^{-7})T^2 + (1.348 \times 10^{-3})T + (3.363 \times 10^{-1}), \quad (250 \le T \le 350) \tag{121}$$

$$\Delta L_T/L_{27}\ (\text{Cooling}) = (4.485 \times 10^{-7})T^2 + (9.370\times 10^{-4})\,T + (3.861 \times 10^{-1}),$$
$$(350 \le T \le 650) \qquad (122)$$

$$\Delta L_T/L_{27}\ (\text{Cooling}) = (-8.453 \times 10^{-7})T^2 + (2.440 \times 10^{-3})T + (-4.42 \times 10^{-2}),$$
$$(650 \le T \le 800) \qquad (123)$$

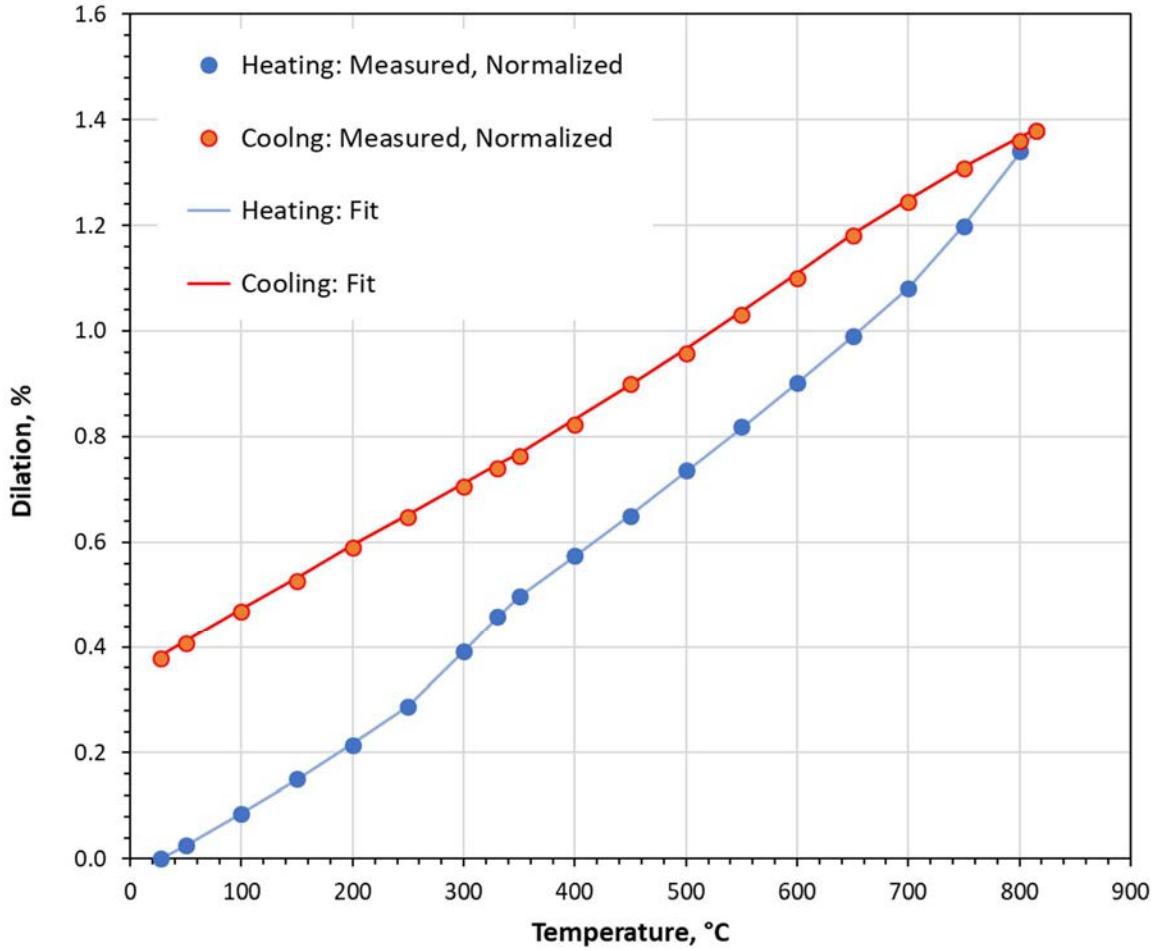

FIG. 50. Average dilations of U–10.3Mo during heating and cooling from Burkes et al.'s dilatometer traces shown in Fig. 49 (Ref. [12]); the results of piecewise quadratic least squares fits to the data points are also shown (courtesy of Argonne National Laboratory).

Burkes et al. state that the coefficient of thermal expansion data presented in table 2 of Ref. [13] represents the "instantaneous coefficient of linear thermal expansion" whose "value is obtained by evaluating the slope of displacement with respect to temperature over a given temperature range." Figure 2 of Ref. [13] shows data with the same designation, but the values of the coefficients are not the same as those in table 2, as can be seen in Table 27. Figure 4 of Ref. [12] presents data labelled the "average instantaneous coefficient of linear thermal expansion." It would seem, from the text from the temperature in the table and both figures being designated as (room temperature – measurement temperature), and from the coefficients of linear thermal expansion and from other data sources to which they are compared (Saller et al. Ref. [42] and Riddle (Ref. [44]), that Burkes et al. are presenting what is commonly defined

as the 'average coefficient of linear thermal expansion' over the various temperature ranges shown.[26]

TABLE 27. COEFFICIENTS OF LINEAR THERMAL EXPANSION FOR AND DENSITIES OF AS-CAST U–10.3Mo UPON HEATING PRESENTED BY BURKES ET AL. IN REFS [12, 13], WITH SOME CALCULATED DILATIONS

T (ºC)	Table 2, Ref. [13]	Fig. 2, Ref. [13]	Fig. 4, Ref. [12]	Fig. 5, Ref. [12]		Fig. 6, Ref. [12]		
	α *or* $\bar{\alpha}$ (10^{-6}ºC^{-1})	α *or* $\bar{\alpha}$ (10^{-6}ºC^{-1})	$\overline{\alpha}$ *or* $\overline{\alpha}$ (Heating) (10^{-6}ºC^{-1})	$\bar{\alpha}$ (10^{-6}ºC^{-1})	$\Delta L_T/L_{27}$ [a] (%)	ρ (g/cm^3)	$\Delta L_T/L_{27}$ [b] (%)	$\Delta L_T/L_{27}$ [c] (%)
27	–	–	–	10.2	0.000	16.42	0.000	0.000
50	–	–	–	10.8	0.025	16.41	0.025	0.025
100	11.8	11.8	11.8	11.6	0.085	16.38	0.085	0.085
150	–	–	–	12.0	0.147	16.35	0.154	0.155
200	12.6	12.4	12.5	12.4	0.214	16.32	0.215	0.215
250	–	–	–	13.1	0.293	16.28	0.295	0.296
300	14.1	13.7	14.1	14.3	0.391	16.23	0.399	0.400
350	–	–	–	15.4	0.498	16.18	0.507	0.509
400	16.1	15.3	16.1	15.4	0.576	16.14	0.581	0.585
450	–	–	–	15.4	0.653	16.10	0.659	0.664
500	16.4	15.6	16.4	15.5	0.734	16.06	0.741	0.747
550	–	–	–	15.6	0.818	16.02	0.823	0.830
600	16.6	15.8	16.6	15.7	0.901	15.99	0.902	0.910
650	–	–	–	15.9	0.989	15.94	0.995	1.005
700	16.7	16.7	16.7	16.1	1.082	15.90	1.081	1.093
750	–	–	–	16.5	1.196	15.85	1.203	1.217
800	17.2	17.2	17.1	17.4	1.344	15.78	1.345	1.363

[a] Calculated from the assumed $\bar{\alpha}$ (heating) using Eq. (56).
[b] Calculated from ρ_T/ρ_{27} using Eq. (68) and normalized to 0.0248% at 50ºC as discussed in the text.
[c] Calculated from ρ_T/ρ_{27} using Eq. (69) and normalized to 0.0248% at 50ºC as discussed in the text.
–: data not available.

In fig. 5 of Ref. [12], Burkes et al. present what they call "average engineering coefficients of linear thermal expansion" as a function of temperature, and in fig. 6 of Ref. [12] they present the density of U–10.3Mo as a function of temperature. Burkes et al.'s use of the unconventional term "average engineering coefficient of linear thermal expansion" may owe to the fact that the average coefficient of linear thermal expansion has been the coefficient of thermal expansion most used to calculate thermal expansion in engineering analyses.

The values of the coefficients plotted in figs 4 and 5 of Ref. [12] and the densities plotted in fig. 6 of Ref. [12] were determined by manual digitization. The densities determined from fig. 6 of Ref. [12] agree with those listed in table 3 of Ref. [13]. The dilation at each temperature was calculated from the density data both using the exact calculation of Eq. (69) and the approximation that $\rho_T/\rho_{27} \approx (1 + 3\Delta L_T/L_{27})^{-1}$ (see Eq. (69), and $\bar{\alpha}_l(27, T)$ was calculated using Eq. (56). The room temperature density was determined to be 16.42 g/cm^3 by minimizing the

[26]The conventional names and symbols for the two coefficients of thermal expansion are described in Section A.5.1 of this Appendix (see Eqs (56)–(59) and accompanying discussion).

sum of the squared differences between the values of the coefficients of linear thermal expansion determined from figs. 5 and 6 of Ref. [12]. These data are listed in .

It was found that if the average heating dilation data from Fig. 49 were normalized to the average value of the dilations at 50°C derived from Burkes et al.'s data plotted in figs 5 and 6 (0.025%), discussed above, and if the value at 27°C were set to zero, the dilation curves based on figs 2, 5, and 6 (using exact calculation) are identical within the uncertainties of the digitisations.[27] Therefore, it is reasonable to assume that the dilations used to calculate the data shown in figs. 5 and 6 came from the traces shown in fig. 2. Since Eq. (57) was used to convert the coefficients plotted in fig. 5 to dilations, Burkes et al.'s average engineering coefficient of linear thermal expansion is indeed the conventional average coefficient of thermal expansion also lists the dilations derived from Burkes et al.'s coefficients of linear thermal expansion from table 2 of Ref. [13], assuming that they are also average coefficients of linear thermal expansion.

The information shown in Table 26 indicates that coefficients of linear thermal expansion shown in table 2 of Ref. [13] agree with those for heating shown in fig. 4 of Ref. [12] but differ significantly from data shown in fig. 2 of Ref. [13] from ~400 to ~600ºC and those from fig. 5 of Ref. [12] from ~400°C to ~700°C. Either these are not average coefficients of linear thermal expansion, or they were derived from a different set of heating curves, or a mistake occurred while preparing the data for table 2 and fig. 2 of Ref. [13] and fig. 4 of Ref. [12]. Because only some of the data from table 2 and fig. 2 of Ref. [13] and fig. 4 of Ref. [12] appear to be inconsistent, a mistake during data preparation the most likely explanation.

In fig. 5 of Ref. [12], Burkes et al. also plot a curve representing coefficients from Klein [7]. As reported in Section A.5.2.3 of this Appendix, the data reported by Klein are the instantaneous coefficients of linear thermal expansion originally published by Del Grosso (Ref. [37]). They should not be compared to Burkes et al.'s average coefficients of linear thermal expansion. Nevertheless, one should be aware that the curve representing Klein's data is misplotted in fig. 5 of Ref. [12]. The portion of the curve from 323–1023 K should be shifted to 373–1073 K, and the linear portion of the curve below 373 K should be extended to 300 K.

A.5.3. Density as a function of temperature

As stated at the beginng of Section A.5, the change of density of an alloy when its temperature changes is a direct result of its change in volume owing to thermal expansion. Equations (69), (70), and (71) relate the change in density to the alloy's dimensional change under the influence of a temperature change. Because the maximum dilation of U–Mo alloys does not exceed 2% at 1000°C, the change in density from room temperature to 1000°C does not exceed 6%. Two of the sources of thermal expansion data also reported density change as a function of temperature.

Del Grosso reported the density of γ quenched U–10Mo as a function of temperature in fig. 3 of Ref. [37]. The data points are not tabulated, but the density from measurements involving two samples is shown in the figure as a linear function of temperature within a scatterband of approximately ±0.07 g/cm^3:

$$\rho^{\text{U–10Mo}}_{\text{Del Grosso}}(T) = 17.15 - 0.00088T, (30 < T \leq 650) \quad (124)$$

where ρ is in g/cm^3 and T is in °C. The density data reported by APDA in Ref. [38] (1959) is consistent with Eq. (124). Klein in table 3-39 of Ref. [7], Farkas in table 11 of Ref. [8], and

[27] The uncertainty in measuring the value of $\Delta L_T/L_{27}$ is at least ±0.006% absolute (±1 pixel), so adjusting the value at 27°C from −0.007% to zero is quite reasonable.

Fackelmann in table A-7 of Ref. [9] reported the APDA density data; Klein cited a personal communication (undated), while Farkas and Fackelmann et al. cited Ref. [38] directly. Fackelmann et al. reported a density for 700°C, which is not listed in Ref. [38] but is consistent with Eq. (124). Beghi also reported Del Grosso's densities in table 3 of Ref. [2], citing Klein as his source. If the average dilations for heating and cooling derived during this work and discussed in Section A.5.1 were to be used to calculate density change, the results would still be within the scatterband stated above, although the shape of the density vs. temperature curve would be quadratic rather than linear. The equation based on the newly derived Del Grosso dilation upon heating and a room temperature density of 17.13 g/cm^3 for Del Grosso's nominally U–10Mo is

$$\rho^{\mathrm{U10Mo}}_{\mathrm{Del\ Grosso}}(T) = 17.15 - (5.7 \times 10^{-4})T - (2.6 \times 10^{-7})T^2, (30 < \mathrm{T} \leq 900°\mathrm{C}) \qquad (125)$$

where ρ is in g/cm^3 and T is in °C. The densities calculated using an average of the heating and cooling dilations are virtually unchanged from those calculated using Eq. (125).

Burkes et al.'s density vs. temperature data were discussed previously in section 4.5.2.6, where their densities, obtained by manual digitization of fig. 6 of Ref. [12], were shown in Table 3 of Burkes et al. [13] lists densities at 100°C intervals from 100–700°C that agree with the densities in fig. 6 at those temperatures. Burkes et al. compare their densities in table 3 [13] with densities from Klein [7] and Bridge [107], although their reference to Bridge should have been to Fackelmann [9].[28] Since both Klein's and Fackelmann et al.'s densities originated with Del Grosso [37], they cannot be treated as independent datasets.

Least squares fits of these data produced the following equations:

$$\rho^{\mathrm{U-10Mo}}_{\mathrm{Burkes}}(T) = 16.45 - 0.00082T, (27 < T \leq 800) \qquad (126)$$

$$\rho^{\mathrm{U-10Mo}}_{\mathrm{Burkes}}(T) = 16.45 - 0.00067T - 0.00000018T^2, (27 < \mathrm{T} \leq 800) \qquad (127)$$

Comparing Del Grosso's and Burkes et al.'s density vs. temperature curves for, respectively, γ quenched and as-cast U–10 Mo, one sees that the curves are similarly shaped but that as-cast material is significantly less dense ($\rho^{\mathrm{U-10Mo}}_{\mathrm{theor}} \approx 17.3$ g/cm^3).

A.6. HEAT CAPACITY

The heat capacity (C) of a material is the ratio of the amount of heat (Q) added to a specimen of the material to the temperature change of the specimen: $C = Q/\Delta T$. The subscript 'P' is added to C if the material is at constant pressure while the heat is being added. In terms of thermodynamic variables, for a material at constant pressure, a change in the enthalpy (dH) of a material is equal to the amount of heat added (δQ) and is related to a change of temperature (dT) of the material by the equation $\mathrm{d}H(T) = C_P(T)\mathrm{d}T$, so $C_P = \mathrm{d}H/\mathrm{d}T$. One cannot measure the enthalpy of a material at a given temperature, only the change of enthalpy between two temperatures; usually, enthalpy changes are given with respect to the enthalpy at 298.15 K (25°C). The specific heat capacity (c), usually shortened to specific heat, is the heat capacity per unit mass of the material, and specific enthalpy (h) is defined in the same manner; when the unit of mass is a mole of the material, one has the molar heat capacity and molar enthalpy. It

[28] A mistake was found in Fackelmann et al.'s table A-7, where the reference numbers listed for Bridge et al [107] and for APDA-124 (Ref. [38]) were interchanged. Burkes et al., in copying Fackelmann et al. [9], also copied Fackelmann et al.'s wrong citation.

appears to be common practice, at least in the literature of alloy fuels, to use the terms 'heat capacity' and 'enthalpy,' along with the uppercase symbols, to denote the specific or molar heat capacity and enthalpy, so the units should be considered to know which quantities are being discussed. For consistency, this common practice is followed in this work.

Defining $H_T \equiv H(T)$ and $H_{T_0} \equiv H(T_0)$, and using a polynomial of degree three or less for the difference in H between T_0 and T, one obtains

$$H_T - H_{T_0} = b_3 T^3 + b_2 T^2 + b_1 T + b_0 \tag{128}$$

$$C_P(T) = 3b_3 T^2 + 2b_2 T + b_1 \tag{129}$$

where the b's are constants, H is in J/kg, J/g, or J/mol, C is in $J \cdot kg^{-1} \cdot K^{-1}$, $J \cdot g^{-1} \cdot K^{-1}$, or $J \cdot mol^{-1} \cdot K^{-1}$, respectively, and T can be in either K or °C. Eqs (128) and (129) are useful when trying to fit measured enthalpy-change data to a polynomial in T. If, instead, the heat capacity has been measured, one can fit those data to a polynomial in T and integrate the polynomial between T_0 and T to determine $H_T - H_{T_0}$:

$$C_P(T) = c_2 T^2 + c_1 T + c_0 \tag{130}$$

$$H_T - H_{T_0} = \frac{c_2}{3}(T^3 - T_0^3) + \frac{c_1}{2}(T^2 - T_0^2) + c_0(T - T_0) \tag{131}$$

where the c's are constants. In the absence of an exothermic or endothermic process during heating or cooling, such as a phase change, b_3 and c_2 are typically zero for U–Mo alloys.

The specific heat is used to determine the heat capacity of a material by integrating the specific heat with respect to the temperature. If a functional form is available for the specific heat, the integration is easily accomplished analytically; if the data are available only in tabular form, numerical integration is required.

Through 2010, the heat capacities of U–Mo alloys as a function of temperature have been measured by four groups of investigators: Farkas and Eldridge [45] in 1968, Matsui et al. [46] in 1989, Parida et al. [47] in 2001, and Burkes et al. [12] in 2010. The first three references include lengthy tables listing either measured U–Mo heat contents or C_P's derived from measured heat contents vs. temperature; because these articles were published in readily accessible journals, the tables will not be reproduced here. Three of the articles included a least squares fit to the heat content data, either a polynomial or a polynomial plus a $1/T$ term. For the purposes of this work, these data have been refit using only a polynomial, which works well even when a $1/T$ term was originally used. These four sources are discussed in chronological order.

A.6.1. Farkas and Eldridge (1968) [45]

Farkas and Eldridge used a U–9.9Mo[29] alloy that had been homogenized in a vacuum at 1000°C for 48 h, hot rolled in a helium furnace at 1000°C, and water quenched; therefore, it is reasonable to assume that specimens initially were in the metastable γ phase. Heat content measurements were made in an ice calorimeter over a temperature range of 0–1001°C. Measurement error was estimated to be no more than ±1%.

Farkas and Eldridge's table I contains heat capacity in cal/g vs. temperature in °C, with $H(0) = 0$. The heat capacity values were converted to J/g, normalized to zero at 25°C, and least

[29]U–9.9Mo produced using natural or depleted uranium contains 21.4 at.% Mo and has a molar mass of 207.6 g.

squares fitted using Eq. (128) with the constraint $H(25) = 0$. The fit, shown with the data in Fig. 51, resulted in the following equation:

$$H_T - H_{25} = \Delta H_T = (3.64 \times 10^{-5})T^2 + 0.135T - 3.40, (25 < T < 1001) \quad (132)$$

where H is in J/g and T is in °C. The fit value of the heat capacity at 1001°C is 168.2 J/g compared to the 166.8 J/g normalized measurement value. The heat capacity fit in Eq. (130) is slightly better than the fit given in Ref. [45]. The heat capacity is given by the equation:

$$C_P = \left(7.28 \times 10^{-5}\right)T + 0.135 \quad (133)$$

where C_P is in $J \cdot g^{-1} \cdot °C^{-1}$ and T is in °C.

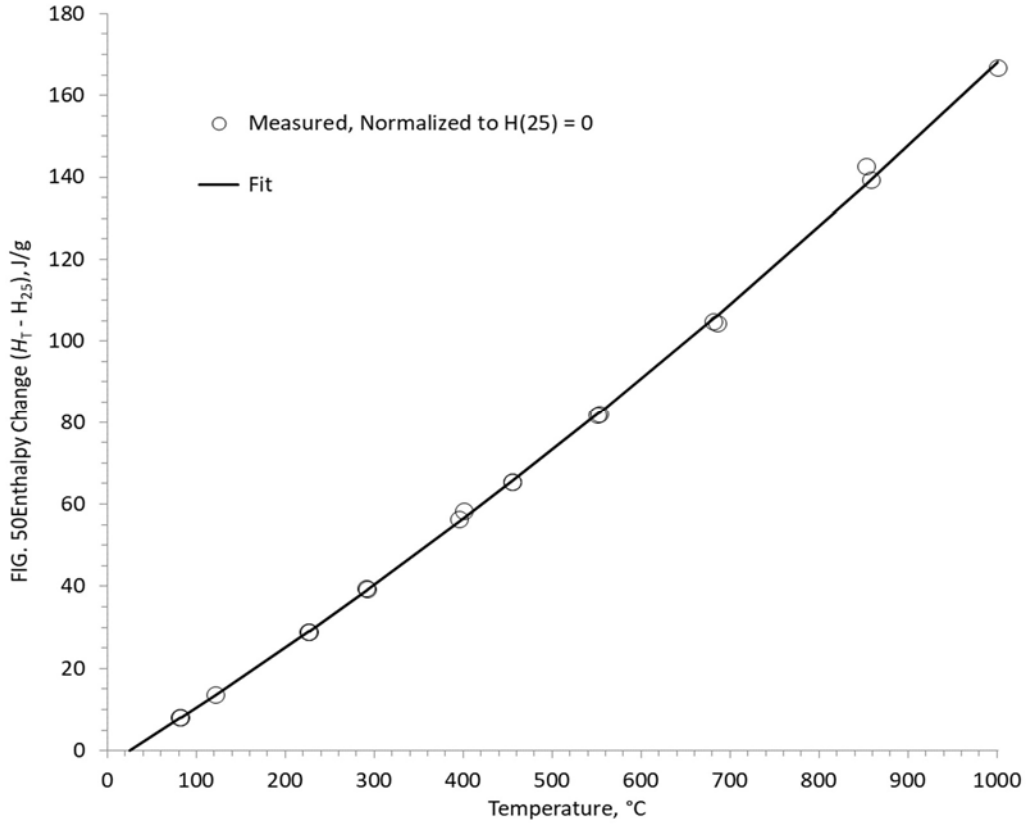

FIG. 51. Normalized heat capacity of U–9.9Mo vs. temperature measured by Farkas and Eldridge [45], shown with the quadratic least squares fit shown in Eq. (130) (courtesy of Argonne National Laboratory).

A.6.2. Matsui et al. (1989) [46]

Matsui et al. directly measured the specific heat capacity of a U–Mo alloy with 20 at.% Mo (U–9.15Mo)[30] at temperatures up to 877°C using a direct heating pulse calorimeter. Prior to measurement, the U–Mo specimens were annealed for three days at 500°C and then

[30]U–9.15Mo produced using natural or depleted uranium has a molar mass of 209.6 g.

cooled to room temperature over a one-day period; therefore, they would have contained a considerable amount of the α and γ' phases.

Matsui et al.'s data from their table 3, in cal · mol^{-1} · K^{-1}, have been converted to J · g^{-1} · K^{-1} and are shown in Fig. 52. They give no information about the accuracy of the data, but it is reported with four significant digits. The data indicates the presence of two phase transitions, which Matsui et al. attribute to the transformation of $\alpha + \gamma'$ to $\alpha + \gamma$ at 560°C followed by $\alpha + \gamma$ to γ at 574°C. They calculate the enthalpy change during the combined phase transitions to be 2.62 J/g. Owing to the effect of the phase transitions, Matsui et al.'s data have a much more complicated shape than the linear curve derived for the essentially γ quenched specimens used by Farkas and Eldridge, where little if any phase transition would have occurred. The shape of the data between ~325 and ~700°C indicates that one or more endothermic processes are occurring up to ~575°C (when an endothermic process occurs, more heat is needed to raise the temperature of the alloy, so C_P will be larger; the opposite will occur for an exothermic process). A five-part piecewise continuous function (within the limit of data uncertainty) has been least squares fitted to Matsui's data, using Eq. (130) for each piece (solid line in Fig. 52), to obtain the following equations:

$$C_{P1} = (4.643 \times 10^{-5})T + 0.1127, (16.83 \leq T \leq 333.0) \quad (134)$$

$$C_{P2} = (2.485 \times 10^{-7})T^2 + (-8.257 \times 10^{-5})T + 0.1281, (333.0 < T \leq 579.3) \quad (135)$$

$$C_{P3} = (-6.990 \times 10^{-4})T + 0.5686, (579.3 < T \leq 601.0) \quad (136)$$

$$C_{P4} = (1.543 \times 10^{-6})T^2 + (-2.092 \times 10^{-3})T + 0.8484, (601.0 < T \leq 697.4) \quad (137)$$

$$C_{P5} = (1.109 \times 10^{-4})T + 0.06256, (697.4 < T \leq 876.84) \quad (138)$$

where H is in J/g, C_P is in J · g^{-1} · K^{-1}, T is in °C. The fit represented by Eq. (136) excluded the second data point below the peak, at ~587°C, to lessen the mismatch between the slopes of C_{P3} and C_{P4} at their intersection.

Parida et al. [47] also published a piecewise discontinuous fit to Matsui et al.'s data, which is also shown in Fig. 52. A quadratic fit of all the data below 560°C reproduces Parida et al.'s fit; their linear fit from 606–877°C is similar to a fit of the high temperature data beginning at 606°C. The fit represented by Eqs (134)– (138) for temperatures within the stated ranges is recommended.

The heat capacities derived by integrating Eqs (134)–(138) agree within 0.3% with those derived by numerical integration of Matsui et al.'s C_P data, except at the temperatures 101.56 and 102.51°C, where the fit value is 0.8% higher than those from numerical integration. At temperatures over ~480°C, the fit values are only 0.1% lower than those from numerical integration. The heat capacity at 877°C obtained by integration of the C_P fit is 116.5 J/g.

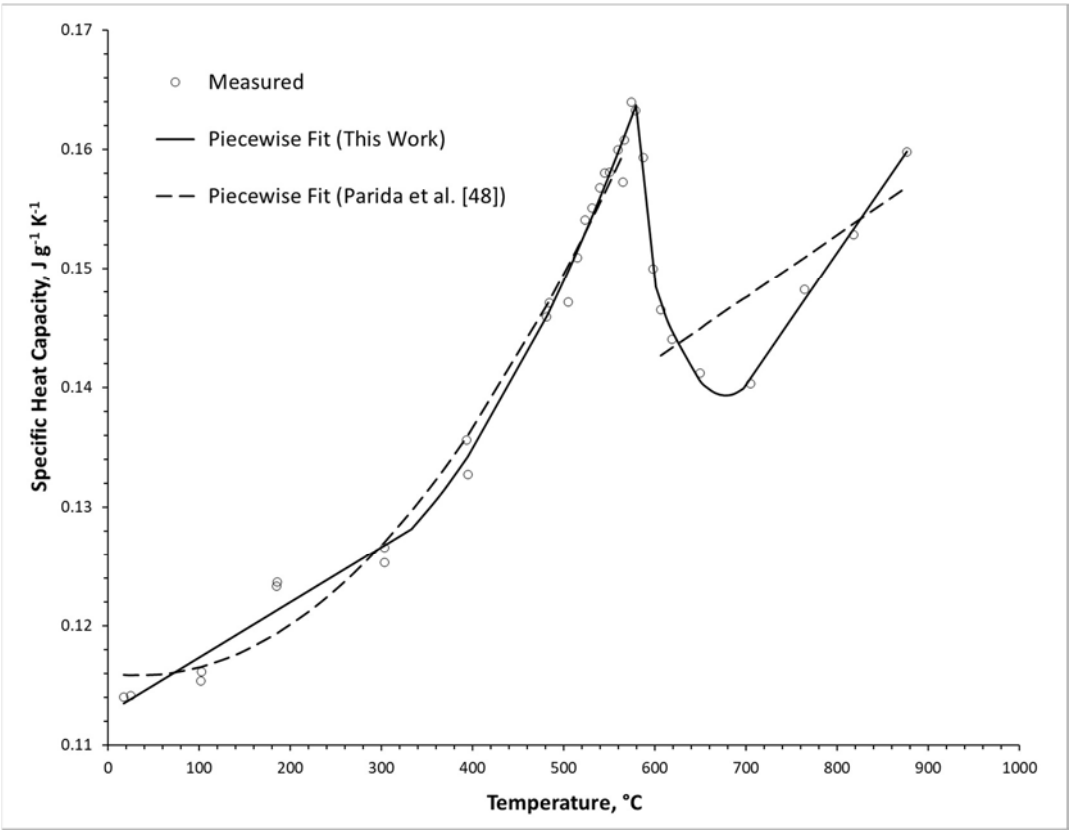

FIG. 52. Specific heat capacity vs. temperature data of Matsui et al. [46], shown with fits from Parida et al. [47] and from this work (courtesy of Argonne National Laboratory).

A.6.3. Parida et al (2001). [47]

Parida et al. measured the heat capacity (in J/mol) vs. temperature of a U–Mo alloy with 17.7at.% (U–7.98Mo)[31] at temperatures up to 547°C using a Calvet calorimeter. The specimens were cut from arc-melted buttons that had been annealed at 950 degrees for 120 h and water-quenched. That the quenched samples contained predominantly γ phase, with a small amount of α' phase, material was confirmed by X ray diffraction and optical metallography. They analysed their data using the constraints that $H(25°C) = 0$ and $C_P(25°C) = 24.83$ J/mol. Parida et al. presented their data, estimated uncertainty, and fit value for each temperature in their table 1. The estimated uncertainties averaged ±1.8% between ~45 and 430°C and ranged up to 9% at 25°C and up to 7.5% at 500°C or above.

Although Parida et al. present fit equations with $1/T$ and $1/T^2$ terms for $H_T - H_{25}$ and $C_P(T)$, respectively, a quadratic function of T has been used in this work to fit Parida et al.'s data. A least squares fit of a quadratic function constrained to equal zero at 25°C gave a reasonable fit for their enthalpy change data; however, an unconstrained fit followed by normalization of the function to zero at 25°C gave a much better fit, yielding the following equations for ΔH and C_P:

$$H_T - H_{25} = (1.983\times 10^{-5})T^2 + 0.1171T - 2.940 \quad (25 < T < 547) \tag{139}$$

[31]U–7.98Mo produced using natural or depleted uranium has a molar mass of 212.9 g.

$$C_P = (3.966 \times 10^{-5})T + 0.1171 \quad (140)$$

where H is in J/g, C_P is in J · g^{-1} · K^{-1}, T is in °C. The ΔH data and the quadratic fit are shown in Fig. 53. Parida et al. published the values of their fit alongside their ΔH data, their fit equation, eq. 3 of Ref. [47] did not produce the published values, although the differences were small (<0.2% low, above 500°C) but not random. Although Parida et al.'s fit is somewhat better overall than the present fit, both fits produce results that are well within Parida et al.'s stated uncertainties.

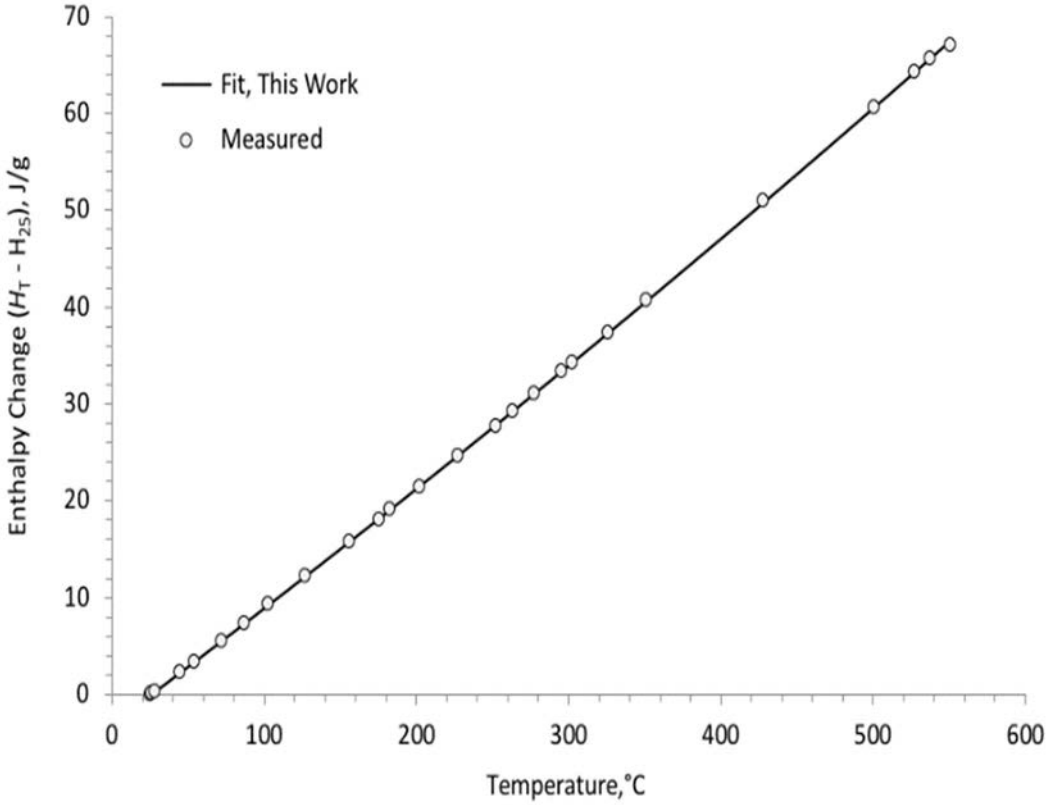

FIG. 53. Heat capacity vs. temperature data of Parida et al. [47], shown with fit discussed above (courtesy of Argonne National Laboratory).

A.6.4. Burkes et al. (2010) [12, 13]

Burkes et al. measured the specific heat capacity (in J · g^{-1} · K^{-1}) vs. temperature of a U–10.4Mo alloy (±5% uncertainty in Mo content) at temperatures up to 800°C using a differential scanning calorimeter. The specimen was punched from a foil which had been rolled from an arc-melted casting at 650°C and then annealed for 2 h at 650°C. The specimen was determined by X ray diffraction measurements to consist of 98.1% γ phase material at the beginning of the experiment. The specimen went through three complete cycles in the calorimeter at heating–cooling rates of 0.167 K/s (600 K/h). No phase changes were evident in the calorimeter traces, and a commercial software package was used to determine the specific heat data from the traces.

Burkes et al. reported their specific heat data at 50°C intervals in fig. 3 of Ref. [12] and at 100°C intervals in table 1 of Ref. [13]. Manual digitization was used to determine the values of the data points in fig. 3 of Ref. [12]; Burkes et al.'s data are listed in Table 28. The specific heat data from Refs [12] and [13] agree extremely well, only differing by 0.001 $J \cdot g^{-1} \cdot K^{-1}$ at 200 and 800°C. Given this good agreement, the values derived from Ref. [12] have been used, because these data were available at 50°C, rather than at 100°C, intervals

The shape of Burkes et al.'s specific heat capacity data resembles that of Matsui et al.'s data shown in Fig. 52, thereby suggesting the possibility of using a piecewise fit. The measured data and a five-part piecewise continuous fit are shown in Fig. 54. The equations of the fit are:

$$C_{P1} = (2.171 \times 10^{-5})T + 0.1408, (25 \leq T \leq 360) \quad (141)$$

$$C_{P2} = (1.60 \times 10^{-4})T + 0.091, (360 < T \leq 452) \quad (142)$$

$$C_{P3} = (2.00 \times 10^{-5})T + 0.1543, (452 < T \leq 555) \quad (143)$$

$$C_{P4} = (-8.00 \times 10^{-7})T^2 + (9.60 \times 10^{-4})T - 0.121, (555 < T \leq 649) \quad (144)$$

$$C_{P5} = (9.40 \times 10^{-5})T + 0.1041, (649 < T \leq 800) \quad (145)$$

where C_P is in $J \cdot g^{-1} \cdot K^{-1}$, T is in °C. The C_P values obtained from Eqs (141)–(145) and the ΔH values obtained by integrating them over the indicated temperature intervals are shown in Table 28.

TABLE 28. SPECIFIC HEAT DATA OF BURKES ET AL. FROM FIG. 3 OF REF. [12] AND TABLE 1 OF REF. [13]

T (°C)	C_P, ($J \cdot g^{-1} \cdot K^{-1}$)				$H(T) - H(25)$ (J/g)
	Ref. [12]	Ref. [13]	Combined	Fit	From C_P Fit
25	–	–	–	0.141	0.0
50	0.146	–	0.146	0.142	3.5
100	0.143	0.143	0.143	0.143	10.7
150	0.144	–	0.144	0.144	17.8
200	0.145	0.144	0.144	0.145	25.1
250	0.146	–	0.146	0.146	32.4
300	0.148	0.148	0.148	0.147	39.7
350	0.148	–	0.148	0.148	47.1
400	0.154	0.155	0.155	0.155	54.7
450	0.163	–	0.163	0.163	62.6
500	0.164	0.165	0.165	0.164	70.8
550	0.165	–	0.165	0.165	79.0
600	0.167	0.167	0.167	0.167	87.3
650	0.165	–	0.165	0.165	95.6
700	0.170	0.170	0.170	0.170	103.9
750	0.175	–	0.175	0.175	112.6
800	0.180	0.179	0.179	0.179	121.4

–: data not available

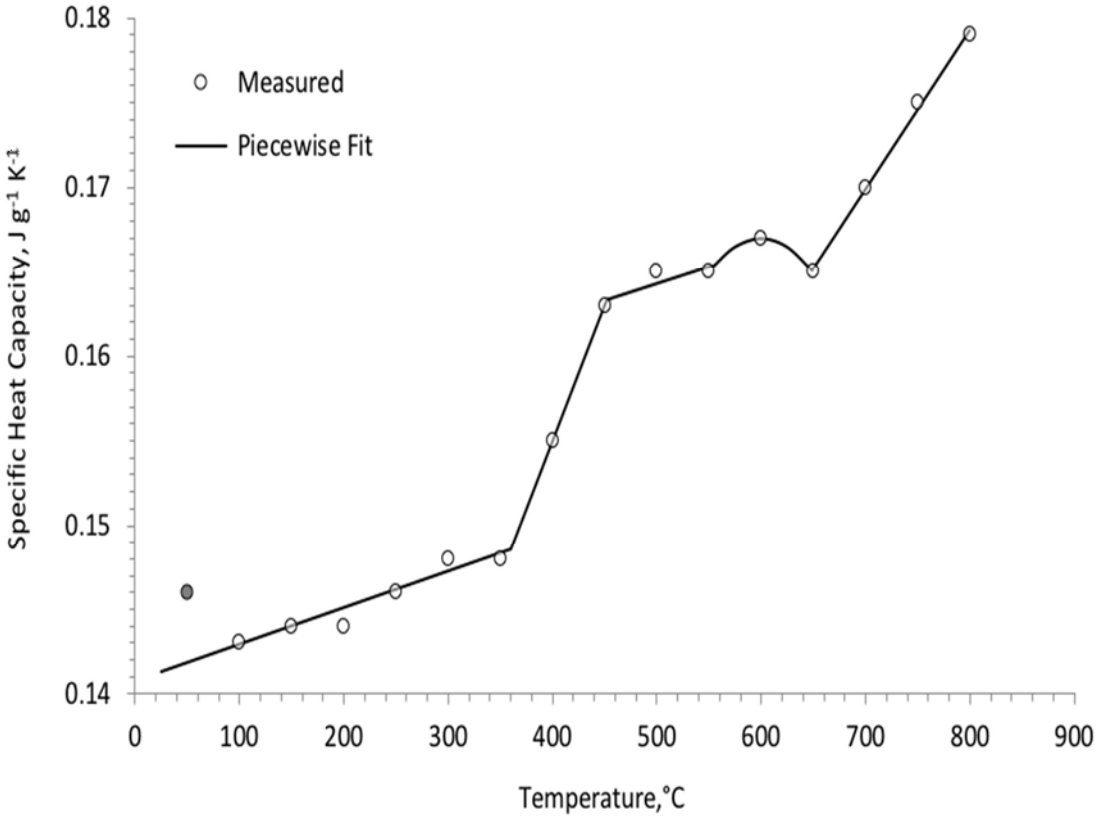

FIG. 54. Specific heat capacity measured as a function of temperature by Burkes, et al. [12, 13]. The solid data point was excluded from the analysis (courtesy of Argonne National Laboratory).

In the fit of Matsui et al.'s C_P data given by Eqs (134)–(138), the pieces of the fit intersect at 333, 579, 601, and 697°C; the intersections for the fit to Burkes et al.'s data are at 360, 452, 555, and 649°C. Also, in Fig. 49 it was seen that the thermal expansion curves from an as-cast specimen having a similar phase composition to that of that of the present sample showed enhanced thermal expansion beginning at ~275°C and ending at ~350°C for the second and third heating–cooling cycles. Therefore, an increase of C_P near 360°C might be triggered by an associated phenomenon. Matsui et al.'s specimen likely contained much more α phase material, and the increase in C_P was much larger than was seen in Burkes et al.'s experiment. Matsui et al. also saw evidence of two endothermic phase changes in the range of ~550–575°C, the effect of which continued to ~600°C. This same phenomenon could account for the broad peak in Burkes et al.'s data between 555 and 649°C; of course, the peak was likely much sharper. The linear portions at the beginning of each of the fits seem to be representative of U–Mo behaviour at temperatures so low that any phase or other changes would be extremely sluggish; at the ends of the fits the linear portion of the curve appears to be representative of γ phase U–Mo alloys. The relatively flat linear portion of the fit of Burkes et al.'s data would indicate the absence of changes in the specimen over that temperature range. Farkas and Eldridge and Parida et al. used specimens that had been γ quenched, and no evidence of any phase or other change was seen in their C_P data.

A.7. THERMAL CONDUCTIVITY

The thermal conductivity data as a function of temperature, $k(T)$ found in the literature of U–Mo alloy properties through 2011 appear to have originated from seven sources, covering a range of molybdenum content from 5.4–14.2 wt% (12.4–29 at.%). These sources are discussed below in order of publication date. All temperatures have been converted to degrees Celsius and thermal conductivities to watts per meter-kelvin.

A.7.1. Sources of thermal conductivity data in the literature

A.7.1.1 Westphal (1954) [48]

Westphal's publication originated as a letter to the US Atomic Energy Commission reporting the results of a search of the available literature on thermal conductivity of reactor fuel element materials. The thermal conductivity at 50°C at 14.3 $W \cdot m^{-1} \cdot K^{-1}$ for U–8Mo and 13.8$W \cdot m^{-1} \cdot K^{-1}$ for U–12Mo was obtained from Ref. [48], but no information about the metallurgical state of the specimens was provided. These data were subsequently published by McGeary [4] and Rest et al. [11], who cited McGeary. Westphal's data are shown in Fig. 56, along with data for some of the other alloys discussed below.

A.7.1.2 Del Grosso (1957) [37]

Del Grosso reported results of thermal conductivity measurements on nominal U–10Mo performed by BMI for APDA in fig. 1 of Ref. [37]; recall that APDA's thermal expansion and density change data as a function of temperature were also reported in Ref. [37]. No information was given on the metallurgical state of the specimen, although it is likely to have been γ quenched because fuel for a specific reactor was being developed. The figure shows only a (presumed) k vs. T fit, without data points, on a sheet of 10 x 10 per centimetre graph paper, so the values of k could be read directly from the curve to three-digit accuracy. These data, converted to SI units, cover a range of 20–820°C and are listed in Table 29. The table also show the results of quadratic and linear least squares fits of Del Grosso's $k(T)$ curve. A quadratic least squares fit of Del Grosso's data vs. temperature essentially reproduces the plotted curve:

$$k(T) = (8.60 \times 10^{-6})T^2 + 0.0258T + 11.60, (20 \leq T < 820) \quad (146)$$

A linear least squares fit gives the following equation:

$$k(T) = 0.0328T + 10.76, (20 \leq T < 820) \quad (147)$$

where $k(T)$ is $W \cdot m^{-1} \cdot K^{-1}$ and T is in °C. The quadratic fit is recommended.

TABLE 29. THERMAL CONDUCTIVITY VS. TEMPERATURE DATA FROM DEL GROSSO [37], AND VARIOUS FITS OF THAT DATA

T (°C)	k ($W \cdot m^{-1} \cdot K^{-1}$)			
	Fit line (Del Grosso)	Quadratic Fit (This Work)	Linear Fit (This Work)	Linear Fit (APDA)[a]
20	12.1	12.1	11.4	11.5
25	12.2	12.3	11.6	11.7
50	13.0	12.9	12.4	12.5
100	14.4	14.3	14.0	14.2
150	15.7	15.7	15.7	15.8
200	17.1	17.1	17.3	17.5
250	18.5	18.6	19.0	19.1
300	20.1	20.1	20.6	20.8
350	21.6	21.7	22.2	22.4
400	23.2	23.3	23.9	24.1
450	24.9	25.0	25.5	25.7
500	26.7	26.7	27.2	27.4
550	28.4	28.4	28.8	29.0
600	30.3	30.2	30.4	30.7
650	32.0	32.0	32.1	32.3
700	33.9	33.9	33.7	34.0
750	35.8	35.8	35.4	35.6
800	37.7	37.7	37.0	37.3
820	38.4	38.5	37.7	37.9

[a] data from fig. 133 of Ref. [38].

Del Grosso's thermal conductivity data have appeared in many subsequent publications, as shown in Fig. 55 and in Table 30, although only one of these authors directly cited him.

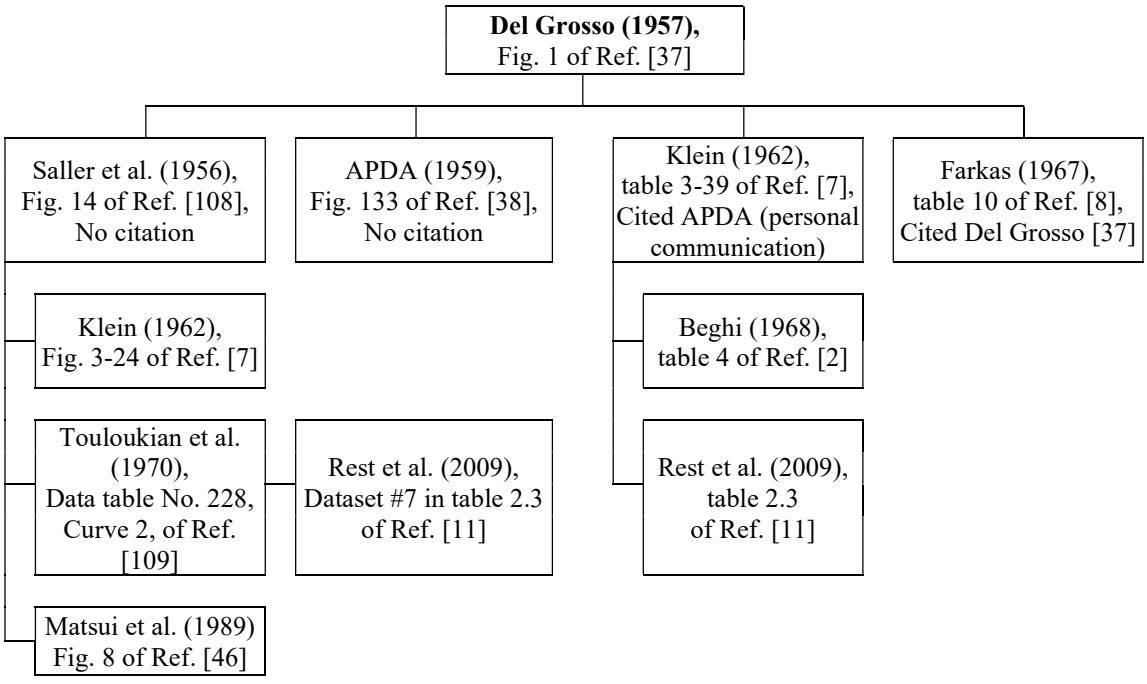

FIG. 55. Authors citing APDA or Del Grosso [37] as the source of their U–Mo alloy thermal conductivity data (courtesy of Argonne National Laboratory).

TABLE 30. DEL GROSSO'S U–10Mo THERMAL CONDUCTIVITY DATA FROM REF. [37] AS REPORTED BY OTHER AUTHORS

T (°C)	k ($W \cdot m^{-1} \cdot K^{-1}$)									
	Del Grosso [37]	Saller [108]	Klein [7][a]	Touloukian [109]	Rest [11]	Matsui [46]	APDA-124 [38]	Klein [7][b]	Rest [11][c]	Farkas [8]
20	12.1	12.0	11.8	12.1	12.1	12.2	–	–	–	12
25	12.2	–	11.9	–	–	–	11.5	12.1	12.1	–
100	14.4	13.8	14.4	13.8	13.8	13.9	11.7	14.4	14.2	–
200	17.1	17.3	17.6	17.3	17.3	17.4	14.2	17.1	17.2	17
300	20.1	20.1	20.8	20.1	20.1	20.2	17.5	20.1	20.1	–
400	23.2	23.3	24.1	23.3	23.3	23.3	20.8	23.2	23.0	23
500	26.7	27.3	27.3	27.2	27.2	27.2	24.1	26.7	26.4	–
550	28.4	–	28.9	–	–	–	27.4	28.4		–
600	30.3	30.2	30.5	30.1	30.1	30.0	29.0	30.3	30.1	30
700	33.9	33.7	33.8	33.5	–	33.5	30.7	33.9	33.9	–
800	37.6	37.5	37.0	37.5	–	37.5	34.0	37.7	37.7	38

[a] From fig. 3–24 of Ref. [7].

[b] From table 3–39 of Ref. [7].

[c] Cited Klein [7].

–: data not available.

Several comments about these various copies of Del Grosso's data are needed:

(a) Saller et al. provided no citation, but Saller was a senior staff member at BMI and may well have led the group that did the measurements under contract to APDA, which would also explain why he had access to the data before Del Grosso published it.
  (i) Klein (1962), fig. 3-24 of Ref. [7], cited Saller et al;
  (ii) Touloukian (1970), data table No. 228, curve 2, of Ref. [109], cited Saller et al;
  — Rest et al. (2009), seventh data group in table 2.3 of Ref. [11], cited Touloukian.
  (iii) Matsui (1989), fig. 8 of Ref. [46], cited Saller et al.

(b) APDA (1959), fig. 133 of Ref. [38], no citation. The thermal conductivity is shown as a linear function of temperature, $k(T) = 0.0330T + 11.85$, which gives conductivities ~1.1 $W \cdot m^{-1} \cdot K^{-1}$ higher that the equation of the linear fit of Del Grosso's data shown above.

(c) Klein (1962), table 3-39 of Ref. [7], cited APDA personal communication.
  (i) Rest et al. (2009), fifth data group in table 2.3 of Ref. [11], cited Klein. In this data group, the first temperature should be 25°C (instead of 23°C), the thermal conductivities listed for 300–1000°C should be shifted to 200–800°C, and the temperature 1000°C should be eliminated.

(d) Farkas (1967), table 10 of Ref. [8], cited Del Grosso. This listing is abbreviated, containing data only at room temperature, 20°C, and at the even hundreds of degrees Celsius.

A.7.1.3 Francis (1958) [49] as quoted by Touloukian [109]

Touloukian et al. [109] reported thermal conductivity vs. temperature data for U–5.4Mo, citing Francis as their source. A copy of Ref. [49] was not available, but it is reasonable to assume that the reported data are correct. The three data points are: 23.0 $W \cdot m^{-1} \cdot K^{-1}$ at 200°C, 25.5 $W \cdot m^{-1} \cdot K^{-1}$ at 380°C, and 28.5 $W \cdot m^{-1} \cdot K^{-1}$ at 487°C. No details were reported on the

specimen, but Fig. 39 of this Appendix shows TTT curves for U–5.4 Mo obtained by Van Thyne and McPherson [27] using different measurement techniques. It shows that U–Mo is near the lower limit of molybdenum content for metastable γ phase retention, so that, unless the sample had been γ quenched before the thermal conductivity measurements, there could be a considerable amount of the α and γ' phases present at the beginning of the measurement. Francis's data are shown in Fig. 56. A linear fit, a bilinear fit (exact), or a quadratic fit (exact) can be used for the three data points. The bilinear fit yields the equations

$$k(T) = 0.0139T + 20.2, (200 \leq T < 380) \quad (148)$$

$$k(T) = 0.0280T + 14.85, (380 \leq T < 487) \quad (149)$$

where k is in $W \cdot m^{-1} \cdot K^{-1}$ and T is in °C. Rest et al. [11] used this bilinear fit to produce the values of k for the composition labelled U–5Mo in his table 2.3. Matsui [46] also shows Francis's data with the bilinear fit in his fig. 8

A.7.1.4 Konobeevsky et al. (1958) [43]

Konobeevsky et al. presented their thermal conductivity vs. temperature data for U–9Mo in fig. 18 of Ref. [43]; five data points and a curve, presumed to be a fit to these data, are shown. No information was provided on the metallurgical state of the specimen. The data points have the following coordinates, determined by manual digitization: (117, 16.7), (188, 20.1), (270, 25.0), (344, 29.6), and (441, 35.4), where the first number is T in °C and the second is k in $W \cdot m^{-1} \cdot K^{-1}$. These data are shown in Fig. 56. Both Beghi in his table 4 [2] and Rest et al. in their table 2.3 reported data obtained from the curve shown in Konobeevsky et al.'s figure. A least squares quadratic fit of Konobeevsky et al.'s data points yields the equation:

$$k(T) = 2.30 \times 10^{-5}T^2 + 0.0454T + 11.02, (100 \leq T < 500) \quad (150)$$

where $k(T)$ is $W \cdot m^{-1} \cdot K^{-1}$ and T is in °C.

Both Rest et al. [11] and Burkes et al. [12] noted the significantly stronger temperature dependence of Konobeevsky et al.'s data and excluded it from consideration when developing their thermal conductivity correlations.

A.7.1.5 Roy et al. (1973) [50]

Roy et al. measured the thermal conductivity of a 5.5 cm long by 1.4 cm diameter cylinder machined from a cast ingot of U–9.50Mo. The U–Mo sample and an Armco iron standard of the same diameter as the sample were placed end to end with a heat source at the end of the standard and a cold source at the end of the sample to provide a thermal gradient. External heaters brought the sample and standard up to the measurement temperature. The thermal conductivity of the sample was calculated by comparing the temperature difference over a known length of the sample to that over a known length of the standard. Roy et al.'s thermal conductivity data are given in Table 31. Note the considerable uncertainty in the sample temperatures and, especially, in the measured thermal conductivities.

TABLE 31. THERMAL CONDUCTIVITY OF U–9.50MO AS A FUNCTION OF TEMPERATURE (ROY ET AL. [50])

Temperature (°C)	Thermal Conductivity ($W \cdot m^{-1} \cdot K^{-1}$)
50 ± 6.5	12.97 ± 1.26
212 ± 6.5	17.99 ± 2.52
308 ± 6.5	21.34 ± 2.52
404 ± 6.5	25.94 ± 2.18

A least squares quadratic fit of Roy et al.'s data vs. temperature essentially reproduces their plotted curve:

$$k(T) = 3.40 \times 10^{-5}T^2 + 0.0209T + 11.87, (50 \leq T < 404) \quad (151)$$

where $k(T)$ is $W \cdot m^{-1} \cdot K^{-1}$ and T is in °C.

A.7.1.6 Lee et al. (2000) [40]

Lee et al. measured the thermal conductivity of three specimens prepared from a nominal U–10Mo ingot; specimens G1 and G2 were γ quenched following 140 h soaks at 900°C, and specimen AG was α soaked for 140 h at 550°C prior to quenching. Their results are shown in table 5 and fig. 9 of Ref. [40] and are listed here in Table 32.

TABLE 32. THERMAL CONDUCTIVITY OF U–10Mo AS A FUNCTION OF TEMPERATURE DETERMINED BY LEE ET AL. FROM THEIR MEASURED VALUES OF THERMAL DIFFUSIVITY, SPECIFIC HEAT AND DENSITY [40]

Temperature (°C)	Thermal Conductivity ($W \cdot m^{-1} \cdot K^{-1}$)		
	Specimen G1	Specimen G2	Specimen AG
25	9.7	9.0	9.1
100	11.7	10.4	10.2
200	14.0	12.6	12.5
300	17.2	15.4	14.8
400	21.6	19.3	19.4
500	25.7	23.2	21.8

A least squares quadratic fit of Lee et al.'s data vs. temperature yield the following equations for (25 ≤ T < 500):

$$k_{G1}(T) = 2.99 \times 10^{-5}T^2 + 0.0179T + 9.34 \quad (152)$$

$$k_{G2}(T) = 3.13 \times 10^{-5}T^2 + 0.0136T + 8.66 \quad (153)$$

$$k_{G(ave)}(T) = 3.06 \times 10^{-5}T^2 + 0.0158T + 9.00 \quad (154)$$

$$k_{AG}(T) = 2.40 \times 10^{-5}T^2 + 0.0153T + 8.55 \quad (155)$$

where $k(T)$ is $W \cdot m^{-1} \cdot K^{-1}$ and T is in °C.

A.7.1.7 Burkes et al. (2010) [12, 13]

As reported in Ref. [12], Burkes et al measured the thermal diffusivity, using the laser flash method, of U–10.3Mo as a function of temperature. Using their values of specific heat and density as functions of temperature, measured on other specimens from the same as-cast ingot, they calculated the thermal conductivity of the as-cast material. This thermal conductivity was corrected for the porosity in the sample using the Maxwell–Eucken expression, which describes the thermal conductivity of a continuous, homogeneous material containing noninteracting spherical inclusions. Burkes et al. assumed the homogeneous material to be the U–10.3Mo and spherical inclusions to be uniformly distributed μm-sized air-filled pores, whose thermal conductivity is negligible compared to the thermal conductivity of the alloy. Their results are shown in fig. 8 of Ref. [12] and in table 4 of Ref. [13]. The numerical values of the thermal conductivities shown in their fig. 6, determined by manual digitization, and in their table 4 agree within the error of the digitization. The values of the thermal conductivity from their table 4 are given in Table 33, along with the value at 50°C from their fig. 6.

TABLE 33. THERMAL CONDUCTIVITY OF U–10.3Mo AS A FUNCTION OF TEMPERATURE (DETERMINED BY BURKES ET AL. FROM THEIR MEASURED VALUES OF THERMAL DIFFUSIVITY, SPECIFIC HEAT, AND DENSITY. [12, 13])

Temperature (°C)	Thermal Conductivity ($W \cdot m^{-1} \cdot K^{-1}$)
50	13.5
100	–
200	20.0
300	23.9
400	27.1
500	31.2
600	35.5
700	36.9
800	37.4

–:data not available.

A least squares quadratic fit of Burkes et al.'s data vs. temperature yield the following equation for ($25 \leq T < 500$):

$$k(T) = -2.25 \times 10^{-5} T^2 + 0.0528T + 10.49 \quad (156)$$

where $k(T)$ is $W \cdot m^{-1} \cdot K^{-1}$ and T is in °C.

A.7.2. Summary of thermal conductivity data

The thermal conductivity data discussed above in Section A.7.1 are displayed in Fig. 56. As discussed in Section A.7.1, least squares quadratic fits have been made for data sets containing more than three points except for the data of Burkes et.al., where a piecewise linear fit was used. These fit lines are also shown in Fig. 56

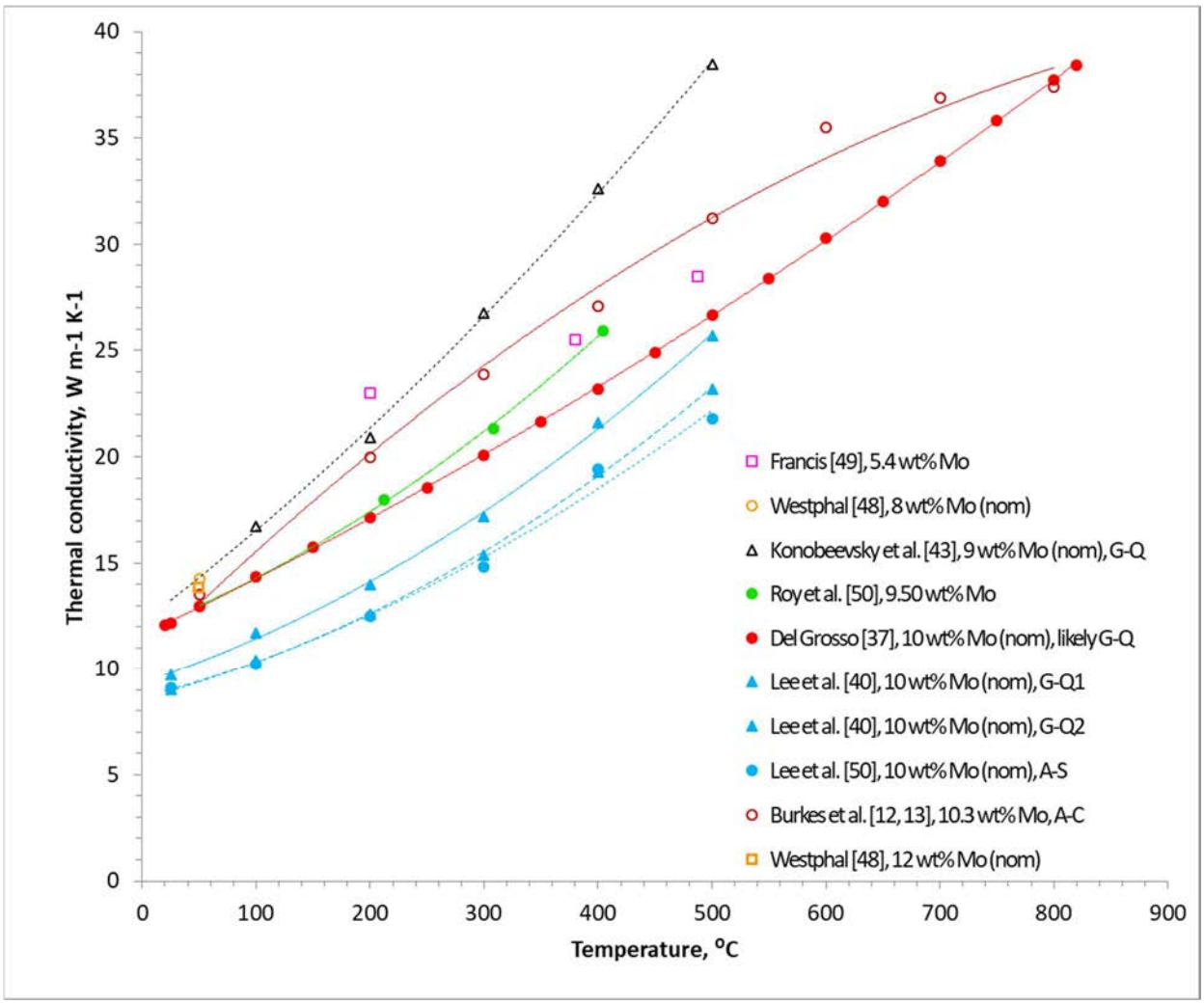

FIG. 56. Original U–Mo thermal conductivity data, shown with least squares quadratic fit lines for data sets containing more than three points. (Courtesy of Argonne National Laboratory).

Several comments can be made about the thermal conductivity datasets based on Fig. 56 and the various fit equations:

(a) Francis's data appear to be anomalous when compared to the other data shown in the figure. Also, as discussed in Section A.7.1.3, there could have been a large amount of γ' phase material in his test specimen; therefore, these data were excluded from further consideration and are denoted by open symbols.

(b) Owing to its anomalously strong temperature dependence, Konobeevky et al.'s data were excluded from further consideration and are also denoted by open symbols. The curvature of Burkes et al.'s data is opposite the that of each of the other datasets shown with filled symbols. Also, in contrast to the other datasets, Burkes et al.'s data from a machined as-cast specimen are not fit well with a quadratic function. It was seen in Section A.5.2.6 that their dilation traces were considerably more complex than those of investigators using γ quenched or α soaked specimens. For these reasons, Burkes et al.'s data also were excluded from further consideration and are denoted by open symbols.

(c) The data from the remaining five investigators fit into three groups:

(i) Del Grosso's and Roy et al.'s room-temperature thermal conductivities range from 12.2 to 13.0 $W \cdot m^{-1} \cdot K^{-1}$;

(ii) Lee et al.'s room-temperature thermal conductivities range from 9.0 to 9.7 W · m^{-1} · K^{-1}. It is not known why Lee et al.'s data are so much lower than the other data. It is also interesting to note that the data from Lee et al.'s second γ quenched specimen and from their α soaked specimen are quite similar;

(iii) Westphal's only reported two data points, 13.8 and 14.3 W · m^{-1} · K^{-1} at 50°C. A reasonable extrapolation to 25°C would lead to a thermal conductivity range of 13.1 to 13.7 W · m^{-1} · K^{-1}, which is close enough to the range of the data in item (c) (i) to be combined with it.

(d) One cannot discern a dependence of U–Mo thermal conductivity on Mo content within the range of 9 to 10.3 wt%.

(e) Even though the lowest thermal conductivity was measured for the one α soaked specimen, data for additional α soaked specimens would be needed to determine if there is a difference between α soaked and γ quenched specimens with Mo content between 9 and 10 wt%.

(f) A least squares quadratic fit of all of Westphal's, Roy et al.'s, and Del Grosso's data yields the equation:

$$k(T) = 6.95 \times 10^{-6}T^2 + 0.0267T + 11.86, (25 \leq T < 820) \quad (157)$$

where $k(T)$ is W · m^{-1} · K^{-1} and T is in °C.

(g) A least squares quadratic fit of all of Lee et al.'s data points yields the equation:

$$k(T) = 3.95 \times 10^{-5}T^2 + 0.00438T + 9.20, (25 \leq T < 500) \quad (158)$$

(h) A least squares quadratic fit of all of Lee et al.'s, Westphal's, Roy et al.'s, and Del Grosso's data points yields the equation:

$$k(T) = 1.69 \times 10^{-5}T^2 + 0.0210T + 10.52, (25 \leq T < 820) \quad (159)$$

REFERENCES

[1] SNELGROVE, J.L., et al., Development of very-high-density, low-enriched-uranium fuels, Nucl. Eng. Des. **178** (1997) 119-126.

[2] BEGHI, G., Gamma Phase Uranium–Molybdenum Fuel Alloys, Rep. EUR 4053 e, EURATOM Joint Nuclear Research Center Ispra Establishment, Brussels (1968).

[3] AHMANN, D., SNOW, A.I., WILSON, A.S., The Uranium–Molybdenum Binary System, Rep. CT-2946, Iowa State College, Ames, IA (1945).

[4] McGEARY, R.K., et al., Development and Properties of Uranium-Base Alloys Corrosion Resistant in High-Temperature Water. Part I Alloys Without Protective Cladding, Rep. WAPD-127, Westinghouse Electric Corp. Atomic Power Div., Pittsburgh, PA, (1955).

[5] KONOBEEVSKY, S.T., PRAVDUYK, N., KUTAITSEV, V., "Effect of irradiation on structure and properties of fissionable materials", International Conference on the Peaceful Uses of Atomic Energy, Geneva (1955).

[6] SALLER, H.A., ROUGH, F.A., "Alloys of uranium", International Conference on the Peaceful Uses of Atomic Energy, Geneva (1956).

[7] KLEIN, J.L., Uranium and its alloys, Nuclear Reactor Fuel Elements – Metallurgy and Fabrication, (KAUFMANN, A.R., Ed.) Interscience Publishers, NY (1962).

[8] FARKAS, M.S., Alloy fuels, Mechanical and Physical Properties of Fuels and Cladding Materials with Potentia for Use in Brookhaven's Pulsed Fast Reactor, Rep. BMI-X-455, Vol. 1 (Farkas, M.S., Ed.), Batelle Memorial Institute, Columbus Labs, OH (1967) 1-20.

[9] FACKELMANN, J.M., BAUER, A.A., MOAK, D.P., Literature Survey on Dilute Uranium Alloys for Sandia Booster Concept to Sandia Corporation, Rep. BMI-X-10264, Battelle Memorial Institute, Columbus, OH (1969).

[10] IVANOV, S.N., et al., Materials-technology investigations of fuel elements, irradiated in a reactor at the Obinsk Nuclear Power Plant, after standing 38 years in a depository, Atomic Energy **88** (2000) 184–189.

[11] REST, J., KIM, Y.S., HOFMAN, G.L., MEYER, M.K., HAYES, S.L., U–Mo Fuels Handbook Version 1.0, Rep. ANL-09/31, Argonne Natl Lab., IL (2006).

[12] BURKES, D.E., PAPESCH, C., MADDISON, A., HARTMAN, T., RICE, F., Thermo-physical properties of DU–10 wt.% Mo alloys, J. Nucl. Mater. **403** (2010) 160-166.

[13] BURKES, D.E., MICKUM, G.S., WACHS, D.M., Thermophysical Properties of U–10Mo Alloy, Rep. INL/EXT-10-19373, Idaho Natl Lab., ID (2010).

[14] BURKES, D. E., PRABHAKARAN, R., JUE, J.F., RICE, F., Mechanical properties of DU–xMo alloys with x = 7 to 12 weight percent, Metallurgical and Materials Transactions A **40A** (2009) 1069-1079.

[15] BURGESS, G.K., The international temperature scale, Bureau of Standards Journal of Research 1 **22** (1928) 635-640.

[16] STIMSON, H.F., The international temperature scale, J. Res. Natl. Bur. Stand. **42** (1949) 209-2017.

[17] COMITE INTERNATIONAL DES POIDS ET MESURES, “The international practical temperature scale of 1968,” Metrologia **5** 2 (1969). 35-44.

[18] PRESTON-THOMAS, H., The international temperature scale of 1990 (ITS-90), Metrologia **27** (1990) 3-10.

[19] CORRUCINI, R. J., Differences between the international temperature scales of 1948 and 1927, J. Res. Natl. Bur. Stand. **42** (1949) 133-136.

[20] ROSSINI, F. D., A report on the international practical temperature scale of 1968, Pure Appl. Chem. **22** 3-4 (1970) 555-570.

[21] MASSALSKI, T.B., et al., Binary Alloy Phase Diagrams, 2nd edn, Vol. 3, ASM International, OH (1990) 2682-2683.

[22] DWIGHT, A.E., The Uranium–Molybdenum equilibrium diagram below 900°C, J. Nucl. Mater. **2** (1960) 81-87.

[23] SALLER, H.A., ROUGH, F.A., VAUGHAN, D.A., The Constitution Diagram of Uranium-Rich Uranium–Molybdenum Alloys, Rep. BMI-72, Battelle Memorial Institute, Columbus, OH (1951).

[24] BOSTRUM, W.A., HALTEMAN, E.K., The metastable gamma phase in uranium base Molybdenum alloys, in Advances in Nuclear Engineering (Proc. 2nd Nuclear Engineering and Science Congress Part 2 Philadelphia,1957), New York and London (1957).

[25] HALTEMAN, E.K., The crystal structure of U–2Mo, Acta Crystallogr. **10** (1957) 166-169.

[26] GARG, S.P., ACKERMANN, R.J., The high temperature phase diagrams for Th–Mo, Th–Re, U–Mo, and U–Re; derived thermodynamical properties of refractory metal solutes in liquid thorium and uranium, J. Nucl. Mater. **64** (1977) 265-274.

[27] VAN THYNE, R.J., McPHERSON, D.J., Transformation kinetics of uranium–molybdenum alloys, Trans. Am. Assoc. Soc. Met. **49** (1957) 598.

[28] BLEIBERG, M., JONES, L., LUSTMAN, B., Phase chages in pile-irradiated uranium–base alloys, J. Appl. Phys. **27** (1956) 1270-1283.

[29] BELLOT, J., DOSIERE, P., HENRY, J., “Etude des alliages uranium–molybdene metaux,” Metaux Corros. Ind. **397** (1958) 1-12.

[30] DONZE, G., CABANE, G., Mechanisme de la decomposition de la phase gamma des alliages uranium–molybdene et uranium–molybdene-ruthenium, Mem. Etud. Sci. Rev. Metall. **LVII** (1960) 450.

[31] PETERSON, C., STEELE, W., DiGIALLONARDO, S., Isothermal Transformation Study of Some Uranium-Base Alloys, Rep. UCRL-7824, Univ. of California Lawrence Radiation Lab., Livermore, CA (1964).

[32] REPAS, P.E., GOODENOW, R., HEHEMANN, R., Transformation characteristics of U–Mo and U–Mo–Ti alloys, Transactions of the American Society of Metals. **57** (1964) 150-163.

[33] WILSON, A.S., RUNDLE, C.M., The structures of uranium metal Acta Crystal. **2** (1949) 126-127.

[34] NOMINE, A.M., BEDERE, D., MIANNAY, D., “Influence of Physio-chemical parameters on the mehanical properties of some isotropic uranium alloys”, in Physical Metallurgy of Uranium Alloys, Proc. Third Army Materials Technical Conference, Vail, CO, 1974, Brooke Hill,Chestnut Hill, MA, (1976).

[35] BURKES, D., HARTMANN, T., PRABHAKARAN, R., JUE, J., Microstructural characteristics of DU– xMo alloys with x = 7–12 wt% J. Alloy Compd. **2009** (2014) 140–147.

[36] LEENAERS, A., Surface-engineered low-enriched Uranium–Molybdenum fuel for research reactors, Gent, Belgium: UGENT/SCK-CEN (2014).

[37] DEL GROSSO, A., Compilation of Uranium–10 w/o Molybdenum Fuel Alloy Properties, Atomic Power Development Associates, Detroit, MI (1957).

[38] ATOMIC POWER DEVELOPMENT ASSOCIATES, "Enrico Fermi Power Plant," APDA, Detroit, MI (1959).

[39] GATES, J.E., et al., Irradiation Studies of U–10Mo Fuel Alloy, Battelle Memorial Institute, Columbus, OH (1961).

[40] LEE, S.H., et al., "An investigation of the thermophysical properties of U–Mo dispersion fuel meats", Proc. Int. Mtg on Reduced Enrichment for Research and Test Reactors, Las Vegas, 2000, Argonne Natl Lab., IL (2001).

[41] KIM, C.K., et al., "Fabrication of atomized U–Mo dispersion rod type fuel for irradiation test related to the qualification program", Proc. Int. Mtg on Reduced Enrichment for Research and Test Reactors, Las Vegas, NV, 2000, Argonne Natl Lab., IL (2001).

[42] SALLER, H.A., DICKERSON, R.F., MURR, W.E., Uranium Alloys for High-Temperature Application, Rep. BMI-1098, Batelle Memorial Institute, Columbus, OH (1956).

[43] KONOBEEVSKY, S.T., et al., "Some physical properties of uranium, plutonium and their alloys", Proc. 2nd United Nations Int. Conf. on the Peaceful Uses of Atomic Energy, Geneva, 1958, vol. 6, United Nations, Geneva (1958) 194–203.

[44] RIDDLE, J.R., "Thermal expansion of uranium–10% molybdenum alloy", Metallurgy Division Annual Progress Report for Period Ending May 31, 1961, Rep. ORNL-3160, Oak Ridge Natl Lab., TN (1961) 129.

[45] FARKAS, M., ELDRIDGE, E., Heat contents and specific heats of some uranium-bearing fuels, J. Nucl. Mater. **27**,(1968) 94–96.

[46] MATSUI, T., NATSUME, T., NAITO, K., Heat capacity measurements of U0.80Zr0.20 and U0.80Mo0.20 alloys from room temperature to 1300 K, J. Nucl. Mater. **167** (1989) 152–159.

[47] PARIDA, S.C., DASH, S., SINGH, Z., PRASAD, R., VENUGOPAL, V., Thermodynamic studies on uranium–molybdenum alloys, J. Phys Chem. Sol. **62** (2001) 585–597.

[48] WESTPAHL, R.C., Thermal Conductivity of Reactor Fuel Materials, Rep. AECD-3864, Westinghouse Electric Corporation, Atomic Power Division, Pittsburgh, PA (1954).

[49] FRANCIS, E. L., Uranium Data Manual, UKAEA, UK (1958).

[50] ROY, C., RADENAC, A., CADO, F., Conductivité thermique d'un alliage d'uranium à 10% en poids de molybdène entre 320 K et 680 K, J. Nucl. Mater. **48** (1973) 369–371.

[51] WALDRON, M.B., BURNETT, R.C., PUGH, S.F., The Mechanical Properties of Uranium–Molybdenum Alloys, Rep. AERE M/R 2554, Atomic Energy Research Establishment, Harwell (1958).

[52] HILLS, R.F., The mechanical properties of quenched Uranium–Molybdenum alloys, J. Nucl. Mater. **11** (1964) 149-162.

[53] HOGE, K.G., Some mechanical properties of uranium–10 weight percent molybdenum alloy under dynamic tension loads, J. Basic Eng. **88** (1966) 509–517.

[54] INTERNATIONAL ATOMIC ENERGY AGENCY, Thermophysical properties of Materials For Nuclear Engineering: A Tutorial and Collection of Data, IAEA, Vienna (2008).

[55] ASM INTERNATIONAL, ASMetals Handbook, Vol. 2 – Properties and Selection: Nonferrous Alloys and Special-Purpose Materials, 10th edn (LAMPMAN, S., ZORC, T., Eds), Materials Park, OH (1990).

[56] AMERICAN SOCIETY FOR METALS, ASMetals Handbook, (BOYER, H.E., GALL, T.L., Eds), Materials Park, OH (1985).

[57] HOLT, J.M., HO, C.Y. (Eds), Structural Alloys Handbook, 1996 ed., CINDAS/Purdue University, West Lafayette, IND (1996).

[58] VAN DEN BERGHE, S., DETAVERNIER, C., LEENAERS, A., AlSi matrices for U(Mo) dispersion fuel plates, J. Nucl. Mater. **439** 1 (2013) 7-18.

[59] TYE, R. HAYDEN, R., SPINNEY, S., The Thermal conductivity of selected alloys at low temperatures, Advances in Cryogenic Engineering **22** (1977) 136-144.

[60] KIM, Y.S., HOFMAN, G.L., ROBINSON, A.B., SNELGROVE, J.L., HANAN, N., Oxidation of aluminum alloy cladding for research and test reactor fuel, J. Nucl. Mater. **378** (2008) 220–228.

[61] WINTERGERST, M., DACHEUX, N., DATCHARRY, F., HERMS, E., KAPUSTA, B. , Corrosion of the AlFeNi alloy used for the fuel cladding in the Jules Horowitz research reactor, J. Nucl. Mater. **393** (2009) 369–380.

[62] MARCUM, W.R., WACHS, D.M., ROBINSON, A.B., LILLO, M.A., Aluminum cladding oxidation of prefined in-pile fueled experiments, J. Nucl. Mater. **471** (2016) 136-148.

[63] GRIESS, J., SAVAGE, H., ENGLISH, J., Effect of the heat flux on the corrosion of Aluminium by water Part IV Tests Relative to the Advanced Test Reactor and Correlation with Previous Results, Rep. ORNL-3451, Oak Ridge Natl Lab., TN (1964).

[64] PAWEL, S.J., FELDE, D.K., PAWEL, R.E., Influence of Coolant pH on Corrosion of 6061 Aluminum Under Reactor Heat Transfer Conditions, Rep. ORNL/TM-13083, Oak Ridge Natl Lab., TN (1995).

[65] FARREL, Performance of Aluminium in Research Reactors, in Comprehensive Nuclear Materials, Material Performance and Corrosion/Waste Materials **5** (2012) 143-175.

[66] JUVENELLE, A., GARRIDO-BERTON, M.H., TUFFERY, B., "RTR spent fuels reprocessing: nitric dissolution of aluminium alloys", Trans. Topical Mtg on Research Reactor Fuel Management, Aix-en-Provence, 2003, European Nuclear Society, Brussels (2003) 212–216.

[67] WANG, N., LEITCH, B., FU, L., DAVIDSON, A., "Measurements of Elastic Modulus of Hot-extruded U–Mo/Al Dispersion Fue", Proc. Int. Mtg on Reduced Enrichment for Research and Test Reactors, Chile, 2011, Argonne National Lab, IL (2011).

[68] LEE, S.H., M.J., PARK, KIM, C.K., Thermophysical Properties of U–Mo/Al Alloy Dispersion Fuel Meats, Int. J. Thermophys. **28** (2007) 1578.

[69] MARELLE, V., HUET, F., LEMOINE, P., "Thermo-mechanical modelling of U–Mo Fuels with MAIA", Trans. Topical Mtg on Research Reactor Fuel Management, München, 2004, European Nuclear Society, Brussels (2004) 164–168.

[70] CUNNINGHAM, M.E., PEDDICORD, K.L., Heat conduction in spheres packed in an infinite regular cubical array, Int. J. Heat Mass Transfer **24** 7 (1981) 1081-1088.

[71] HOFMAN, G.L., SNELGROVE, J.L., HAYES, S.L., MEYER, M.K., "Progress in development of low-enriched U–Mo dispersion fuels", Trans. Topical Mtg on Research

Reactor Fuel Management, Ghent, 2002, European Nuclear Society, Brussels (2002) 50-58.

[72] PORTER, D.L., EWH, A., Interaction Layer Characteristics in U–xMo Dispersion/Monolithic Fuels, Rep. INL/EXT-10-17972 Rev. 1, Idaho Natl Lab., ID (2010).

[73] ENIN, A., et al., "The review of fuel types for Russian research reactors, their fabrication and quality control", Trans. Topical Mtg on Research Reactor Fuel Management, Aachen, 2001, European Nuclear Society, Brussels (2001).

[74] RYU, H.J., KIM, Y.S., HOFMAN, G.L. PARK, J. M., KIM, C.K., Heats of formation of (U, Mo) Al3 and U (Al, Si) 3, J. Nucl. Mater. **358** (2016) 52-56.

[75] RYU, H.J., HAN, Y.S., PARK, J.M., PARK, S.D., KIM, C.K., Reaction layer growth and reaction heat of U–Mo/Al dispersion fuels using centrifugally atomized powders, J. Nucle. Mater. **321** (2003) 210-220.

[76] LEENAERS, A., VAN DEN BERGHE, S., DETAVERNIER, C., Determination of activation energies of the U(Mo)/Si and U(Mo)/Al solid state reaction using in-situ X-ray diffraction and Kissinger analysis, Solid State Sciences **14** 8 (2012) 1133-1140.

[77] BARIN, I., Thermochemical data of pure substances, VCH, Weinheim (1995).

[78] PFEIL, P.L., The constitution of uranium–molybdenum alloys, J. Inst. Met. **77** (1950) 553-570.

[79] SEYBOLT, A.U., MCKECHNIE, R.K., Discussion on the paper by Dr. P.C.L. Pfeil: The constitution of uranium–molybdenum alloys, J. Inst. Met. **78** (1951) 760.

[80] TUCKER Jr., C.W., Discussion on The constitution of uranium–molybdenum alloys by Dr. P.C.L. Pfeil, Rep. AECD-3092, Knolls Atomic Power Lab, NY (1951).

[81] PFEIL, P.L., Discussion on the paper by Dr. P.C.L. Pfeil: The constitution of uranium–molybdenum alloys, J. Inst. Met. **78** (1951) 762-763.

[82] SALLER, H.A., ROUGH, F.A., Alloys of Uranium with Zirconium, Chromium, Columbium, Vanadium, and Molybdenum, Rep. BMI-752, Battelle Memorial Institute, Columbus, OH (1952).

[83] ROUGH, F.A., BAUER, A.A., Constitution of Uranium and Thorium Alloys, Rep. BMI-1300, Battelle Memorial Institute, Columbus, OH (1958).

[84] LEHMANN, J., Processus des trasformations dans les alliages uranium–molybdene de faibles teneurs en molybdene, J. Nucl. Mater. **2** 2 (1960) 152-168.

[85] DWIGHT, A.E., Phase Diagrams of the Uranium–Fissium Elements, in Quarterly Report July, August, and September, 1957 Metallurgy Division, Rep. ANL-5797, Argonne Natl Lab., IL (1957) 51.

[86] STREETS, F., STOBO, J., The uranium–molybdenum–carbon equilibrium diagram, J. Inst. Metal **92** (1964) 171–174.

[87] ACKERMANN, R.J., RAUH, E.G., Determination of liquidus curves for the Th–W, Th–Ta, Zr–W, and Hf–W systems: the annomalous behavior of metallic thorium, High Temp. Sci. **4** (1972) 272-282.

[88] LUNDBERG, L.B., High-temperature interdiffusion and phase equilibria in U–Mo, J. Nucl. Mater. **167** (1989) 64-75.

[89] HANSEN, M., Anderko, K., Constitution of Binary Alloys, 2nd ed., New York: McGraw-Hill, 1958.

[90] ELLIOT, R.P. HANSEN, M., Constitution of Binary Alloys, First Supplement, New York: McGraw-Hill, 1965.

[91] SHUNK, F.A., HANSEN, M.A.K., Constitution of Binary Alloys, Second Supplement, McGraw-Hill, NY (1969).

[92] HULTGREN, R., DESAI, P., GLEISER, M., HAWKINS, D., Select values of thermodynamic properties of binary alloys, American Society for Metals (1973).

[93] HAWKINS, D.T. HULTGREN, R., Constitution of binary alloys, in Metals Handbook, 8th ed., Vol. 8, (LYMAN, T., Ed.), American Society for Metals, Metals Park, OH (1973).

[94] BREWER, L. LAMOREUX, R.H., II. Phase Diagrams, Molybdenum: Physico-Chemical Properties of its Compounds and Alloys, no. Atomic Energy Review, Special Issue No. 7, (1980) 195-358.

[95] GOMOZOV, L.I., LYUTINA, Eh.M., IVANOV, O.S., Solubility of zirconium, niobium and molybdenum in α–uranium, Izv. Akad. Nauk SSSR, Metally **2** (1970) 210–215 (in Russian).

[96] BRANDES, E., BROOK, G., Smithells Metals Reference Book, 7th (paperback) edition with corrections, 7th Ed., Butterworth–Heinemann, Oxford (1998).

[97] GALE, W., TOTEMEIER, T., Smithells Metals Reference Book 8th Ed., Oxford (2004).

[98] OKAMOTO, H., Mo–U (Molybdenum–Uranium), Journal of Phase Equilibria and Diffusion, **33** (2012) 497.

[99] BERCHE, A. et al., Calphad thermodynamic description of some binary systems involving U, J. Nucl. Mater. **411** (2011) 131–143.

[100] DAHL, A.I., CLEAVES, H.E., The freezing point of uranium, J. Res. Natl. Bur. Stand. **42** (1949) 513-517.

[101] BRAGG, Conversion of kX Units to Angstrom Units, Journal of Scientific Instruments **24** (1947).

[102] BECKER, P., History and progress in the accurate determination of the Avogadro constant, Rep. Prog. Phys. **64** (2001) 1945-2008.

[103] PARK, J.M., Neutron diffraction analyses of U–(6–10 wt.%)Mo alloy powders fabricated by centrifugal atomization, J. Nucl. Mater. **397** (2010) 27-30.

[104] VEGARD, L., Die konstitution der mischkristalle und die raumfullung der atome, Zeit. Phys. **5** 2 (1921) 17-26.

[105] FERRO, R., MARAZZA, R., III. Crystal structure and density data, III-1. Alloys and compounds other than halides and chalcogenides, Molybdenum: Physico-Chemical Properties of its Compounds and Alloys, no. Atomic Energy Review, Special Issue No. 7, (1980) 359-508.

[106] BLESSING, W.G., et al., Summary of the APDA Fuel Development Programs, Rep. APDA-143, Atomic Power Development Associates, MI (1961).

[107] BRIDGE , J.R., et al., X ray diffraction determination of the coefficients of expansion of alpha uranium, Transactions of the American Institute of Mining Engineers **206** (1956) 1282.

[108] SALLER, H.A., DICKERSON, R.F., BAUER, A.A., DANIEL, N.E., Properties of a Fissium-Type Alloy, Battelle Memorial Institute, (1956).

[109] TOULOUKIAN, Y.S., POWELL, R.W., HO, C.Y., KLEMENS, P.G., Thermophysical Properties of Matter, vol. 1 Thermal Conductivity - Metallic Elements and Alloys, IFI/Plenum, New York and Washington (1970).

[110] COPLAN, T.B., PEISER, H.S., History of recommended atomic weight values from 1882 to 1997: a comparison of differences from current values to the estimated uncertainties of earlier values, Pure Applied Chemistry **70** 1 (1998) 237-257.

[111] MEJIA, J., et al., Atomic weights of the elements 2013 (IUPAC technical report), Pure Applied Chemistry **88** 3 (2016) 265-291.

[112] HOFMAN, G.L., SNELGROVE, J.L., Dispersion Fuels, Materials Science and Technology: A Comprehensive Treatment (CAHN, R.W., HAASEN, P., KRAMER, E.J., Eds), vol. 10A Nuclear Materials (FROST, B.R.T., Ed.), VCH, New York (1994)

[113] TOULOUKIAN, Y.S., KIRBY, R.K., TAYLOR, R.E., DESAI, P.D., Thermophysical Properties of Matter, vol. 12 Thermal Expansion - Metallic Elements and Alloys, IFI/Plenum, New York and Washington (1975).

ABBREVIATIONS

AECL	Atomic Energy of Canada Limited
ANL	Argonne National Laboratory
APDA	Atomic Power Development Associates, Inc.
bcc	body centred cubic
BMI	Battelle Memorial Institute
DPH	diamond pyramid hardness
DU	depleted uranium
IPTS	International Practical Temperature Scale
ITS	International Temperature Scale
IUPAC	International Union of Pure and Applied Chemistry
KAERI	Korean Atomic Energy Research Institute
KAPL	Knolls Atomic Power Laboratory
LEU	low enriched uranium
ORNL	Oak Ridge National Laboratory
RERTR	Reduced Enrichment for Research and Test Reactors
SI	International System of Units
TTT	time-temperature-transformation
U–Mo	uranium molybdenum
UTS	ultimate tensile strength

CONTRIBUTORS TO DRAFTING AND REVIEW

Adelfang, P.	International Atomic Energy Agency
Arkhangelsky, N.	Joint Stock Company Atomic Energy Power Corporation, Russian Federation
Dobrikova, I.	Rosatom, Russian Federation
Finlay, M. R.	Australia's Nuclear Science and Technology Organisation, Australia
Fuentes Solis, N.O.	International Atomic Energy Agency
Hofman, G.L.	Argonne National Laboratory, United States of America
Jarousse, C	French Alternative Energies and Atomic Energy Commission, France
Koonen, E.	SCK•CEN, Belgium
Keiser, D.	Idaho National Laboratory, United States of America
Lemoine, P.	French Alternative Energies and Atomic Energy Commission, France
Leenaers, A.	SCK•CEN, Belgium
Marshall, F.	International Atomic Energy Agency
Meyer, M.	Idaho National Laboratory, United States of America
Muhammad Nor, A.W.	International Atomic Energy Agency
Park, Jong-Man	Korean Atomic Energy Research Institute, Republic of Korea
Ryu, Ho Jin	Korean Atomic Institute of Science and Technology, Republic of Korea
Shropshire, K.	Consultant, United States of America
Snelgrove, J.	Argonne National Laboratory, United States of America
Swainson, I.	International Atomic Energy Agency
Van den Berghe, S.	SCK•CEN, Belgium
Wachs, D.	Idaho National Laboratory, United States of America
Wang, N.	Canadian National Laboratories, Canada

Consultants meetings
Vienna, Austria, 8–10 December 2009, 16–17 October 2014
Bucharest, Romania, 19 April 2015
Berlin, Germany, 13 March 2016

IAEA
International Atomic Energy Agency

No. 26

ORDERING LOCALLY

IAEA priced publications may be purchased from the sources listed below or from major local booksellers.

Orders for unpriced publications should be made directly to the IAEA. The contact details are given at the end of this list.

NORTH AMERICA

Bernan / Rowman & Littlefield

15250 NBN Way, Blue Ridge Summit, PA 17214, USA
Telephone: +1 800 462 6420 • Fax: +1 800 338 4550

Email: orders@rowman.com • Web site: www.rowman.com/bernan

REST OF WORLD

Please contact your preferred local supplier, or our lead distributor:

Eurospan Group

Gray's Inn House
127 Clerkenwell Road
London EC1R 5DB
United Kingdom

Trade orders and enquiries:

Telephone: +44 (0)176 760 4972 • Fax: +44 (0)176 760 1640
Email: eurospan@turpin-distribution.com

Individual orders:

www.eurospanbookstore.com/iaea

For further information:

Telephone: +44 (0)207 240 0856 • Fax: +44 (0)207 379 0609
Email: info@eurospangroup.com • Web site: www.eurospangroup.com

Orders for both priced and unpriced publications may be addressed directly to:

Marketing and Sales Unit
International Atomic Energy Agency
Vienna International Centre, PO Box 100, 1400 Vienna, Austria
Telephone: +43 1 2600 22529 or 22530 • Fax: +43 1 26007 22529
Email: sales.publications@iaea.org • Web site: www.iaea.org/publications

International Atomic Energy Agency
Vienna